Internal Report
DESY F1-87-01

On the Optimization of the Energy Resolution of Hadron Calorimeters

DISSERTATION

zur Erlangung des Doktorgrades
des Fachbereichs Physik
der Universität Hamburg

vorgelegt von

Edgar Bernardi
aus Bendorf-Mülhofen

Hamburg 1987

On the Optimization of the Energy Resolution of Hadron Calorimeters

DISSERTATION

zur Erlangung des Doktorgrades
des Fachbereichs Physik
der Universität Hamburg

vorgelegt von

Edgar Bernardi

aus Bendorf-Mülhofen

Hamburg
1987

Gutachter der Dissertation: Prof. Dr. E. Lohrmann
Prof. Dr. F.-W. Büßer

Gutachter der Disputation: Prof. Dr. E. Lohrmann
Prof. Dr. G. Heinzelmann

Datum der Disputation: 20. 1. 1988

Sprecher des
Fachbereichs Physik
und Vorsitzender des
Promotionsausschusses: Prof. Dr. P. E. Toschek

Abstract

Measurements on hadron sampling calorimeters are presented. The calorimeters consisted of lead- or depleted uranium plates and of scintillator plates of different thicknesses. Design properties which influence the energy resolution were investigated. It is shown that the thickness of absorber- and scintillator plates is a very important parameter. The absorber material and plate thickness leading to the optimum energy resolution of a hadron calorimeter are determined.

A high energy resolution is indispensable to reconstruct precisely jets in scattering processes at high Q^2 with the ZEUS detector at the electron-proton storage ring HERA. The measurements on hadron sampling calorimeters show that the energy resolution of such instruments can be optimized if one reduces parts of the strongly fluctuating fraction of nondetectable energy. This can be done indirectly by elastic collisions of the released spallation- and fission-neutrons with protons of the hydrogen atoms in the scintillator material. In addition, the fluctuating electromagnetic fraction of the hadronic shower due to neutral pion decays has to be compensated such that there is, on the mean, an equal response in the calorimeter to electromagnetic and purely hadronic showers. This is described by the fraction e/h. The strength of compensation can be influenced by the choice of the absorber material and the thickness ratio of the absorber plates to make $e/h = 1$. In this case the energy resolution reaches its optimum value.

The hadronic energy resolution of a lead-scintillator calorimeter with a thickness ratio of passive to active absorber of $R_d = 0.95$ is measured to $\frac{\sigma_E}{E}(\mathrm{h}) = \frac{41.0\%}{\sqrt{E[GeV]}} + 6.1\%$ between 3 and 9 GeV. The e/h-ratio is $< e/h >= 1.34$ and its deviation from 1 causes the large additive term in the hadronic energy resolution. The energy resolution for hadrons improves for a depleted uranium-scintillator calorimeter of $R_d = 0.64$ to $\frac{\sigma_E}{E}(\mathrm{h}) = \frac{29.6\%}{\sqrt{E[GeV]}} + 3.2\%$ between 3 and 9 GeV at $< e/h >= 1.10$. With a depleted uranium-scintillator calorimeter of $R_d = 2.0$ one can achieve overcompensation, i.e. $< e/h >= 0.76$, at an hadronic energy resolution of $\frac{\sigma_E}{E}(\mathrm{h}) = \frac{37.7\%}{\sqrt{E[GeV]}} + 3.4\%$ between 5 and 40 GeV. The optimum energy resolution of $\frac{\sigma_E}{E}(\mathrm{h}) = \frac{32.9\%}{\sqrt{E[GeV]}} + 0.5\%$ between 10 and 100 GeV at $< e/h >= 1.00$ is achieved for $R_d = 1.07$.

Starting from predictions obtained from Monte Carlo calculations, compensation is also achieved with a lead-scintillator calorimeter for $R_d = 4.0$. The measured energy resolution is $\frac{\sigma_E}{E}(\mathrm{h}) = \frac{44.2\%}{\sqrt{E[GeV]}}$ between 3 and 75 GeV at $< e/h >= 1.05$.

The results are discussed and compared with results of other measurements and with predictions from Monte Carlo simulations.

Zusammenfassung

In dieser Arbeit werden Messungen vorgestellt, die an Hadron-'Sampling'-Kalorimetern vorgenommen wurden. Die Kalorimeter bestanden aus Blei- oder abgereicherten Uranplatten und aus Szintillatorplatten unterschiedlicher Dicke. Es wurden Konstruktionseigenschaften untersucht, die die Energieauflösung beeinflussen. Es kann gezeigt werden, daß die Dicke der Absorber- und Szintillatorplatten ein sehr wichtiger Parameter darstellt. Das Absorbermaterial und die Plattendicken, die zur optimalen Energieauflösung eines Hadron-Kalorimeters führen, werden ermittelt.

Eine hohe Energieauflösung ist unerläßlich, um 'jets' in Streuprozessen bei hohem Q^2 mit dem ZEUS-Detektor am Elektron-Proton Speicherring HERA präzise rekonstruieren zu können. Die Messungen an Hadron-'Sampling'-Kalorimetern zeigen, daß die Energieauflösung dieses Instruments optimiert werden kann, wenn der stark fluktuierende Anteil nicht nachweisbarer Energie reduziert wird. Dies kann indirekt über elastische Stöße der freiwerdenden Spallations- und Spaltneutronen mit den Protonen des wasserstoffhaltigen Szintillatormaterials geschehen. Zusätzlich muß der fluktuierende elektromagnetische Anteil des hadronischen Schauers, der im wesentlichen von neutralen Pion-Zerfällen herrührt, so kompensiert werden, daß der elektromagnetische und der rein hadronische Schauer ein gleichgroßes Signal im Kalorimeter erzeugt. Dies wird durch das e/h-Verhältnis ausgedrückt. Die Stärke dieser Kompensation kann durch Wahl der Absorbermaterialien und durch das Verhältnis der Absorberplattendicke beeinflußt werden, um $e/h = 1$ zu erzielen. Die Energieauflösung erreicht dann ihren optimalen Wert.

Die Energieauflösung für Hadronen eines Blei-Szintillator Kalorimeters mit einem Verhältnis der passiven zu aktiven Absorberplattendicken von $R_d = 0.95$ wird zu $\frac{\sigma_E}{E}(\mathrm{h}) = \frac{41.0\%}{\sqrt{E[GeV]}} + 6.1\%$ zwischen 3 und 9 GeV gemessen. Das gemessene e/h-Verhältnis beträgt $< e/h >= 1.34$ und seine Abweichung von 1 verursacht den großen additiven Beitrag in der hadronischen Energieauflösung. Die Energieauflösung für Hadronen verbessert sich für ein Kalorimeter aus abgereichertem Uran und Szintillator mit $R_d = 0.64$ auf $\frac{\sigma_E}{E}(\mathrm{h}) = \frac{29.6\%}{\sqrt{E[GeV]}} + 3.2\%$ zwischen 3 und 9 GeV bei $< e/h >= 1.10$. Mit einem abgereicherten Uran-Szintillator Kalorimeter mit $R_d = 2.0$ läßt sich Überkompensation, d.h. $< e/h >= 0.76$, erreichen bei einer hadronischen Energieauflösung von $\frac{\sigma_E}{E}(\mathrm{h}) = \frac{37.7\%}{\sqrt{E[GeV]}} + 3.4\%$ zwischen 5 und 40 GeV. Die optimale Energieauflösung von $\frac{\sigma_E}{E}(\mathrm{h}) = \frac{32.9\%}{\sqrt{E[GeV]}} + 0.5\%$ zwischen 10 und 100 GeV bei $< e/h >= 1.00$ wird für $R_d = 1.07$ erreicht.

Ausgehend von Vorhersagen aus Simulationsrechnungen wird Kompensation ebenso mit einem Blei-Szintillator Kalorimeter bei $R_d = 4.0$ erzielt. Die gemessene Energieauflösung beträgt $\frac{\sigma_E}{E}(\mathrm{h}) = \frac{44.2\%}{\sqrt{E[GeV]}}$ zwischen 3 und 75 GeV bei $< e/h >= 1.05$.

Die Ergebnisse werden vergleichend gegenübergestellt, mit denen anderer Messungen und mit Vorhersagen aus Simulationsrechnungen verglichen.

Contents

List of Figures

List of Tables

Chapter 1

Introduction

According to the present understanding the proton has a rather complicated structure, which in the description of the theory of the strong interaction (QCD) is constituted by valence quarks and a sea of quarks and antiquarks, bound by the strong gluonic forces. This structure can be probed by lepton-proton scattering, as examplified by the pioneer experiments on deep inelastic electron-proton scattering, and later on by experiments with high energy muon and neutrino beams. The HERA storage ring, which is presently beeing constructed, will allow such measurements at momentum transfers and therefore at an equivalent spatial resolution which greatly surpasses investigations that have been carried out so far.

In the final state of the inelastic electron-proton scattering process the quarks manifest themselves as 'jets', i.e. as particle streams of high multiplicity and high energy density.

Hadron calorimeters are suitable instruments for the detection of jets. The importance of these devices as the essential part of detectors grows with the present construction of new particle accelerators like HERA or LEP and may command the center of attention for still larger projects presently under discussion [1]. Several workshops on HERA experiments [EXP83, DIS85] and SSC studies for detector research and development [SSC86] reflect the need of hadron calorimeters for future experiments.

A calorimeter is a detector absorbing the total incident energy of a particle while generating a signal that is proportional to this energy. One of the first large detectors of this kind built by N.L. Grigorov and coworkers in 1957 was used in cosmic ray physics [MUR67]. It is desirable to use a dense material in such a calorimeter in order to absorb and an active material to detect all the energy of the incoming particle. Those features are combined in materials like *NaI* or lead glass; hence compact electromagnetic calorimeters have been built by using *NaI* forming the Crystal Ball Detector at SPEAR or by using lead glass for the electromagnetic calorimeter of the JADE detector at PETRA. Another way to combine these features is to stack thin plates of dense material alternating with thin layers of detector material. An electromagnetic calorimeter like the lead-liquid argon calorimeter of the TASSO detector at PETRA or an hadron calorimeter out of marble and proportional tubes/scintillator plates forming the CHARM detector at the SPS at CERN have been built in this manner.

In electromagnetic calorimeters the energies of electrons, positrons and photons are measured. The underlying physics is well understood and recent developments aim at finding new materials (e.g. *BGO*, *CsI*) with excellent energy resolution (e.g. $\sim 0.02/\sqrt{E[GeV]}$ for *BGO*) and studying new readout methods with new light collection (e.g. fibers) and conversion systems (e.g. photo diodes, vacuum triodes).

Hadron calorimeters, however, have a poorer energy resolution of $0.5-1.0/\sqrt{E[GeV]}$, depending on the calorimeter configuration. The reason for the poor energy resolution is attributed to the following fact: a hadronic particle penetrating into a calorimeter deposits its energy in form of ionization loss, in nuclear interactions like excitation, spallation and fission of nuclei and consumption of nuclear binding energy. Only part of the deposited energy can be detected directly in the readout medium, while fluctuating fractions of the deposited energy remain undetectable. These fluctuations may be large, thus generating a broad distribution of the detected signal.

---

[1] SSC: Superconducting Super Collider, USA

The idea to compensate for the undetected energy due to nuclear interactions was first introduced by W.J. Willis who proposed to use fissionable material like ^{238}U in order to recover some of the undetected energy [FAB75].

A huge effort went into the theoretical investigations to understand the shower development in hadron calorimeters and the mechanism of compensation. By the help of simulation programs one has tried to describe the generation and development of a nuclear cascade in a hadron calorimeter [GAB73], including nuclear fission of ^{238}U later on [GAB78]. Only recently a major breakthrough has been achieved based on extended theoretical and experimental studies.

T.A. Gabriel and coworkers improved the simulation package called CALOR, using the HETC (High-Energy Nucleon-Meson Transport Code), a three dimensional simulation of the transport of a nucleon and meson cascade together with the neutron transport program MORSE and the EGS code for electromagnetic shower calculations [GAB85]. This program package has also been used by J. Brau [BRA85] for a comparison with measurements of different calorimeter configurations.

H. Brückmann and coworkers [BRÜ86] used a simulation program called HERMES that includes a modified version of HETC (HETC-KFA), MORSE-KFA and EGS-KFA [BRÜ87].

With the help of simplified simulation programs, R. Wigmans investigated the various influences of the shower components on the energy resolution of a hadron calorimeter. Predictions for the energy resolution of different hadron calorimeters have thus been made [WIG87].

On the experimental side, measurements with uranium-scintillator calorimeters have been performed to investigate the energy resolution and its dependence on the electromagnetic to hadronic response (e/h-ratio) [BOT81b, AKE85, AKE87, AND86, DEV86, CAT87a].

Furthermore, a massive uranium stack as well as different uranium-scintillator calorimeter configurations have been exposed to a hadron beam by C. Leroy and coworkers and the induced radioactivity has been measured after dismanteling the stacks [LER86]. From this measurement the total neutron yield in the shower development and the number of fissions, the shower profile, the influence of the readout material on the composition of the shower etc. could be deduced.

Taking the predictions of R. Wigmans and H. Brückmann, a lead-scintillator calorimeter was built by U. Kötz and coworkers and tested in trying to achieve compensation with lead absorber as well [BER87].

Many of those theoretical and experimental studies were motivated by the requirement of achieving the best energy resolution possible in hadron calorimeters for new detectors. A high energy resolution of a hadron calorimeter is essential to measure the transverse momentum spectrum of scattering processes or the missing energy carried away by neutrinos.

The Axial Field Spectrometer (AFS) at the Intersecting Storage Ring (ISR) at CERN is one of the detectors with a hadron calorimeter of high energy resolution. This calorimeter is made of uranium/copper-scintillator plates and achieved an energy resolution of $\sigma_E/E(\mathrm{h}) = 0.36/\sqrt{E\,[GeV]}$ [AKE85].

Many experimental investigations were carried out in the framework of the development of the HELIOS and the ZEUS detector. HELIOS is a detector at the Super Proton Synchrotron (SPS) at CERN to study reactions of heavy-ion collisions and the calorimeter used is an upgraded version of the AFS hadron calorimeter [AKE87]. The ZEUS detector presently under construction at DESY will be able to detect reactions of electron-proton scattering processes at HERA [ZEU85]. The kinematic quantities of those processes, in particular of charged current events, have to be known very precisely from the calorimeter measurements of the jet energy and the angle. A good energy resolution will allow a precise measurement of the cross sections in the entire possible kinematic range.

This work describes investigations carried out in the framework of the ZEUS collaboration

- to understand the mechanism of compensation and the dependence on the energy resolution of a hadron calorimeter on different parameters like absorber material, thicknesses of absorber plates, light yield and uniformity of the light read-out, longitudinal and transverse leakage, etc.;
- to learn how to build an hadron calorimeter by eliminating the sources of detector imperfections like nonuniform readout, air gaps, attenuation lengths of the scintillator plate,

etc.;

- to come to a fundamental understanding of calorimetry, which can lead to a scientific design of a hadron calorimeter well suited for the use within the ZEUS detector.

Chapter 2

The ZEUS Detector at the HERA Storage Ring

2.1 Physics at the HERA Storage Ring

2.1.1 Survey

HERA is a high energy electron-(positron-) proton beam facility presently under construction at the DESY laboratory in Hamburg [HER81]. At nominal beam energies of $30\,GeV$ for electrons (positrons) and $820\,GeV$ for protons it will provide collisions yielding a center-of-mass (cms) energy of $\sqrt{s} = 314\,GeV$. Fig. 2.1 shows the layout of the storage ring HERA with the linear accelerators, two synchrotrons and the PETRA storage ring as preaccelerators.

Electron-proton collisions at HERA open the opportunity to study the following main areas of physics [ECF80, EXP83, ZEU85, CAS87]:

1. Measurements of Structure Functions at the Highest Momentum Transfers and Test of Quantum Chromodynamics (QCD)
2. Test of Electroweak Interactions at the Highest Energies
    - search for further weak bosons
    - search for right handed currents
3. Search for New Particles
    - leptoquarks
    - excited quarks and leptons
    - supersymmetric particles
    - pair production of heavy quarks
    - substructure of quarks.

2.1.2 Kinematics

Considering the kinematics of *ep*-collisions at HERA energies one can derive kinematic limits for the occurence of various processes starting from the *ep*-scattering diagrams Fig. 2.2 (neutral current) and Fig. 2.3 (charged current).

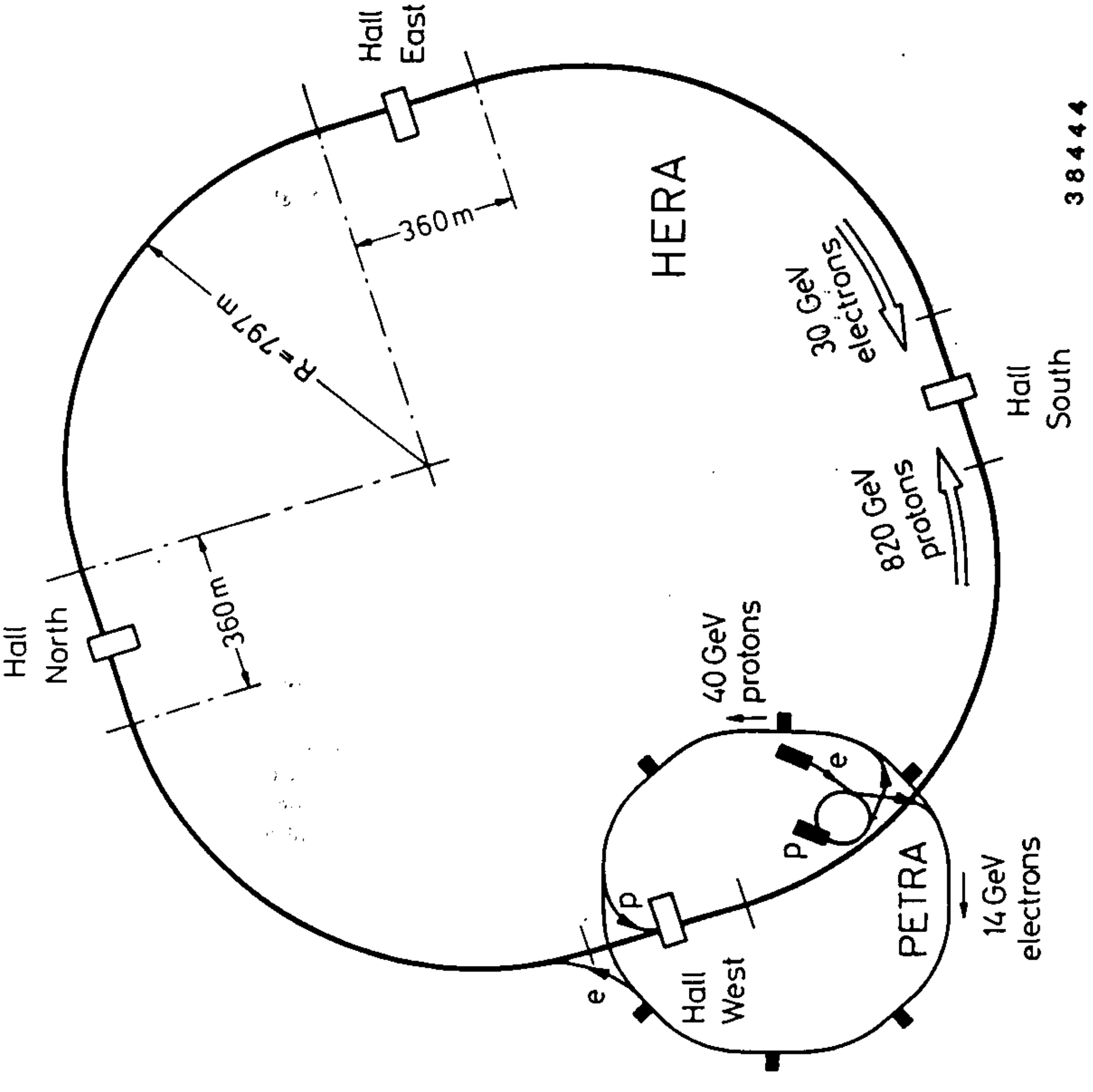

Figure 2.1: Schematic View of the *ep* Storage Ring HERA with its Preaccelerators [WOL86]

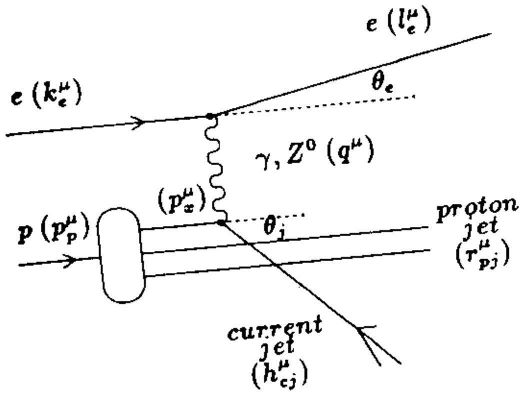

Figure 2.2: Neutral Current *ep*-Scattering Diagram (four vectors of particles are given in brackets)

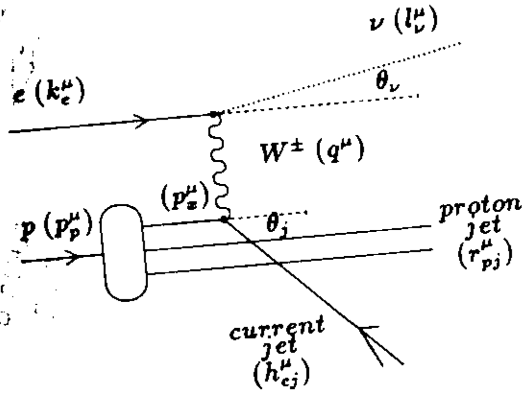

Figure 2.3: Charged Current *ep*-Scattering Diagram (four vectors of particles are given in brackets)

The four momentum vectors of the particles given in brackets are k_e^μ for the incoming electron of total energy E_e, p_p^μ for the incoming proton of total energy E_p, $l_{e,\nu}^\mu$ for the scattered lepton of total energy $E'_{e,\nu}$, r_{pj}^μ, h_{cj}^μ for the proton and current jets and p_x^μ for the incoming parton. The center of mass (cms) energy of the reaction is known from the colliding particle energies, and at the high energies considered here:

$$\sqrt{s} = 2\sqrt{E_e\, E_p} \tag{2.1}$$

$\sqrt{s}\ldots$ center of mass energy
$E_e\ldots$ beam energy of electrons
$E_p\ldots$ beam energy of protons.

The inclusive scattering process can be described by the two variables

$$\begin{aligned} q^2 &= (k_e^\mu - l_{e,\nu}^\mu)^2 \\ &\equiv -Q^2 \end{aligned} \tag{2.2}$$

$q^2\ldots$ four momentum transfer squared
$k_e^\mu\ldots$ four momentum of incoming electron
$l_{e,\nu}^\mu\ldots$ four momentum of scattered electron or neutrino

and

$$W^2 = (q^\mu + p_p^\mu)^2 \tag{2.3}$$

W^2... total mass of final hadronic state squared
q^μ... four momentum transfer

or,

$$x = \frac{Q^2}{2\,(q_\mu\, p_p^\mu)} = \frac{Q^2}{2\, m_p\, \nu} \tag{2.4}$$

x... in the quark parton model fraction of the four momentum of the proton carried by the struck quark
m_p... proton mass

and

$$y = \frac{q_\mu\, p_p^\mu}{k_e^\mu\, p_{p,\mu}} = \frac{2\, m_p\, \nu}{s} \tag{2.5}$$

with

$$\nu = \frac{q_\mu\, p_p^\mu}{m_p}. \tag{2.6}$$

The variables Q^2, x and y can be determined in the limit of small rest masses from the outgoing lepton energy E_e' and its scattering angle θ_e:

$$Q^2 = 4\, E_e\, E_e' \sin^2\frac{\theta_e}{2}\,, \tag{2.7}$$

$$x = \frac{E_e' \sin^2\dfrac{\theta_e}{2}}{E_p\left(1 - \dfrac{E_e'}{E_e}\cos^2\dfrac{\theta_e}{2}\right)} \tag{2.8}$$

$$y = 1 - \frac{E_e'}{E_e}\cos^2\frac{\theta_e}{2}. \tag{2.9}$$

In the case of charged currents the energy E_ν' and the scattering angle θ_ν of the outgoing lepton are not measureable so one has to determine x, y and Q^2 from the energy E_j and the angle θ_j of the current jet:

$$Q^2 = \frac{E_j^2 \sin^2\theta_j}{1 - \dfrac{E_j}{E_e}\cos^2\dfrac{\theta_j}{2}} \tag{2.10}$$

$$x = \frac{E_j \sin^2\dfrac{\theta_j}{2}}{E_p\left(1 - \dfrac{E_j}{E_e}\cos^2\dfrac{\theta_j}{2}\right)} \tag{2.11}$$

$$y = \frac{E_j}{E_e}\cos^2\frac{\theta_j}{2}. \tag{2.12}$$

In reconstructing the kinematics of a charged current event the problem of the missing final neutrino and the loss of hadrons in the beam pipe arises. This problem can be solved by using a method introduced by Blondel and Jacquet ([EXP83], and references therein): from the measurement of the momenta of all hadrons outside the beam pipe it is possible to reconstruct the quantities x, y and Q^2 from the formulae:

$$y = \frac{\sum_i (E_{h,i} - p_{z,i})}{2\,E_e} \tag{2.13}$$

$$Q^2 = \frac{(\sum_i p_{T,i})^2}{1 - y} \tag{2.14}$$

$$x = \frac{Q^2}{s\,y} \tag{2.15}$$

where:

$p_{z,i}\ldots$ momentum component along the proton beam direction z of the i-th final hadron
$p_{T,i}\ldots$ momentum components perpendicular to $p_{z,i}$ (transverse momentum)
$E_{h,i}\ldots$ energy of the i-th final hadron.

In eq. 2.13, 2.14 the sum is taken over all final hadrons. As can be seen from eq. 2.13, hadrons travelling along the initial proton direction will not contribute to this quantity because $p_T = 0$ and therefore $E_h = p_z$. The quantities Q^2 and x (eqs. 2.14, 2.15) are not very sensitive to hadrons of high energy and low p_T travelling along the beam pipe. If those hadrons are missed, then x and Q^2 will only slightly be underestimated except at $Q^2 < 1000\,GeV^2$ [ECF80].

2.1.3 Standard Model Cross Sections and Physics at HERA

The cross section of the neutral current process in terms of the quark distribution functions $q(x, Q^2)$ and $\bar{q}(x, Q^2)$ for left (right) handed electrons is:

$$\begin{aligned} \frac{d^2\sigma(\gamma + Z^0)}{dx\,dy} &= \frac{\pi\,\alpha^2}{s\,x^2\,y^2} \sum_q \Big\{ x\,q(x,Q^2)\, \left[A_q + (1-y)^2\, B_q\right] \\ &\quad + x\,\bar{q}(x,Q^2)\, \left[B_q + (1-y)^2\, A_q\right] \Big\} \quad . \end{aligned} \tag{2.16}$$

$\alpha\ldots$ fine structure constant.

It receives contribution from Z^0 and from γ-exchange. The coefficients A_q, B_q in eq. 2.16 are different for left handed and right handed electrons (see [LOH83] for the explicit expression).

In the case of charged current processes mediated by a single W of coupling G_F the cross section for left handed electrons is:

$$\left.\frac{d^2\sigma(W^\pm)}{dx\,dy}\right|_{e_L^-} = \frac{G_F^2\, s}{\pi} \frac{1}{(1 + \frac{Q^2}{M_W^2})^2} x \left\{ q(x,Q^2) + (1-y)^2\, \bar{q}(x,Q^2) \right\} \tag{2.17}$$

$G_F\ldots$ Fermi coupling constant; $G_F = 1.2 \cdot 10^{-5}\,[GeV^{-2}]$
$M_W\ldots$ mass of W boson; $M_W = 82\,GeV$.

The cross section for right handed electrons vanishes in the standard model because the outgoing ν has helicity -1.

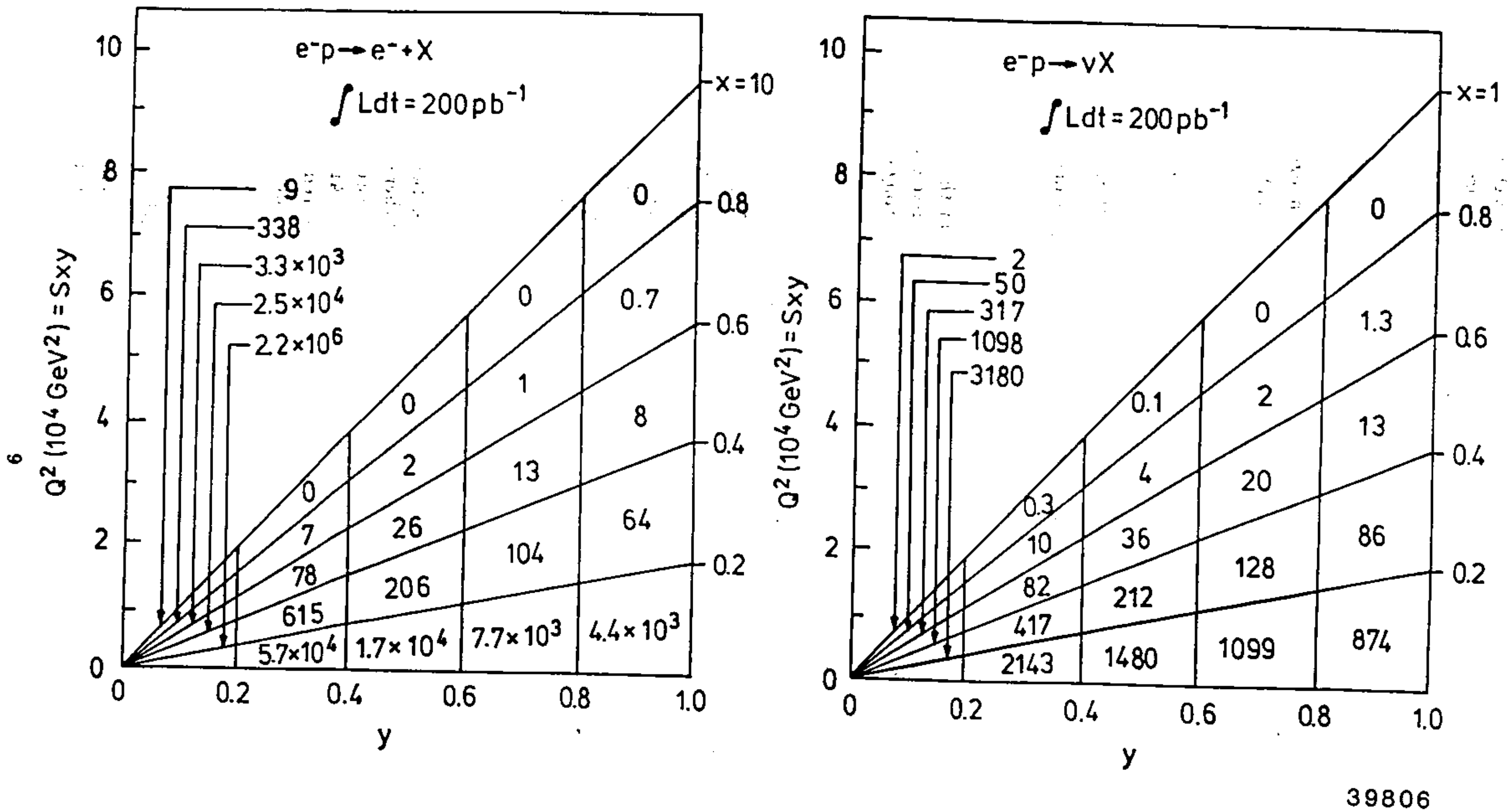

Figure 2.4: Expected Event Rates for $e^- p \to e^- X$ and $e^- p \to \nu X$ with $x > 0.01$ and $y > 0.01$ [WOL86]

Using these formulae the expected event rates have been calculated ([WOL86], and references therein) for an integrated luminosity of $200\,pb^{-1}$ which is the estimate for 2 years of data taking with $2\cdot10^{31}cm^{-2}s^{-1}$ peak luminosity. The results are plotted in Fig. 2.4, where one reads off the following event rates:

- Neutral Current:
  - $\approx 3\cdot10^6$ events with $3 \le Q^2 \le 10^4\,GeV^2$
  - $\approx 10^3$ events at $Q^2 > 10^4\,GeV^2$ where the contribution from Z^0 exchange starts to dominate
  - neutral current studies with event rates of the order of $\sim$ 10 up to $Q^2 \approx 3\cdot10^4\,GeV^2$
- Charged Current:
  - $\approx 10^4$ events at $Q^2 < 10^4\,GeV^2$
  - $\approx 10^3$ events at $Q^2 > 10^4\,GeV^2$
  - charged current studies with event rates of the order of $\sim$ 10 up to $Q^2 \approx 4\cdot10^4\,GeV^2$.

Only precise measurements of Q^2, x and y may address the physics topics mentioned previously:

1. QCD Tests and Substructure
   - **Test of QCD**
     The Feynman diagram describing deep inelastic *ep*-scattering in the standard model are shown in Fig. 2.2 and Fig. 2.5. Fig. 2.5 shows the diagram in first order α_s leading to a quark and gluon jet in the final state. The determination of the strong coupling constant α_s at the presently accessible Q^2 range is difficult because of 'higher twist' effects: beside the q^2 dependence of α_s that can be calculated in perturbative QCD there are non-perturbative 'higher twist' contributions like $1/q^2$, $1/q^4$ ... terms, hadron masses in the final state or resonance formation that are not calculable at present [PER81]. At the high Q^2 range of HERA those effects should become small so that a precise measurement of α_s and a check of perturbative QCD without these uncertainties should be possible.

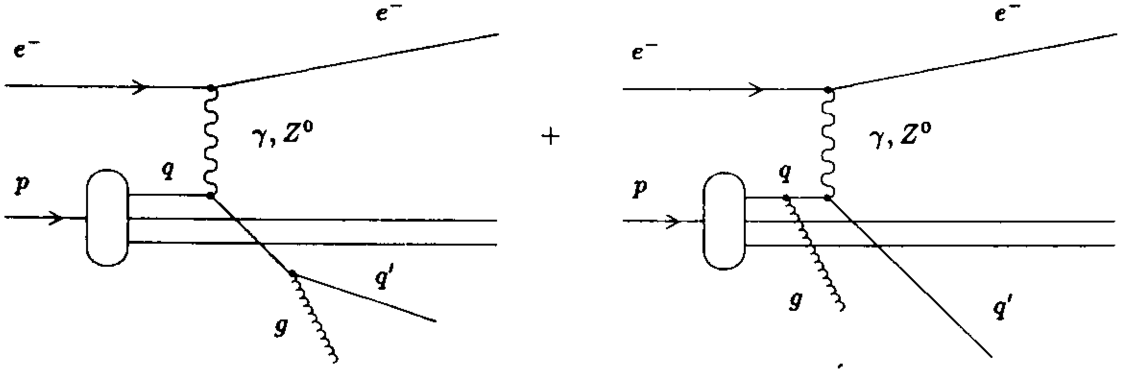

Figure 2.5: First Order QCD Diagram in ep-Scattering

The Q^2 dependence of a structure function $F(x,Q^2)$ as predicted by the standard model is of the form [BAR87]

$$F(x,Q^2) \approx \frac{F(x,Q_0^2)}{1 + c\,\ln((Q^2 - Q_0^2)/\Lambda^2_{QCD})}. \qquad (2.18)$$

The present Q^2 range of the available structure function measurements is $0 - 300\,GeV^2$ while HERA will increase it to $40000\,GeV^2$. The QCD scale parameter Λ_{QCD} can then be measured with high reliability.

- **Substructure**

  At $Q^2 \simeq 40000\,GeV^2$ HERA will be able to probe spatial distances of

$$\begin{aligned} d &\lesssim \frac{2\cdot 10^{-14}}{Q[GeV]}\,cm \\ &\lesssim 10^{-16}cm. \end{aligned} \tag{2.19}$$

  If electrons and quarks are composed of common constituents one expects [EIC83] residual 4-fermion interactions as shown in Fig. 2.6 arising, for example, from the interchange of preons with a coupling $\approx \frac{g_H^2}{\Lambda_H^2}$, where g_H is the dimensionless coupling constant of the new force and Λ_H the new substructure scale. Assuming a strong preon coupling, e.g. $\frac{g_H^2}{4\pi} \approx 1$, large effects in neutral and charged current cross sections are expected already at $Q^2 \ll \Lambda_H^2$ [RÜC84]. The structure function $F_2(x, Q^2)$ should be sensitive to that.

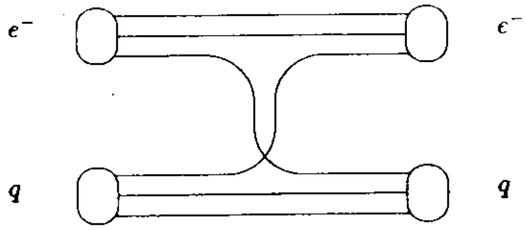

Figure 2.6: Electron and Quark Scattering by Common Constituent Interchange

  Substructure effects due to residual interactions are characterized by the ratio of structure functions

$$\frac{F_2(x,Q^2)|_{RI}}{F_2(x,Q^2)|_{SM}}$$

  where

  $F_2(x,Q^2)|_{SM} \cdots$ dimensionless structure function of the nucleon in the standard model

  $F_2(x,Q^2)|_{RI} \cdots$ dimensionless structure function of the nucleon if residual interactions occur.

  The ratio is plotted in Fig. 2.7 for left handed electrons or right handed positrons [RÜC84].

2. Test of Electroweak Interactions

   - **Search for a second W_2**

     In the cross section eq. 2.17 it was assumed that the reaction is mediated by a single W with its coupling g given by

$$\frac{g^2}{M_W^2} = G_F. \tag{2.20}$$

     A second boson W_2 with higher mass would modify the propagator in eq. 2.17,

$$\frac{g^2}{Q^2 + M_W^2} \rightarrow \frac{g_1^2}{Q^2 + m_1^2} + \frac{g_2^2}{Q^2 + m_2^2} \tag{2.21}$$

     where g_1, g_2 are chosen to retain G_F in the low Q^2 region:

$$G_F = \frac{g_1^2}{m_1^2} + \frac{g_2^2}{m_2^2}. \tag{2.22}$$

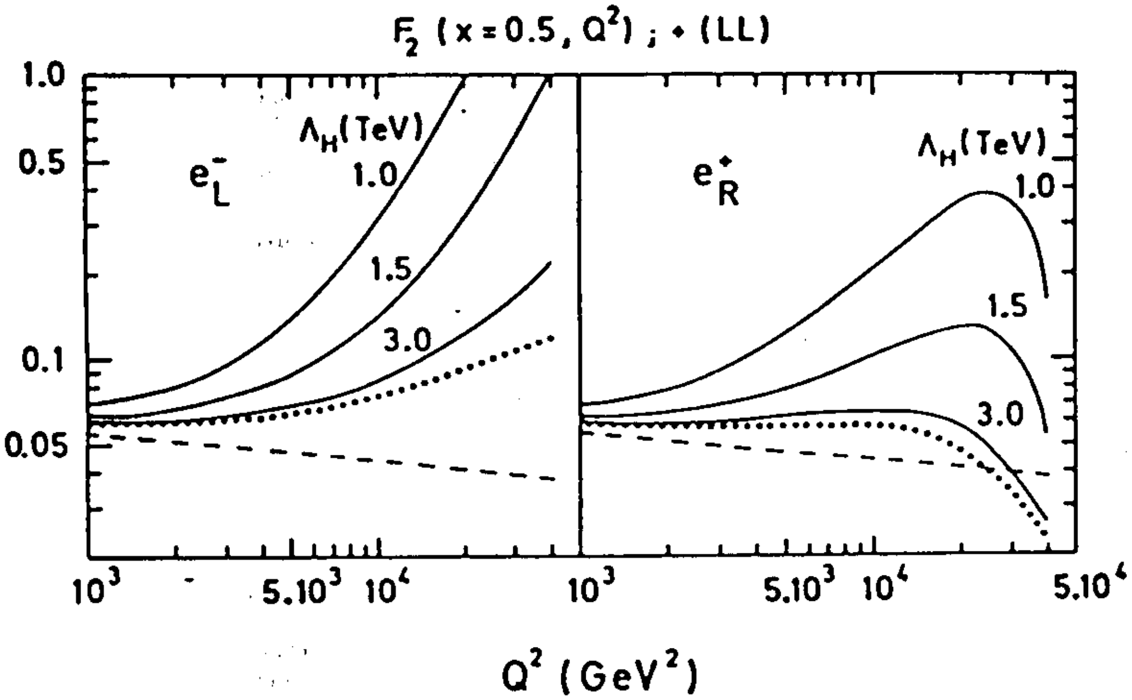

Figure 2.7: The Expected Ratio $\frac{F_2(x,Q^2)|_{RI}}{F_2(x,Q^2)|_{SM}}$ due to Residual Interactions of Left Handed Fermions for various Values of Λ_H [RÜC84]; (dotted curve: Standard Model Results ($\gamma + Z^0$); dashed curve: One Photon Exchange Contribution)

In Fig. 2.8 the ratio $\frac{\sigma(W_1 + W_2)}{\sigma(W_1)}$ for different masses of W_2 is shown assuming $g_1 = g_2$. Within the expected errors, two years of data taking leads to a sensitivity of possible W_2 masses up to $\approx 800\,GeV$. Similar estimates hold for neutral currents and additional Z^0s [WOL86].

- **Right handed currents**
  In the standard model the right handed charged current cross section is zero. If measurements with longitudinally polarized electrons at HERA would show deviations from zero then this would indicate the presence of a right handed charged current. From present experiments there have been put lower limits on the mass of the right handed charged boson W_R, ranging from 200 to 10000 GeV depending on the underlying assumptions [WOL86]. For neutral current processes the contribution from right handed Z^0 would lead to deviations from the standard model cross section as shown in Fig 2.9. The lower limit on a right handed neutral boson Z^0_R is $M_{Z_R} \geq 150\,GeV$ [WOL86].

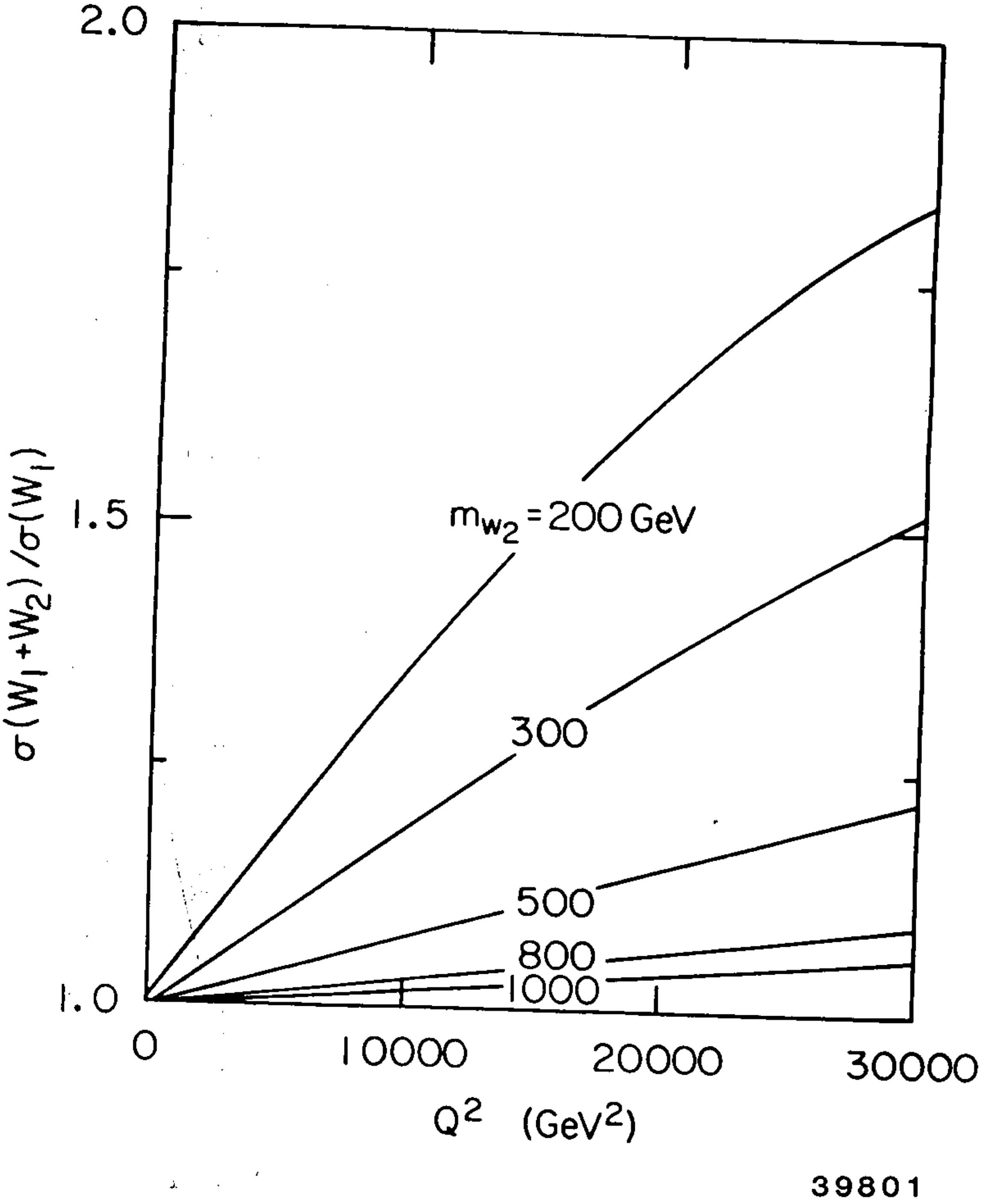

Figure 2.8: $\sigma(W_1 + W_2)/\sigma(W_1)$ for Different Masses of W_2 [WOL86]

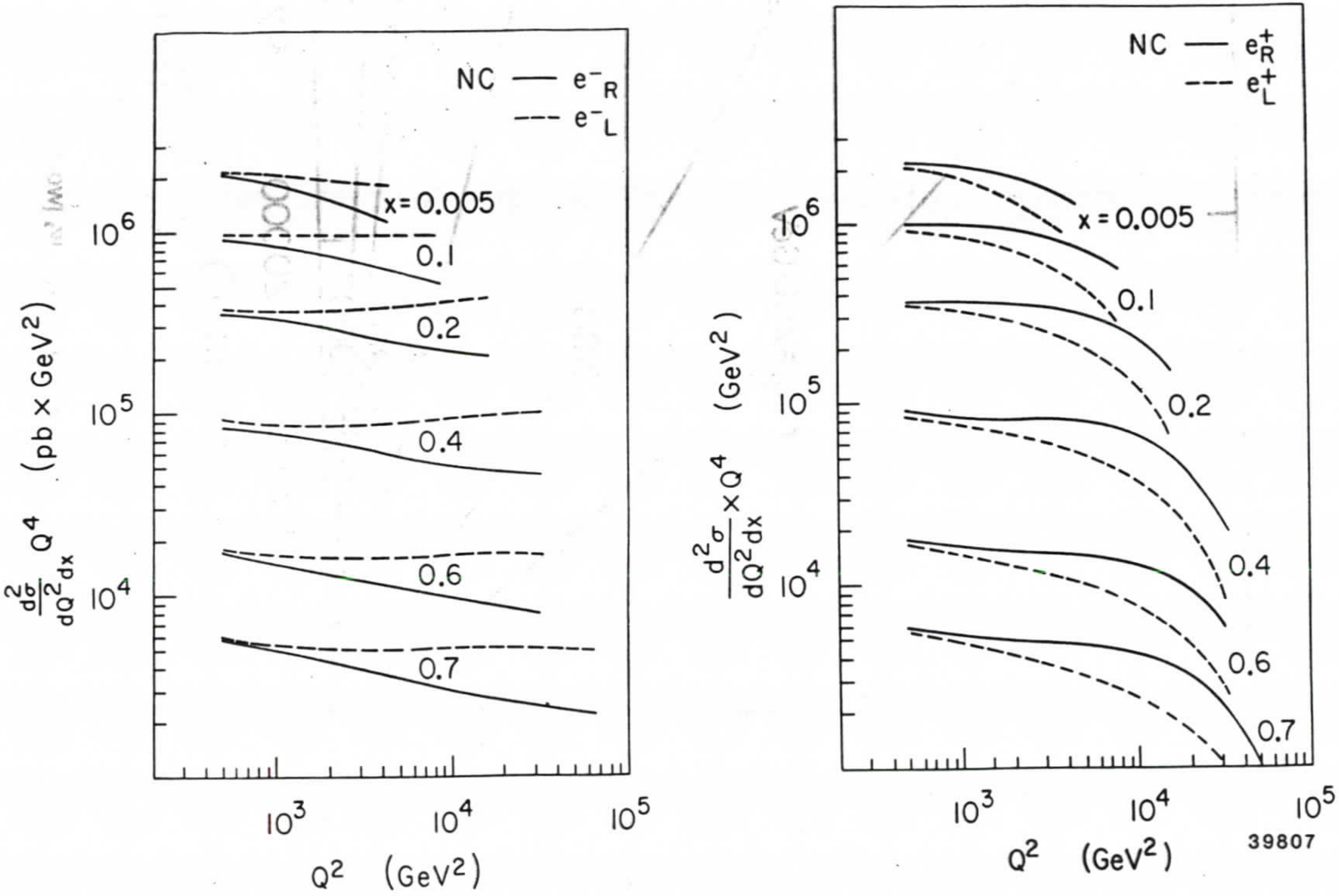

Figure 2.9: Cross Section $\sigma(Z^0)$ for Right Handed Currents [WOL86]

3. New Particles

- **Leptoquarks**
  Leptoquarks result from superstring models, grand-unified theories, technicolor theories and models of quark-lepton substructure [LOH87]. They occur as resonances in eq-collisions, so HERA would be ideal to search for such particles [RÜC87]. They may be detected in the inclusive x-distribution determined from the scattered electron variables, up to a mass limit of $m_{LQ} \gtrsim 200\,GeV$ [LOH87].
- **Excited Quarks and Leptons**
  compositeness of quarks and leptons would consequently lead to excited states q^*, l^* of quarks and leptons. Masses of q^* and l^* up to $250\,GeV$ can be studied at HERA [WOL86].
- **Supersymmetric Particles**
  although there is still no evidence for supersymmetric particles, HERA will open a new mass range of their production, if they exist . Supersymmetric partners $(\tilde{q}, \tilde{e})$ of the standard quarks and leptons will be produced via the exchange of $\tilde{\gamma}$, $\tilde{Z}$ or $\tilde{W}$, the supersymmetric partners of the standard bosons. Calculated cross sections of these reactions give a mass limit of $m_{\tilde{q}} + m_{\tilde{e}} = 160\,GeV$ if 10 events per $200\,pb^{-1}$ can be detected [WOL86].
- **Pair production of heavy quarks**
  a heavy quark-antiquark pair can be produced by photon gluon fusion according to the diagram in Fig. 2.10. The total cross section of this process decreases steeply with the heavy quark mass as:

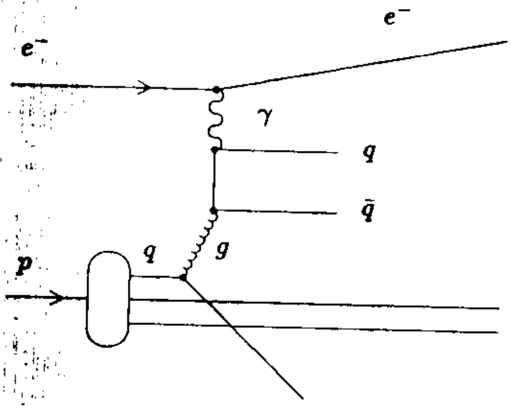

Figure 2.10: **Quark Pair Production by Photon Gluon Fusion in *ep* Scattering**

$$\sigma(eq \rightarrow q\bar{q}X) \sim M_q^{-4}; \tag{2.23}$$

however, event rates of $\sim$ 7000 for b-quarks and $\sim$ 50 for t-quarks ($M_t = 40\,GeV$) per $100\,pb^{-1}$ are expected [RÜC86]. HERA will be sensitive to top quark masses up to $100\,GeV$ [WOL86].

2.2 The ZEUS Detector

The layout of the ZEUS detector is shown in Fig. 2.11 and Fig. 2.12 [ZEU86]. It will be composed of

- a vertex detector (VXD) with an estimated resolution of $30\mu m$
- a central track detector (CTD) consisting of a cylindrical stereo wire drift chamber

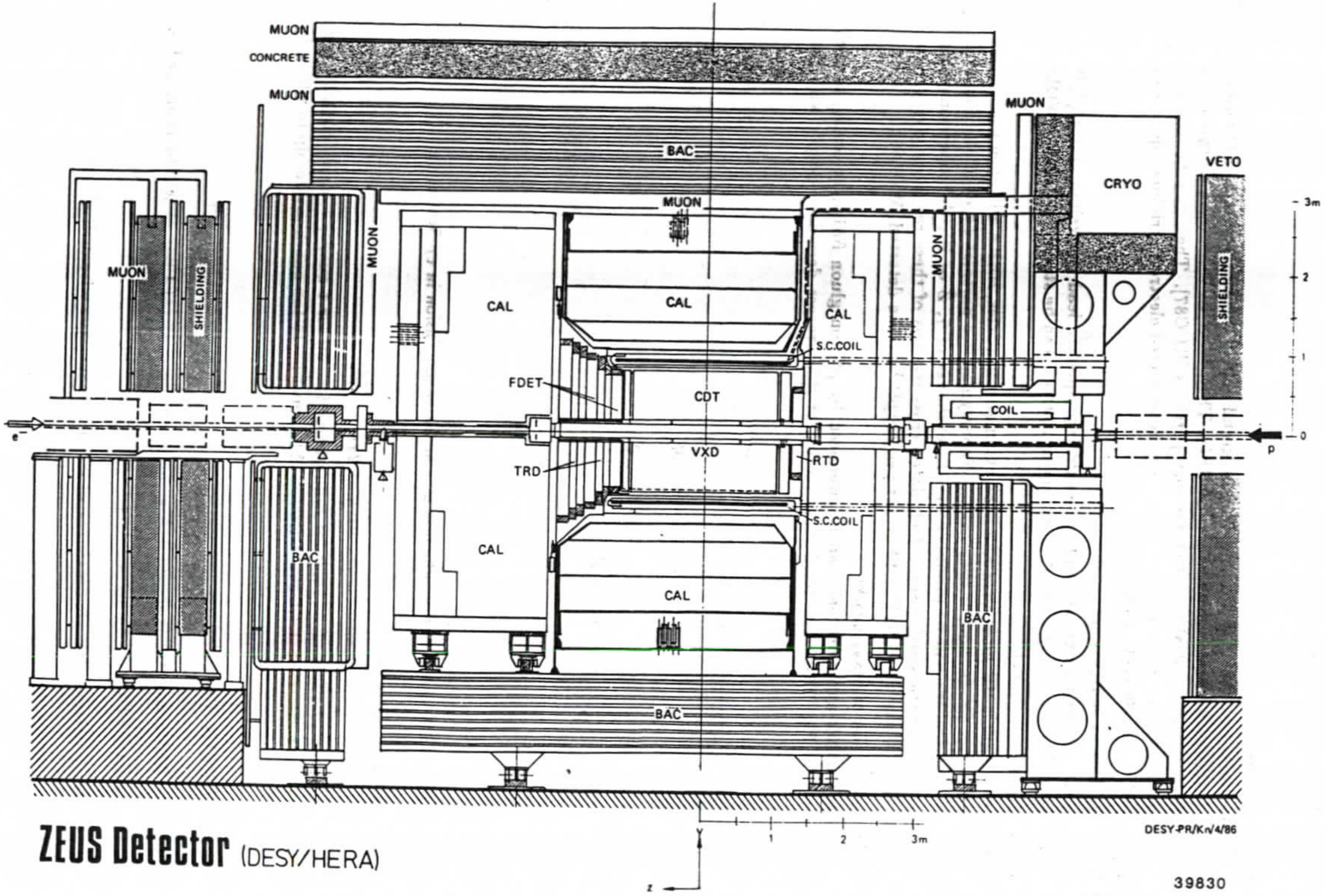

Figure 2.11: The ZEUS Detector (Side View) [ZEU86]

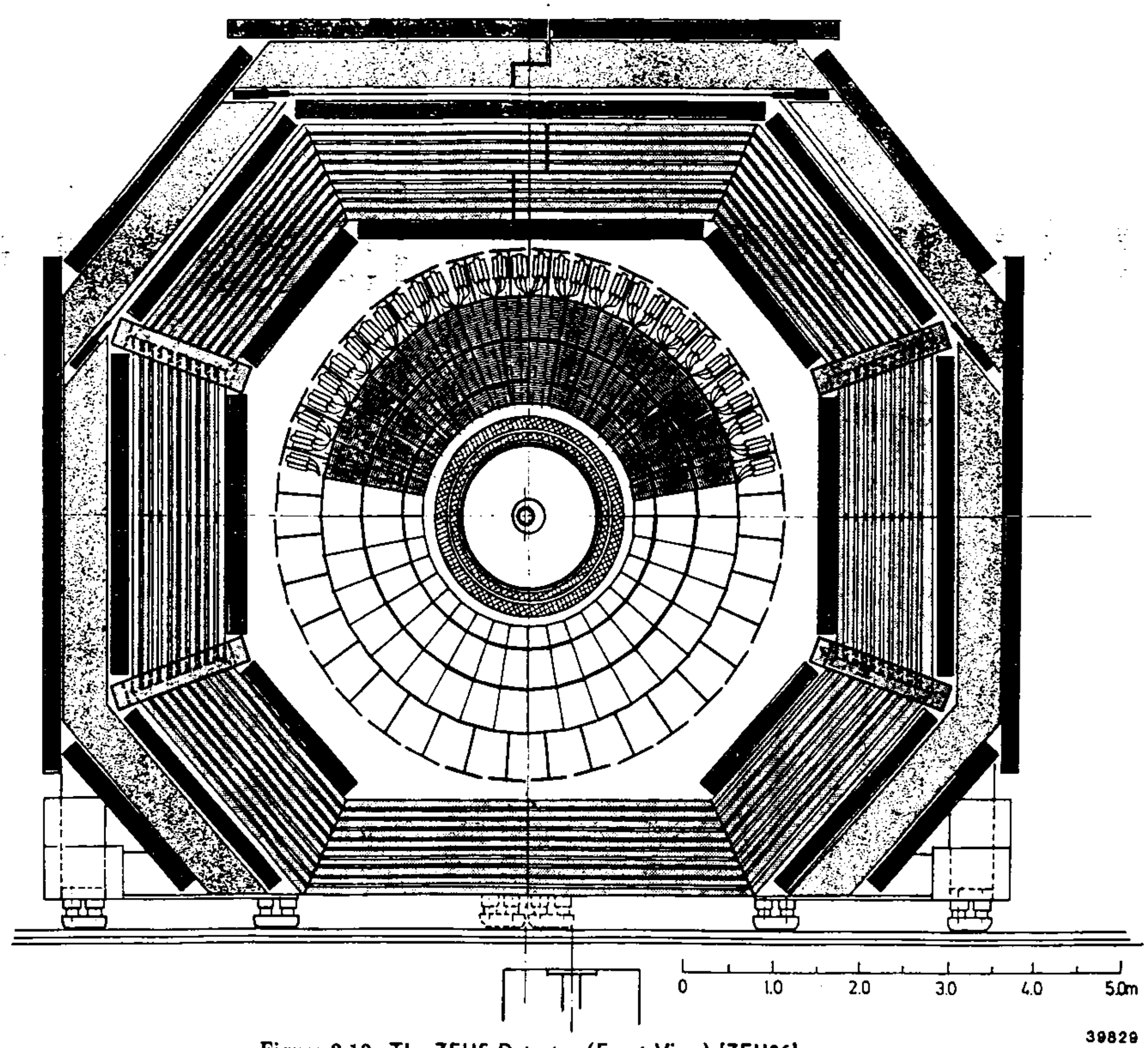

Figure 2.12: The ZEUS Detector (Front View) [ZEU86]

- a transition radiation detector (TRD) with $30\mu m$ thick polypropylene foils acting as radiator, a planar drift chamber (FTD) in the forward as well as one (RTD) in the backward direction
- all these tracking chambers are enclosed within a thin superconducting solenoid coil (SOLENOID) with a magnetic field of 1.8 T
- a high resolution electromagnetic (EMC) and hadron calorimeter (HAC) of depleted uranium-scintillator layers with wavelength shifter readout, surrounding the coil over the full solid angle
- a backing calorimeter (BAC) with limited streamer tube readout and iron absorber plates which act as iron yoke for the magnetic flux
- a barrel and rear muon detector (MU) of drift chamber and limited streamer tube type
- a forward muon spectrometer (FMU) of plastic proportional tubes operating in the limited streamer mode.

Details on each of the listed components can be found in [ZEU86, ZEU87]. In this section the requirements for the hadron calorimeter to measure precisely the physics quantities mentioned in the previous section will be discussed only.

The decisive quantities of a hadron calorimeter which determine the attainable physics are:

- the relative response to electrons and hadrons (e/h-ratio)
- the energy resolution σ_E/E for electrons as well as hadrons
- the angular resolution

The e/h-ratio, formally expressed by:

$$\frac{E(e)_{vis}}{E(h)_{vis}}$$

where:

$E(e)_{vis}\ldots$ visible energy of an electron or photon in a calorimeter

$E(h)_{vis}\ldots$ visible energy of a hadron in a calorimeter

is a crucial parameter: if the response to the electromagnetic component of the hadronic shower is different from that of the pure hadronic component ($e/h \neq 1$), then the large fluctuations in the π^0 fraction of the hadronic shower will deteriorate the hadronic energy resolution. This will be discussed in more detail in sec. 3.3.

For jets with a fluctuating number of π^0 particles the energy resolution of a noncompensating calorimeter ($e/h \neq 1$) is degraded, too. A longitudinal segmentation of a noncompensating calorimeter into an electromagnetic and hadronic compartment improves the energy resolution for jets, as can be seen from Fig. 2.13 [ZEU85]. The π^0 content of the jet deposits most of its energy in the electromagnetic part and, by knowing the e/h-ratio which is about 1.4 for a noncompensating calorimeter, one can adjust the electromagnetic response with respect to the hadronic response, leading to a total sum with better resolution.

Even for compensating calorimeters a longitudinal segmentation would be advantageous because a calorimeter subdivided into an electromagnetic and hadronic part provides the ability of electron-hadron separation.

For the specification of the required energy resolution of a hadron calorimeter some major aspects of the physics to be measured have been considered [ECF80, EXP83]:

- Neutral Current Events
  Studies of inclusive processes require the identification of the scattered electron and a precise measurement of its momentum (see eqs. 2.7, 2.8, 2.9); a good electron-hadron separation

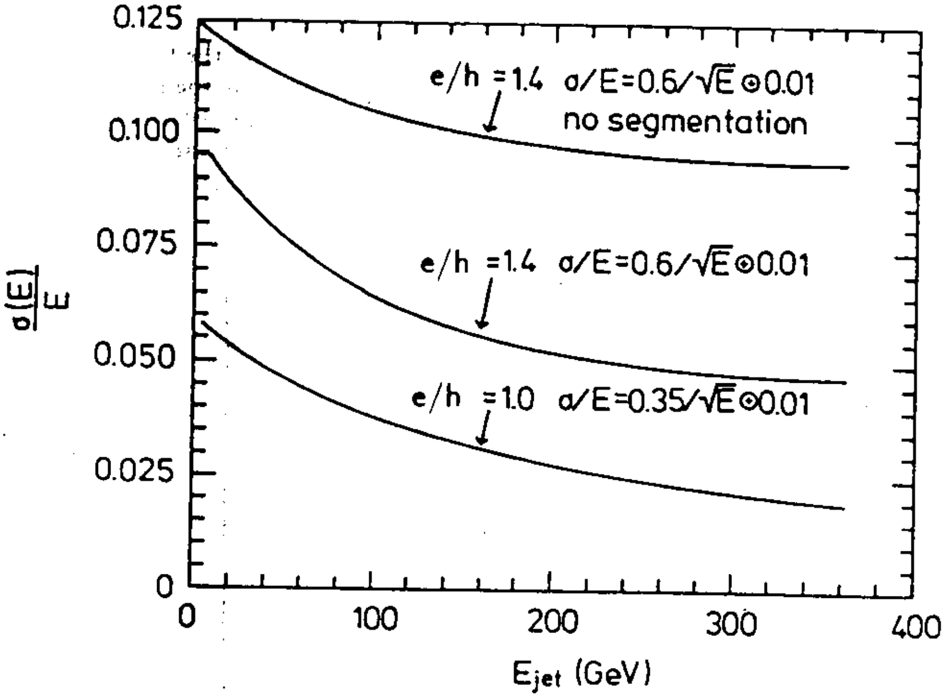

Figure 2.13: Calculated Energy Resolution for Jets with given Calorimeter Characteristics [ZEU85]; (top curve: without Longitudinal Segmentation; middle curve: with 20 X_0 Deep Longitudinal Segmentation; bottom curve: Compensating Calorimeter; $\oplus$ denotes quadratic addition)

is essential for the electron identification. Exclusive investigations like study of details of the current jet or new particle observations require a good particle identification and momentum resolution of individual tracks.

- Charged Current Events
  The scattered neutrino will not be observed in this class of events. The variables x, y and Q^2 have to be extracted from the current jet alone (see eqs. 2.14, 2.13, 2.15). Hence, a hadron calorimeter with high energy resolution is important for charged current events. In addition, an almost 4π coverage is needed for the reasons discussed in sec. 2.1.2. Also, a good electron-hadron separation is necessary to make sure that the scattered lepton is not an electron.

Table 2.1: Specified Energy Resolution for the Electromagnetic (EMC) and the Hadron Calorimeter (HAC) for Neutral (NC) and Charged Current (CC) Events

	NC	CC
EMC	$\frac{\sigma_E}{E}(\mathrm{e}) = \frac{0.1}{\sqrt{E\,[GeV]}}$	$\frac{\sigma_E}{E}(\mathrm{e}) = \frac{0.1}{\sqrt{E\,[GeV]}}$
HAC	$\frac{\sigma_E}{E}(\mathrm{h}) = \frac{0.6}{\sqrt{E\,[GeV]}}$	$\frac{\sigma_E}{E}(\mathrm{h}) = \frac{0.3}{\sqrt{E\,[GeV]}}$

Under these considerations the required energy resolution of the electromagnetic and hadron calorimeter for the precise measurement of neutral and charged current events could be specified and are given in Tab. 2.1 [ECF80].

The general aim in the measurement of structure functions is to cover the largest range in the x, Q^2 area as possible. In achieving this aim one would be able to determine the slope of the structure functions versus Q^2 with a large lever arm. In addition, one can put constraints on the shape of structure functions if one covers the full x range at different Q^2. One will also be able to match the highest Q^2 values reachable at HERA with the present values, provided x and Q^2 are measured with high accuracy.

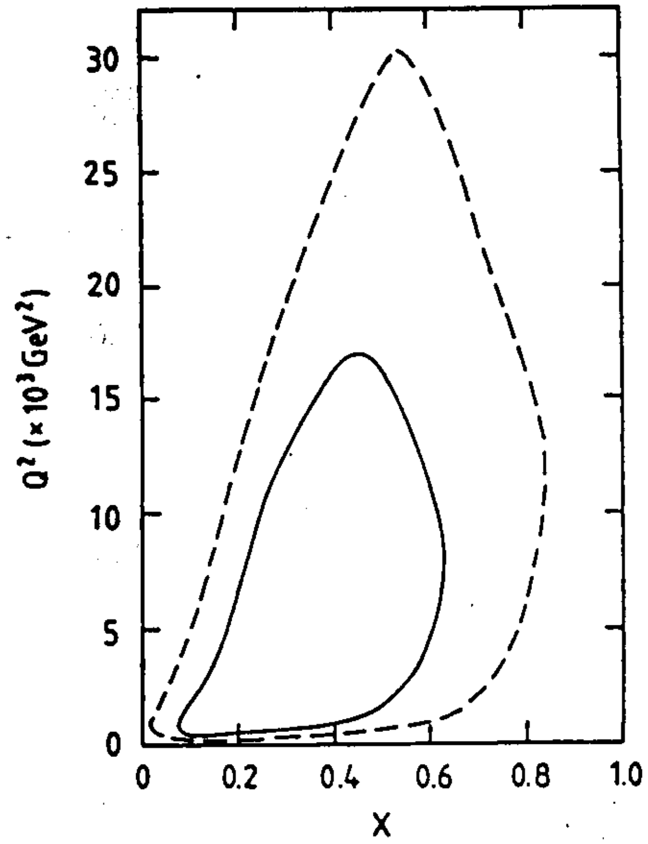

Figure 2.14: Accessible Regions in the x, Q^2 Plane for two Calorimeter Configurations [ZEU85]; (dashed line: $\sigma_E/E(h) = 35\%/\sqrt{E[GeV]}$, $e/h = 1$; full line: $\sigma_E/E(h) = 60\%/\sqrt{E[GeV]}$, $e/h = 1.4$)

For the specifications of the hadron calorimeter the ZEUS collaboration performed further calculations with two alternative calorimeter configurations:

1. $$\frac{\sigma_E}{E}(\mathrm{h}) = \frac{60\%}{\sqrt{E[GeV]}} \qquad \text{and} \qquad \frac{e}{h} = 1.4$$
2. $$\frac{\sigma_E}{E}(\mathrm{h}) = \frac{35\%}{\sqrt{E[GeV]}} \qquad \text{and} \qquad \frac{e}{h} = 1.0.$$

In order to estimate measurement errors in the determination of the deep inelastic cross section, the x and Q^2 plane was subdivided into bins of equal distance on the Q^2 scale ($\log Q^2 = 3.0 \rightarrow$

$4.6, \Delta \log Q^2 = 0.2$) and of increasing distance on the x scale ($x = 0.0 \rightarrow 0.06, \Delta x = 0.03; x = 0.06 \rightarrow 0.10; x = 0.10 \rightarrow 0.20, \Delta x = 0.05; x = 0.2 \rightarrow 0.5, \Delta x = 0.1$). The migration of events out or into those bins was recorded according to the criteria given by Longo [EXP83] which requires a fraction $f_1 > 0.6$ of original events remaining in the specified x and Q^2 bin and in addition a fraction $f_2 < 0.4$ of events migrating into the bin. Fig. 2.14 shows the covered region in the x, Q^2 plane for the two calorimeter configurations assumed. Obviously, a much larger area in the x and Q^2 plane can be measured with a compensating calorimeter than with a noncompensating one.

Thus the ZEUS collaboration concluded that a compensating calorimeter with the following properties provides an important physics gain over a noncompensating one [ZEU85]:

- electromagnetic energy resolution: $\frac{\sigma_E}{E}(\mathrm{e}) \approx \frac{15\%}{\sqrt{E[GeV]}}$
- hadronic energy resolution: $\frac{\sigma_E}{E}(\mathrm{h}) \approx \frac{35\%}{\sqrt{E[GeV]}}$
- equal response to electrons and hadrons: $\frac{e}{h} = 1.0$.

At the time when the ZEUS detector was designed there was only a partial understanding of how to build a compensating calorimeter ($e/h = 1$) with the required energy resolution of $\sigma_E/E(\mathrm{h}) = 35\%/\sqrt{E[GeV]}$ for hadrons. Therefore the ZEUS collaboration started a large program to study the various parameters influencing the energy resolution and the e/h-ratio of hadron calorimeters.

Chapter 3

Hadronic Showers in Sampling Calorimeters

3.1 Structure and Operation of Calorimeters

Calorimeters are used to measure the energy of high energetic elementary particles. The principle of such a detector is to absorb the entire energy of the primary particle while generating a measurable signal that is proportional to this energy. A calorimeter can either be made out of an absorption material that simultaneously generates a detectable signal or out of alternating passive and active layers of different substances where the active layer produces the signal to be measured. The former is called *homogeneous*, the latter *sampling* calorimeter. A homogeneous calorimeter can be realized with materials like H_2O, lead-glass, *NaI*, *CsI*, *BGO* etc., a sampling calorimeter with iron, lead, uranium, marble etc. as passive absorber and liquid argon, gas, scintillator etc. as active detector.

Depending on the type of the primary particle that enters the calorimeter various interactions with the calorimeter material take place, creating secondary particles and thus giving rise to a *cascade* or *shower*. The development of such a shower and the energy deposition within the calorimeter result in large fluctuations which limits the energy resolution.

Two kinds of showers can be distinguished, the electromagnetic and the hadronic one, with the hadronic shower containing also an electromagnetic component.

3.1.1 Electromagnetic Showers and the Energy Resolution

Electrons and positrons within an electromagnetic shower lose their energy by collisions with atomic electrons and by radiation of photons in the field of a nucleus. At the beginning of the shower where the energy of the electrons is high the radiation loss dominates and determines the propagation of the shower within the calorimeter material. The average fractional energy loss in a certain substance due to radiation (integrated over the bremsstrahlung spectrum) in MeV per radiation length X_0 is:

$$< \frac{dE}{dt} > = - \frac{E}{X_0} \tag{3.1}$$

where:

$t\,[X_0]\ldots$ thickness of material in $[X_0]$
$E\,[MeV]\ldots$ energy of incident electron in $[MeV]$.

The radiation length X_0 can be calculated using the following formula [ROS52]:

$$\frac{1}{X_0} = \frac{4\,\alpha\,\frac{N_A}{A}\,Z\,(Z\,+\,1)\;r_e^2\;\ln\,(183\,Z^{-1/3})}{1\,+\,0.12\,(Z/82)^2}\;\frac{cm^2}{g} \tag{3.2}$$

with:

$\alpha \ldots$	$\frac{e^2}{\hbar c}$
$A \ldots$	mass number of material in $[g]$
$Z \ldots$	atomic number of material
$N_A \ldots$	Avogadro number
$r_e \ldots$	classical electron radius in $[cm]$

Table 3.1: Values of the Radiation Length X_0 for Some Materials

. Material	Z	$A\,[g]$	$\rho\left[\frac{g}{cm^3}\right]$	$X_0\left[\frac{g}{cm^2}\right]$	$X_0[cm]$
Polystyrene	< 3.4 >	-	1.060	43.8	41.3
Al	13	26.98	2.70	24.01	8.89
Fe	26	55.85	7.87	13.84	1.76
Pb	82	207.19	11.35	6.37	0.56
U	92	238.03	18.95	6.00	0.32

In Tab. 3.1 the values of X_0 are given for some materials of interest in this work [PDG86, LOH85]. Approximately, 1 X_0 is given by [AMA81]:

$$1\,X_0\left[\frac{g}{cm^2}\right] \simeq 180\,\frac{A}{Z^2} \qquad \left(\frac{\Delta X_0}{X_0} < \pm 20\% \text{ for } 13 \leq Z \leq 92\right) \tag{3.3}$$

(throughout this work an abbreviation like $Q[u]$ means that the quantity Q is given in units of u).

At lower energies of the electrons the collision loss will be the dominating process. There exists no simple expression for the probablilty of collisions in which the electron acquires an energy of the order of the binding energy of electrons in atoms. One therefore replaces these collision losses by a continous energy dissipation to introduce a collision loss per radiation length [ROS52]:

$$\epsilon\,(E)\,\left[\frac{MeV}{X_0}\right] := -<\frac{dE}{dt}> \tag{3.4}$$

In a wide energy range around a certain energy ϵ_0 the variable collision loss $\epsilon\,(E)$ varies only slowly with energy E [ROS52]. Therefore one replaces the variable collision loss $\epsilon\,(E)$ by a constant collision loss $\epsilon_0 = \epsilon\,(\epsilon_0)$, the collision loss per radiation length of electrons with energy ϵ_0. Under this approximation [1] the *critical energy* ϵ_0 is the energy at which the radiation and collision loss of electrons are equal. It is given by [AMA81]:

$$\epsilon_0\,[MeV] \simeq \frac{550}{Z} \qquad \left(\frac{\Delta\epsilon_0}{\epsilon_0} < \pm 10\% \text{ for } 13 \leq Z \leq 92\right) \tag{3.5}$$

Values of the critical energy ϵ_0 are given in Tab. 3.2 [ROS52] for some substances.

In the following a qualitative description of the electromagnetic shower development will be given by considering a very simple model [ROS52].

It is assumed that each electron penetrating some material with an energy well above the critical energy ϵ_0 emits a photon after a distance of one radiation length and that half of the energy of each electron is carried away by the photon. Let each photon annihilate into an e^+e^- pair after a second radiation length and let each initial electron emit a second photon. The photon energy in the annihilation process is supposed to be equally shared between the pair of particles. Compton scattering and collision loss of electrons with energy greater than ϵ_0 has been neglected [2] in the simple model. Those electrons with energy less than ϵ_0 are assumed to deposit their energy immediately via collision loss without any further radiation. The particle and energy balance under this consideration looks as given in Tab.3.3.

---

[1] This approximation is called "Approximation B" [ROS52] under the following additional assumption: Compton

Table 3.2: Values of the Critical Energy ϵ_0 for Some Materials

Material	ϵ_0 $[MeV]$
Polystyrene	≈ 80
Al	48.8
Fe	24.3
Pb	7.8
U	≈ 6

Table 3.3: Particle and Energy Balance under the Consideration of the Simple Shower Model (see Text)

Depth $[X_0]$	Number of Particles	Energy	Process
0	1	E	e^-
1	2	$\frac{E}{2}+\frac{E}{2}$	$e^- + \gamma$
2	4	$\frac{E}{4}+\frac{E}{4}+\frac{E}{4}+\frac{E}{4}$	$e^- + \gamma + e^+e^-$
$\vdots$	$\vdots$	$\vdots$	
t	2^t	$E \cdot 2^{-t}$	

Thus after t radiation lengths the total number of electrons and photons $N_{e,\gamma}$ is:

$$N_{e,\gamma} = 2^t \tag{3.6}$$

with:

$t\ldots$ depth in $[X_0]$

while the energy ϵ of each particle decreases with increasing t:

$$\epsilon = E \cdot 2^{-t} \tag{3.7}$$

with:

$E\ldots$ incident energy of primary electron $[MeV]$.

The total number of particles exceeding a certain energy ϵ increases exponentially from $t = 0$ to $t = \tau(\epsilon)$, where $\tau(\epsilon)$ is the depth in units of radiation length at which the particle energy has fallen to ϵ:

$$\epsilon = E \cdot 2^{-\tau(\epsilon)} \tag{3.8}$$

$$\Rightarrow \quad \tau(\epsilon) = \frac{\ln E/\epsilon}{\ln 2}. \tag{3.9}$$

In the discussion so far the shower particles in one step have been assumed to carry all the same energy. Actually, at a given depth t they follow an energy distribution from which one can obtain

---

scattering is neglected and the bremsstrahlung and pair production processes can be described by asymptotic formulae for complete screening of the electric field of the nucleus by atomic electrons

[2] This is called "Approximation A" [ROS52]

the total number of shower particles that exceed the energy ε, averaged over the depth in radiation length:

$$\begin{aligned} < N_\varepsilon > &= \int_0^{\tau(\varepsilon)} N_{e,\gamma}\, dt \\ &= \int_0^{\tau(\varepsilon)} 2^t\, dt \\ &\approx \frac{e^{\tau(\varepsilon)\cdot \ln 2}}{\ln 2} \\ &= \frac{E\,/\varepsilon}{\ln 2}. \end{aligned} \tag{3.10}$$

This shows that the average number of shower particles exceeding ε is inverse proportional to their energy ε. The result is only valid for energies greater than the critical energy ε_0. As long as the particle energies are above ε_0 the multiplication process continues. For $\varepsilon = \varepsilon_0$ the maximum number of particles is reached at t_{max}:

$$\begin{aligned} t_{max} &= \tau(\varepsilon_0) \\ &= \frac{\ln E\,/\varepsilon_0}{\ln 2}. \end{aligned} \tag{3.11}$$

One expects that at the depth where the number of shower particles has its maximum the energy deposition of the shower reaches its maximum, too. Behind this depth the remaining energy is deposited immediately via collision loss, according to the assumption above.

The total average number of charged particles can be determined by the use of eq. 3.10, 3.11. This number is equal to the average total track length $< T > [X_0]$ of charged particles in units of X_0:

$$\begin{aligned} < T > [X_0] &= \frac{2}{3} \int_0^{t_{max}} N_{e,\gamma}\, dt \\ &= \frac{2}{3 \ln 2} \frac{E}{\varepsilon_0} \\ &\approx \frac{E}{\varepsilon_0}. \end{aligned} \tag{3.12}$$

The factor 2/3 is the ratio of charged (e^+, e^-) to neutral (γ) particles under the assumption made in the simple model that they all carry away an equal amount of energy after each radiation or materialization process.

The average total track length $< T > [X_0]$ of the charged particles is proportional to the energy E of the primary particle. This is the important result that makes calorimetry possible.

The average detectable track length $< T_d > [X_0]$ is always smaller than $< T > [X_0]$ by a factor $F(z)$:

$$< T_d > [X_0] \simeq F(z)\, \frac{E}{\varepsilon_0}, \tag{3.13}$$

where, under "Approximation B" [AMA81],

$$F(z) \simeq e^{-z}\left[1 + z \ln\left(\frac{z}{1.53}\right)\right] \qquad \left(\frac{\Delta F(z)}{F(z)} \simeq 10\% \quad \text{for } z \leq 0.3\right). \tag{3.14}$$

with:

$$z = 2.29\, \frac{E_{thr}}{\varepsilon_0} \tag{3.15}$$

E_{thr} ... threshold energy (minimum detectable energy).

"Approximation B" is only valid for light materials, for different materials eq. 3.15 has to be redefined to [AMA81]:

$$z = 4.58 \, \frac{Z}{A} \, \frac{E_{thr}}{\epsilon_0}. \tag{3.16}$$

The factor $F(z)$ in eq. 3.13 depends upon the threshold energy E_{thr}, the minimum detectable energy below which the detector is no more sensitive to electrons or positrons [AMA81].

In the discussion so far the average behaviour of the shower has been concerned only. A description of the fluctuations around the average shower development can not be done on the basis of a simplified model. A quantitative investigation of the fluctuations within an electromagnetic shower and of the resulting energy resolution is only possible by the use of the Monte Carlo technique, e.g. the EGS4 shower simulation program [NEL85].

A homogeneous lead-glass calorimeter configuration has been simulated by [LON75]. The calculated intrinsic energy resolution was:

$$\frac{\sigma_E}{E}(e) \simeq \frac{0.7\%}{\sqrt{E[GeV]}}. \tag{3.17}$$

Experimentally, an energy resolution of

$$\frac{\sigma_E}{E}(e) \simeq \frac{4-5\%}{\sqrt{E[GeV]}} \tag{3.18}$$

was obtained with several lead-glass calorimeters large enough to fully contain the whole electromagnetic shower ([IWA79], and references therein). The obtainable energy resolution with lead-glass detectors is limited by fluctuations in the number of photoelectrons ($\approx$ 400 per GeV [PRE84]) produced by the conversion of the Cherenkov light in the photomultipliers. The fluctuations in the number of photoelectrons scales as $1/\sqrt{E[GeV]}$ [AMA81, HOF82].
A total energy resolution of

$$\frac{\sigma_E}{E}(e) \simeq \frac{0.25\%}{(E[GeV])^{1/4}} \qquad 0.1 \leq E \leq 20GeV \tag{3.19}$$

was measured with a homogeneous calorimeter of $NaI(Tl)$-crystals 24 X_0 deep [HUG72]. High light yield can be achieved with this material, so photostatistics should not be a limiting factor [PRE84]. The minimum detectable energy E_{thr} is very low in this detector and hence the contribution from shower fluctuations, too. The major effects influencing the resolution probably come from non-uniformity in light collection throughout the volume and leakage of shower particles out of the crystal blocks [HUG72, PRE84].

3.2 Sampling Calorimeters

A sampling calorimeter with alternating layers of dense passive and active absorber materials has the advantage of being

- rather compact in order to fully contain a shower in a reasonable length;
- adaptable to specific experimental requirements like electron-hadron separation or position measurements [FAB85].

On the other hand, it has the disadvantage of giving an additional contribution to the energy resolution because the total track length of the shower, which is proportional to the total energy to be measured, is randomly subdivided ('*sampled*') into visible and non visible parts of the total track. This leads to fluctuations around the visible fraction of the total energy.

These fluctuations have experimentally been studied for *electromagnetic sampling* calorimeters and compared with Monte Carlo calculations or analytic expressions.

3.2.1 Sampling Fluctuations

Several effects contribute to the total sampling fluctuations [FAB85] :

- 'intrinsic' sampling fluctuations
- 'Landau' fluctuations
- 'path-length' fluctuations.

Intrinsic Electromagnetic Sampling Fluctuations

The average detectable total track length of an electromagnetic shower in radiation lengths $< T_d >[X_0]$ (eq. 3.13) in a sampling calorimeter is composed of the track lengths of charged particles that cross the individual active plates of the calorimeter. With a constant thickness $d[X_0]$ of the calorimeter layer (one active and one passive plate) one obtains, under "Approximation B", the average number of charged particle crossings ('*samples*') N_s in the scintillator plates:

$$N_s \simeq \frac{< T_d > [X_0]}{d\,[X_0]}. \tag{3.20}$$

With eq. 3.13:

$$N_s \simeq F(z) \cdot \frac{E}{\epsilon_0 \cdot d\,[X_0]}. \tag{3.21}$$

Assuming that the number of tracks in the individual crossings are independent and that N_s is normally distributed one obtains a relative width of the distribution of N_s given by [AMA81]:

$$\frac{\sigma_{N_s}}{N_s} = \frac{1}{\sqrt{N_s}} \tag{3.22}$$

and with eq. 3.21:

$$\frac{\sigma_E}{E}(e) = 3.2\% \cdot \sqrt{\frac{\epsilon_0\,[MeV]}{F(z)} \cdot \frac{d\,[X_0]}{E\,[GeV]}}. \tag{3.23}$$

Equation 3.23 does not hold for very small layer thicknesses were the number of crossings are no longer uncorrelated. In addition, eqs. 3.20, 3.21, 3.23 are derived under "Approximation B" which is only valid for light material, and it ignores transverse shower properties.

The transverse shower propagation scales in units of the Molière radius [AMA81], defined by:

$$\begin{aligned} R_M\left[\frac{g}{cm^2}\right] &= \frac{E_{ms}}{\epsilon_0} \\ &\simeq 7\,\frac{A}{Z} \qquad \left(\frac{\Delta R_M}{R_M} < \pm 10\% \text{ for } 13 \leq Z \leq 92\right) \end{aligned} \tag{3.24}$$

with:

$$E_{ms} = m_e \sqrt{\frac{4\,\pi}{\alpha}} \; \ldots \; \text{constant in multiple scattering theory.}$$

The Molière radius describes the average lateral deflection of electrons with critical energy ϵ_0 after traversing 1 X_0. For absorber elements of high atomic number Z the transverse spread of the electromagnetic shower in $[X_0]$, given by the deflection angle θ of the track with respect to the shower axis, is much larger than for absorber elements of low Z. The angle θ depends on R_M, i.e. on E_{ms}/ϵ_0, and from Monte Carlo calculations one obtains [AMA81]:

$$< \cos\theta > \simeq \cos\left(\frac{E_{ms}}{\pi \cdot \epsilon_0}\right). \tag{3.25}$$

Equation 3.25 is valid for threshold energies not too large, i.e. $E_{thr}\,[MeV] \leq 10/\varepsilon_0\,[MeV]$. The effective thickness of the layer for a shower particle is $d\,[X_0]/\cos\theta$ and, using eq. 3.23, one obtains for the intrinsic sampling fluctuations of an electromagnetic calorimeter:

$$\frac{\sigma_E}{E}(e) \geq 3.2\% \cdot \sqrt{\frac{\varepsilon_0\,[MeV]}{F(z)\cdot\cos\left(\frac{E_{ms}}{\pi\cdot\varepsilon_0}\right)}\cdot\frac{d\,[X_0]}{E\,[GeV]}}\;. \tag{3.26}$$

Equations 3.26 and 3.21 show that one has to increase the number of charged-particle crossings in order to decrease the contribution of sampling fluctuations to the total energy resolution. This can be done by increasing the number of samples N_s per radiation length, i.e. making the layer thickness $d\,[X_0]$ as small as possible.

Landau Fluctuations

Landau fluctuations arise in thin absorbers (see Appendix A) and are small for ionization losses of a few MeV (i.e. few mm of scintillator), but are comparable to the intrinsic sampling fluctuations if the amount of ionization loss is in the keV range, e.g. for gaseous detectors [FAB85]. The contribution is estimated to [AMA81]:

$$\frac{\sigma_E}{E}(e) \simeq \frac{2}{\sqrt{N_s}\,\ln\left(10^4\,\Delta x_a\,[g\,cm^{-2}]\right)} \tag{3.27}$$

where:

$\Delta x_a \ldots$ thickness of active absorber plate in $[g\,cm^{-2}]$.

Path-Length Fluctuations

Charged particles can cross the active plates of a sampling calorimeter under large as well as small deflection angles. The large deflection is due to multiple scattering of low-energy particles. Different crossing angles result in path-length fluctuations. In addition, the increased multiple scattering in dense materials makes straight crossings less probable and therefore reduces the path-length fluctuations.

In summary the Landau as well as the path-length fluctuations are small compared to the intrinsic sampling fluctuations in a sampling calorimeters with dense active absorbers of a few millimeter. The overall sampling fluctuations are dominated by the layer thickness of the calorimeter, as given by eq. 3.26, that determines the sampling frequency of an electromagnetic shower.

Hadronic Sampling Fluctuations

Sampling fluctuations have been discussed so far only for electromagnetic showers. For a hadronic shower in a sampling calorimeter no equivalent description has been given so far. However, a parametrization has been derived by [FAB85] from measurements on different hadron calorimeters:

$$\frac{\sigma_E}{E}(h) \gtrsim 9\% \sqrt{\frac{\Delta E[MeV]}{E[GeV]}} \tag{3.28}$$

where:

$\Delta E = \frac{dE}{dx}(mip)\,\Delta x \ldots$ minimum ionization loss in $[MeV]$ of all particles of the different hadronic shower components in a calorimeter layer (one active and one passive absorber plate) of thickness Δx in $[\frac{g}{cm^2}]$.

Compared to eq. 3.26 one can conclude that the hadronic sampling fluctuations are considerably larger than the electromagnetic ones.

3.2.2 Sampling Fractions

By describing the shower development in a calorimeter using the total average track length $< T > [X_0]$ one can define an absolute energy scale in the response to an electromagnetic or hadronic shower. In the case of a sampling calorimeter, the part of the energy that is carried away by the different kinds of shower particles is deposited in the active (E_{vis}) and passive (E_{invis}) layers of the calorimeter; this leads to the definition of the ***sampling fraction*** [BRÜ86], i.e. the fraction of the deposited energy detected in the active absorber layers of the sampling calorimeter, for the different components $i = e, \gamma, h, mip, n$ etc. of a shower:

$$\begin{aligned} S(i) &= \frac{E_{vis}(i)}{E_{vis}(i) + E_{invis}(i)} \\ &\equiv \tilde{i} \end{aligned} \tag{3.29}$$

where:

$E_{vis}(i)\ldots$	visible energy in the active absorber plate of shower component i
$E_{invis}(i)\ldots$	invisible energy in the passive absorber plate of shower component i
$e, \gamma, h, mip, n\ldots$	shower component, consisting of electrons or positrons (e), photons (γ), hadrons (h), minimum ionizing particles (mip), where for neutrons (n) the energy deposition is understood to occur indirectly in the form of inelastic or elastic collisions of neutrons with nuclei or protons.

The various sampling fractions $S(i)$ are usually given relative to the sampling fraction of a minimum ionizing particle, $S(mip) \equiv \widetilde{mip}$, where:

$$E(mip) = \frac{dE}{dx}(mip) \cdot \Delta x \tag{3.30}$$

with:

$E(mip)\ldots$	energy loss of a minimum ionizing particle in the active (visible) or passive layer (invisible)
$\frac{dE}{dx}(mip) \cdot \Delta x\ldots$	*mean* energy loss of a minimum ionizing particle (see Appendix A) in the active or passive absorber of thickness Δx, tabulated in [LOH85, STE84, PDG86].

In this section a discussion of the $\tilde{e}/\widetilde{mip}$-ratio for the electromagnetic shower will be given. The ratios for the components of the hadronic shower are described in sec. 3.4.

According to the definition of the sampling fraction eq. 3.29, the $\tilde{e}/\widetilde{mip}$-ratio is:

$$\frac{\tilde{e}}{\widetilde{mip}} \equiv \frac{S(e)}{S(mip)}. \tag{3.31}$$

To measure the electromagnetic sampling fraction $\tilde{e}$ one has to rescale from the measured average pulse height of electrons ($< PH(e) >$), mostly given in units of *ADC CHANNELS*, to units of energy (GeV) by taking muons of the same energy as the electrons. The measured electromagnetic sampling fraction is then given as follows:

$$\begin{aligned} \tilde{e} &\equiv S(e) \\ &= \frac{< PH(e) >}{E} \cdot \frac{\Delta E_a(\mu)}{PH(\mu)|_m} \end{aligned} \tag{3.32}$$

where:

$< PH(e) > \ldots$ measured average pulse height in $[ADC\ CH.]$ of electrons in the calorimeter

$E \ldots$ incident energy in $[GeV]$ of electrons or muons

$\Delta E_a(\mu) \ldots$ *mean* deposited energy of muons with energy E in $[GeV]$ in the active absorber plates of the calorimeter (see eq. 3.33)

$PH(\mu)|_m \ldots$ *mean* value of measured pulse height distribution of muons in $[ADC\ CH.]$ with energy E (see Appendix A for detailed discussion on *mean* and *most probable* values of pulse height distribution of muons).

Under the assumption that none of the energy lost by the muons in the passive absorber is transferred to the active plate or vice versa, the deposited energy of muons $\Delta E_a(\mu)$ in the active layer is due to ionization, bremsstrahlung and pair production:

$$\Delta E_a(\mu) = \left(\frac{dE}{dx}(\mu)\bigg|_a^{ION} + \frac{dE}{dx}(\mu)\bigg|_a^{BREMS} + \frac{dE}{dx}(\mu)\bigg|_a^{PAIR} \right) \cdot \Delta x_a \ MeV \qquad (3.33)$$

with:

$\frac{dE}{dx}(\mu)\big|_a^{ION} \cdot \Delta x_a \ldots$ *mean* energy loss of muons due to ionization in the active absorber of thickness Δx_a in $[MeV]$

$\frac{dE}{dx}(\mu)\big|_a^{BREMS} \cdot \Delta x_a \ldots$ *mean* energy loss of muons due to bremsstrahlung in the active absorber of thickness Δx_a in $[MeV]$

$\frac{dE}{dx}(\mu)\big|_a^{PAIR} \cdot \Delta x_a \ldots$ *mean* energy loss of muons due to pair production in the active absorber of thickness Δx_a in $[MeV]$.

Instead of the $\frac{\tilde{e}}{\widetilde{mip}}$-ratio the $\frac{\tilde{e}}{\tilde{\mu}}$-ratio of a sampling calorimeter is sometimes quoted, for example in [BOT81a,b; AKE85]. This ratio is defined as follows [AMA81, FAB85]:

$$\frac{\tilde{e}}{\tilde{\mu}} = \frac{< PH(e) >}{PH(\mu)|_{mp}} \cdot \frac{\epsilon(\mu)|_a^{ION} + \epsilon(\mu)|_p^{ION}}{E \cdot \epsilon(\mu)|_a^{ION}} \qquad (3.34)$$

with:

$PH(\mu)|_{mp} \ldots$ *most probable* value of measured pulse height distribution of muons in $[ADC\ CH.]$ with energy E (see Appendix A for detailed discussion on *mean* and *most probable* values of pulse height distribution of muons)

$\epsilon(\mu)|_a^{ION} \ldots$ *most probable* energy loss of a muon at minimum ionization in $[MeV]$ in the active absorber of given thickness

$\epsilon(\mu)|_p^{ION} \ldots$ *most probable* energy loss of a muon at minimum ionization in $[MeV]$ in the passive absorber of given thickness.

The $\tilde{e}/\widetilde{mip}$- and $\tilde{e}/\tilde{\mu}$-ratio are different because of the following effects:

- muons are only minimum ionizing at energies of $300 - 400\ MeV$; normally, calorimeter measurements are performed in the GeV-range so the deposited energy is larger than at the minimum of the $\frac{dE}{dx}$-curve because of the relativistic rise (Fig. 3.1);
- in addition, relativistic muons lose their energy by bremsstrahlung, e^+e^- pair production [LOH85] and by normal ionization where in high-energy transfers to the atomic electrons of the absorber material δ-rays are produced; depending on the thickness of the absorber plate this may lead to a tail to high energies in the distribution, known as Landau distribution [LAN44] (see Appendix A);

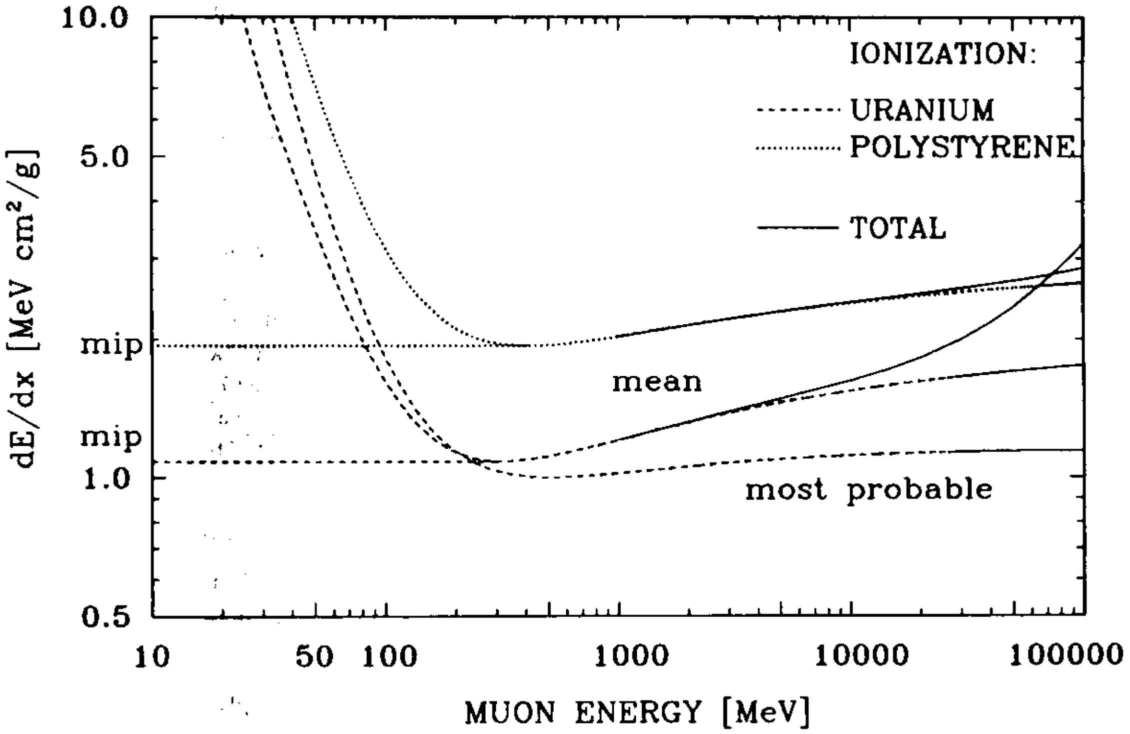

Figure 3.1: Ionization Loss (dotted and dashed lines) and Total Energy Loss (full lines), Including Ionization, Bremsstrahlung and Pair Production, of Muons in Uranium and Polystyrene (Scintillator) as a Function of the Muon Energy [LOH85]. The most probable Ionization Loss of Muons in Uranium is plotted for Comparison

- the muon sampling fraction is therefore energy dependent and hence the $\tilde{e}/\tilde{\mu}$-ratio, too; this is not the case for the sampling fraction of the minimum ionizing particle and hence the $\tilde{e}/\widetilde{mip}$-ratio does not depend on the energy;
- to obtain an approximately energy independent muon signal the *most probable* value of the muon distribution $PH(\mu)|_{mp}$ and the *most probable* energy loss $\varepsilon(\mu)|_a^{ION}$ is used which is almost energy independent as can be seen from Fig. 3.1; the *most probable* value is, however, not proportional to the thickness of the absorber that is traversed by the muon, which is true for the *mean* value (see Appendix A).

As suggested also by [BRÜ86, WIG87] it is therefore more convenient to express the various sampling fractions normalized to the $\widetilde{mip}$ rather than to the $\tilde{\mu}$ sampling fraction because $\tilde{e}/\tilde{\mu}$-ratios of different calorimeters and different energies are difficult to compare.

Measurements with calorimeters of different sampling configuration have been performed and the response to electrons in an absolute energy scale were given [ABR81, AKE85, BOT81a, CAT87b, DRE83, HOF82, LOR87]. A survey is given in Tab. 3.4, the $\tilde{e}/\widetilde{mip}$-ratios have in many cases been recalculated according to eqs. 3.32, 3.33. Despite of some uncertainties in the quoted numbers, in particular in the obtained values from the *Cu*-scintillator calorimeter, the measurements indicate that

- the $\tilde{e}/\widetilde{mip}$-ratio is always *smaller* than 1 for sampling calorimeters;
- the $\tilde{e}/\widetilde{mip}$-ratio *decreases* with *increasing* difference $\Delta Z = Z_p - Z_a$, where Z_a and Z_p are the atomic numbers of the active and passive absorber materials;

- in addition, measurements with a lead-scintillator electromagnetic calorimeter of different lead thicknesses [HOF82, Fig. 2] indicate that the electromagnetic sampling fraction and hence the $\tilde{e}/\widetilde{mip}$-ratio *decreases* with *increasing* thickness of the lead plates at a constant thickness of scintillator plates.

Table 3.4: Recalculated $\tilde{e}/\widetilde{mip}$-ratios from given References of Performed Measurements with Different Sampling Calorimeters

$\frac{\tilde{e}}{\widetilde{mip}}$	E $[GeV]$	ΔZ	Calorimeter Configuration	Reference
0.72	10	≈ 23	$25\,mm$ Fe/$5\,mm$ Scintillator	[ABR81]
0.78	5	≈ 26	$5\,mm$ Cu/$2.5\,mm$ Scintillator	[BOT81a]
0.80	5	≈ 26	$5\,mm$ Cu/$4\,mm$ Scintillator	[LOR87]
0.65	1	≈ 79	$1\,mm$ Pb/$5\,mm$ Scintillator	[DRE83]
0.57	10-40	≈ 89	$10\,mm$ U/$2\,mm$ Fe/ $5\,mm$ Sci	[CAT87b]

The observed facts have been confirmed with EGS4-Monte Carlo calculations [NEL85] by [FLA85, BRÜ86, WIG87] and are explained with the different Z-dependences of the different processes involved:

- at the beginning of the electromagnetic shower (high energies of the shower particles) the bremsstrahlung ($\propto Z^2$) and pair production ($\propto Z^2$) processes dominate;
- as the shower develops, the total energy is shared between an increasingly larger number of shower particles and therefore their average energies become lower (see eq. 3.10); electrons and positrons start to lose their energy via ionization ($\propto Z$), low energy photons by Compton scattering ($\propto Z$) or by the highly material-dependent photoeffect ($\propto Z^5$; see for instance photon mass attenuation curves in [PDG86, WIG87]).

Hence, low-energy electrons get produced in high-Z absorber materials by the photoeffect and their small amount of energy is also deposited there, cutting off significantly the low-energy component of the electromagnetic shower.
Making the absorber plates thinner improves the ability of the low-energy electrons (created by the photoeffect) to escape from the high-Z absorber plate. They therefore contribute more to the measured signal in the active layer. This effect becomes saturated with a thickness of the passive absorber plates of about $\geq 5\,mm$ for lead (measurement by [HOF82]) or $\geq 3mm$ for uranium (simulation by [BRÜ86, WIG87]).

3.3 Development and Components of a Hadronic Shower in a Sampling Calorimeter

3.3.1 Hadronic Showers

A hadronic-initiated shower in a calorimeter arises by successive inelastic hadronic interactions of the secondary particles with the nuclei of the absorber material. Pions and nucleons are most abundant, their relative fraction depends only weakly on the incident energy [IWA79]. Interactions with nuclei can be considered as quasi-free collisions on bound nucleons at high energies, where the primary energy is much larger than the binding energy of the nucleons. The inelastic cross-section for primary nucleons is approximately proportional to $A^{2/3}$ and proportional to $A^{3/4}$ for mesons [IWA79].

The scale for the longitudinal development of hadronic showers is given by the nuclear absorption length

$$\lambda_0 = \frac{A}{N_A\,\sigma_i} \quad \frac{g}{cm^2} \tag{3.35}$$

σ_i ...	inelastic nuclear coss section $[cm^2]$
A, N_A ...	see eq. 3.2.

In Tab. 3.5 values of λ_0 are listed for some materials [PDG86, LOH85].

Table 3.5: Values of the Nuclear Interaction Length for Some Materials

Material	$\lambda_0\left[\frac{g}{cm^2}\right]$	$\lambda_0[cm]$
Polystyrene	82.0	77.4
Al	106.4	39.4
Fe	131.9	16.8
Pb	194.0	17.1
U	199.0	10.5

A hadronic shower consists of two components:

1. an electromagnetic component with electrons, positrons and photons due to π^0-, η- etc. decay;
2. a hadronic component consisting of protons, pions ($\pi^\pm$), kaons ($K^\pm$), neutrons, nuclear γ-rays, light ions etc.; there are also neutrinos and muons from π- and K-decays and a certain fraction of neutrons that escape from detection; excitation, break-up, rearrangement and recoil of nuclei consumes a major fraction of the available energy which will not be detected ('lost' energy).

The incident energy of the primary hadron initiating the shower is shared among these two components:

$$f_{em} = \frac{E_{em}}{E} \tag{3.36}$$

$$f_h = \frac{E_h}{E} \tag{3.37}$$

with:

$$f_{em} + f_h = 1 \tag{3.38}$$

where:

f_{em} ...	electromagnetic fraction (mostly neutral pions) of the incident energy E available in the calorimeter from particles of the electromagnetic component
f_h ...	purely hadronic fraction (including 'lost' energy) of the incident energy E available in the calorimeter from particles of the hadronic component
E_{em} ...	available energy from the electromagnetic component
E_h ...	available energy from the purely hadronic component, including 'lost' energy
E ...	incident energy of primary particle.

The relative fluctuations between f_{em} and f_h lead to fluctuations between the visible part of the electromagnetic and hadronic component in a sampling calorimeter. This is one source of fluctuations that contributes to the energy resolution of a hadron calorimeter. A further contribution to the energy resolution comes from large fluctuations in the hadronic component caused by the fluctuating fractions of energy consumption for nuclear binding energy, break-up and recoil of nuclei etc..

In order to optimize the energy resolution of a hadron calorimeter one has to minimize both kinds of fluctuations. The mentioned fluctuations will be minimized if the e/h-ratio becomes equal to 1. To explain this one has to look at the *measurable* e/h-ratio that is defined as follows:

$$\left.\frac{e}{h}\right|_m := \frac{< PH(e) >}{< PH(h) >} = \frac{\frac{\tilde{e}}{\widetilde{mip}}}{< f_{em} > \cdot \frac{\tilde{\pi}^0}{\widetilde{mip}} + < f_h > \cdot \frac{\tilde{h}}{\widetilde{mip}}} \qquad (3.39)$$

where:

$< PH(e) > \ldots$	measured average pulse height in $[ADC\ CH.]$ of electrons with incident energy E in the calorimeter
$< PH(h) > \ldots$	measured average pulse height in $[ADC\ CH.]$ of hadrons with incident energy E in the calorimeter
$\frac{\tilde{e}}{\widetilde{mip}} \ldots$	visible fraction of available energy from electrons, relative to that of a minimum ionizing particle (mip) (sec. 3.2.2)
$< f_{em} > \ldots$	average fraction of incident energy available from the electromagnetic component (mostly π^0s) in the hadronic shower: $< f_{em} > \approx 0.12 \ln E\,[GeV]$ for few $GeV \leq E \leq$ few $100\,GeV$ [FAB85] (3.40)
$\frac{\tilde{\pi}^0}{\widetilde{mip}} \ldots$	visible fraction of available energy from electromagnetic component (mostly π^0s), relative to that of a minimum ionizing particle (mip)
$< f_h > \ldots$	average fraction of incident energy available from the purely hadronic component of the shower, i.e. without the electromagnetic component
$\frac{\tilde{h}}{\widetilde{mip}} \ldots$	visible fraction of available energy of purely hadronic component, relative to that of a minimum ionizing particle (mip).

The visible parts of the available energy (sampling fractions) due to neutral pions ($\tilde{\pi}^0$), electrons ($\tilde{e}$) and hadrons (except neutral pions) ($\tilde{h}$) are determined by the kind of absorber material and the calorimeter configuration. This was discussed in the last section for electrons and will be described in the next section for hadrons. If the relative sampling fractions of all three components $\tilde{e}/\widetilde{mip}$, $\tilde{\pi}^0/\widetilde{mip}$ and $\tilde{h}/\widetilde{mip}$ can be made equal by the use of the appropriate absorber material and configuration, the measurable e/h-ratio will be equal to 1, as can be seen from eqs. 3.39, 3.38. This means that the average response of the calorimeter to hadrons would be independent of the fluctuations between the electromagnetic and hadronic component of the hadronic shower thus improving the energy resolution.

For equal configuration of the electromagnetic and hadronic section of a calorimeter the sampling fraction $\tilde{\pi}^0/\widetilde{mip}$ of the electromagnetic component, (mostly neutral pions) is equal to the sampling fraction of electrons, $\tilde{e}/\widetilde{mip}$. This was shown by Monte Carlo simulations [AND87b, ZEU87]. One therefore has to *compensate* for the undetectable part of the available energy of the hadronic component to achieve $\tilde{e}/\widetilde{mip} = \tilde{h}/\widetilde{mip}$ and hence an optimum energy resolution.

The hadronic component can be decomposed into fractions with different responses in the calorimeter [BRÜ86]. Together with the underlying nuclear processes, this will be discussed in more detail in sec. 3.4.

In the following some values of the energy resolution and of e/h-ratios obtained with different hadron calorimeters will be listed to illustrate the connection between both quantities. Most of the hadron calorimeters are sampling calorimeters but for comparison the result of a measurement with a *homogeneous* liquid scintillator hadron calorimeter (8.7 λ_0 deep) will be given [BEN75] (no e/h-ratio is quoted from this measurement). With this latter calorimeter an energy resolution for hadrons of

$$\frac{\sigma_E}{E}(h) \simeq 12\% \qquad 20\,GeV \leq E \leq 150\,GeV \qquad (3.41)$$

was measured, parametrized [AMA81] for fully contained hadronic showers as:

$$\frac{\sigma_E}{E}(h) = \frac{11\%}{\sqrt{E[GeV]}} + 9\% \tag{3.42}$$

with:

$E\ldots$ energy of incident hadrons in $[GeV]$.

With a fine grained *sampling* hadron calorimeter of 38 units of 8 cm thick marble ($CaCO_3$) plates as passive absorber and 3 cm thick scintillator plates and proportional tubes as active media (7.7 λ_0 in total) the CHARM collaboration [CHA87] achieved an energy resolution of

$$\frac{\sigma_E}{E}(h) = \frac{48.7\%}{\sqrt{E[GeV]}} + 1.27\% \pm 0.3\% \qquad \text{Scintillator} \tag{3.43}$$

$$\frac{\sigma_E}{E}(h) = \frac{44.3\%}{\sqrt{E[GeV]}} + 8.10\% \pm 1.8\% \qquad \text{Proportional Tubes} \tag{3.44}$$

for hadrons in the energy range of 7.5 to 140 GeV. An additional contribution to the energy resolution is included in the given numbers due to sampling fluctuations (see sec. 3.2.1).

A much finer sampling calorimeter with 3 modules of 5 mm copper and 2.5 mm scintillator and 3 modules of 5 mm lead and 2.5 mm scintillator (6.9 λ_0 deep in total) was exposed to pions of 5, 7 and 10 GeV [BOT81b]. The obtained energy resolution for hadrons was:

$$\frac{\sigma_E}{E}(h) = \frac{(50.6 - 53.8)\%}{\sqrt{E[GeV]}}. \tag{3.45}$$

The presented calorimeter configurations yield a measured e/h-ratio larger than 1, i.e. for the CHARM-calorimeter [CHA87]

$$\frac{e}{h} = 1.27|_{7.5\,\mathrm{GeV}} \rightarrow 1.13|_{50\,\mathrm{GeV}} \qquad \text{Scintillator} \tag{3.46}$$

$$\frac{e}{h} = 1.18|_{7.5\,\mathrm{GeV}} \rightarrow 1.09|_{50\,\mathrm{GeV}} \qquad \text{Proportional Tubes} \tag{3.47}$$

and for the Cu/Pb-calorimeter [BOT81b]

$$\frac{e}{h} = 1.42\,|_{5,7\,\mathrm{GeV}}\,. \tag{3.48}$$

As discussed in sec. 3.3.1 a compensating calorimeter ($e/h \approx 1$) should give a better energy resolution for hadrons. This was experimentally verified by [BOT81b] with a calorimeter configuration of 2 and 3 mm uranium and 2.5 mm scintillator plates (total depth: 6.9 λ_0). The obtained energy resolution for hadrons was:

$$\frac{\sigma_E}{E}(h) = \frac{33\%}{\sqrt{E[GeV]}}. \tag{3.49}$$

The e/h-ratio was measured to 1.09 - 1.15, but is probably influenced by transverse and longitudinal leakage and by the light attenuation length of the wavelength shifter through which the signal is transported to the photomultipliers (see sec. 4.5.4).

3.3.2 Longitudinal and Transverse Hadronic Shower Development

The average longitudinal and lateral propagation of hadronic showers will be considered first before the individual components are discussed in more detail.

The average longitudinal distribution scales approximately in units of the interaction length λ_0. The first interaction of the incoming hadron with the absorber material is important for the further longitudinal development of the shower. Close to the shower vertex one observes an enhancement in the longitudinal distribution due to the contribution of the electromagnetic component. For larger distances from the shower vertex the distribution decreases exponentially [CAT87b].

The vertices of hadronic showers are distributed over the whole depth of the calorimeter. Its number decreases exponentially as the distance from the front end of the calorimeter increases. The resulting average shower distribution rises close to the front end of the calorimeter and falls almost exponentially with growing depth. This behaviour results from the superposition of many showers close to the front end of the calorimeter and a diminishing number of interactions far away.

In transverse direction the distribution depends on the longitudinal propagation with a rather narrow core of the shower (0.1-0.5 λ_0 fwhm) that increases with the depth in the calorimeter [FAB85]. This core consists of high-energetic particles while it is surrounded by low-energetic ones, mainly neutrons and photons, at a considerable distance (few cm) away from the shower axis. The following parametrizations are found from experimental data [FAB85]:

- the position of the shower maximum:

$$t_{max}[\lambda_0] \sim 0.2 \ln E\,[GeV] + 0.7 \tag{3.50}$$

  where:

  t_{max} ... depth in $[\lambda_0]$ at which the maximum of the shower occurs
  E ... energy of incident hadron in $[GeV]$;

- longitudinal containment of 95% of the shower energy:

$$L_{95\%}[\lambda_0] \simeq t_{max}\,[\lambda_0] + 2.5\,\lambda_{att}\,[\lambda_0] \tag{3.51}$$

  where λ_{att} is the exponential decay length of the shower beyond t_{max} in $[\lambda_0]$ given approximately by:

$$\lambda_{att}\,[\lambda_0] \simeq \lambda_0\,(E[GeV])^{0.13};$$

- transverse radius for 95% of energy containment (very approximative):

$$R_{95\%} \leq \lambda_0. \tag{3.52}$$

There is an additional leakage from the front side of the calorimeter called albedo. It is due to neutrons and backscattered secondaries. The resulting energy leakage is estimated to be 2-3% with large fluctuations because of the small number of secondaries at the early stage of the shower [IWA79].

The energy resolution of a calorimeter is more effected by longitudinal than by transverse leakage because the fluctuations among the average longitudinal energy deposition are much larger than that in transverse direction. Incomplete containment of the hadronic showers deteriorates the energy resolution because of the following effects:

- in the case of energy leakage the total pulse height becomes smaller resulting in an asymmetric distribution of the hadronic response;
- the average hadronic response of the calorimeter will not scale linearly with the energy E of the incident hadron as well as the resolution will not scale with $1/\sqrt{E[GeV]}$.

The total length of a hadron calorimeter should be about 8 λ_0 in order to contain 95% of the energy of 350 GeV carried by an incident pion [FAB85]. With a calorimeter set-up described in sec. 5.2.1 more detailed criteria have been derived for the longitudinal containment of a hadron calorimeter at different energies [KRÜ86, CAT87b].

3.3.3 Hadronic Shower Composition

Although the individual physical processes involved in hadronic showers are quite well understood, the interplay of the various hadronic processes, influenced in addition by the alternation of active (low-Z) and passive (high-Z) material of a sampling calorimeter, leads to a very complex development of such a shower. This makes a description of its various stages rather complicated. Therefore, only a brief generalized picture of a hadronic shower in a uranium-scintillator sampling calorimeter will be given. Emphasis is put on those components that give a main contribution to the energy resolution; a pure hadronic shower is assumed, i.e. without an electromagnetic component.

The first interaction of a charged pion or proton with the calorimeter material will probably be ionization loss (see Fig. 3.2) in the passive $\left(\frac{dE}{dx}(p,\pi^{\pm})\Big|_{p}^{ION}\cdot\Delta x_p\right)$ and active $\left(\frac{dE}{dx}(p,\pi^{\pm})\Big|_{a}^{ION}\cdot\Delta x_a\right)$ layer. A signal will be created in the active layer only. The hadronic interaction with the absorber material at high energies ($\gtrsim 50\,MeV$) is a spallation process, i.e. a series of independent particle-particle collisions inside the nucleus and subsequent deexcitations by particle emissions and evaporation [ARM83]. For heavy nuclei, the spallation process is accompanied by high-energy proton induced fission and by fast neutron induced fission in the case of ^{238}U at each step of the deexcitation process. The fraction on the total inelastic cross section due to proton induced fission is (see Appendix B):

- in p-Pb reactions [PAP66, BRA71]:

$$\frac{\sigma_f\,(Pb(p,f))}{\sigma_t} = 0.05 - 0.1 \tag{3.53}$$

  where:

  $\sigma_f\,(Pb(p,f))\ldots$ cross section of proton induced fission in $[b]$
  $\sigma_t\ldots$ total inelastic cross section in $[b]$

- in p-U reactions:

$$\frac{\sigma_f\,(U(p,f))}{\sigma_t} = 0.6 - 0.8\,, \tag{3.54}$$

  where the maximum fissionability occurs in the energy region of the protons of $100 - 300\,MeV$ [PAP66].

Several competing nuclear reactions occur if a high energy hadron interacts with a nucleus and, because they are the decisive mechanisms in hadron calorimeters, they will be described in more detail. The description is based on the cascade model for higher energies ($\gtrsim 50\,MeV$) of the projectile, introduced by R. Serber (see, for instance, [ARM83, ATC79, HIN81, HYD64, SNQ81]) and on the model of the compound nucleus (see, for instance, [SEG77, MAY79]) for the low energy range (few MeV up to $\sim\ 50\,MeV$).

A spallation process with its subsequent steps of deexcitations develops as follows:

1. At high energies ($\gtrsim 50\,MeV$) the charged penetrating particle interacts with individual nucleons inside the target nucleon because of their low binding energy ($\simeq\ 8\,MeV$) relative to the energy of the incoming particle; this leads to an *intranuclear cascade* propagating through the nucleus during a short time interval of $t\ \approx\ 10^{-22}s$ while a few nucleons and mesons of relatively high energy ($\sim\ 100\,MeV$) can leave the target nucleus. Some of them will excite further (*internuclear*) cascades or, mostly *high-energy* or *cascade neutrons*, will leave the entire target. A long-lived ($\sim\ 10^{-17}s$) so called compound nucleus is formed in the medium energy range (few MeV up to $\sim\ 50\,MeV$) of the incoming charged projectile.

2. The excited rest nuclei undergo deexcitation within $t\ \approx\ 10^{-18}s$ [PAP66, BRÜ87] in successive *evaporation* steps of nucleons; for heavy nuclei deexcitation is in competition with either further evaporation, mostly neutrons because of the Coulomb barrier for protons and light ions, or high-energy ($\gtrsim\ 100\,MeV$) n- as well as p- and π- induced *primary fission*. The highly excited fragments will subsequently evaporate further neutrons, which in the case of ^{238}U will result in *secondary fissions*.

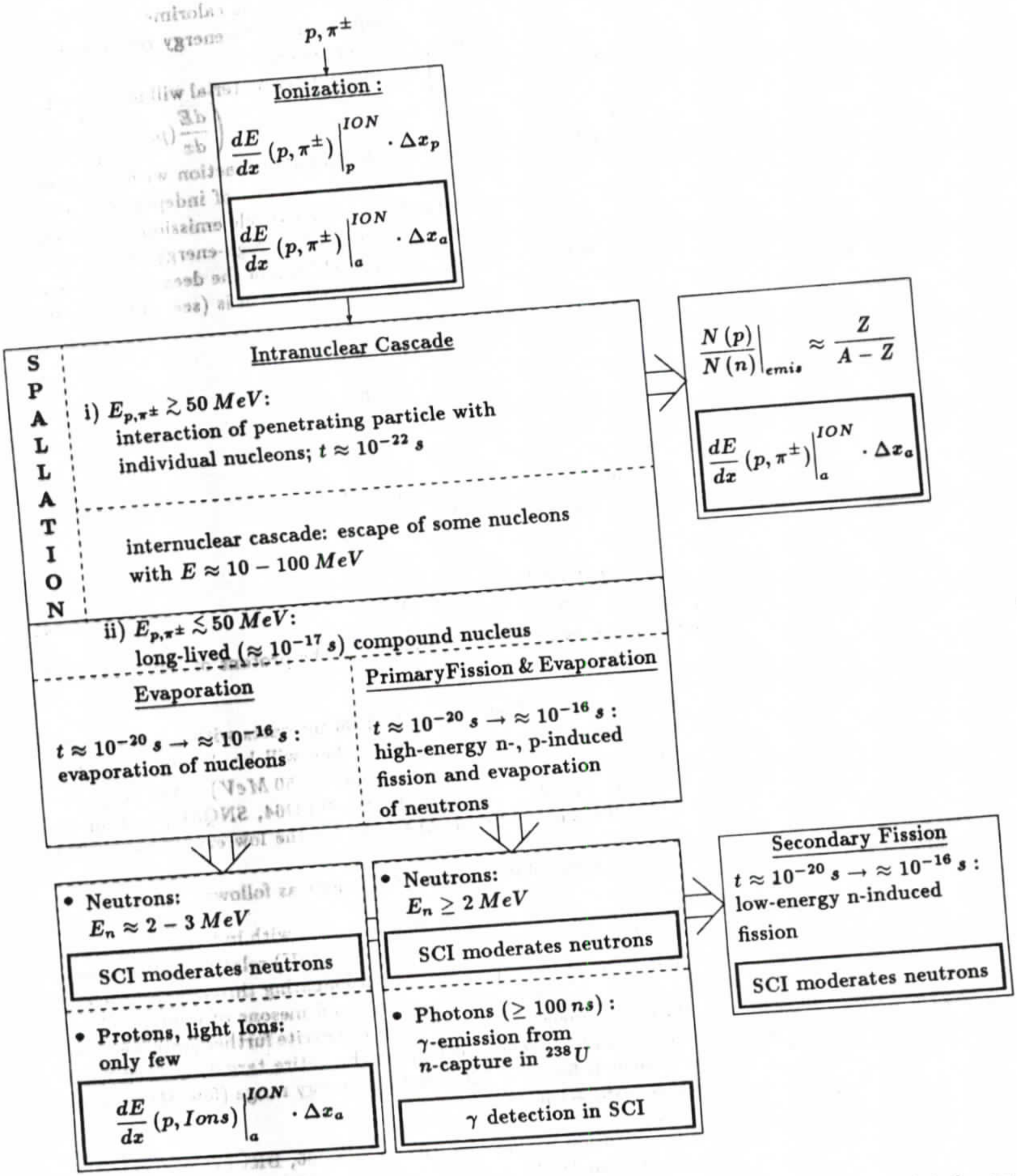

Figure 3.2: Block Diagram of a Simplified Pure Hadronic Shower in a ^{238}U-Scintillator Calorimeter (the bold frames are the sources of measurable signals); $dE/dx\,(p,\pi^\pm,Ions)|^{ION}\,\Delta x_{a(p)}$ denotes the Ionization Loss of Protons, Charged Pions and Light Ions in the Active (Passive) Absorber Plates of the Calorimeter, $N(p)/N(n)$ is the Ratio of the Number of Protons to the Number of Neutrons Released during the Intranuclear Cascade Step, Z and A are the Atomic and Mass Numbers of the Target Nucleus; SCI Means scintillator

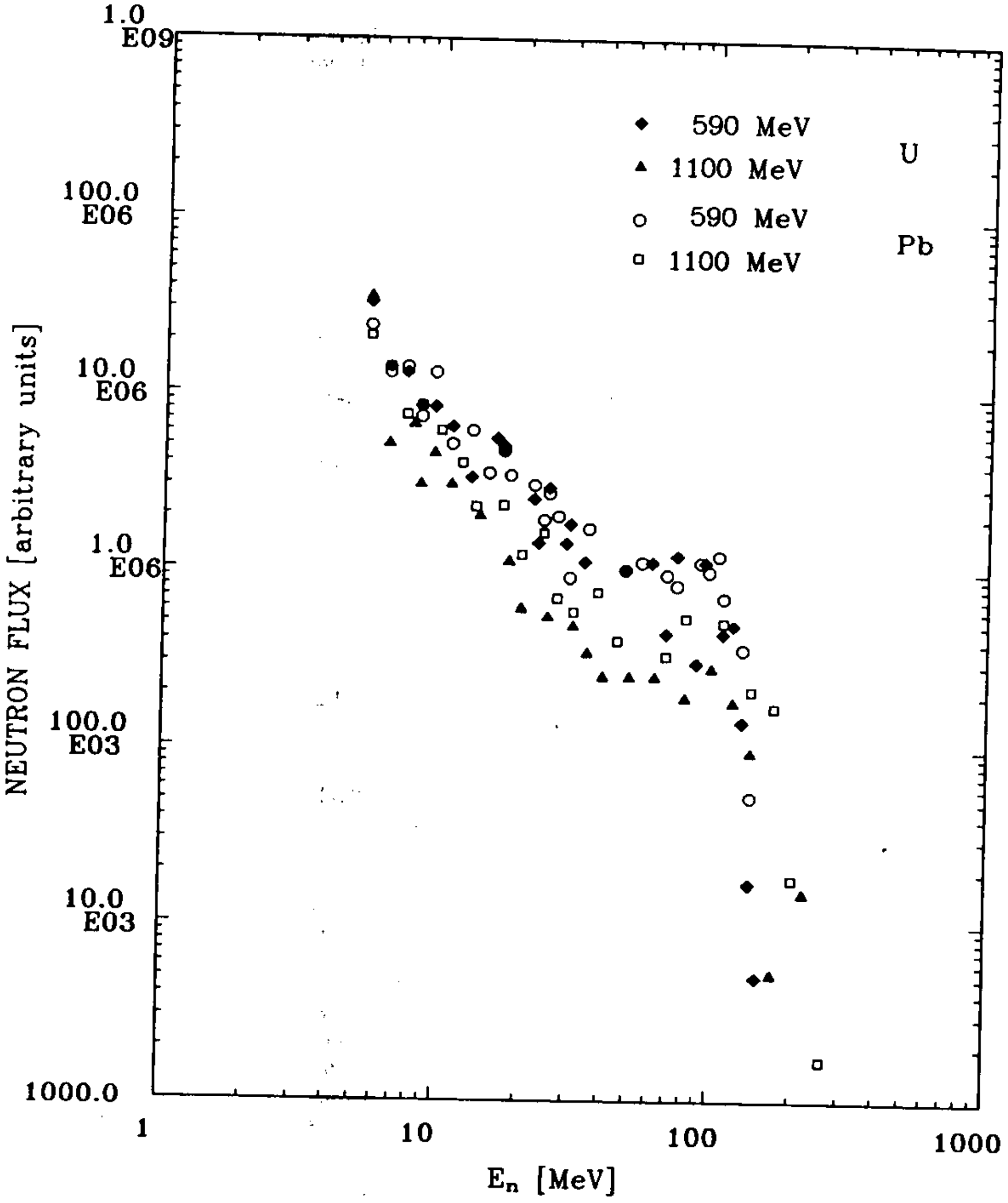

Figure 3.3: High Energy Neutron Spectrum from Moderated Sources (U Target, Pb Target) Bombarded with Protons of 590 MeV and 1100 MeV (E_n: Neutron Energy; Values copied from [HIN81])

Fig. 3.3 shows the measured neutron spectrum from a moderated source, built of a *Pb*- or *U*-target that was surrounded by light water or polyethylene for neutron moderation and bombarded by protons of 590 MeV and 1100 MeV [HIN81]. One observes an enhancement in the neutron energy range from $\sim$ 20 to $\sim$ 100 MeV which is due to the high-energetic neutrons released during the intranuclear cascade step.

The highly excited fission fragments evaporate neutrons with a higher average kinetic energy than the evaporated neutrons from the parent ^{238}U nuclei of the same excitation energy. This is shown in Fig. 3.4 [ATC79] as a result from a statistical model calculation for a parent ^{238}U nucleus and is simply because the excitation energy per nucleon is higher in the fission fragments than in the parent nucleus. Fragments of n-induced fission of ^{238}U have an excitation energy of $20 - 30\,MeV$ [HÜB81]. This will lead to neutron emissions with an average kinetic energy of the neutrons of about 1.9 MeV, according to the parametrization of the evaporation spectrum of neutrons from fission fragments [SEG77]:

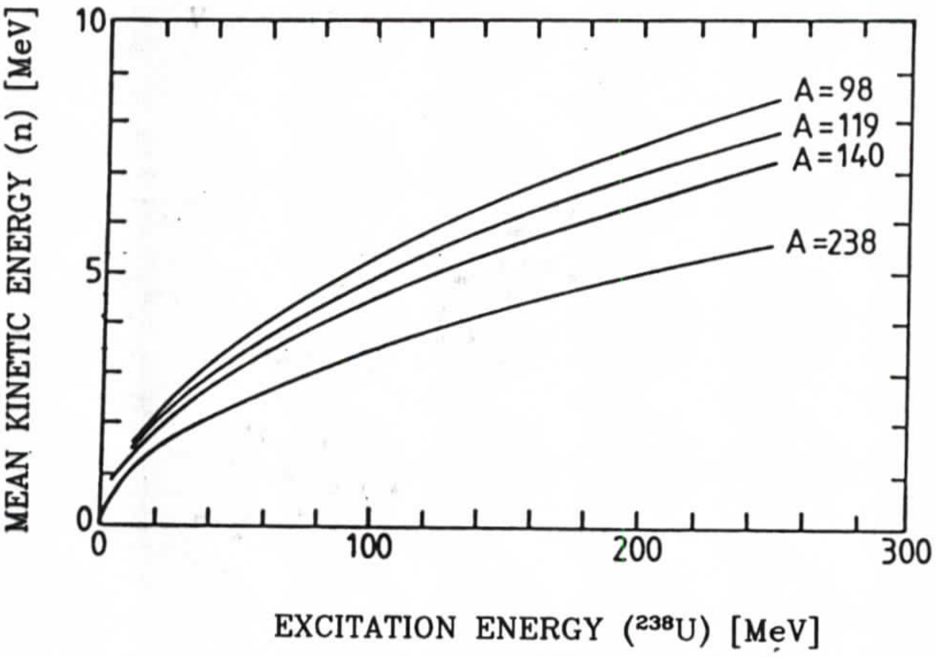

Figure 3.4: Dependence of the Mean Kinetic Energy of the Evaporation Neutrons on the Excitation Energy of the Parent ^{238}U Nucleus for Atomic Masses 238 (Parent Nucleus), 119 (Symmetric Fission) and 98, 140 (Asymmetric Fission) [ATC79]

$$f(E) = 2\,a\sqrt{\frac{a\,E}{\pi}}\;\exp\left(-a\,E\right)\quad MeV^{-1} \tag{3.55}$$

where:

$E \ldots$	kinetic energy in $[MeV]$ of the evaporated neutrons from fission fragments
$a = 0.775\,[MeV^{-1}] \ldots$	parameter obtained from measurements.

Those neutrons are able to induce further fissions in ^{238}U nuclei because of the low fission threshold at $\sim 1.2\,MeV$. Hence, the fission capability of ^{238}U leads to an enhancement above $\sim 2\,MeV$ in the total neutron spectrum of spallation reactions ("hardening" of the neutron spectrum) [ARM83].

In summary, the neutron spectrum due to spallation processes in heavy nuclei consists of the following components:

- a low energy component (few MeV) of evaporation neutrons from compound nuclei with a neutron enhancement above $\sim 2\,MeV$ for ^{238}U (slow neutrons);
- a high energy component ($\sim$ 20 to several $100\,MeV$) of cascade neutrons released in the intranuclear cascade process (high-energy neutrons).

During the evaporation step only very few charged particles like protons and alpha particles are released because of the Coulomb barrier of the excited nucleus. It is proportinal to $\frac{Z}{A^{\frac{1}{3}}}$ and amounts to $\simeq 14\,MeV$ for a proton in ^{238}U. Almost all protons are therefore produced in the fast cascade step with a fraction approximately equal to the fraction of protons to neutrons of the target nucleus, i.e. $\frac{N(p)}{N(n)} \approx \frac{Z}{A-Z} = 63\%$ for ^{238}U.

Measured spectra for secondary proton and pion production cross section for $590\,MeV$ incident protons on uranium and lead under two different laboratory emission angles are shown in Fig. 3.5 [HIN81]. The data are corrected for energy loss in the target material, the target thicknesses are $3.1\,mm$ (U) and $4.4\,mm$ (Pb). Measurements with $1100\,MeV$ protons on a $2.5\,cm$ thick lead target indicate that the energy of the emitted protons is almost proportional to the energy of the incident protons [HIN81]. Integrating over the observed energy range yields the cross section given in Tab. 3.6. At this particular proton energy and the given emission angles one observes that proton production in the spallation process is more abundant than pion production.

Table 3.6: Differential Cross Section for Secondary Proton- and Pion-Emission from Uranium and Lead for Bombardment by 590 MeV Protons

Emission Angle [°]	Particle	Pb $\frac{d\sigma}{d\Omega}\left[\frac{mb}{sr}\right]$	U $\frac{d\sigma}{d\Omega}\left[\frac{mb}{sr}\right]$
90	p	88.3	97.6
	$\pi^{\pm}$	5.0	7.4
157	p	25.1	26.0
	$\pi^{\pm}$	10.4	10.5

If the remaining excitation energies of the hit nuclei or the fission fragments are less than the binding energy of a nucleon, further deexcitation will proceed via γ-emission. Most of the photons are prompt, whereas n-capture of ^{238}U leads to a delayed γ-radiation [BRÜ85].

Having discussed so far only the individual nuclear reactions, their interplay in a massive ^{238}U as well as in a calorimeter stack of ^{238}U or Pb and plastic scintillator will now be explained. An experimental investigation has been done by [LER86] to study the components of a hadronic shower and to determine the neutron yield in massive ^{238}U, in a uranium-scintillator stack and also in lead.

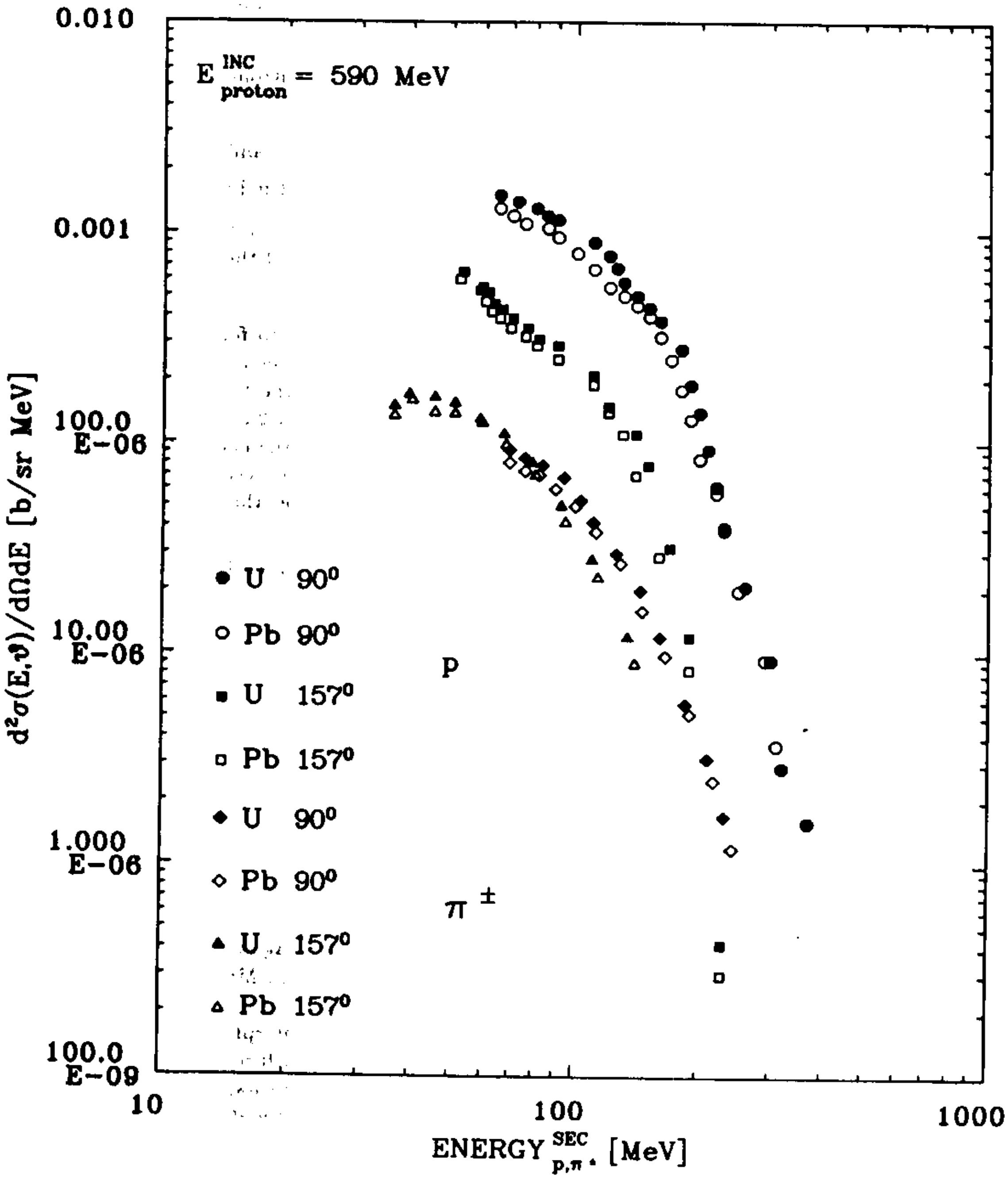

Figure 3.5: Differential Cross Section for Secondary Protons and Pions Emitted from Uranium and Lead at a Laboratory Angle of 90° and 157° for 590 MeV Incident Protons (Data are corrected for Energy Loss in Target Material; Values copied from [HIN81])

These measurements are based on the analysis of radioactivity induced by protons of 591 MeV and negative charged pions of 300 GeV incident on a massive ^{238}U stack, a calorimeter stack with 3 mm and 9 mm thick ^{238}U and 2.5 mm scintillator plates as well as a stack of 50 mm thick Pb plates interleaved with 3 mm ^{238}U plates to measure the neutron yield. From the measurement of the radioactive isotope distribution after the dismanteling of the stack one was able to deduce informations on the hadronic shower composition at different positions (see [LER86] for details of measurements). Protons of 591 MeV have been selected because π^0 production is negligible at this energy [LER86], but increases with energy according to eq. 3.40.

The result of the measurements shows that after 0.6 λ_0 in the massive ^{238}U stack the spallation products are strongly concentrated near the beam axis since they are predominantly produced by primary particles (see Fig. 3.6). The same is true for fission products which in addition give a wider tail in the transverse direction due to the n-induced part. This is because of the mean free path of the neutrons, which lies in the order of a few cm. For the same reason the products of the neutron capture process are widely distributed laterally.

Table 3.7: **Number of Fissions generated and Number of Neutrons captured per GeV of deposited Hadronic Energy for Different Calorimeter Configurations [LER86]**

Calorimeter Configuration	Incident Particle and Energy	Massive ^{238}U	3 mm ^{238}U 2.5 mm Scint.	9 mm ^{238}U 2.5 mm Scint.	50 mm Pb 3 mm ^{238}U †
Total Number of Fissions per GeV	p (591 MeV) π^- (300 GeV)	9.8 ± 1.3 4.1 ± 0.4	8.0 ± 1.1	8.9 ± 1.2	5.7 ± 0.8
Fraction on Total Number of Fissions per GeV induced by Charged Particles	p (591 MeV)		14 % ± 2 %		
Neutron Induced Fission Yield Relative to Yield in Massive ^{238}U	p (591 MeV)	100 %	80% ± 3%	90% ± 3%	53% ± 5%
Number of Neutrons captured per GeV	p (591 MeV)	43 ± 7	47 ± 8	51 ± 13	14 ± 3
Number of Neutron-Induced Fission to Number of Neutron Captures	p (591 MeV)	20% ± 1%	14%± 1%	15%± 2%	33%± 3%

† The given numbers are the neutron-induced fission or the neutron captures measured with thin uranium plates inserted in a massive lead block (see text)

The longitudinal distributions of the spallation and fission products measured in the massive ^{238}U stack are shown in Fig. 3.7. The number of spallation products decreases smoothly with increasing depth until a proton range of ~ 1.3 λ_0, where it drops steeply. At ~ 0.3 λ_0 the number of fissions shows its maximum and decreases until a rapid drop occurs again at ~ 1.3 λ_0. This is the range of the protons that may induce fission in the ^{238}U target. From this measurement it can also be concluded that pion production is not significant at this energy. For completeness, the distribution of neutron capture products is also shown.

Photonuclear reactions like $^{238}U(\gamma\,,n)^{237}U$ or $^{238}U(\gamma\,,p)^{237}Pa$ could also be detected in this measurement: the transverse distribution of ^{237}U nuclides is much more concentrated near the beam axis than that of the fission products; longitudinally a pronounced deviation from a smooth curve was found at around 10 X_0 that was attributed to the maximum of the electromagnetic shower generated by the high-energy γ-component.

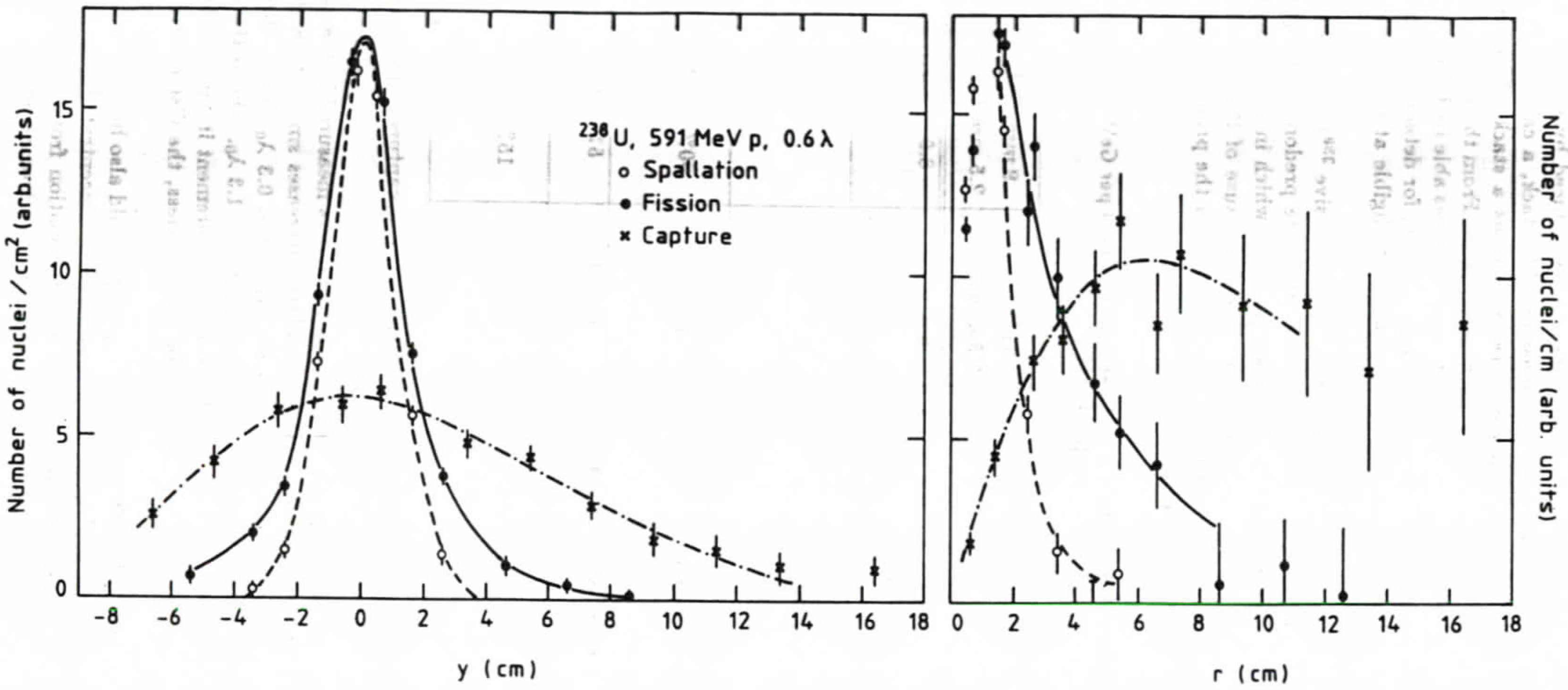

Figure 3.6: Transverse Distribution of Spallation, Fission and n-Capture Products in Massive ^{238}U at a Depth of 0.6 λ_0 after an Exposure with 591 MeV Protons [LER86]

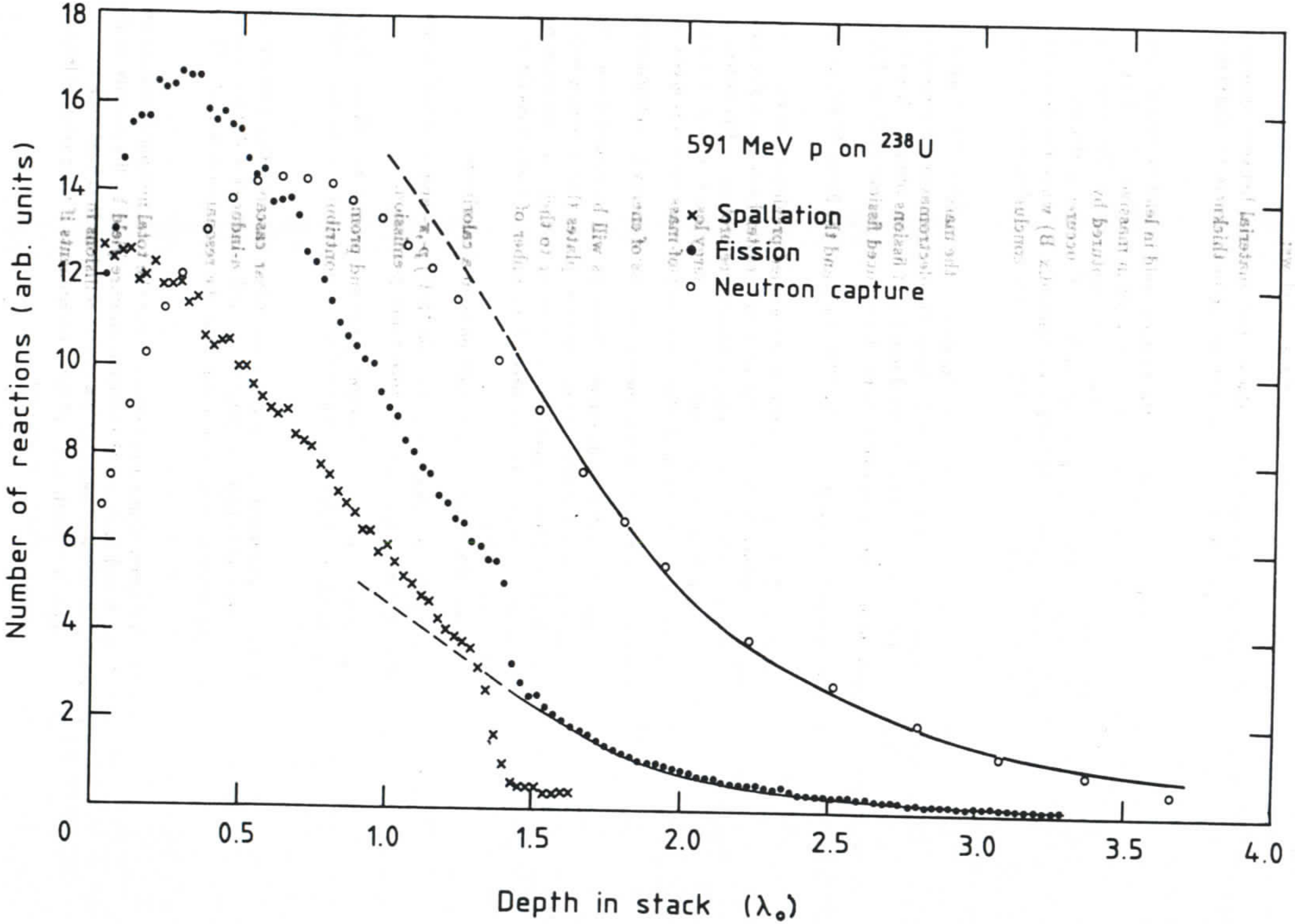

Figure 3.7: Longitudinal Distribution of Spallation, Fission and n-Capture Products after 591 MeV Proton Bombardment of a Massive ^{238}U Stack [LER86]

The results obtained from these measurements have been used [LER86] to derive the number of fissions per GeV for the different stack configurations, which are listed in Tab. 3.7.

The results of the fission yield measurements can be summarized as follows:

- **the total number of fissions decreases if scintillator is the readout material between uranium plates and this effect becomes stronger if the ratio of uranium plate thickness to scintillator plate thickness becomes smaller;**
- **comparing the massive ^{238}U with the Pb configuration the neutron yield in lead (measured with inserted uranium plates) is 53% of the neutron-induced fission yield in massive ^{238}U. Furthermore, the neutron yield in lead is 33% of the number of neutrons captured by ^{238}U which has to be compared with 20% for massive ^{238}U. Neutron capture by ^{238}U occures in the resonance region of the neutron energy of $10 - 1000\,eV$ [HÜB81] (see Appendix B) while the neutrons, capable to induce fission in ^{238}U, must have energies $\geq 1.2\,MeV$; the conclusion is that in lead the neutron spectrum is harder;**
- **in the measurements performed with a $300\,GeV\ \pi^-$ beam incident on the massive ^{238}U stack one observes that 58% ± 7% of the deposited energy results from the electromagnetic component (in fair agreement with eq. 3.40 yielding $\sim 68\%$); the total number of fissions obtained from the measurements at this energy includes an estimated fraction of γ-induced fissions of about 1%.**

A remarkable difference has been seen between the massive ^{238}U stack and the $3\,mm$ ^{238}U-$2.5\,mm$ scintillator configuration:
Slow neutrons produced in spallation or fission reactions have, as mentioned previously, an energy of $\leq 20\,MeV$, but before they eventually induce further fissions they will scatter both elastically and inelastically off the target nuclei. Organic scintillator material contains free protons so the neutrons will undergo elastic np-collisions with the protons of the scintillator. The energy loss E of neutrons with energy E_0 in an elastic collision under the scattering angle θ in the center-of-mass system is given by $\frac{E}{E_0} = \frac{A^2 + 1 + 2\,A\cos\theta}{(A+1)^2}$. Elastic np-scattering is the dominating process of energy loss of neutrons in the scintillator whereas in ^{238}U inelastic collisions dominate. Neutrons will be slowed down very fast (moderation) if scintillator plates are inserted between the uranium plates thus dropping below the fission threshold of ^{238}U of $1.2\,MeV$ and beeing captured much closer to their creation point by ^{238}U nuclei in the resonance region $10 - 1000\,eV$. As measured, the number of fissions decreases if scintillator plates interleave the uranium plates.

Summarizing, the following hadron induced interactions take place in a calorimeter:

- **the main nuclear reactions are spallation, high energy ($\sim 100\,MeV$) p-,π- and n- as well as low energy ($\sim 2\,MeV$) n-induced fission, evaporation, n-capture and γ-emission;**
- **neutrons of different energy, protons, to a smaller extend pions and prompt as well as delayed nuclear γ-rays are secondary products of these reactions that can contribute to the measurable signal in a hadron calorimeter;**
- **fast neutrons ($\sim 100\,MeV$) are produced during the intranuclear cascade step, neutrons of ~ 2 to $\sim 20\,MeV$ are evaporated after high-energetic p-, π- and n-induced and low-energetic n-induced fission, respectively, while neutrons are captured in the resonance region of ^{238}U at $10 - 1000\,eV$.**

Interleaving $3\,mm$ ^{238}U plates with $2.5\,mm$ scintillator plates reduces the total number of fissions per GeV from 9.8 in massive ^{238}U to 8.0 and increases the neutron capture yield by 9% relative to the yield in massive ^{238}U due to the moderation of neutrons via elastic collisions in the scintillator.

The total visible calorimeter signal will result from all these components if their relative fraction is taken into account. This is the subject of the next section.

3.4 Calorimeter Response to the Shower Components

The average response of the hadronic shower has been considered in terms of an average fraction on the incident energy available from the electromagnetic and the pure hadronic component (sec. 3.3.1). This average hadronic response has been compared to the average response of an electromagnetic shower ($(e/h)_m$) and it was shown that the fluctuations in the detected energy can be minimized if the measureable e/h-ratio is 1. A discussion of the different components, of their influences on the average hadronic response and on the e/h-ratio will be given in this section.

The purely hadronic component of a shower, i.e. without the electromagnetic component, will be considered in this discussion; accordingly, the e/h-ratio to be considered here is not the *measurable* but the *intrinsic* e/h-ratio of the calorimeter. The *intrinsic* e/h-ratio is defined as follows:

$$\left.\frac{e}{h}\right|_i := \frac{\frac{\tilde{e}}{\widetilde{mip}}}{< f_I > \cdot \frac{\widetilde{ION}}{\widetilde{mip}} + < f_n > \cdot \frac{\tilde{n}}{\widetilde{mip}} + < f_\gamma > \cdot \frac{\tilde{\gamma}}{\widetilde{mip}}} \qquad (3.56)$$

where:

$< f_I > \ldots$ average fraction of the incident energy available from ionization due to protons, pions and muons, excluding the electromagnetic fraction

$\frac{\widetilde{ION}}{\widetilde{mip}} \ldots$ sampling fraction of protons, muons and pions, relative to the sampling fraction of a minimum ionizing particle (mip) (see eq. 3.29)

$< f_n > \ldots$ average fraction of the incident energy excluding the electromagnetic component available from neutrons with $E \leq 20\,MeV$ from evaporation, from fission induced by high-energy protons, pions and neutrons and from fission induced by slow neutrons of $E \leq 20\,MeV$

$\frac{\tilde{n}}{\widetilde{mip}} \ldots$ sampling fraction of energy deposit of neutrons, relative to the sampling fraction of a minimum ionizing particle (mip) (see eq. 3.29)

$< f_\gamma > \ldots$ average fraction of the incident energy excluding the electromagnetic component available from nuclear γ-rays of deexcitation i) during spallation reactions, ii) via inelastic $(n, n'\gamma)$ reactions and iii) during fission or iv) neutron capture reactions; i) - iii) are prompt γ-rays while iv) are delayed

$\frac{\tilde{\gamma}}{\widetilde{mip}} \ldots$ sampling fraction of photons, relative to the sampling fraction of a minimum ionizing particle (mip) (see eq. 3.29)

with:

$$\begin{aligned} f_I + f_n + f_\gamma + f_L &= 1 \\ &= \frac{E_I + E_n + E_\gamma + E_L}{E - E_{em}} \end{aligned} \qquad (3.57)$$

where:

$f_L \cdots$ fraction of incident energy that is 'lost' because it goes into nuclear binding energy
break-up of nuclei, recoil energy of the target nucleus and neutrinos
$E_I \cdots$ available energy in form of ionization
$E_n \cdots$ available energy from neutrons
$E_\gamma \cdots$ available energy from nuclear γ-rays
$E_{em} \cdots$ available energy from the electromagnetic component (mostly π^0s)
$E_L \cdots$ nondetectable energy that goes into binding energy,
break-up of nuclei, recoil energy of the target nucleus and neutrinos.

Both $(e/h)_m$- and $(e/h)_i$-ratios become identical if the $\bar{e}/\widetilde{mip}$-ratio is equal to the $\bar{h}/\widetilde{mip}$-ratio as can be seen from eq. 3.39 assuming that $\bar{e}/\widetilde{mip} = \bar{\pi}^0/\widetilde{mip}$. Except for low energies ($\lesssim 2\,GeV$) where the incident hadron does not generate a hadronic shower the average fractions of the incident energy $< f_I >, < f_n >, < f_\gamma >$ are almost energy independent and are specific constants determined by the absorber material of the calorimeter. The intrinsic e/h-ratio is therefore a specific quantity of a specific calorimeter configuration while the measurable e/h-ratio contains the energy dependent variable $< f_{em} >$ (eqs. 3.39, 3.40). It is possible to achieve a measurable e/h-ratio equal to 1 if the average fraction $< f_{em} >$ can be measured on an event-by-event basis. Eq. 3.39 shows that in this case the measured fraction f_{em} has to be multiplied by a certain factor for each event in a way that $(e/h)_m$ becomes 1. To estimate the fraction f_{em} the sampling calorimeter has to have a fine longitudinal segmentation to resolve the electromagnetic shower. This method of achieving a measurable e/h-ratio equal to 1 is known as CDHS correction [ABR81] and has been introduced by [DIS79].

The average fractions of the incident energy available from the different hadronic shower components have been calculated by the use of simulation programs, of which the HETC [CHA72] can be regarded as the most elaborate one. Various calorimeter configurations have been studied with the program package CALOR including the HET-Code (e.g. [GAB73, GAB78, GAB85, BRA85]), but only results for the configurations of interest will be given here [GAB85]. One calorimeter consists of $3.6\,mm$ *Pb* embedded into two $1.2\,mm$ *Al* plates and $3\,mm$ plastic scintillator plates, the second is a design of 72 cells with $2\,mm$ *U* and $3\,mm$ plastic scintillator plates followed by 275 cells of $3\,mm$ *U* and $3\,mm$ plastic scintillator plates. In Tab. 3.8 the available energies from a proton of $5\,GeV$ incident on the two calorimeter configurations mentioned above are listed. The absolute values of the available energy in the entire calorimeter (passive and active absorber plates) in MeV are given in the first column for each configuration. There is energy deposited directly in form of *ionization energy* (primary and secondary protons, charged pions and muons) and *electromagnetic energy* from electrons, positrons and photons of electromagnetic interactions (mainly from π^0-decay) or source energy from *neutrons* during spallation and fission reactions and *nuclear γ-rays*. For each of these forms of energy the fractional available energy is listed in the second column. In order to discuss the average fractions $< f >$ of the incident energy contributing to the *intrinsic* e/h-ratio (eq. 3.56) the pure hadronic energy without the electromagnetic energy $(E - E_{em})$ will be considered. Taking the pure hadronic energy as 100% the average fractions of the different forms of available energy is given in the third column of Tab. 3.8. The results given in Tab. 3.8, subdivided into the different forms of energy deposition, can be interpreted as follows:

- **Energy in Form of Ionization**
  The overwhelming part of the ionization loss is due to secondary protons, most of them released in spallation processes, as explained above. The fraction on the total ionization due to secondary protons is 71.6% for the *Pb-SCI* calorimeter and 70.4% for the *U-SCI* calorimeter (for *Fe-SCI* it is 74.5%, taken from the same reference [GAB85]). As discussed above, this energy loss depends on Z/A, the fraction of protons in the target nuclei and on $Z/A^{\frac{1}{3}}$, the Coulomb barrier for charged particles. The smaller the ratio Z/A, the smaller the number of protons released during spallation and hence the ionization loss. For $^{238}_{92}U$, $Z/A = 38.7\%$, which is about 2.4% smaller than for $^{207}_{82}Pb$. Hence, the ionization loss due to secondary protons is smaller in the *U-SCI* (29.4%) than in the *Pb-SCI* (33.4%) configuration.

Table 3.8: Energy Available from a 5 GeV Proton in a *Pb*-Scintillator and *U*-Scintillator Calorimeter as calculated with CALOR (the time cut is $50\,ns$) [GAB85]; $< f >$ denotes the Average Fraction of the Hadronic Energy available from the Different Components of the Hadronic Shower (eq. 3.56); (for an Explanation of the Different Components see Text)

	Pb-Scintillator			*U*-Scintillator		
	Deposited Energy		$< f >$	Deposited Energy		$< f >$
	$[MeV]$	[%]	[%]	$[MeV]$	[%]	[%]
Energy in Form of Ionization	**1977**	**100.0**	**46.7**	**1838**	**100.0**	**41.8**
Primary p	211	10.7	5.0	216	11.8	4.9
Secondary p	1415	71.6	33.4	1294	70.4	29.4
$\pi^{\pm}$	344	17.4	8.1	323	17.5	7.4
$\mu^{\pm}$	7	0.3	0.2	5	0.3	0.1
Electromagnetic Energy ($e^{\pm}$, γ, mostly from π^0-decay)	**764**			**607**		
Neutrons	**516**	**100.0**	**12.1**	**855**	**100.0**	**19.5**
neutrons with $E_n \leq 20\,MeV$ (neutrons from high-energy p-,π- and n-induced fission included, but neutrons from induced fission by neutrons of $E_n \leq 20\,MeV$ excluded)	516	100.0	12.1	646	75.6	14.7
fission produced neutrons with $< E_n > = 2\,MeV$ from n-induced fission with $E_n \leq 20\,MeV$				209	24.4	4.8
Photons from Nuclear Interactions	**308**	**100.0**	**7.3**	**949**	**100.0**	**21.6**
γ (excitation)	106	34.4	2.5	89	9.4	2.0
γ (high-energy p-, π-, and n-induced fission)	0	0.0	0.0	120	12.6	2.7
γ (neutron capture, (n,n$'\gamma$)-reactions and n-induced fission ($E_n \leq 20\,MeV$))	202	65.6	4.8	740	78.0	16.9
$\mathbf{E_{SUM}}$	**3565**			**4249**		
$\mathbf{E - E_{em}}$	**4236**		**100.0**	**4393**		**100.0**
E	**5000**			**5000**		

The pion yield during spallation is small (8.1% *Pb-SCI*, 7.4% *U-SCI*). In ^{238}U, the minimum-ionizing protons lose about $220\,MeV$ on the average before they undergo a nuclear interaction; below $\sim 150\,MeV$ this is the only way of energy loss for about 90% of the protons, i.e. they do not perform any further nuclear interaction [WIG87]. This leads to a nonlinear hadron response at low energies ($\leq 2\,GeV$).

- **Neutrons**
  The fraction on the incident energy going into neutron production in high-energy p-,π- and n-induced fissions is higher in the *U-SCI* configuration because there is an additional contribution from fissions induced by low-energy neutrons ($\geq 1.2\,MeV$) if ^{238}U is used as passive absorber material.

  - Neutrons with $E_n \leq 20\,MeV$ from p-,π- and n-induced fission except neutrons from induced fission by neutrons of $E_n \leq 20\,MeV$:
    those neutrons are created during the intranuclear cascade or in high-energetic p-,π- and n-induced fissions; although an energy of about $200\,MeV$ per high-energetic p-,π- and n-induced fission is released (almost all of it ($\sim 170\,MeV$) in form of heavy fragment recoil), this energy remains almost invisible because it is deposited within the lead or uranium plate [GAB78].

  - Neutrons with $< E_n > = 2\,MeV$ from induced fission by neutrons of $E_n \leq 20\,MeV$:
    the fragments of slow neutron-induced fission of ^{238}U evaporate further neutrons with a mean energy of $2\,MeV$; at this energy the cross section for elastic np-scattering in ^1_1H (see Appendix B) becomes larger than the cross section for inelastic np-scattering in uranium.

- **Nuclear γ-Rays**
  The deexcitation of the nucleus occurs in form of photon emission during spallation reactions, in inelastic (n, $n'\gamma$) reactions or during fission or n-capture processes. Photons from n-capture processes are delayed because the neutrons to be captured have to be slowed down until they reach the low energy range where the cross section for neutron capture is high. Photons emitted in all the other deexcitation processes are prompt. The yield of γ-rays is much greater in the *U-SCI* configuration (21.6%) than in the *Pb-SCI* one (7.3%) because of the induced fission by slow neutrons ($E_n \leq 20\,MeV$) and neutron capture in ^{238}U.

After the discussion of the deposited fraction of the incident energy by the different components of the hadronic shower the visible part (sampling fraction) of each component (see eq. 3.56) in a sampling calorimeter will be described:

- The $\tilde{e}/\widetilde{mip}$-ratio has been discussed previously (sec. 3.2.2); it decreases with increasing atomic number Z_p of the passive absorber, and the larger the difference $Z_p - Z_a$ the smaller this ratio becomes. Below a thickness of $\sim 6\,mm$ of the passive absorber plate it increases with decreasing thickness of the passive absorber plate if the thickness of the active absorber plate remains constant [BRÜ86, WIG87].

- The $\widetilde{ION}/\widetilde{mip}$-ratio is the visible ionization loss of the protons, charged pions and muons in the hadronic shower, relative to the sampling fraction of a minimum ionizing particle; because protons are dominant (see Tab. 3.8), the $\tilde{p}/\widetilde{mip}$-ratio determines this visible energy fraction in the calorimeter. The $\tilde{p}/\widetilde{mip}$-ratio shows the different dependences stated below [WIG87]:

  1. Limited range of low energy protons in dense absorber material (e.g. a $40\,MeV$ proton has a range of $3\,mm$ in uranium): therefore $\tilde{p}/\widetilde{mip}$ ***decreases*** for low energy protons.
  2. The ratio of ionization losses in the active and passive absorbers, $\left.\frac{dE}{dx}(p)\right|_a \,/\, \left.\frac{dE}{dx}(p)\right|_p$, for protons at low energies differs from the ratio of a minimum ionizing particle, $\left.\frac{dE}{dx}(mip)\right|_a \,/\, \left.\frac{dE}{dx}(mip)\right|_p$, depending on the material combination. This ratio relative to

that of a minimum ionizing particle is given in Tab. 3.9 (dE/dx-values are calculated according to the formula given in [LOH85]). Therefore $\widetilde{p/mip}$ *increases* for proton energies $< 1\,GeV$.

Table 3.9: $\left.\frac{dE}{dx}(p)\right|_a \Big/ \left.\frac{dE}{dx}(p)\right|_p$ for Protons in Different Material Combinations at the given Energies, Relative to $\left.\frac{dE}{dx}(mip)\right|_a \Big/ \left.\frac{dE}{dx}(mip)\right|_p$ of a Minimum Ionizing Particle (a: active, p: passive absorber layer)

E [MeV]	Polystyrene Uranium	Polystyrene Lead	Polystyrene Iron
10	1.6367	1.6050	1.2233
100	1.0894	1.0893	1.0355
1000	0.9405	0.9400	0.9732

3. The light output of a scintillator does not increase linearly with the specific energy loss of a traversing particle due to saturation effects. Those effects are caused by ionization quenching of particles with higher ionization than fast electrons ($\geq 100\,keV$) according to the semiempirical relation [BIR64]:

$$\frac{dL_p}{dx} = \frac{S\,\frac{dE}{dx}}{1 + kB\cdot\frac{dE}{dx}} \quad \frac{cm^2}{g} \tag{3.58}$$

where:

$\frac{dL_p}{dx}\ldots$ specific light yield in the scintillator due to the ionization loss of protons $\left[\frac{cm^2}{g}\right]$

$S\ldots$ absolute scintillation efficiency per $1\,MeV$ electron

$k\ldots$ quenching parameter; kB in $\left[\frac{g}{MeV\cdot cm^2}\right]$

$B\cdot\frac{dE}{dx}\ldots$ specific density of ionized and excited molecules along the particle track.

The factor kB has a specific value for a certain scintillator type. It has been measured by [BEC85] for three types of scintillators. The results are given in Tab. 3.10. These measurements show that SCSN-38 provides a higher light yield from proton ionizations compared to the other organic scintillators because of the small kB-value. Because of the nonlinear response of the scintillator to protons the $\widetilde{p/mip}$ *decreases* at lower energies of the protons.

Table 3.10: Values of kB for Different Scintillator Types

Scintillator	kB $\left[\frac{g}{MeV\,cm^2}\right]$
NE 102A	0.00893 ± 0.00007
Altustipe UV	0.00978 ± 0.00009
SCSN-38	0.00835 ± 0.00007

4. For very low-energy protons the influence of multiple scattering in the absorber material with high atomic number Z will become larger: therefore $\widetilde{p/mip}$ *decreases* for low energy protons.

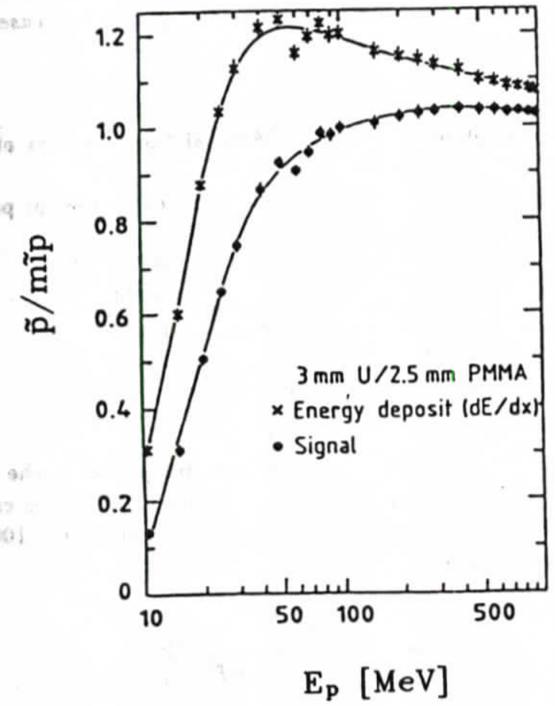

Figure 3.8: The $\tilde{p}/\widetilde{mip}$-Ratio as a Function of the Proton Energy for 3 mm Thick Uranium and 2.5 mm Thick Scintillator Plates [WIG87] (upper curve: energy deposit $\frac{dE}{dx}$; lower curve: visible signal, including saturation)

The combined effects as function of the proton energy (Fig.3.8) and thicknesses of the uranium as well as the scintillator plates (Fig.3.9) have been studied by the use of a simulation program [WIG87]. At low proton energies (Fig.3.8) the energy deposition $\frac{dE}{dx}$ in the $2.5\,mm$ scintillator plates increases before it falls steeply for proton energies below $50\,MeV$. The $\tilde{p}/\widetilde{mip}$-ratio decreases rapidly for proton energies below $\sim$ $100\,MeV$. The thicknesses of the absorber plates influences the $\tilde{p}/\widetilde{mip}$-ratio (Fig.3.9) in a way that for a fixed scintillator-plate thickness ($2.5\,mm$) the $\tilde{p}/\widetilde{mip}$-ratio increases slightly with the uranium-plate thickness until it becomes constant above $\sim$ $3\,mm$. For a fixed thickness of the uranium-plate the $\tilde{p}/\widetilde{mip}$-ratio decreases considerably with the thickness of the scintillator plates.

In summary, the $\widetilde{ION}/\widetilde{mip}$-ratio and hence the hadronic calorimeter response can be increased if one uses thin scintillator plates in connection with passive absorber material of high atomic number Z.

- The dominating energy deposition of neutrons at low energies ($\leq$ $20\,MeV$) is by np-scattering (see cross section for $n \rightarrow {}^1_1 H$ in Appendix B) and, because $2.5\,mm$ scintillator corresponds to the range of a proton possessing $\sim$ $17\,MeV$ [WIG87], all the energy carried by recoil protons will be deposited in the scintillator [BRÜ85]. Again, saturation effects in the scintillator at low proton energies according to Birk's law (eq. 3.58) make the signal due to proton recoil less dependent on the low energy of the neutrons. Because this signal is produced within the scintillator plate the energy deposited in form of proton recoil due to neutron-proton collisions is not sampled by the calorimeter in the same way as the signal of a minimum ionizing particle. Hence, in a sampling calorimeter with active layers containing free protons the $\tilde{n}/\widetilde{mip}$-ratio depends mainly on the sampling fraction of a minimum ionizing particle in such a way that [BRÜ86, WIG87]:

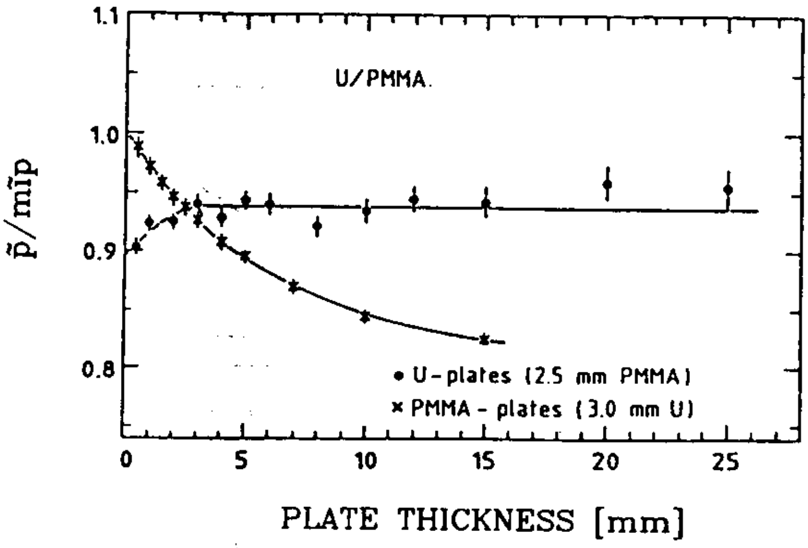

Figure 3.9: The $\tilde{p}/\widetilde{mip}$-Ratio as a Function of the Plate Thickness [WIG87] (dots: Uranium Plate Thickness varies, 2.5 mm Scintillator; crosses: Scintillator Plate Thickness varies, 3.0 mm Uranium)

1. *decreasing* the scintillator thickness *decreases* the sampling fraction of a minimum ionizing particle ($\widetilde{mip}$) which in turn *increases* $\tilde{n}/\widetilde{mip}$ and leads to a smaller value of $(e/h)_i$;
2. this effect will be more pronounced if the fraction of free protons in the readout material is enlarged or if its saturation tendency can be reduced. The first effect has experimentally been observed with a uranium-gas calorimeter, where gas mixtures of different hydrogen contents have been used [GAL86]: the higher the hydrogen content the higher the calorimeter response to pion initiated hadronic showers.
   To reduce the saturation effects in the readout material one has to use scintillator materials with small kB values, as mentioned above.

- The $\tilde{\gamma}/\widetilde{mip}$-ratio in a calorimeter configuration of $3\,mm$ ^{238}U and $2.5\,mm$ scintillator is about 0.5 to 0.6 above a photon energy of $\sim\ 2\,MeV$ according to an EGS4 simulation performed by [WIG87]. More than 90% of the prompt nuclear γ-rays have an energy below $2\,MeV$; in this energy region the $\tilde{\gamma}/\widetilde{mip}$-ratio decreases sharply from 0.5 at $\sim\ 2\,MeV$ to almost 0 at $\sim\ 0.1\,MeV$ [WIG87]. An average value of ≈ 0.3 is given by [BRÜ86] for a nuclear fission γ-ray spectrum. The $\tilde{\gamma}/\widetilde{mip}$-ratio decreases with increasing atomic number of the passive absorber.

The energy deposited by neutrons and deexcitation γ-rays from nuclear reactions is time dependent: most of the neutrons are prompt, but it takes a finite time until they are slowed down by elastic collisions with the protons in the scintillator material. The neutrons will reach thermal energies where the n-capture cross section of ^{238}U becomes the dominating process. The γ-rays from these processes are delayed. The detection efficiency of plastic scintillator, however, is very low for γ-rays ($\sim$ 2 % [BRÜ86]), but due to the delayed neutron contribution to the hadronic signal one would expect an increase of the hadron response of the calorimeter with increasing integration time. According to [GAB78], low energetic neutrons ($E\ \leq\ 20\,MeV$), high-energy particle-induced fission γ-rays and deexcitation γ-rays deposit their energy in the time interval of 0 to $\sim\ 30\,ns$. Photons from n-capture processes start to contribute after $\sim\ 100\,ns$ [BRÜ86]. The individual time dependence of those components (p-recoil due to $n-p$ elastic collisions, γ-rays from fission fragments and n-capture processes) have been simulated with the DYMO program [BRA86, BRÜ86]. A qualitative description according to this Monte Carlo program is shown in Fig. 3.10 where the visible energy of the three components and the total sum is plotted versus the integration time. The simulated calorimeter configuration consisted of $3\,mm$ depleted uranium, cladded with $2 \times 0.4\,mm$ Cu sheets and interleaved with $2.5\,mm$ scintillator.

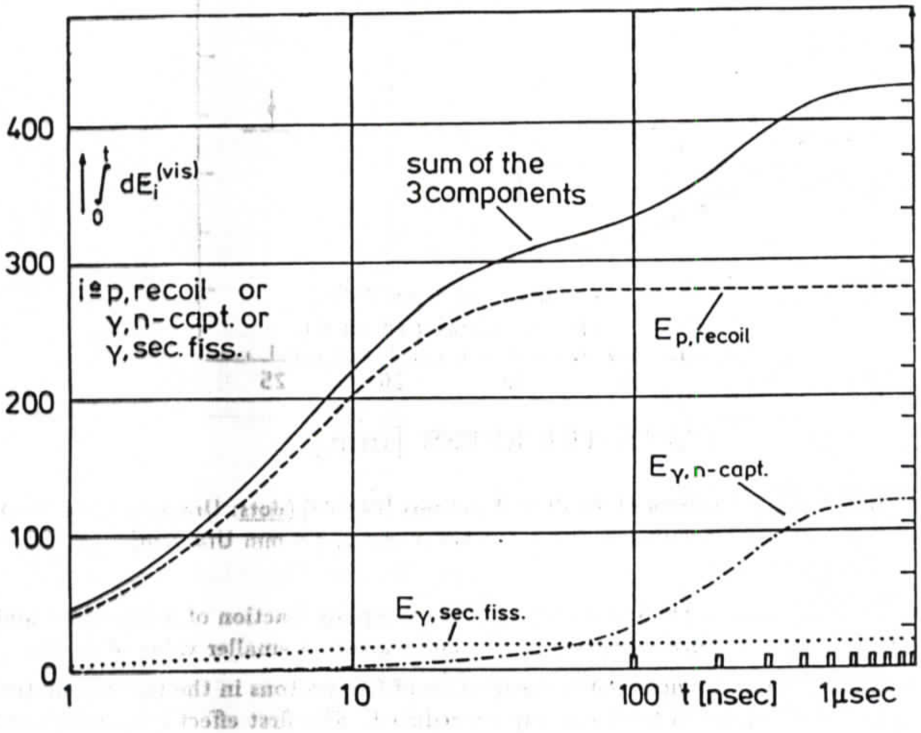

Figure 3.10: Visible Energy as a Function of the Integration Time due to p-Recoil in n-p Collisions, γ-Rays from Fission Fragments and from n-capture Processes calculated with the DYMO Simulation Program [BRÜ86]

Tab. 3.11 summarizes the discussion on the contributions to the visible signal in a sampling calorimeter. From the discussion one concludes that a passive absorber with a high neutron contribution ($< f_n >$) to the hadron signal has a slightly decreased contribution due to ionization ($< f_I >$) compared to other absorbers. The thickness of the absorber plates plays a significant role in the hadronic response of a sampling calorimeter. The $(e/h)_i$-ratio of a sampling calorimeter with scintillator readout can be tuned to 1 by the following parameters:

1. the passive absorber has to be a material with a high atomic number Z_p; in this case the $\tilde{e}/\widetilde{mip}$-ratio is smaller and the neutron contribution to the hadron signal is larger than for a passive absorber material with low atomic number Z_p;
2. using thin scintillator plates, which means that the sampling fraction of a minimum ionizing particle is small, one can profit by the released neutrons because the $\tilde{n}/\widetilde{mip}$-ratio increases in this case. There is, however, a practical limit in making the thickness of the scintillator plates very thin.

In a first approximation, the sampling fraction is inversely proportional to the ratio of the thickness of the passive to the active absorber plate, $R_d = \frac{\Delta x_p}{\Delta x_a} \equiv \frac{d_p}{d_a}$. It was predicted by [BRÜ85, WIG87]

Table 3.11: Components of the Visible Hadronic Signal in a Sampling Calorimeter (R_d means thickness ratio of passive to active absorber plate; the $\tilde{e}/\widetilde{mip}$- and $\tilde{\gamma}/\widetilde{mip}$-ratios are taken from [WIG87])

	Calorimeter Configuration			Influence of Passive Absorber	Influence of Active Absorber
	Fe-SCI	Pb-SCI	U-SCI		
$< f_I >$	57.0%	46.7%	41.8%	–	–
$< f_n >$	7.8%	12.1%	14.7%	–	–
$< f_n >$ of low energy n-induced fission			4.8%		
$< f_\gamma >$	8.3%	7.3%	18.9%	–	–
$< f_\gamma >$ of high energy p, n-induced fission			2.7%		
$\frac{\tilde{e}}{\widetilde{mip}}$	0.84	0.61	0.59	increases with decreasing thickness $\leq 6\,mm$	–
$\frac{\tilde{p}}{\widetilde{mip}}$	increases with Z of passive absorber at proton energies $< 1\,GeV$			almost constant as function of thickness	decreases with increasing thickness saturation at low proton energies
$\frac{\tilde{n}}{\widetilde{mip}}$	–			increases with increasing $R_d = \frac{d_p}{d_a}$	
$\frac{\tilde{\gamma}}{\widetilde{mip}}$	0.74	0.42	0.36	increases with decreasing thickness $\leq 6\,mm$	–

that in the case of a 2.5 *mm* organic scintillator plate and a varying thickness of the uranium plate the following relation hold between the $(e/h)_i$-ratio and the thickness ratio R_d:

$$\begin{array}{lll} (e/h)_i \approx 1 & \text{if} & R_d \approx 1 \\ (e/h)_i < 1 & \text{if} & R_d \gtrsim 1 \\ (e/h)_i > 1 & \text{if} & R_d \lesssim 1. \end{array}$$

A similar relation holds for lead plates with a scintillator plate thickness as above. A higher ratio R_d is needed in order to reach compensation:

$$\begin{array}{lll} (e/h)_i \approx 1 & \text{if} & R_d \approx 4 \\ (e/h)_i < 1 & \text{if} & R_d \gtrsim 4 \\ (e/h)_i > 1 & \text{if} & R_d \lesssim 4. \end{array}$$

3.5 The Energy Resolution of a Hadron Calorimeter

The energy resolution of a hadronic sampling calorimeter can be expressed as the sum of several terms listed below:

- *intrinsic energy resolution*
  The total nuclear binding energy loss in a hadron shower is a huge source of fluctuations that contributes to the total energy resolution. If neutron and γ-ray detection is neglected these contributions give rise to an intrinsic energy resolution of [WIG87]:

$$\frac{\sigma_E}{E}(h) \approx \frac{30 - 35\%}{\sqrt{E[GeV]}}. \tag{3.59}$$

  The amount of the nuclear binding energy loss is correlated with the amount of energy going into neutron and nuclear γ-ray production. The detection efficiency of the scintillator for photons is very low ($\sim$ 2% [BRÜ85]), so only a good neutron detection in a calorimeter will lower the fluctuations in the amount of nuclear binding energy loss. For a calorimeter with hydrogenous readout material, i.e. where elastic *np*-scattering occurs, the total intrinsic energy resolution has been calculated [WIG87] to be of the order of:

$$\frac{\sigma_E}{E}(h) \approx \frac{20\%}{\sqrt{E[GeV]}} \tag{3.60}$$

  for a compensating calorimeter ($(e/h)_i = 1$). The neutron detection capability of a calorimeter influences the intrinsic e/h-ratio via the $\bar{n}/\widetilde{mip}$-ratio. Improving the neutron detection in a way that the intrinsic e/h-ratio becomes 1 leads to minimized fluctuations in the deposited fraction of the incident energy due to the electromagnetic component (see eq. 3.39).

- *sampling fluctuations*:
  The contribution of sampling fluctuations in hadron calorimeters have been estimated from measurements with different hadron calorimeters, given by eq. 3.28. Those fluctuations are proportional to $\sqrt{\Delta E[MeV]/E[GeV]}$, i.e. to the thickness of the calorimeter layer.

In sec. 3.1.1 the shower development has been described under simplifying assumptions. One of the results was that the total average number of shower particles which is proportional to the number of ionizations in the active absorber plates of a sampling calorimeter increases with the incident energy (eq. 3.10). The width of the corresponding distribution then decreases with $1/\sqrt{E}$. The average deposited energy fraction due to the electromagnetic component (eq. 3.40) depends on the incident energy, but in the case that the intrinsic e/h-ratio is 1 these fluctuations will not contribute to the energy resolution. Any deviation from $(e/h)_i$=1 results in a deteriorated energy resolution which can be expressed as follows [WIG87]:

$$\frac{\sigma_E}{E}(h) = \frac{a}{\sqrt{E[GeV]}} + b\left(\frac{e}{h}\bigg|_i - 1\right) \tag{3.61}$$

with [WIG87]:

$a \sim 32\%$ for 2.3 *mm* U-2.5 *mm* PMMA $(e/h)_i$=1
$a \sim 39\%$ for 4.3 *mm* U-5.0 *mm* PMMA $(e/h)_i$=1
$a \sim 57\%$ for 24.0 *mm* Pb-5.0 *mm* PMMA $(e/h)_i$=1
$a \sim 44\%$ for 12.0 *mm* Pb-2.5 *mm* PMMA $(e/h)_i$=1
$b \approx 1.7\%$ if $|(e/h)_i - 1| = 0.1$
$b \approx 4.8\%$ if $|(e/h)_i - 1| = 0.2$

Simplified calculations have been performed by [WIG87] to predict the energy resolutions according to eq. 3.61 for calorimeters with different passive and active absorber materials of different thickness ratios R_d. The parameter a is a quadratic addition of the contribution from the intrinsic energy resolution and the sampling fluctuations. The given values for a are obtained from [WIG87] for $(e/h)_i = 1$, the quoted values for b are also taken from [WIG87].

There are two independent predictions for the measurable e/h-ratio of different calorimeter configurations, based on the simplified calculations by [WIG87] and more elaborated Monte Carlo simulations by [BRÜ86, BRÜ87, ZEU87].

The predictions for the measurable e/h-ratio and the hadronic energy resolution for the calorimeter configurations on which experimental results will be presented in the following chapters, are stated below, calculated for $10\,GeV$ ([BRÜ86, BRÜ87, WIG87, ZEU87]) and $100\,GeV$ [WIG87] incident energy. All e/h-ratios have been calculated for an integration time of $100\,ns$.

(a) $4.75\,mm$ Pb - $5\,mm$ Scintillator *SCSN-38*:
  - $< R_d > = 0.95$
  - $\left.\frac{e}{h}\right|_m \sim 1.21$ [ZEU87]
  - $\left.\frac{e}{h}\right|_m \sim 1.17$ [WIG87]
  - $\frac{\sigma_E}{E}(\mathrm{h})\sqrt{E[GeV]} \sim 48\%$ for $E = 10\,GeV$ [WIG87]

(b) $10\,mm$ Depleted Uranium (DU) - $5\,mm$ Scintillator *NE110*
(DU plates with $1\,mm$ Fe cladding on each side [BRÜ86] as used for the measurement; *PMMA* scintillator [WIG87] similar to *NE110* used for the measurement):
  - $R_d = 2.00$
  - $\left.\frac{e}{h}\right|_m = 0.82$ [BRÜ87]
  - $\left.\frac{e}{h}\right|_m \sim 0.81$ [WIG87]
  - $\frac{\sigma_E}{E}(\mathrm{h})\sqrt{E[GeV]} \sim 51\%$ for $E = 10\,GeV$ [WIG87]
  - $\frac{\sigma_E}{E}(\mathrm{h})\sqrt{E[GeV]} \sim 63\%$ for $E = 100\,GeV$ [WIG87]

(c) $3.2\,mm$ DU - $5\,mm$ Scintillator *SCSN-38*:
  - $R_d = 0.64$
  - $\left.\frac{e}{h}\right|_m \sim 1.08$ [BRÜ87]
  - $\left.\frac{e}{h}\right|_m \sim 1.02$ [WIG87]
  - $\frac{\sigma_E}{E}(\mathrm{h})\sqrt{E[GeV]} \sim 38\%$ for $E = 10\,GeV$ [WIG87]

(d) $3.2\,mm$ DU - $3\,mm$ Scintillator *SCSN-38*:
  - $R_d = 1.06$
  - $\left.\frac{e}{h}\right|_m = 1.03$ [BRÜ87]
  - $\left.\frac{e}{h}\right|_m \sim 0.96$ [WIG87]
  - $\frac{\sigma_E}{E}(\mathrm{h})\sqrt{E[GeV]} \sim 34\%$ for $E = 10\,GeV$ [WIG87]

- $\frac{\sigma_E}{E}(\mathrm{h})\sqrt{E[GeV]} \sim 36\%$ for $E = 100\,GeV$ [WIG87]

(e) $10\,mm$ Pb - $2.5\,mm$ Scintillator *SCSN-38*:

- $R_d = 4.00$
- $\left.\frac{e}{h}\right|_m = 1.13$ [ZEU87]
- $\left.\frac{e}{h}\right|_m \sim 0.95$ [WIG87]
- $\frac{\sigma_E}{E}(\mathrm{h})\sqrt{E[GeV]} \sim 40\%$ for $E = 10\,GeV$ [WIG87]
- $\frac{\sigma_E}{E}(\mathrm{h})\sqrt{E[GeV]} \sim 41\%$ for $E = 100\,GeV$ [WIG87].

There are contributions to the energy resolution resulting from detector imperfections, namely:

- fluctuations in transverse and longitudinal *leakage* of energy out of the detector;
- fluctuations of the *signal from the active layers* resulting from the finite number of photoelectrons in the photomultiplier [HOF82]:

$$\left.\frac{\sigma_E}{E}(h)\right|_{ph} = \frac{c}{\sqrt{E}} \tag{3.62}$$

with:

c ... few percent, depending on the readout system.

Because these contributions on the energy resolution are detector dependent they will be determined from the measurement for the individual calorimeter configurations.

Chapter 4

Measurements with a Noncompensating Lead-Scintillator Calorimeter

4.1 The T60 Lead-Scintillator Calorimeter and the Beam Set-Up

To study the influence of absorber material and scintillator thickness on the energy resolution of hadron calorimeters the ZEUS collaboration started the investigation by exposing a lead-scintillator calorimeter to a beam of different particles at different energies.

The entire calorimeter consisted of 4 identical modules with dimensions and specifications given in Tab. 4.1, while in Fig. 4.1 one of these modules is sketched.

In this measurement (T60Pb) 30 layers of $4\,mm$ thick lead plates were inserted in the first module (downstream), alternated with $5\,mm$ thick scintillator layers, while the last 3 modules contained $5\,mm$ thick lead plates instead, again alternated with $5\,mm$ scintillator layers. In total the calorimeter was $103.7\ X_0$ or $4.3\ \lambda_0$ deep.

One scintillator layer consists of 12 strips, each of them with a sensitive area of $50 \times 600\,mm^2$. Each strip was wrapped first in white paper and additionally in aluminized mylar foil in order to achieve good reflectivity and to decouple each scintillator strip optically.

At both $50\,mm$ wide ends the light was collected by a $50\,mm$ wide and $3\,mm$ thick wavelength shifter bar almost perpendicular to the scintillator ends. The wavelength shifter bars were wrapped in a similar manner as the scintillator strips with the open side area pointing to the scintillator edge. A $0.3\,mm$ nylon thread serves to maintain a small air gap between the wavelength shifter bar and the passive absorber plates. This air gap is required to ensure the total internal reflection of the light trapped into the wavelength shifter.

At one end the wavelength shifter bars were glued to a plexiglass lightguide that was bent by 180° with a radius of $\sim 11\,cm$. The lightguide was fed into a XP2011 type photomultiplier. In total there are 12 readout channels on the left and 12 on the right side of each module, and a group of 12 photomultipliers at one side was supplied by the same high voltage.

The analog output signals of the photomultipliers were digitized by the ADC[1] type 2282 A (LeCroy), a current integrating ADC with a dynamic range of 12 bits and a gain of 4 counts/pC ± 10 %. One module has 48 input channels so that for the entire calorimeter 2 modules were necessary in addition to a 2280 CAMAC[2] System Processor module (LeCroy). The CAMAC crate was connected to a PDP 11/73 online computer acted as a supervisor of three microprocessors. The readout of the ADCs, the histogramming and the control of run parameters has been done by the three microprocessors while the PDP 11/73 performed the tape writing.

---

[1] Analog Digital Converter

[2] Computed Automated Measurement And Control Standard

Table 4.1: Dimensions and Specifications of the T60Pb Calorimeter inserted with 4 and 5mm thick Lead and 5mm thick Scintillator Plates

Calorimeter				
Lateral Dimensions	**600 × 600 *mm*^{2}**	**Mod 1**	**46.13X_0**	**1.97λ_0**
		Mod 2-4	**51.92X_0**	**2.11λ_0**
Number of Modules	**4**			
Number of Layers per Module	**30**			
Total Depth of 1 Layer	**13 *mm***	**Mod 1**	**0.73X_0**	**0.031λ_0**
		Mod 2-4	**0.91X_0**	**0.037λ_0**
Total Depth of 1 Module	**390 *mm***	**Mod 1**	**21.92X_0**	**0.93λ_0**
		Mod 2-4	**27.26X_0**	**1.11λ_0**
Total Depth of Calorimeter	**1560 *mm***		**103.7X_0**	**4.3λ_0**
Airgap per Layer	**3.5 *mm***	**Mod 1**		
	2.5 *mm*	**Mod 2-4**		
Passive Layer				
Lateral Dimensions	**600 × 600 *mm*^{2}**			
Thickness of Plates	**2 *mm Pb***	**Mod 1**		
	0.5 *mm Al*			
	2 *mm Pb*			
Total	**4.5 *mm***		**0.72X_0**	**0.025λ_0**
Thickness of Plates	**3 *mm Pb***	**Mod 2-4**		
	0.5 *mm Al*			
	2 *mm Pb*			
Total	**5.5 *mm***		**0.90X_0**	**0.031λ_0**
Material	***Pb***			
Active Layer				
Dimension of Scintillator Strip	**50 × 600 *mm*^{2}**			
Number of Strips	**12**			
Thickness of Plates	**5 *mm***		**0.01X_0**	**0.007λ_0**
Material	**SCSN-38 (Polystyrene Base)**			
Readout				
Wavelength Shifter	**50 × 390 *mm*^{2}**			
Thickness of WLS	**3 *mm***			
Material	**PMMA Base, UV absorbant** **K27 (120 mg/l)**			
Lightguide	**Bent Plexiglass**			
Photomultiplier	**XP 2011**			

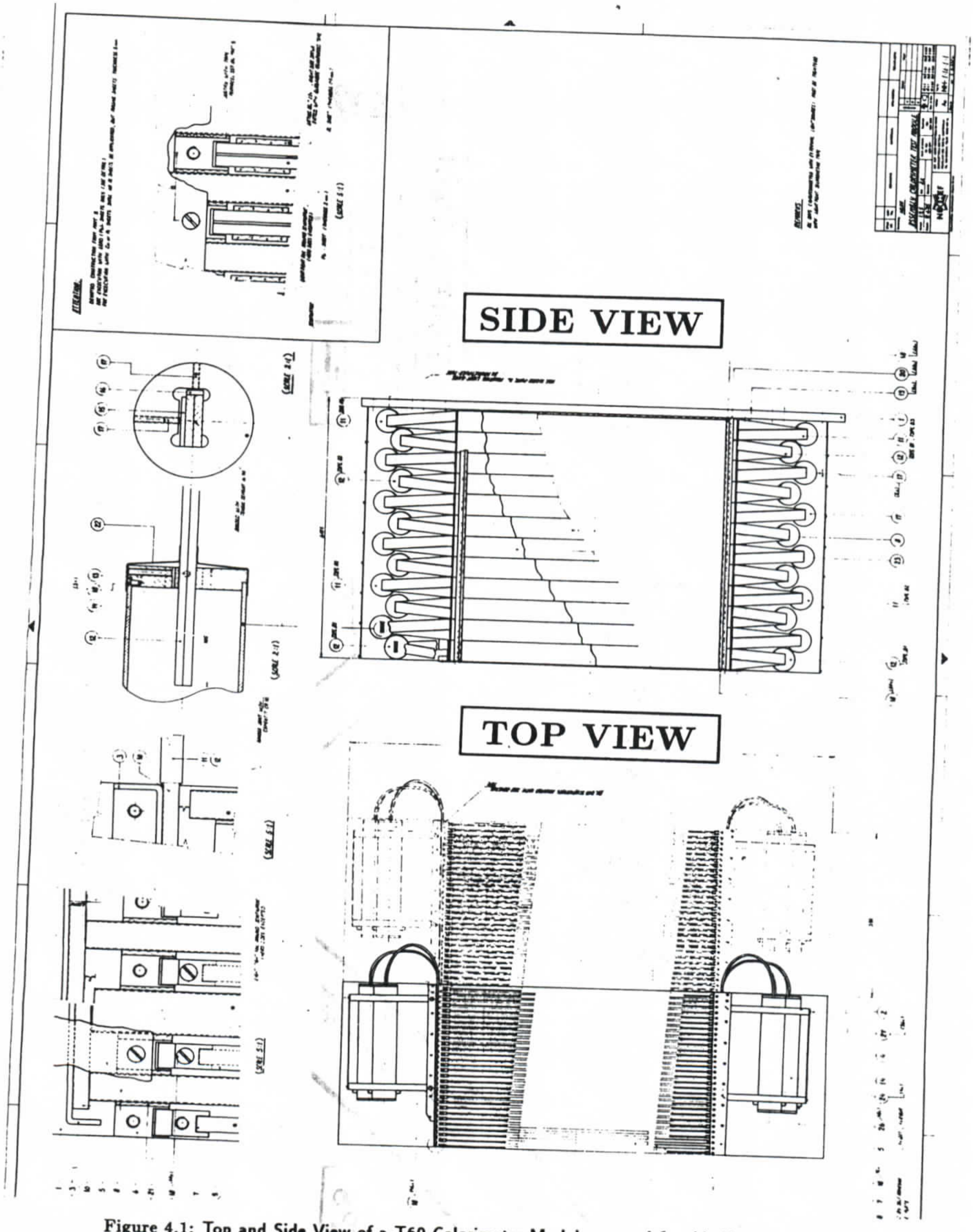

Figure 4.1: Top and Side View of a T60 Calorimeter Module as used for this Measurement

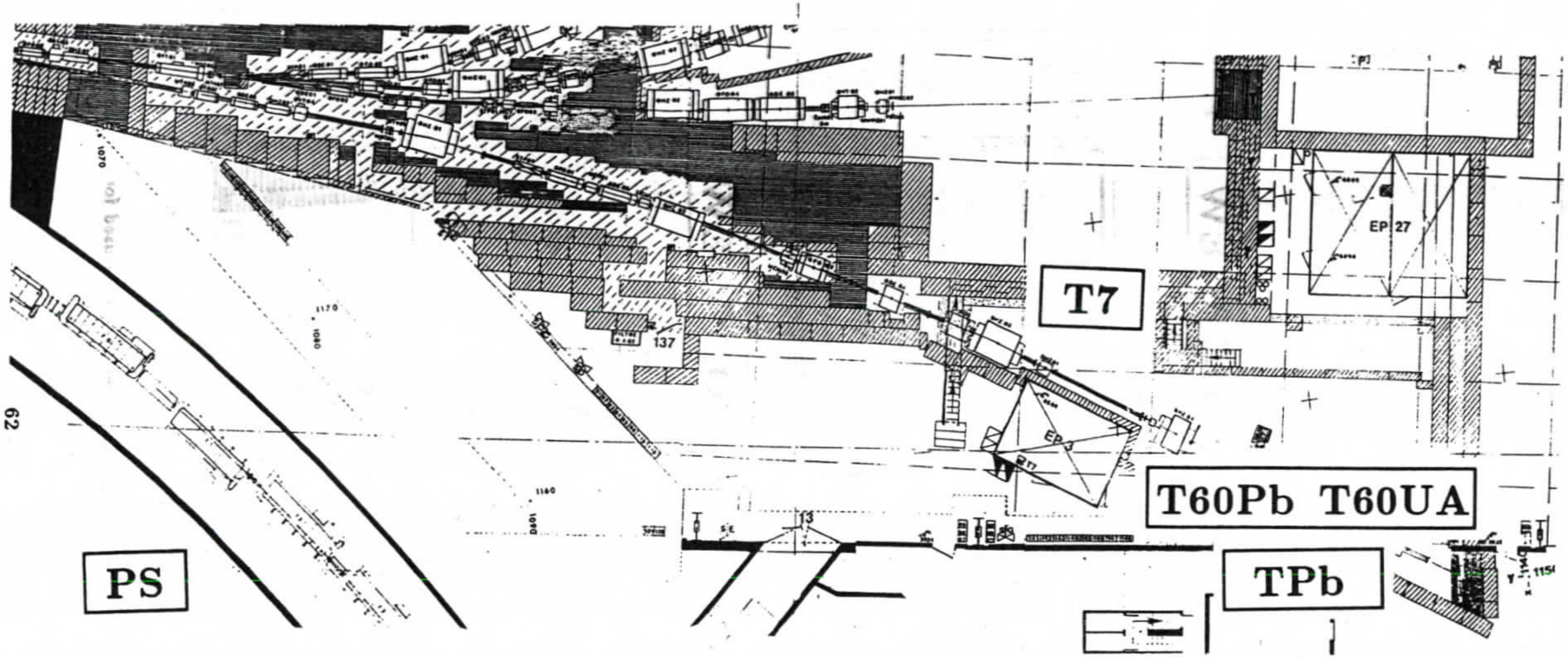

Figure 4.2: Beam Line T7 at the Proton Synchrotron (PS) at CERN (T60Pb, T60UA and TPb indicate the Place of the Calorimeter Modules in the Beam Line)

The measurement was done at the T7-beam in the East Hall at the Proton-Synchrotron (PS) at CERN. The PS operated at a magnetic field cycle time of $1.2\,s$ including a spill time at the flat top of $\sim 300\,ms$. Only every 7th burst was used for the beam lines in the East Hall because of the multiple tasks of the PS. The primary beam was slowly extracted by a septum magnet and hit an external target. Fig. 4.2 shows the described beam line. The experimental set-up is sketched in Fig. 4.3 with beam defining scintillation counters; for electron-hadron separation a threshold Cherenkov counter filled with CO_2 was installed. The beam halo was suppressed by the B_3 counter, having a hole of $2\,cm$ in diameter. The whole calorimeter was put on a moveable stage in order to reach different scintillator strips of the calorimeter.

Particle selection was done by a trigger defined as follows:

$$\begin{array}{lcll} \text{Beam:} & BEAM & = & B_1 \cdot B_2 \cdot \bar{B}_3 \\ \text{Electrons:} & e & = & BEAM \cdot \check{C} \\ \text{Muons:} & \mu & = & BEAM \cdot S_1 \cdot S_2 \end{array}$$

Typical event rates at $5\,GeV$ for example with a collimator width of $\pm\,8\,mm$ were:

$$\begin{array}{lcl} B_1 \cdot B_2 & = & 67\,500 \\ B_1 \cdot B_2 \cdot \bar{B}_3 & = & 50\,000 \end{array}$$

The beam content has been measured using the calorimeter as well as the beam counters. The results are given in Tab. 4.2.

Table 4.2: Contents of T7-Beam at the CERN PS, measured with the T60Pb calorimeter

E [GeV]	μ [%]	e [%]	h [%]
1	0.5	83.9	15.6
3	0.9	29.6	69.6
5	3.1	6.8	90.1
7	1.9	2.9	95.2
8.75	3.6	2.0	94.4

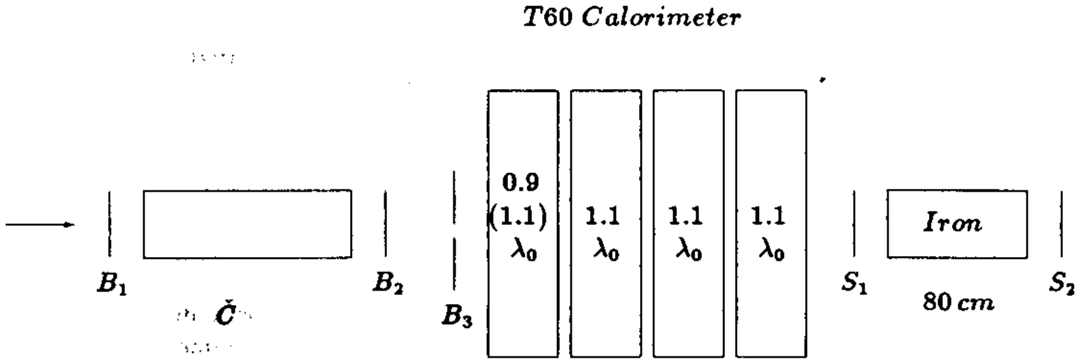

Figure 4.3: Beam Set-Up for the T60 Measurements at the CERN PS

Measurements have been performed as follows:

1. first the pedestal values were determined for each ADC input with the high voltage (HV) of the photomultipliers switched on. Thus the pedestals include possible effects from the photomultipliers, cables, ADCs and cosmic ray particles. The pedestal values were stored in the memory of the System Processor 2280 and subtracted from the actual measured values before

transfered to the computer. The gate width was 150 *ns* for the pedestal and the actual measurements. Pedestals have been determined in regular time intervals of about 1/2 hour in order to correct for fluctuations due to temperature variations. The pedestal values were stable within 5 – 7 *ADC CH.*, with a few input channels of greater variation < 16 *ADC CH.*;

2. actual measurements have been done under one of the trigger conditions mentionend above; usually 500 electron or muon triggers and 1000 hadron triggers could be taken per run ($\sim$ 30 resp. $\sim$ 60 bursts).

4.2 Calibration and Particle Selection

4.2.1 Calibration

The relative response of each channel has to be calibrated to a certain reference signal in order to obtain a uniform response of each readout channel. For this purpose muons with an energy of 5 *GeV* have been selected. The modules were mounted individually on the moveable stage. The stage was moved to various vertical positions so that the beam could hit the center of each scintillator strip. Due to the low beam height the two outer strips 11 and 12 at the top could not be reached. They have been calibrated in a different way to be described below. For the measurements with electrons and hadrons all four modules were put behind each other.

A final check of all modules in this arrangement has been done with muons traversing the center of the entire calorimeter.

To determine the calibration constant of each readout channel the most probable value (E_{mop}) of the muon distribution was taken from a Moyal function [MOY55] convoluted with a Gauss function (see Appendix A) that has been fitted to the data. As an example such a distribution with the fitted function is plotted in Fig. 4.4. The statistical error on the obtained most probable value was 1%.

The calibration with muons was compared with that of electrons. Therefore the central strip of each individual module has also been exposed to electrons of 5 *GeV* immediately after the muon run. The ratio of the muon response (most probable value) of the left to the right side in the central strip was compared to that of the electrons (mean pulse height). The deviations are given in Tab. 4.3 for the central strip of each module.

Table 4.3: **Deviations of the Signal Ratio of the Left to the Right Side in the Central Strip for Muons from that for Electrons at 5 GeV**

Module	Deviation in [%]
1	$+2.01 \pm 1.40$ %
2	-6.47 ± 1.66 %
3	$+3.25 \pm 1.38$ %
4	-0.86 ± 1.34 %

Strip 11 and 12 were calibrated by using the transverse hadronic shower distribution (see section 4.3.1) at 8.75 *GeV*; the pulse height distribution was assumed to be symmetric with respect to the central strip. This allowed a very rough calibration of strip 11 and 12 of each module. Because of the very low pulse heights in module 4 in the outer strips the calibration is not very precise for those strips. From the left-over-right ratio of the average pulse height of hadrons the accuracy of the calibration for the outer strips was estimated to be 7% and 10% for strip 11 and 12.

The intercalibration between the 4 modules was checked by taking the electron response in the central strip of each individual module when this module was put in front. The modules were calibrated with the constants obtained from the muons as described above. Tab. 4.4 shows the deviation of the mean pulse height in the front module from the average pulse height of all four modules for electrons at 5 *GeV*. For module 1 the deviation is large because the different thicknesses of the lead plates have been taken into account by a factor of 0.8, i.e. 4 *mm* / 5 *mm*. Necessarly the modules had to be moved which may have disturbed the system after having measured the electron reference signal. The effect

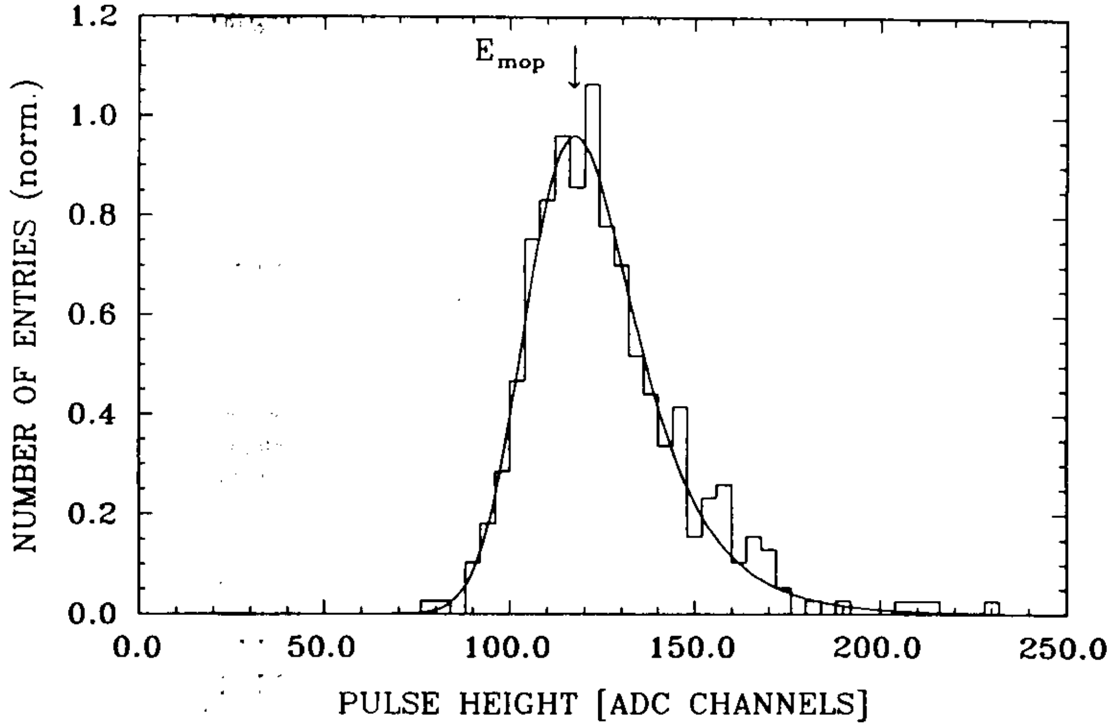

Figure 4.4: Muon Signal at 5 GeV in one Readout Channel (E_{mop} denotes the most probable energy loss of the muons)

Table 4.4: Deviations of the Mean Pulse Height of the front Module from the average Signal of all 4 Modules for Electrons at 5 GeV; the Modules are calibrated with Muons

Module	Deviation in [%]
1	$-3.92 \pm 0.23\%$
2	$+0.79 \pm 0.29\%$
3	$+0.71 \pm 0.23\%$
4	$+2.42 \pm 0.26\%$

on the calibration constants due to the movement of the modules can be seen from Tab. 4.5. In this table the deviations of the calibration constants obtained with muons for the central strip of each module before and after the rearrangement are given. There is no deviation for module 1 because it has not been moved.

After the calibration procedure with muons the corrected pulse heights have been used throughout the whole analysis.

4.2.2 Particle Selection

With the trigger described in the previous section almost clean electron, hadron and muon samples could already be selected online. Inefficiencies of the trigger made some additional selections necessary:

1. Random Trigger
   During normal runs a few random trigger occured. The few events (< 0.4 %) are observed around 0 in the total sum PH_T (e, μ, h) so a cut of less than 1% of the total sum rejected those events.

2. Pile Up due to High Particle Rate
   The high particle rate at the T7-beam caused pile up effects. More than one particle within

Table 4.5: Deviations of Calibration Constants obtained with Muons after moving the Calorimeter Modules

Module	Deviation in [%]
1	—
2	$+0.25 \pm 2.17$ %
3	-2.91 ± 2.07 %
4	$+5.03 \pm 3.67$ %

the 150 ns of the ADC gate causes higher pulse heights in the calorimeter than a single particle. These events could be rejected by a cut in a scatter plot

$$PH_M^{MAX}(e,h) \quad vs \quad PH_T(e,h)$$

where $PH_M^{MAX}(e,h)$ is the pulse height of the module that contains the maximum pulse height of the shower. Events with a pulse height almost twice as large as the mean pulse height were clearly separated. They have been rejected by a cut of 3σ above the average values of $PH_M^{MAX}(e,h)$ and $PH_T(e,h)$.

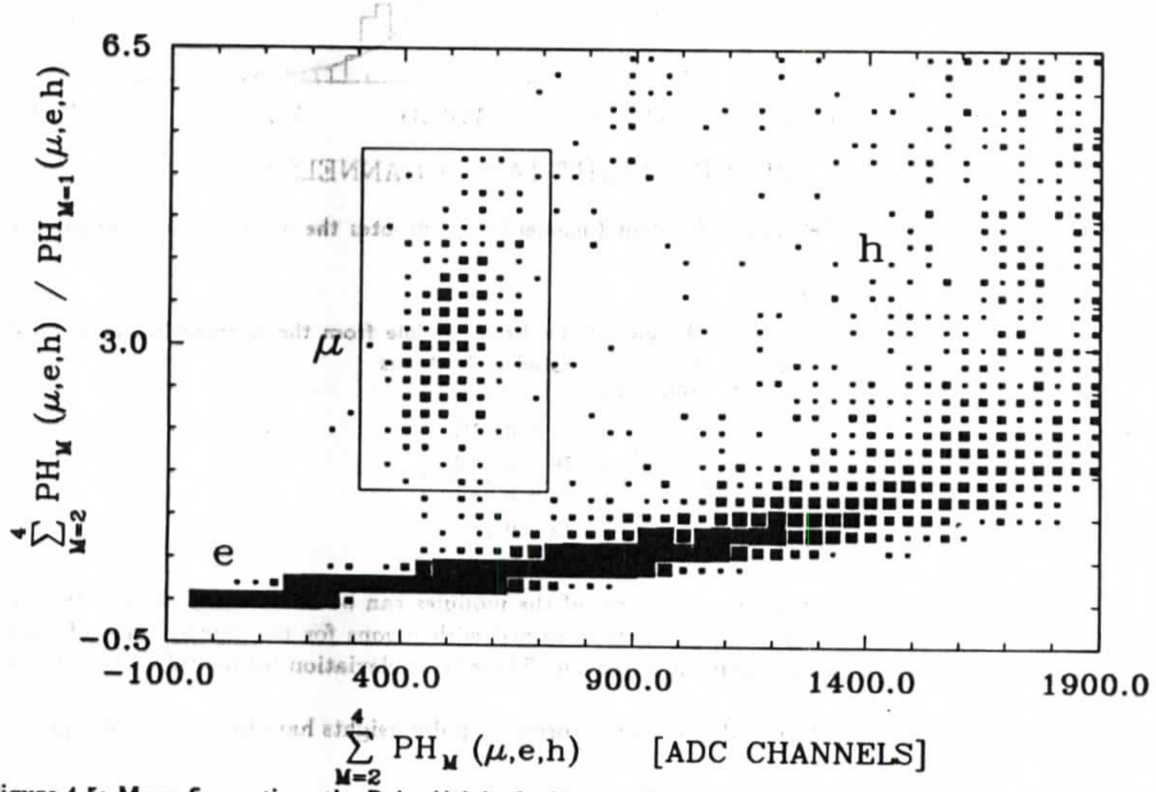

Figure 4.5: Muon Separation: the Pulse Height for Muons, Electrons and Hadrons from the last 3 Modules relative to the Pulse Height for all Particles from Module 1 versus the Pulse Height for all Particles from the last 3 Modules (see text)

3. Muons

   Muons have been identified with a cut indicated in Fig. 4.5 where the following correlation is plotted:

$$\frac{\sum_{M=2}^{4} PH_M(\mu,e,h)}{PH_{M=1}(\mu,e,h)} \quad vs \quad \sum_{M=2}^{4} PH_M(\mu,e,h)$$

with:

$PH_M(\mu, e, h)$... pulse height for muons, electrons and hadrons in one module.

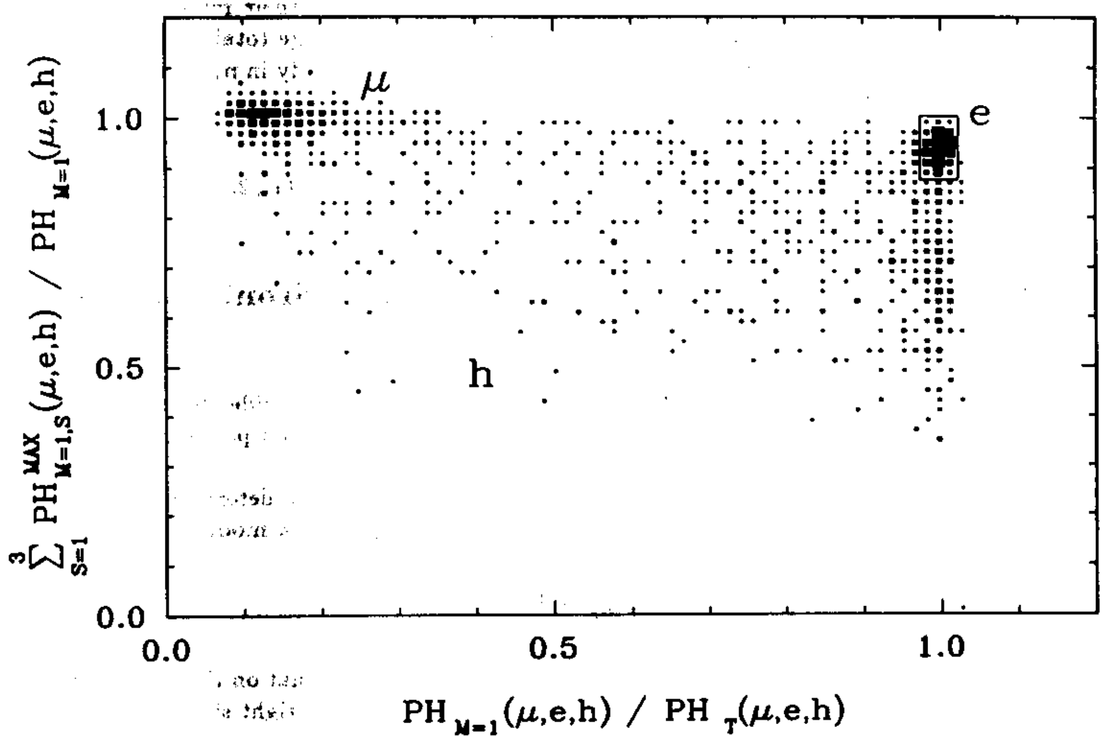

Figure 4.6: Electron Separation: the Signal of Muons, Electrons and Hadrons of the 3 adjacent Strips of Module 1 with Maximum Pulse Height Relative to the Total Pulse Height in Module 1 versus the Fraction of Module 1 on the Total Pulse Height

4. Electrons
   They were separated from hadrons by their different longitudinal and transverse energy deposition in a calorimeter. Longitudinally 98% of the electromagnetic shower is contained within 21 X_0 at $5\,GeV$, i.e. within the first module of the considered calorimeter. Transversally a cylinder of radius 4 R_M encloses 95% of the total electromagnetic energy which is a diameter of $\sim 7\,cm$ for the present calorimeter. Accordingly, two quantities of transverse and longitudinal energy deposition have been defined:

$$\frac{\sum_{S=1}^{3} PH^{MAX}_{M=1,S}(\mu,e,h)}{PH_T(\mu,e,h)} \quad vs \quad \frac{PH_{M=1}(\mu,e,h)}{PH_T(\mu,e,h)}$$

with:

$PH_M(\mu,e,h)$	pulse height for muons, electrons and hadrons in one module
$PH_T(\mu,e,h)$	pulse height for muons, electrons and hadrons in entire calorimeter
$\sum_{S=1}^{3} PH^{MAX}_{M=1,S}(\mu,e,h)$...	muon, electron and hadron signal from 3 adjacent strips with maximum pulse height in module 1.

They are plotted in Fig. 4.6: electrons are located in 3 adjacent strips of the first module so the quantity $y = \sum_{S=1}^{3} PH_{M=1,S}^{MAX}(\mu,e,h)/PH_T(\mu,e,h)$ is about ~ 1 as well as the quantity $x = PH_{M=1}(\mu,e,h)/PH_T(\mu,e,h)$; the cut for electron selection around this region is indicated in the figure; muons are located at $x \approx 0.25$ but because of the low muon rate they are hardly visible; hadrons which do not interact in the first module deposit their minimum ionization energy in one strip of the first module, i.e. $y = 1$; because of the huge total pulse height PH_T they are observed at very low values of x; hadrons that interact already in module 1 are located below the electron region.

5. Hadrons
   The hadron sample consists of all the events left over from the rejection (1., 2.) and the separation (3., 4.).

4.3 Transverse and Longitudinal Leakage of Hadronic Energy

4.3.1 Transverse Leakage

The vertical segmentation of the modules into 12 scintillator strips each 5 *cm* wide allows to determine the amount of energy leaking out of the calorimeter in form of hadronic shower particles in transverse direction.

For this purpose the transverse shower profile of the whole calorimeter was determined by summing up the pulse height $PH_M^{S_i}(h)$ of the selected hadrons in the i-th strip of all 4 modules:

$$CS_i = \sum_{M=1}^{4} PH_M^{S_i}(h). \tag{4.1}$$

This results in the plot given in Fig. 4.7. Note the logarithmic y-scale and that on the x-axis the lower strip (1) of the calorimeter is on the left and the upper strip (12) on the right side. Excluding the central strips on which the beam was directed the pulse heights of the neighbouring strips decrease towards the top and bottom sides of the calorimeter.

The shower is radial symmetric with respect to the beam axis but the distribution is measured in a calorimeter of quadratic cross section. It is found that the transverse distribution in rectangular coordinates of the calorimeter is described by the exponential function $f(x)$:

$$f(x) \propto \exp\left(-\left|\frac{x - x_0}{b}\right|\right) \tag{4.2}$$

with:

$x\ldots$	transverse coordinate in [*cm*]
$x_0\ldots$	impact point of the shower.

The function was fitted to the data (full line) taking b as free parameter. Values of the parameter b as obtained from the fit are given in Tab. 4.6 together with the values of χ^2 for 3 (top) and 2 (bottom) degrees of freedom.

The dashed areas (left and right) represent the amount of energy leaking out of the top and bottom side of the calorimeter and, under the assumption mentioned above, this is almost half of the transverse leakage of the whole calorimeter. Note that the transverse leakage in diagonal direction from the central strips is not taken into account by this method. Therefore the determined amount of transverse leakage is less than half of the transverse leakage of the whole calorimeter. In Tab. 4.7 the values of transverse leakage in percent of the measured energy are given for all energies. The first two columns of the table give the values of transverse leakage from the top and bottom side of the calorimeter, determined by integrating over the dashed areas. Under the assumption of radial symmetry of the shower the leakage from the left and right sides of the calorimeter should be the same

Table 4.6: Values for the Parameter b as obtained from a Fit of eq. 4.2 to the Transverse Shower Distribution

E [GeV]	b (top) [cm]	χ^2	b (bottom) [cm]	χ^2
3	8.75 ± 1.05	0.9	8.60 ± 1.45	0.2
5	9.20 ± 0.85	1.2	9.05 ± 1.15	1.3
7	8.90 ± 0.70	1.5	8.45 ± 0.90	0.1
8.75	8.80 ± 0.60	0.8	9.40 ± 0.95	0.1

as the leakage from the top and bottom sides. The sum of the leakage from the top and bottom sides is given in the third column of Tab. 4.7 while the total transverse leakage given in the fourth column is twice the sum of the top and bottom leakage.

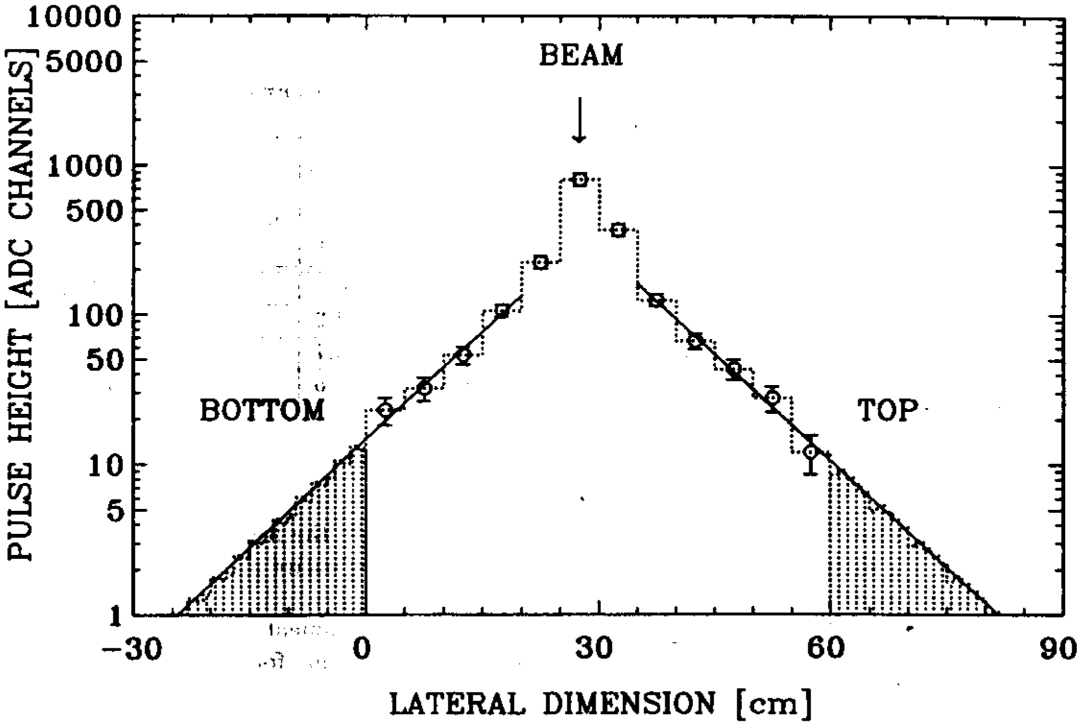

Figure 4.7: Transverse Shower Profile at 5 GeV: the Curves are Fits of an Exponential Function to the Data, the Dashed Areas indicate the Amount of Transverse Leakage out of the Top and Bottom Side of the Calorimeter

Table 4.7: Transverse Leakage out of the Top and Bottom Side of the Entire T60Pb Calorimeter

E [GeV]	top [%]	bottom [%]	top + bottom [%]	total [%]
3	0.84 ± 0.40	1.10 ± 0.64	1.94 ± 0.75	3.88
5	1.03 ± 0.37	1.40 ± 0.60	2.43 ± 0.70	4.86
7	0.96 ± 0.30	1.10 ± 0.41	2.06 ± 0.51	4.12
8.75	0.94 ± 0.26	1.42 ± 0.47	2.36 ± 0.54	4.72

The average transverse shower profile has been described by the exponential function eq. 4.2. Assuming that it also describes the transverse propagation of the shower on an event-by-event basis one can correct the total pulse height of each individual event for the leakage from the top and bottom sides. Therefore for each hadronic event one calculates the pulse heights in the two outer strip at the bottom and the top (strip 1 and 12) of the entire calorimeter, i.e.

$$CS_{S=1,(S=12)} = \sum_{M=1}^{4} PH_{S=1,(S=12);M}(h). \tag{4.3}$$

The value of $CS_{S=1}$ (from now on the correction for the bottom side will be considered only; for the top side it is similar) is compared for each hadronic event to the function value of eq. 4.2 with the parameters as obtained from the fit. If $CS_{S=1}$ is less than the function value $f_1(x)$ then x is increased until $CS_{S=1}$ is equal or greater than $f_1(x = x_>)$. The integral of the function $f_1(x)$ from $x = x_>$ to $x \gg x_>$, which is the amount of leakage from the bottom side of the calorimeter under the assumption mentioned above, is added to the total pulse height of the individual shower. The difference between the total average pulse height corrected in this way (for the top and bottom sides) and the uncorrected one is given in Tab. 4.8. The quoted errors reflect uncertainties in the calibration, especially for the outer strips 11 and 12, and statistical errors.

Table 4.8: Corrected Hadronic Response on an Event-by-Event Basis for Transverse Leakage out of the Top and Bottom Side of the T60Pb Calorimeter

	without Trans. Leak. Corr.		with Trans. Leak. Corr.		
E [GeV]	$< PH(h)_{1-4} >$ [ADC CH.]	$\sigma(h)_{1-4}$ [ADC CH.]	$< PH(h)_{1-4} >$ [ADC CH.]	$\sigma(h)_{1-4}$ [ADC CH.]	$\frac{\Delta < PH(h)_{1-4} >}{< PH(h)_{1-4}^{without\ TLC} >}$ [%]
3	1119.5 ± 11.1	326.9 ± 8.6	1124.2 ± 11.6	338.3 ± 9.3	0.42 ± 1.43
5	1879.2 ± 16.2	443.4 ± 12.7	1917.4 ± 16.5	448.1 ± 13.2	2.03 ± 1.23
7	2543.1 ± 20.5	582.6 ± 15.6	2584.3 ± 20.1	567.0 ± 14.7	1.62 ± 1.13
8.75	3236.5 ± 28.5	681.5 ± 22.8	3288.2 ± 28.6	683.2 ± 23.0	1.60 ± 1.25

4.3.2 Longitudinal Leakage

The total depth of the lead calorimeter is 4.3 λ_0 (Tab. 4.1); at 10 GeV the fraction of energy beyond this depth is about 6% while $\sim$ 80% of all events are contained in the entire calorimeter with > 95% of their total energy, according to [CAT87b].

Because of the strong fluctuations in the hadronic shower development the fraction of leaking energy also fluctuates thus deteriorating the energy resolution. Correction for longitudinal leakage is thus necessary and can be done in two ways:

1. a cut in the last module; this, however, effectively reduces the total depth of the entire calorimeter by $\sim$ 1.1 λ_0 because only those events contained in the first 3 modules (3.2 λ_0) with some small contribution from the 4. module depending on the cut will be accepted. The event sample selected this way is biased toward showers with a dominant electromagnetic part. The shower vertices are distributed over the whole calorimeter depth.

2. selection of showers with their vertices located within the first module. The shower vertex selection has been performed in the following way:

    - for each event the module i with maximum pulse height was tagged. If this was already module 1 the event was added to the sample of showers with the vertex in this module. If not, the pulse height of the module in front of the tagged one (i-*1*) was checked whether it exceeded a certain threshold value. If this was found to be the case the shower was assumed having started already in module i-*1* and the event was attributed to the appropriate event sample. Otherwise, module i with the maximum pulse height was considered as the one containing the vertex.
    - the threshold pulse height was determined in two ways:

(a) non-showering particles deposit an energy equivalent to a minimum ionizing particle (mip) in the calorimeter modules; the threshold energy was set to a value of 2 times the energy deposition of a muon: this corresponds to $\sim 1.1\,GeV$ of incident energy.

(b) the number of vertices should decrease exponentially; by varying the threshold value iteratively the distribution of the vertices was thus influenced and the deviation from an exponential function was minimized by comparing the χ^2-values of the fit. The threshold values found in this way are listed below and are almost consistent with the one of method 1.

E [GeV]	Threshold Value [GeV]
3	1.0
5	1.3
7	1.0
8.75	1.4

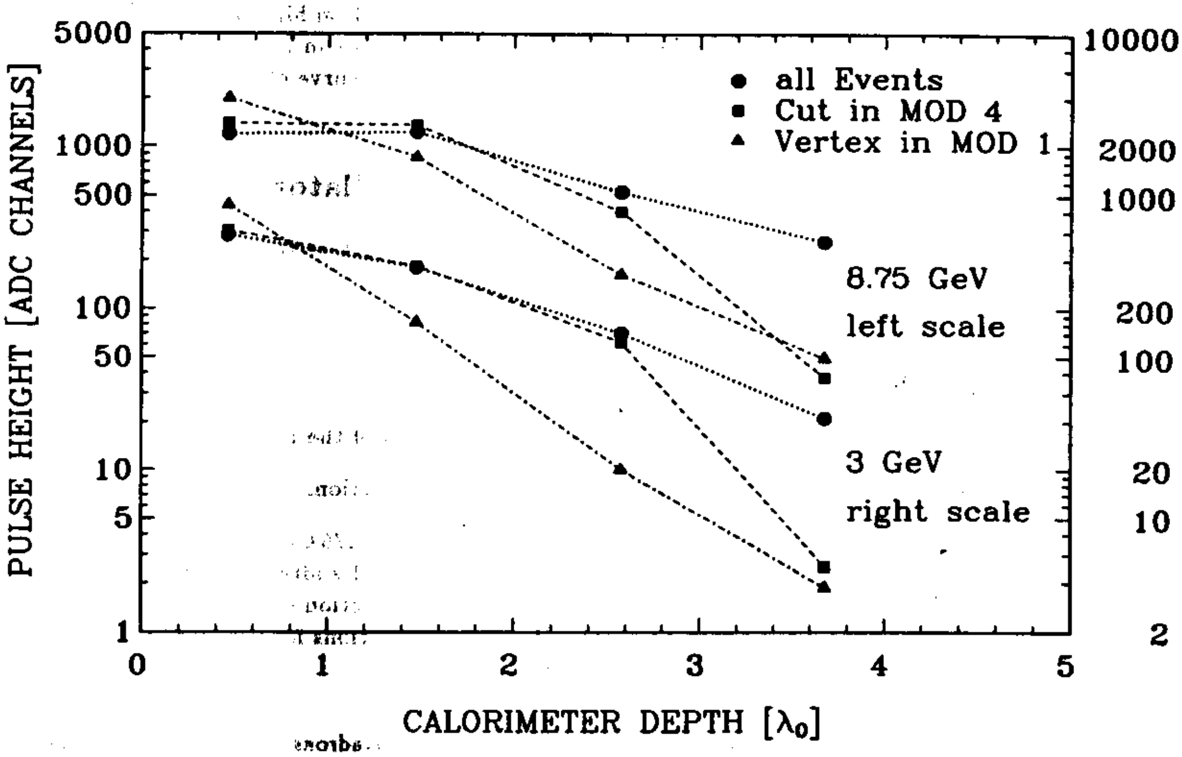

Figure 4.8: Longitudinal Shower Development at 3 and 8.75 GeV for i) all Events; ii) Events of Showers Depositing less than 10 % of the total Energy in Module 4; iii) Events of Showers with their Vertices in Module 1

The different longitudinal shower developments are shown in Fig. 4.8 at the lowest ($3\,GeV$; right scale) and highest ($8.75\,GeV$; left scale) energy point of this measurement. For comparison the distribution for all hadronic events, i.e. without any treatment of the longitudinal leakage is given, too. Note that the lines are only drawn to guide the eye and that the $3\,GeV$ points are shifted in y-direction. The showers starting in the first module show an almost exponential decrease. The longitudinal profile of those showers selected by method 1 is similar to the one of all showers except in module 4 where the cut against pulse heights exceeding 10% of the total pulse height has been performed.

For reasons of longitudinal nonuniformity in the wavelength shifter readout that will be discussed in section 4.5.4 the longitudinal leakage correction was done according to the first method. The effect

Table 4.9: Effect of the Longitudinal Leakage Cut which rejected Hadronic Events that deposited 10% or more of the total Energy in Module 4 of the T60Pb Calorimeter

	without Long. Leak. Cut		with Long. Leak. Cut		
E [GeV]	$< PH(h)_{1-4} >$ [ADC CH.]	$\sigma(h)_{1-4}$ [ADC CH.]	$< PH(h)_{1-4} >$ [ADC CH.]	$\sigma(h)_{1-4}$ [ADC CH.]	Event Rejection [%]
3	1119.5 ± 11.1	326.9 ± 8.6	1110.2 ± 11.7	326.3 ± 8.9	6.5
5	1879.2 ± 16.2	443.4 ± 12.7	1861.6 ± 17.9	443.7 ± 14.3	13.8
7	2543.1 ± 20.5	582.6 ± 15.6	2514.8 ± 21.6	560.7 ± 16.3	15.0
8.75	3236.5 ± 28.5	681.5 ± 22.8	3200.8 ± 31.6	677.7 ± 25.4	18.5

of the longitudinal leakage cut can be read off from Tab. 4.9. The width of the distribution ($\sigma(h)$) improves at 7 and 8.75 GeV due to the longitudinal leakage cut that rejects those hadron events which are not fully contained in the first 3.2 λ_0. However, the mean pulse height decreases slightly for all energies if the longitudinal leakage cut is applied. One would not expect this decrease because the low energy tail in the distribution that includes leakage vanishes if fully contained events are selected. For this measurement the last module of the calorimeter was used to cut on high pulse heights in this module. This results in a lower total pulse height of the calorimeter as can be seen in Fig. 4.8: the area under the curve of all events is larger compared to that under the curve of the events remaining after the longitudinal leakage cut in module 4.

4.4 Energy Resolution of the T60 Lead-Scintillator Calorimeter

The electron and hadron response of the lead calorimeter was determined at the different steps of the leakage correction, i.e.

- without leakage correction,
- with longitudinal leakage cuts according to method 1,
- with transverse leakage correction for the top and bottom sides of the calorimeter,
- with both longitudinal leakage cuts and transverse leakage correction.

The measured distributions for electrons and hadrons at 3, 5, 7 and 8.75 GeV are shown in Fig. 4.9. The hadronic distribution is the sum of the pulse heights of all 4 modules after a cut against longitudinal leakage (method 1) of $\leq 10\%$ of the total sum and after a correction of transverse leakage for the top and bottom side of the calorimeter, as described. The distributions for electrons and hadrons were fitted by a gaussian function over $\pm 3\sigma$ around the mean.

Table 4.10: Mean Response and Energy Resolutions for Electrons and Hadrons at 1 (Electrons only), 3, 5, 7 and 8.75 GeV as measured with the T60Pb Calorimeter (Resolutions quoted are within $\pm 3\sigma$; only Statistical Errors are given)

	ELECTRONS		HADRONS	
E [GeV]	$< PH(e)_{1-2} >$ [ADC CH.]	$\frac{\sigma_E(e)_{1-2}}{\sqrt{E[GeV]}}$ [%]	$< PH(h)_{1-4} >$ [ADC CH.]	$\frac{\sigma_E(h)_{1-4}}{\sqrt{E[GeV]}}$ [%]
1	460.2 ± 2.7	12.2 ± 0.5	-	-
3	1431.6 ± 4.9	12.1 ± 0.4	1115.2 ± 8.7	52.7 ± 1.1
5	2387.4 ± 7.5	13.6 ± 0.6	1879.6 ± 21.7	53.4 ± 1.3
7	3274.7 ± 6.6	13.5 ± 0.4	2547.4 ± 15.9	59.9 ± 1.4
8.75	4151.4 ± 11.9	13.7 ± 0.7	3234.7 ± 22.2	60.6 ± 1.7

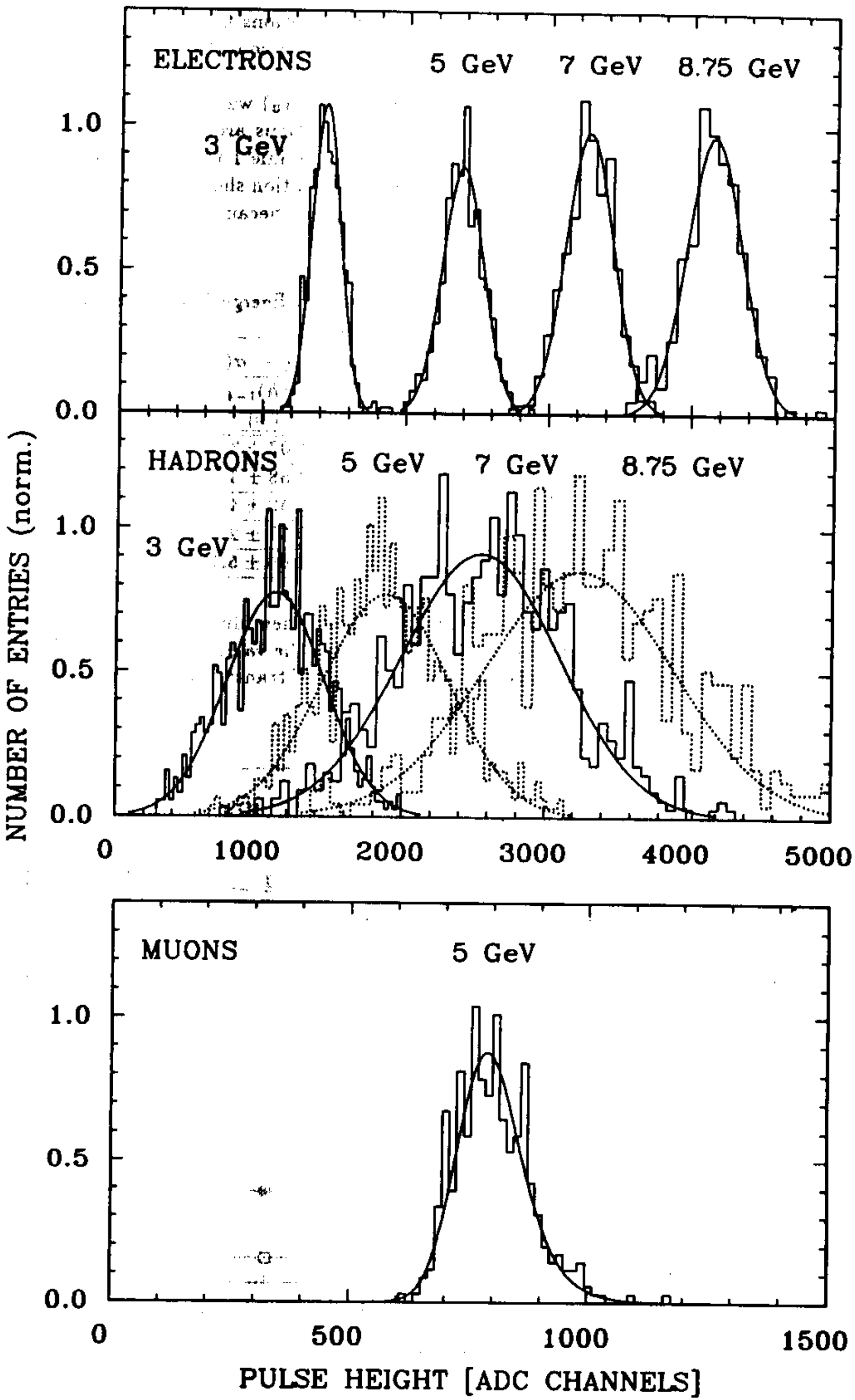

Figure 4.9: Pulse Height Distributions of Electrons and Hadrons at 3, 5, 7 and 8.75 GeV and *Muons* at 5 GeV Measured with the T60Pb Calorimeter (Fits are within ±3σ for Electrons and Hadrons)

The results given in Tab. 4.10 are mean values and standard deviations from the fits. The muon response of the calorimeter at 5 GeV is also shown in this figure with a convolution of a Moyal- and a Gauss-function fitted to it (see Appendix A).

For electrons the pulse height sum of module 1 and 2 only (43.8 X_0) was considered in order to add no further signal from module 3 and 4 due to pedestal fluctuations around 0. The difference between the mean pulse heights for the sum of module 1 to 2 and module 1 to 4 is negligible within the statistical errors, as can be seen from Tab. 4.11. The energy resolution should improve if the sum of module 1 to 2 is taken, but this is not significant in this measurement because of the large statistical errors.

Table 4.11: Relative Deviation in [%] of the Mean Pulse Height and the Energy Resolution for Electrons if the Sum of Module 1 and 2 is considered instead of Module 1 to 4

E [GeV]	$\frac{< PH(e)_{1-2} > - < PH(e)_{1-4} >}{< PH(e)_{1-4} >}$ [%]	$\frac{\sigma(h)_{1-2} - \sigma(h)_{1-4}}{\sigma(h)_{1-4}}$ [%]
1	$+0.29 \pm 0.60$	-4.07 ± 3.82
3	-0.29 ± 0.35	-2.58 ± 3.48
5	-0.23 ± 0.31	$+6.49 \pm 4.26$
7	$+0.04 \pm 0.20$	-0.37 ± 2.82
8.75	$+0.001 \pm 0.29$	$+4.00 \pm 5.10$

Within the quoted statistical errors there is no significant improvement due to longitudinal leakage corrections even in the case of showers that start in the first module the values of which are not given in Tab. 4.10. There is a slight improvement in the energy resolution if transverse leakage correction is applied.

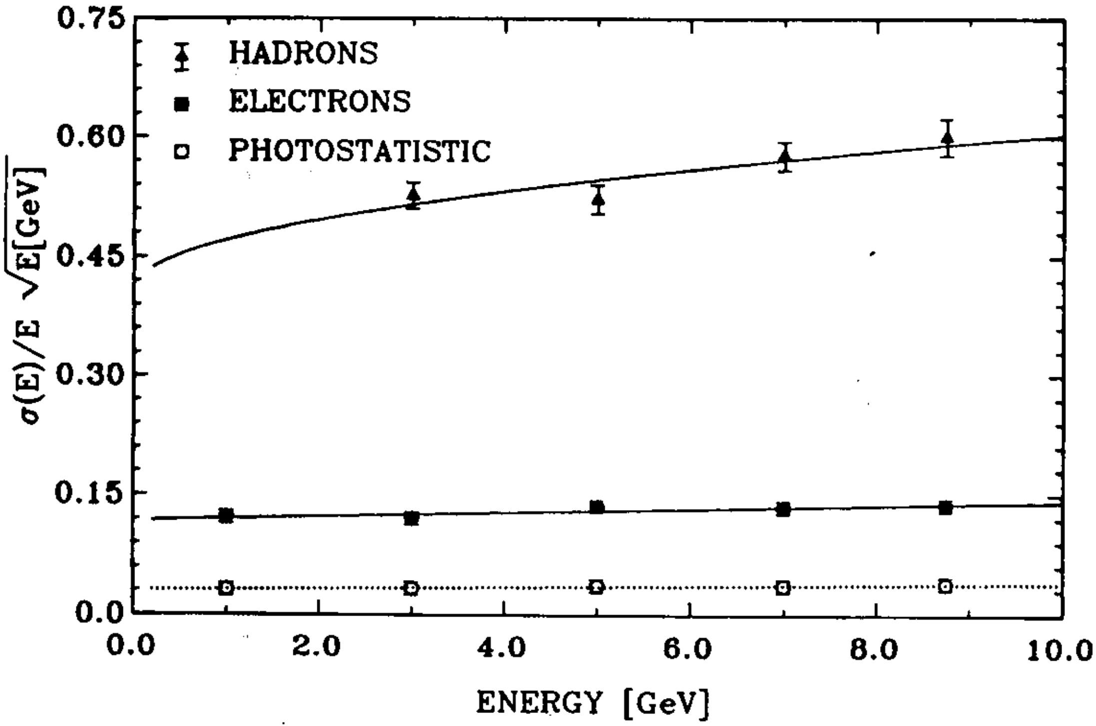

Figure 4.10: Energy Resolution of the T60Pb Calorimeter for Electrons and Hadrons as a Function of the Energy, and the Contribution from Photostatistics

However, the energy resolution deteriorates with higher energies which is a clear indication of the fact that the described lead calorimeter does not compensate. Fig. 4.10 shows the energy resolution for electrons and hadrons as a function of energy, parametrized for electrons as

$$\frac{\sigma_E}{E}(e) = \frac{a}{\sqrt{E[GeV]}} \oplus b \tag{4.4}$$

yielding

$$\begin{aligned} a &= 11.7\% \pm 0.8\% \\ b &= 2.5\% \pm 0.4\% \end{aligned} \tag{4.5}$$

while for hadrons the parametrization

$$\frac{\sigma_E}{E}(h) = \frac{a}{\sqrt{E[GeV]}} + b \tag{4.6}$$

according to eq. 3.61 has been used, yielding

$$\begin{aligned} a &= 41.0\% \pm 4.8\% \\ b &= 6.1\% \pm 2.1\%. \end{aligned} \tag{4.7}$$

The quoted errors are obtained from the fit. The uncertainty of the calibration which is supposed to have the largest influence on this measurement has been estimated to be about 7%.

The values of the energy resolution for hadrons are those with longitudinal leakage cut and transverse leakage correction (see Tab. 4.10). The large constant term $b = 2.5\% \pm 0.4\%$ in the parametrization for electrons may be caused by different effects: the uncertainty in the calibration with muons, the crude calibration of the first module that was equipped with thinner lead plates than the other modules, the contribution from momentum spread of the beam of $\frac{\Delta p}{p} = 1\%$ [TIE87] and contributions from imperfect light readout (sec. 4.5.1). The errors quoted on the mean pulse heights and the energy resolution are statistical errors. The systematic error is mainly due to the uncertainty of the calibration and is estimated to be about 7%.

The contribution from photoelectron statistics is also shown in Fig. 4.10. The determination will be described in the next section.

The response to the incident energy is linear within ± 2.5% as can be read off from Fig. 4.11 showing the deviation from the mean linearity.

4.5 Light Yield and Influence of the Readout System

4.5.1 Light Yield

The amount of light produced in the scintillator plates of a sampling calorimeter is proportional to the deposited energy in the calorimeter. The light will be collected via the wavelength shifter bars and converted into a measureable signal.

The light yield of a calorimeter can be expressed in the average number of photoelectrons per GeV of incident energy, $< n >$, converted at the photocathode of the photomultiplier:

$$< n > \equiv \frac{< N_{pe} >}{E} \tag{4.8}$$

with:

$< N_{pe} > \ldots$	mean number of photoelectrons
$E \ldots$	incident energy in $[GeV]$

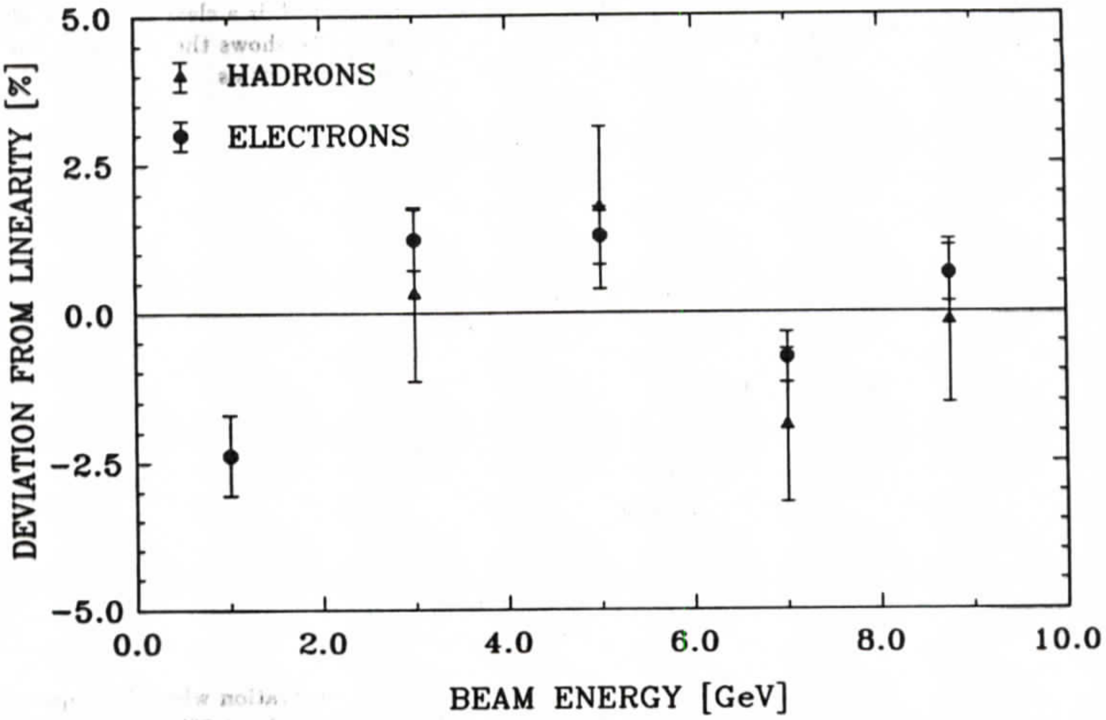

Figure 4.11: Deviation from Linearity in [%] for Electrons and Hadrons in the T60Pb Calorimeter

It is important to know the fluctuations around this average value because they give rise to an additional contribution to the energy resolution of a calorimeter. The relative width of those fluctuations are given [HOF82] by:

$$\begin{aligned} \frac{\sigma_{pe}(<N_{pe}>)}{<N_{pe}>} &= \frac{1}{\sqrt{<N_{pe}>}} \\ &\propto \frac{1}{\sqrt{E[GeV]}}. \end{aligned} \tag{4.9}$$

One can use eq. 4.9 to determine the mean number of photoelectrons of a photomultiplier by measuring the width of the distribution of a monochromatic light source. This can be done by illuminating the photocathode with an light emitting diode (LED).

In order to measure the number of photoelectrons per deposited energy in a calorimeter one can use a method proposed by [KLA86] if the calorimeter is readout from two edges of the scintillator plates. Under the assumption of equal light transport and quantum efficiencies of the left and right photomultipliers the relative width of the difference spectrum of the left and right readout channel is related to the mean number of photoelectrons collected by both photomultipliers by:

$$\frac{\sigma_{L-R}(e)}{<PH_{L+R}>} = \frac{1}{\sqrt{<N_{pe}>}} \tag{4.10}$$

$$= \frac{a_{L-R}}{\sqrt{E[GeV]}} \tag{4.11}$$

where:

$<N_{pe}>\ldots$	average number of photoelectrons per GeV of incident energy collected by both photomultipliers
$a_{L-R}\ldots$	photostatistical contribution to the energy resolution of the calorimeter in [%]

The contribution of photostatistics to the total energy resolution as measured with electrons in the T60Pb calorimeter according to eq. 4.11 is:

$$\frac{\sigma_{L-R}}{< PH_{L+R} >}(e) = \frac{(2.95 \pm 0.09)\%}{\sqrt{E[GeV]}} \oplus (0.80 \pm 0.07)\%. \tag{4.12}$$

The sampling fluctuation calculated with EGS4 is:

$$\frac{\sigma_s(e)}{E} = \frac{(11.85 \pm 0.16)\%}{\sqrt{E[GeV]}}. \tag{4.13}$$

The quadratic sum of the sampling fluctuations and the contribution from photostatistic yields:

$$\frac{\sigma_t(e)}{E} = \frac{(12.21 \pm 0.18)\%}{\sqrt{E[GeV]}} \oplus (0.80 \pm 0.07)\%. \tag{4.14}$$

and is compatible with the measured energy resolution given in eq. 4.5.

With eq. 4.11 the average number of photoelectrons of the T60Pb calorimeter per GeV of incident energy has been calculated to $< N_{pe} > = 1070 \pm 70$. This corresponds to 11 photoelectrons per MeV of visible electromagnetic shower energy at an electromagnetic sampling fraction of $\hat{e} = 9.52\%$, as calculated with EGS4.

4.5.2 Influence of the Readout System

The quoted absolute values of the measured electron and hadron response (Tab. 4.10) are influenced by nonuniformities of the light collection system which have to be taken into account in order to determine the correct e/h-ratio. The main sources of nonuniformities are:

- transversal:
  - attenuation length of the scintillator following an exponential function,
  - deviation from exponential behaviour at the scintillator edges with an increase of light yield,
  - nonuniformities because of tolerances (scintillator, absorber thicknesses);
- longitudinal:
  - attenuation length of the wavelength shifter, which includes the following items:
    - influence of the reflectivity at the edges, essentially at the far end from the readout side (end reflector),
    - influence of the reflectivity at the side face of the wavelength shifter bar (back reflector).

4.5.3 Nonuniformity of the Scintillator

The attenuation length of SCSN-38 scintillator used in the T60 calorimeter was measured by scanning the calorimeter horizontally with electrons and muons. Determining the light yield from the left and right side of the scanned scintillator strip one can deduce the attenuation length of the scintillator from the ratio of both pulse heights, assuming that the light absorption follows an exponential function far away from the edges:

$$\frac{PH_L}{PH_R} \propto \exp\left(-\frac{2\,x}{\lambda_{att}}\right) \tag{4.15}$$

$PH_{L(R)} \dots$	pulse height at the left (right) side of the scintillator strip
$x \dots$	beam impact position
$\lambda_{att} \dots$	attenuation length of the scintillator

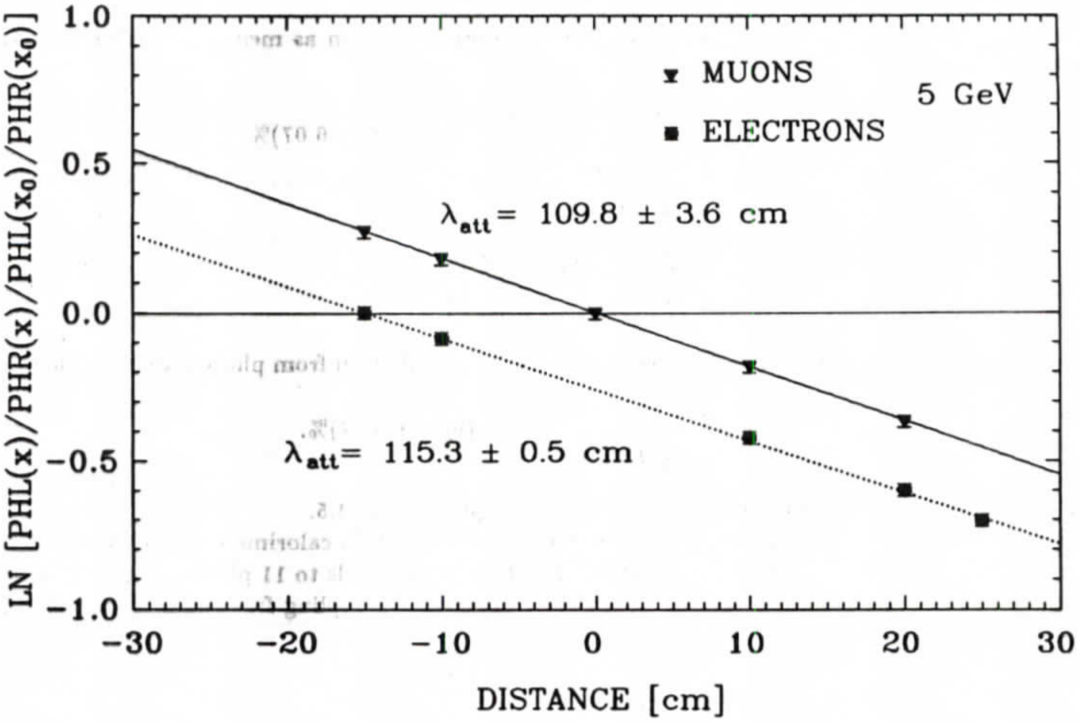

Figure 4.12: Logarithm of the Ratio of the Pulse Heights at the Left and Right Side of the Scintillator Strip from Muons and Electrons, Relative to the Pulse Height Ratio at $x_0 = 0\,cm$ (Muons) and $x_0 = -15\,cm$ (Electrons), as a Function of the Beam Impact Position x

The logarithm of the ratio relative to the pulse height ratio at $x_0 = 0\,cm$ (muons) and $x_0 = -15\,cm$ (electrons) is plotted in Fig. 4.12 as a function of x for both muons and electrons as incident particles. The logarithm of the function 4.15 was fitted to the data points, from which the attenuation length of the scintillator was obtained:

$$\begin{aligned}\lambda^{\mu}_{att} &= 109.8 \pm 3.6\,cm\\ \lambda^{e}_{att} &= 115.3 \pm 0.5\,cm.\end{aligned}$$

The result is in fair agreement with other measurements which have been done for SCSN-38 scintillators with different geometry:

λ^{Ru}_{att}	$= 91.0 \pm 11.5\,cm$	[KAM83]
λ^{e}_{att}	$= 82.1 \pm 1.6\,cm$	[KLA86]
λ^{μ}_{att}	$= 86.0 \pm 24.9\,cm$	[BER86].

The superscripts e, μ, Ru denote the kind of light generating sources in the scintillator.

Assuming again an exponential light attenuation, one expects the product $PH_L \cdot PH_R$ to be independent on the position x:

$$PH_L \cdot PH_R \propto \exp\left(-\frac{l}{\lambda_{att}}\right). \tag{4.16}$$

Deviations from this constant value should reflect nonuniformities caused by deviations from the exponential light attenuation in the scintillator. Fig. 4.13 shows the square root of the product of the pulse height at the left and right side of the scintillator strips which is normalized to the pulse height at $x_0 = 0\,cm$ (muons) and $x_0 = -15\,cm$ (electrons). The deviations from a uniform light collection along the scintillator are -2 to 7% as obtained with muons and -1 to 3% as measured with electrons. This may be one source of detector imperfections that limits the energy resolution leading to the constant term in the parametrization given above.

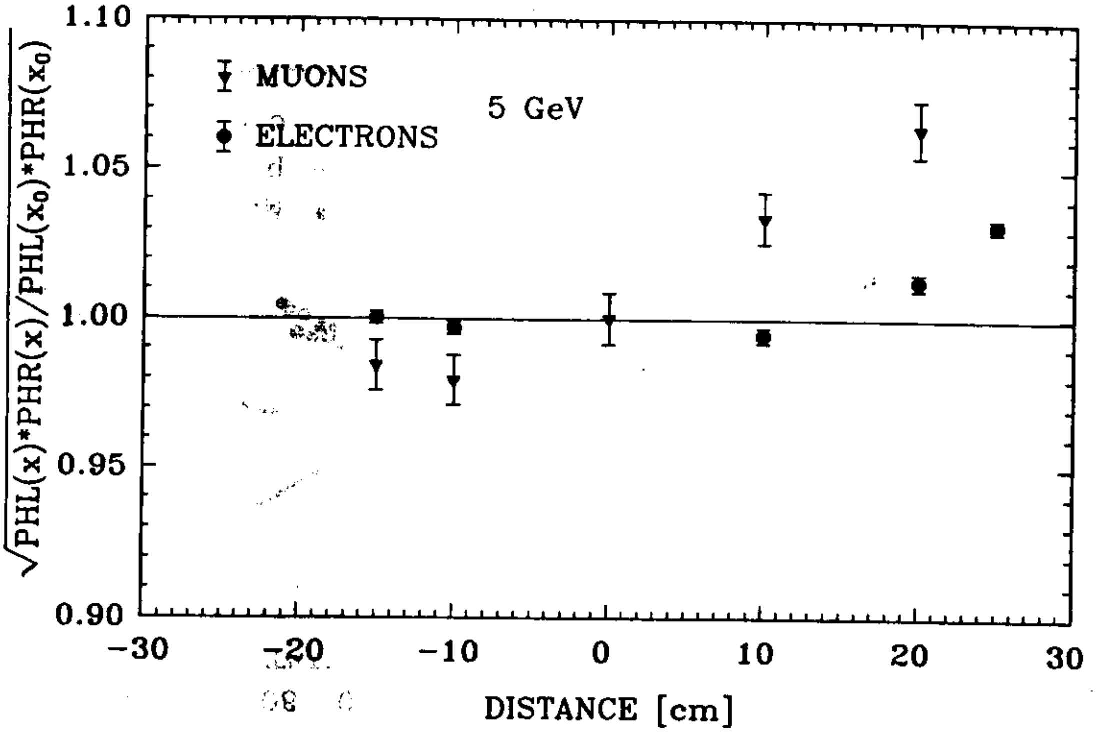

Figure 4.13: Deviations from Uniform Light Yield in one Scintillator Strip measured with Muons and Electrons

4.5.4 Nonuniformity of the Wavelength Shifter

The energy deposition and hence the amount of light produced along the wavelength shifter depends on the depth of the shower within the calorimeter. As the electromagnetic and hadronic shower distributions are quite different, longitudinal nonuniformities will effect electromagnetic and hadronic showers differently. The correction for this nonuniformity is thus important for a determination of the e/h-ratio. In the case of the T60 calorimeter the mean response of the electron shower is significantly influenced by this nonuniformity because the electron shower penetrates only partially into one calorimeter module ($\sim 22\ X_0$ in depth, T60Pb) with its maximum at the $\sim$ 10 th layer (see Fig. 4.14). The electromagnetic shower curve is convoluted with a small part of the attenuation curve which means that the mean electron signal will be suppressed (Fig. 4.14). The hadronic shower, on the other hand, is averaged over the attenuation curves of all modules and hence the mean pulse height will not be influenced significantly. However, the fluctuating longitudinal depositions of the hadronic energy will be suppressed or enhanced with different attenuation factors depending on the longitudinal position. This leads to a stronger influence on the spread of the pulse height distribution than for the electromagnetic shower.

A correction for the wavelength shifter nonuniformity in the T60 measurements has been done by two methods:

1. The relative light yield across the wavelength shifter bar was measured by scanning one calorimeter module with a ^{60}Co source (185 MBq) in longitudinal direction. The light response curve

measured this way was used for an offline correction of the average electron and hadron response.

2. A more precise measurement of the light response curve have been performed with a dismantled wavelength shifter bar scanning across it with a scintillator plate irradiated by a ^{106}Ru source. According to this curve an optical grey filter was produced and put in between the edges of the scintillator strips and the wavelength shifter bars.

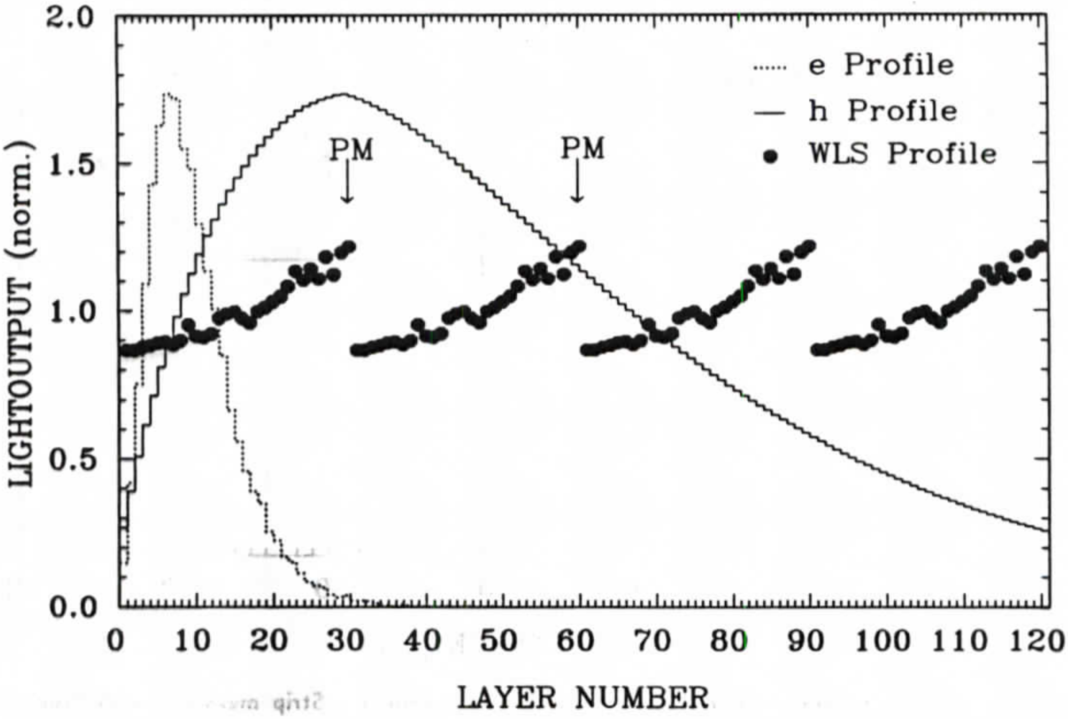

Figure 4.14: Light Response Curve of Wavelength Shifter Bars in the 4 Modules of the T60 Calorimeter measured with a ^{60}Co Source by scanning along one Module (EGS4 simulated Electron Shower Profile and Hadronic Shower Profile Parametrization at 5 GeV for the T60 Pb/SCI Calorimeter overlayed for Illustration; PM: Photomultiplier Side)

The second method was applied only during the measurement with 3.0 mm thick scintillator plates and will be described later. For the measurement with lead the offline correction (method 1) was done using the measured light response curve shown in Fig. 4.14 together with an EGS4 simulated shower profile at 5 GeV for electrons and the shower parametrization eq. 5.7 for hadrons. The correction was done as follows:
the average measured pulse height of the entire calorimeter, $< PH^m(e,h) >$, influenced by the wavelength shifter nonuniformity can be written as:

$$< PH^m(e,h) >= \frac{1}{\frac{1}{N_L}\sum_{i=1}^{N_L} f_i\,(WLS)} \sum_{i=1}^{N_L} PH_i^{MC,SP}(e,h) \cdot f_i\,(WLS) \qquad (4.17)$$

with:

$N_L \ldots$ number of scintillator layers
$f_i\,(WLS) \ldots$ measured light response curve of the wavelength shifter.

For electrons the pulse height $PH_i^{MC}(e)$ in the i-th layer according to the EGS4 Monte Carlo is:

$$PH_i^{MC}(e) = E_i^{MC}(e)\,\frac{< PH^t(e) >}{E_T^{MC}(e)} \tag{4.18}$$

where:

$E_i^{MC}(e)\ldots$	deposited energy in the i-th scintillator plate according to the electron shower profile simulated with EGS4
$< PH^t(e) >\ldots$	mean electron pulse height not influenced by the nonuniformity of the wavelength shifter
$E_T^{MC}(e)\ldots$	total deposited energy of electrons in the scintillator plates.

For hadrons the shower parametrization eq. 5.7 has been used:

$$PH_i^{SP}(h) = E_i^{HProf}(h)\,\frac{< PH^t(h) >}{E_T^{HProf}(h)} \tag{4.19}$$

$E_i^{HProf}(h)\ldots$	deposited energy in the i-th scintillator plate according to the hadronic shower profile parametrization (see eq. 5.7)
$< PH^t(h) >\ldots$	mean hadron pulse height not influenced by the nonuniformity of the wavelength shifter
$E_T^{HProf}(h)\ldots$	total deposited energy of hadrons in the scintillator plates.

The corrected (true) pulse height follows from eq. 4.17, 4.18 and 4.19:

$$< PH^t(e,h) > = \frac{< PH^m(e,h) > \cdot E_T(e,h) \sum_{i=1}^{N_L} f_i\,(WLS)}{N_L \sum_{i=1}^{N_L} E_i\,(e,h)\cdot f_i\,(WLS)} \quad . \tag{4.20}$$

4.6 The e/h- and $\tilde{e}/\widetilde{mip}$-Ratio of the T60 Lead-Scintillator Calorimeter

In Tab. 4.12 the values of Tab. 4.10 ($< PH_{M=1+2}(e) >$) for electrons and ($< PH_{M=1-4}(h) >$, LLK Cut 10%, TLK Corr t+b) for hadrons, corrected for the longitudinal nonuniformity are given; the values for hadrons were additionally corrected for the transverse leakage out of the right and left side of the calorimeter under the assumption mentioned in section 4.3.1.

These corrections led to the e/h- and $\tilde{e}/\widetilde{mip}$-ratios quoted in Tab. 4.12 and are plotted as a function of energy in Fig. 4.15. The total errors on both ratios result from the propagation of the statistical errors on the measured pulse heights, the errors on the measurement of the light attenuation curve, the statistical errors on the electromagnetic shower simulation and the errors on the parametrization of the hadronic shower profile.

The $\tilde{e}/\widetilde{mip}$-ratio of this calorimeter configuration given in Tab. 4.12 was calculated using eqs. 3.32, 3.33; the values for the muons quoted are mean pulse heights of the whole calorimeter; the $\frac{dE}{dx}$-values inserted in eq. 3.33 are listed in Tab. 4.13; they are taken from [LOH85, PDG86], interpolated to the corresponding beam energies. Also given in Tab. 4.13 are the measured electromagnetic sampling fraction defined by eq. 3.32 in comparison with results from EGS4 simulations. The cut-off energies

Table 4.12: Electron, Muon and Hadron Response of the T60Pb Calorimeter, Corrected for Longitudinal Nonuniformity (e, h) and for Leakage (h), and the resulting e/h- and $\bar{e}/\widetilde{mip}$-ratio at 1, 3, 5, 7 and 8.75 GeV

E [GeV]	e [ADC CH.]	h [ADC CH.]	$\frac{e}{h}$	$\frac{\bar{e}}{\widetilde{mip}}$	μ [ADC CH.]
1	504.9 ± 6.4	-	-	0.60 ± 0.13	193.0 ± 41.3
3	1549.1 ± 18.6	1138.3 ± 46.6	1.36 ± 0.06	0.74 ± 0.12	172.8 ± 26.9
5	2563.9 ± 32.7	1933.0 ± 78.4	1.33 ± 0.06	0.65 ± 0.08	206.3 ± 25.9
7	3504.1 ± 42.9	2598.5 ± 104.9	1.35 ± 0.06	0.65 ± 0.07	204.4 ± 19.7
8.75	4432.8 ± 56.1	3315.4 ± 134.6	1.34 ± 0.06	0.62 ± 0.08	221.6 ± 28.8

Table 4.13: Values for Ionization Loss of Muons in SCSN-38 and the Resulting Electromagnetic Sampling Fraction from the Measurement and from EGS4 Simulations of the T60Pb Calorimeter

E [GeV]	$\frac{dE}{dx}\Big\vert^{ION}$ (μ) in SCSN-38 $[\frac{MeV\,cm^2}{g}]$	$\bar{e}$ [%] measured	$\bar{e}$ [%] EGS4
mip	1.950 ± 0.034	-	-
1	2.027 ± 0.035	8.43 ± 1.81	9.54 ± 0.04
3	2.206 ± 0.038	10.48 ± 1.65	9.55 ± 0.02
5	2.298 ± 0.040	9.41 ± 1.16	9.56 ± 0.02
7	2.353 ± 0.041	9.44 ± 0.90	9.55 ± 0.02
8.75	2.388 ± 0.041	9.48 ± 1.14	9.56 ± 0.02

for this simulations were chosen to $E_C = 1000\,keV$ (electrons) and $P_C = 10\,keV$ (photons). The agreement of the measured values with the ones predicted from EGS4 is quite well.

From the measurement with the T60 4.75 mm Pb - 5 mm scintillator calorimeter one can draw the first conclusion that an e/h-ratio $\neq 1$ is correlated with an unsatisfying hadronic energy resolution; on the other hand, it became not clear from this measurement whether only another absorber material or a different ratio of scintillator to absorber plate thicknesses would improve the energy resolution. Therefore, as a next measurement, only the absorber plates were changed while staying with the same scintillator thickness.

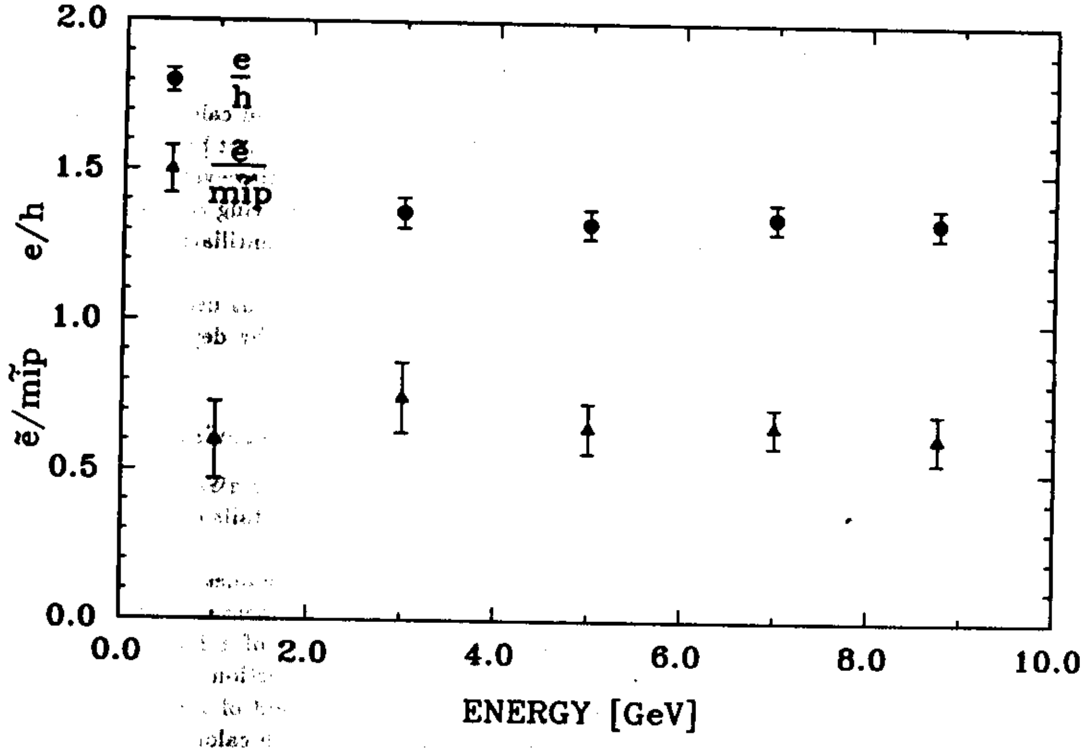

Figure 4.15: e/h- and $\tilde{e}/\widetilde{mip}$-Ratio of the T60Pb Calorimeter as a Function of the Energy

Chapter 5

Measurements with Uranium-Scintillator Calorimeters

5.1 Replacing Lead by Uranium

The measured hadronic energy resolution as well as the e/h-ratio of the lead calorimeter described in the previous section shows that with this configuration compensation could not be achieved. A way to reach $e/h = 1$ is to use depleted uranium plates as proposed by [FAB75]. However, the thickness ratio of the passive to the active absorber plates plays an essential rule in achieving compensation. Therefore measurements on hadron calorimeters with depleted uranium and scintillator plates of different thickness ratios have been performed.

The first measurement has been carried out with the same equipment as used before leaving the active layers unchanged but replacing the 4 and 5 *mm* thick lead plates by depleted uranium (*DU*) plates of 3.2 *mm* thickness.

5.1.1 The T60A Uranium-Scintillator Calorimeter Characteristics

In Tab. 5.1 the dimensions and specifications of the T60A calorimeter are given in the 3.2 *mm DU*-5.0 *mm* scintillator configuration used in this measurement (T60UA). Details of the readout system which remained unchanged can be found in Tab. 4.1.

The measurements have been performed in the same beam line as the ones with the T60Pb calorimeter with identical trigger definitions (see sec. 4). The beam rate as measured by the coincidence of the beam counters $B_1 \cdot B_2$ was 45 000 per spill at a collimator setting of ± 8 *mm*. The contents of the beam during this period was estimated after applying the particle selection cuts in the calorimeter and is listed in Tab. 5.2. It is different to the contents during the period of the T60Pb calorimeter measurement because of the uncertainties in the calibration of the T60Pb calorimeter.

5.1.2 Calibration and Particle Selection

The natural radioactivity of depleted uranium (see Appendix C) used as passive absorber provides an elegant source of calibration and monitoring the stability.

The major part of the measurable uranium noise is due to electrons from the β-decay in the energy range of $0 - 2310\,keV$ [PEG85] penetrating a few millimeters into a scintillator plate, dependent on their energy. One can estimate the energy deposition at the surface to be a factor of ~ 40 higher than the overall energy deposition in a scintillator plate of 5 *mm*. Hence the calibration with uranium noise has a different dependence on the scintillator thickness than the response from muons, hadrons and electrons.

The following procedure of pedestal determination and calibration has been used during this measurements:

- Pedestal Determination
  the pedestal values that have been subtracted during the physics runs were measured when the

Table 5.1: Dimensions and Specifications of the T60UA Calorimeter inserted with 3.2mm thick Depleted Uranium and 5mm thick Scintillator Plates

Calorimeter			
Lateral Dimensions	**600 × 600 mm^2**	**$70.21X_0$**	**$2.56\lambda_0$**
Number of Modules	**4**		
Number of Layers per Module	**30**		
Total Depth of 1 Layer	**13 mm**	**$1.02X_0$**	**$0.037\lambda_0$**
Total Depth of 1 Module	**390 mm**	**$30.68X_0$**	**$1.11\lambda_0$**
Total Depth of Calorimeter	**1560 mm**	**$122.7X_0$**	**$4.4\lambda_0$**
Airgap per Layer	**4.8 mm**		
Passive Layer			
Lateral Dimensions	**600 × 600 mm^2**		
Thickness of Plates	**3.2 mm DU**	**$1.01X_0$**	**$0.031\lambda_0$**
Material	**DU:** **$\sim 0.2\%\ ^{235}U$** **$\sim 99.8\%\ ^{238}U$**		
Active Layer			
Dimension of Scintillator Strip	**50 × 600 mm^2**		
Number of Strips	**12**		
Thickness of Plates	**5 mm**	**$0.01X_0$**	**$0.007\lambda_0$**
Material	**SCSN-38 (Polystyrene Base)**		

beam was off, but with the high voltages (HV) applied to the photomultipliers. The gate length was 150 ns for the pedestal measurement as well as for the physics runs. In this way, the uranium noise was measured, too, integrated over 150 ns and randomly triggered. This increased the true pedestal values (HV off) by approximately 5 ADC channels, while the width of the pedestal distribution has become broader. Because the uranium noise is also present as background signal during physics runs the pedestal values including the contribution due to uranium noise have been subtracted.

- Calibration
  as a reference signal for the calibration the randomly triggered signal from the uranium plates were accumulated with an integration time of 10μs. For this purpose the ADC 2282 B (Le Croy) was used throughout the whole measurements capable to extend the gate to a time interval of this order. Before each calibration run the pedestal values at the 10μs gate were determined by disconnecting the signal cables in order to avoid switching off the HV of the photomultipliers. The difference in the pedestal values determined by disconnecting the cables and switching off the HV is about 10 $ADC\ CH$.. The uranium noise distribution of one photomultiplier measured this way is shown in Fig. 5.1. The mean value of the individual spectra were taken as reference to calculate the calibration constant for each readout channel. The calibration procedure has been done regularly thus monitoring possible drifts. The relative calibration of the 4 modules

Table 5.2: Contents of T7-Beam at the CERN PS as measured with the T60UA Calorimeter

E [GeV]	μ [%]	e [%]	h [%]
3	2.5	39.0	58.5
5	3.2	17.7	79.2
7	3.1	9.5	87.4
8.75	3.3	5.4	91.4

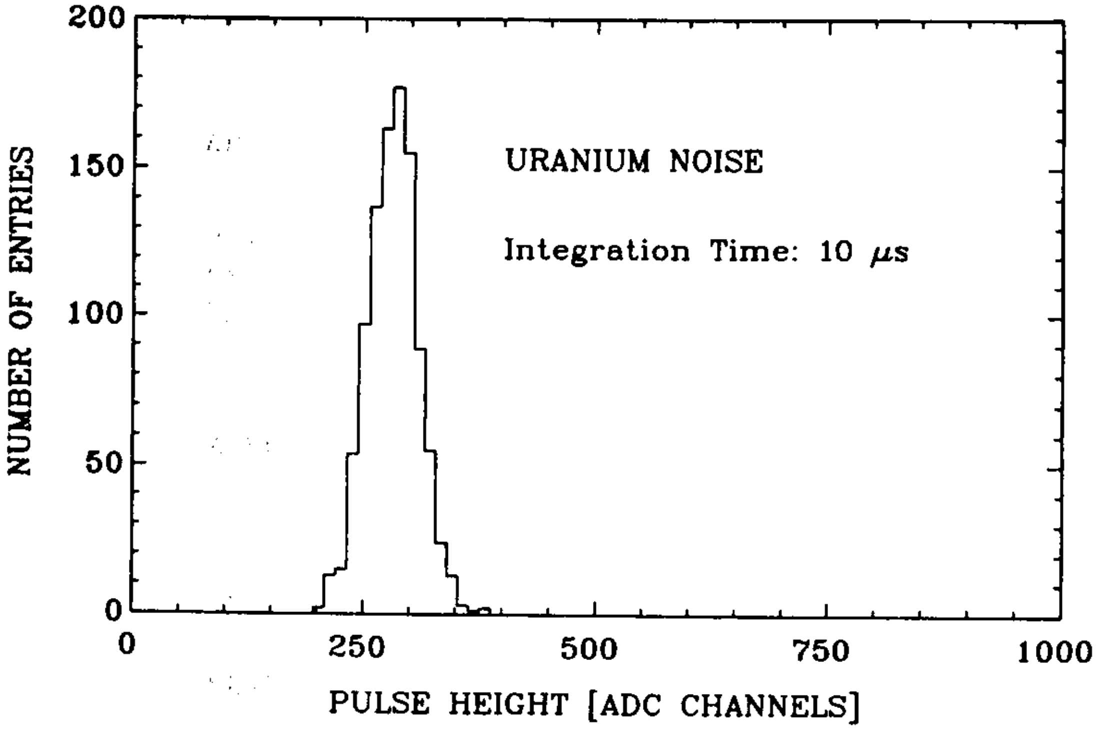

Figure 5.1: Uranium Noise Distribution in one Readout Channel (Photomultiplier), Integrated over 10μs

was checked with the most probable value from the muon spectrum of each module (Fig. 5.2). Deviations from the average of all modules were found to be +0.3% (mod. 1), +7.0% (mod. 2), -6.6% (mod. 3) and -0.7% (mod. 4). No global calibration constant for all strips of each module could be derived because the muons hit only the central strips of the modules.

- Particle Selection
  the particle selection was done in the same manner as described already for the T60Pb calorimeter (sec. 4.2). The same cuts have been applied including those for pile-up and random triggers.

5.1.3 Transverse and Longitudinal Leakage of Hadronic Energy

Transverse Leakage

The method for determining the transverse leakage was already described in sec. 4.3.1. Applying the same method here results in the amount of transverse leakage listed in Tab. 5.3.

Table 5.3: Transverse Leakage out of the Top and Bottom Side of the Entire T60UA Calorimeter

E [GeV]	top [%]	bottom [%]	top + bottom [%]	total [%]
3	3.24 ± 1.75	1.16 ± 0.59	4.40 ± 1.85	8.80
5	2.57 ± 1.06	1.40 ± 0.54	3.97 ± 1.19	7.94
7	2.03 ± 0.68	1.46 ± 0.45	3.49 ± 0.81	6.98
8.75	1.82 ± 0.55	1.48 ± 0.42	3.30 ± 0.69	6.60

The fraction of transverse leakage slightly decreases with increasing beam energy in that energy range; the same is true if one applies a cut against longitudinal leakage of 10% of the total energy in the last module before estimating the transverse leakage so the decrease is not effected by longitudinal leakage.

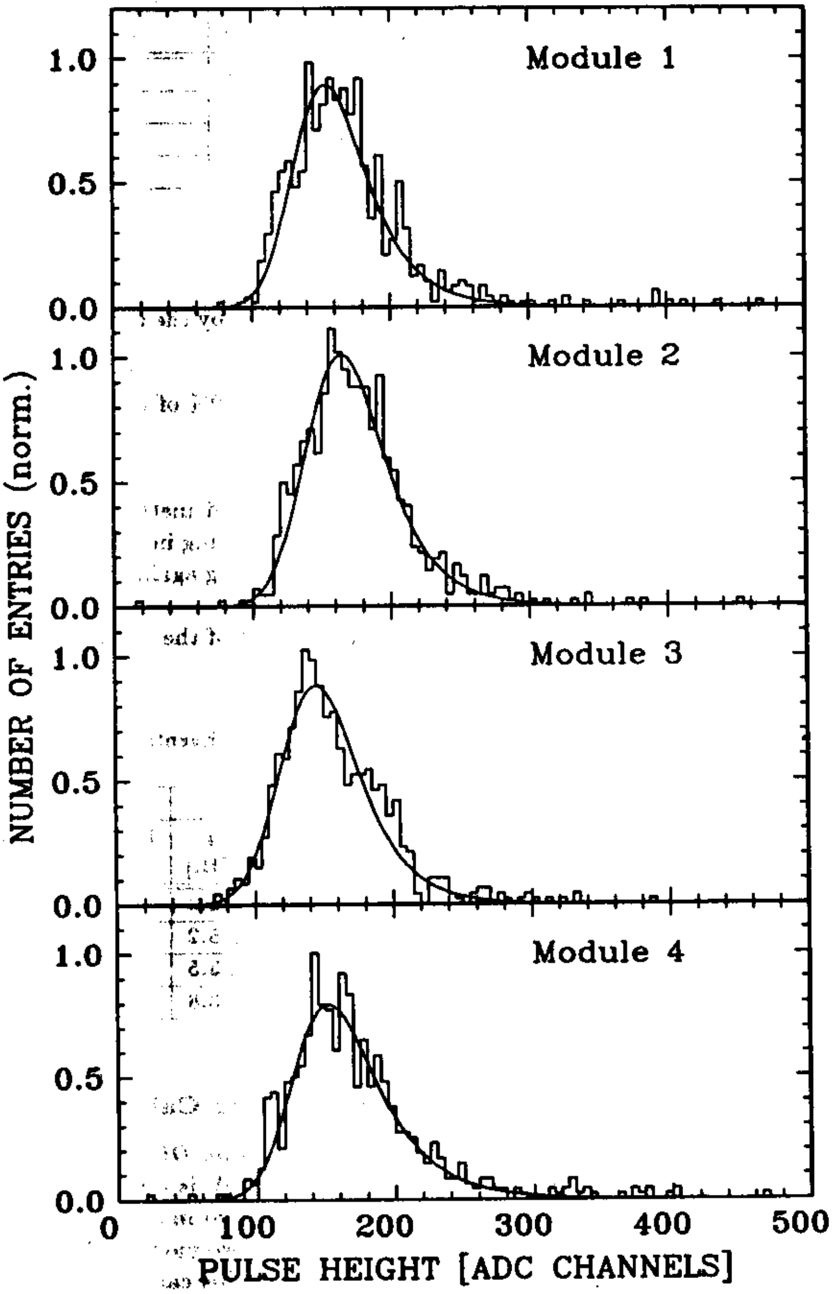

Figure 5.2: Muon-Response at 5 GeV in each of the four T60UA Calorimeter Modules

The correction for the transverse leakage from the top and bottom side (see sec. 4.3.1) enhances the mean pulse heights by simultaneously narrowing slightly the width of the distribution (Tab. 5.4).

Table 5.4: Corrected Hadronic Response on an Event-by-Event Basis for Transverse Leakage out of the Top and Bottom Side of the T60UA Calorimeter

	without Trans. Leak. Corr.		with Trans. Leak. Corr.		
E [GeV]	$< PH(h)_{1-4} >$ [ADC CH.]	$\sigma(h)_{1-4}$ [ADC CH.]	$< PH(h)_{1-4} >$ [ADC CH.]	$\sigma(h)_{1-4}$ [ADC CH.]	$\frac{\Delta < PH(h)_{1-4} >}{< PH(h)_{1-4}^{without\ TLC} >}$ [%]
3	1079.6 ± 3.6	228.1 ± 2.8	1120.3 ± 3.5	225.8 ± 2.7	3.77 ± 0.46
5	1749.5 ± 6.4	309.6 ± 5.0	1812.7 ± 6.4	312.2 ± 5.1	3.61 ± 0.52
7	2460.5 ± 4.3	383.8 ± 3.3	2538.1 ± 4.3	384.3 ± 3.3	3.16 ± 0.25
8.75	3039.5 ± 4.8	425.1 ± 3.6	3131.2 ± 4.8	423.1 ± 3.6	3.02 ± 0.22

Longitudinal Leakage

The longitudinal leakage of the T60UA calorimeter has been investigated by the two methods described in sec. 4.3.2, i.e.

1. a cut against events with an energy deposition in module 4 of $\geq 10\%$ of the total energy and
2. selection of events with the shower vertex within the first module.

Again, the effect of the longitudinal nonuniformity makes the second method less applicable for the treatment of longitudinal leakage: the maximum of the showers starting in module 1 coincidences with the step from a maximum to a minimum of light output deteriorating again the energy resolution that primarly improves if longitudinal leakage is absent.

Thus the first method has been applied leading to the improvement of the energy resolution given in Tab. 5.5.

Table 5.5: Effect of the Longitudinal Leakage Cut which rejected Hadronic Events that deposited 10% or more of the Total Energy in Module 4 of the T60UA Calorimeter

	without Long. Leak. Cut		with Long. Leak. Cut		
E [GeV]	$< PH(h)_{1-4} >$ [ADC CH.]	$\sigma(h)_{1-4}$ [ADC CH.]	$< PH(h)_{1-4} >$ [ADC CH.]	$\sigma(h)_{1-4}$ [ADC CH.]	Event Rejection [%]
3	1079.6 ± 3.6	228.1 ± 2.8	1069.1 ± 3.7	223.0 ± 2.9	10.7
5	1749.5 ± 6.4	309.6 ± 5.0	1741.6 ± 6.8	303.4 ± 5.2	14.6
7	2460.5 ± 4.3	383.8 ± 3.3	2458.6 ± 4.6	373.6 ± 3.5	17.4
8.75	3039.5 ± 4.8	425.1 ± 3.6	3045.3 ± 5.1	409.8 ± 3.8	18.9

5.1.4 Energy Resolution of the T60 Uranium-Scintillator Calorimeter

The electron and hadron response of the T60UA calorimeter with $3.2\,mm$ DU and $5\,mm$ Scintillator plates at 3, 5, 7 and 8.75 GeV together with the muon response at 5 GeV is illustrated in Fig. 5.3.

The electron response is the sum of the pulse heights in the first two modules in order to avoid contributions from pedestal fluctuations and uranium noise of the last two modules. The effect on the mean pulse height is negligible while the energy resolution improves. This can be seen from Tab. 5.6 where the relative deviations of the mean pulse heights and the energy resolution for electrons are given if the sum of module 1 to 2 and the sum of module 1 to 4 is considered. For hadrons the pulse heights of all four modules were added, corrected for the transverse (top and bottom) and longitudinal leakage ($\leq 0.1\,E_{tot}$ in Module 4).

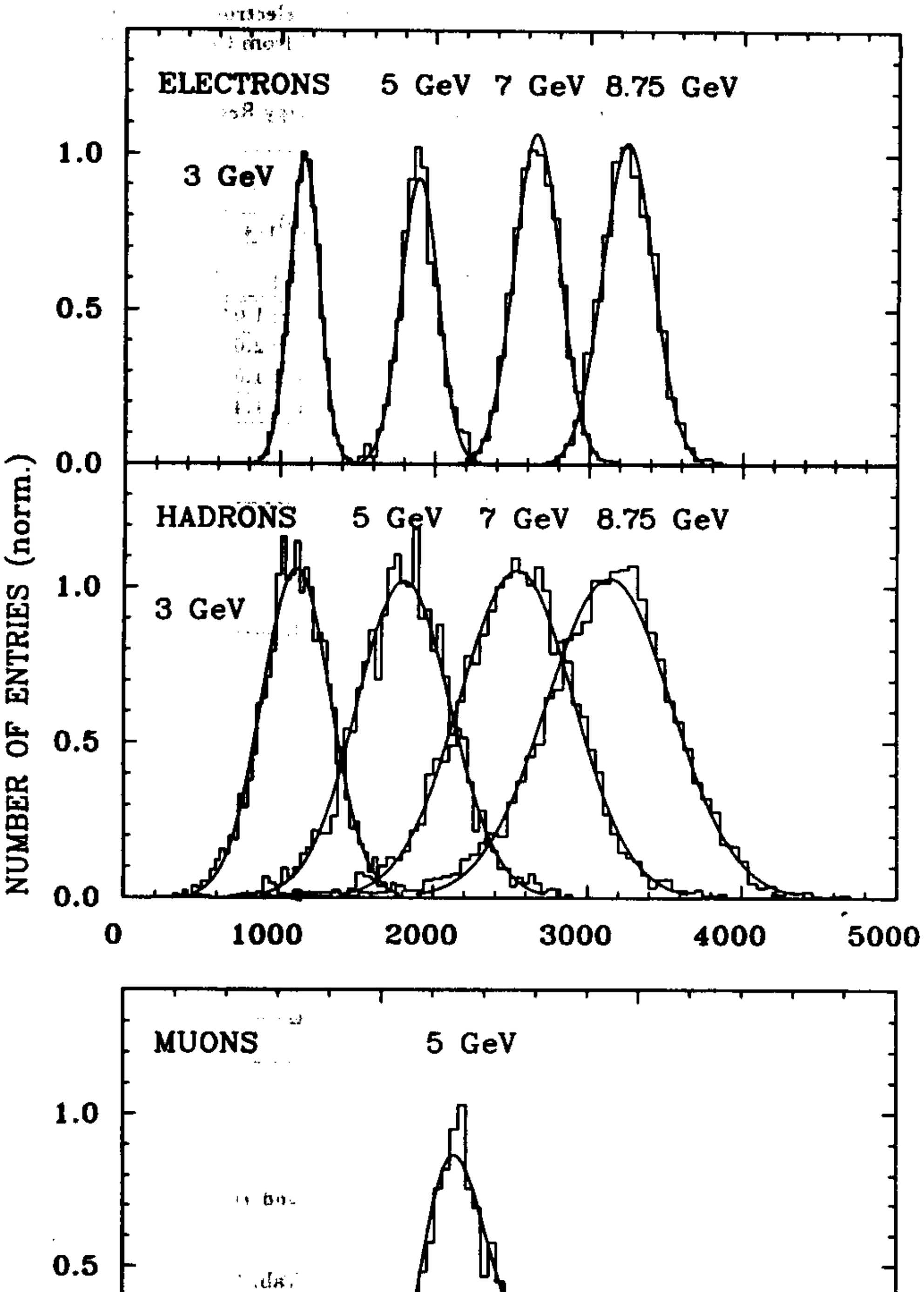

Figure 5.3: Electron-, Hadron- and Muon-Response of the T60UA Calorimeter at Different Energies

The curves shown in Fig. 5.3 are gaussian fits with a cut of $\pm 3\sigma$ for electrons and hadrons and a fit of a Moyal-Gauss convolution for muons. The mean values obtained from the fits on the electron and hadron distributions as well as the energy resolutions are listed in Tab. 5.7.

Table 5.6: Relative Deviation in [%] of the Mean Pulse Height and the Energy Resolution for Electrons if the Sum of Module 1 and 2 is considered instead of Module 1 to 4

E [GeV]	$\frac{<PH(e)_{1-2}> - <PH(e)_{1-4}>}{<PH(e)_{1-4}>}$ [%]	$\frac{\frac{\sigma_E(e)_{1-2}}{E} - \frac{\sigma_E(e)_{1-4}}{E}}{\frac{\sigma_E(e)_{1-4}}{E}}$ [%]
3	-0.29 ± 0.12	-2.87 ± 1.04
5	$+0.19 \pm 0.22$	-2.24 ± 2.64
7	-0.22 ± 0.08	-1.91 ± 1.03
8.75	$+0.10 \pm 0.11$	-1.31 ± 1.48

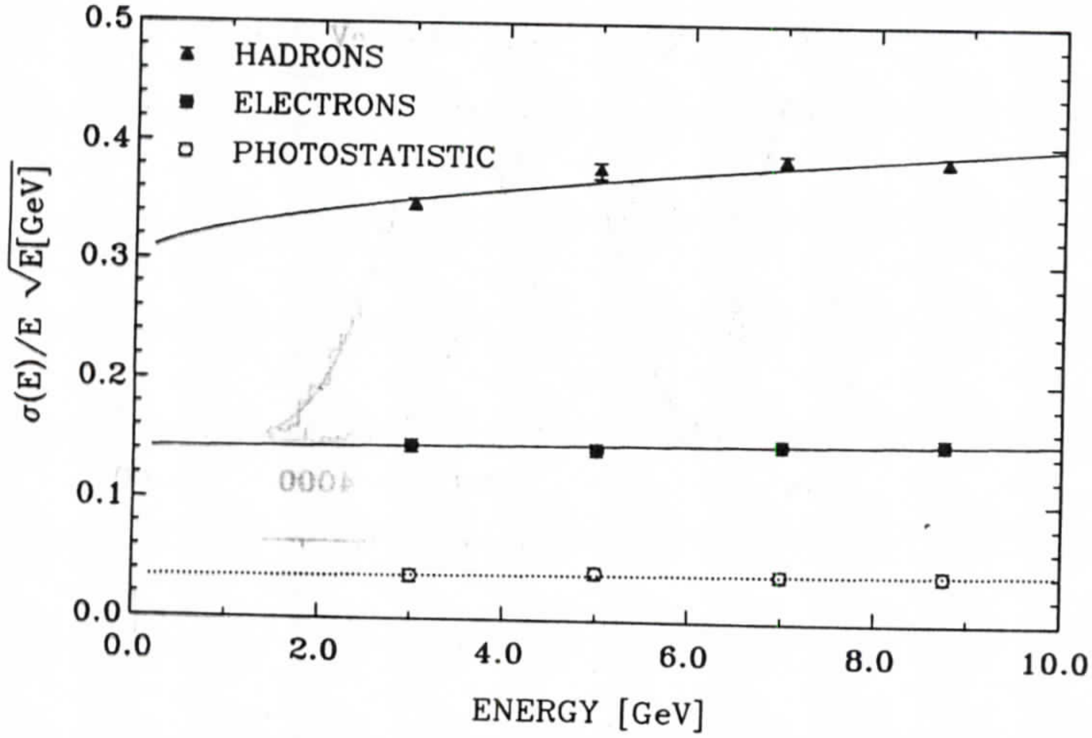

Figure 5.4: Energy Resolution of the T60UA Calorimeter for Electrons and Hadrons as a Function of Energy and the Contribution from Photostatistics

The values for the energy resolution are plotted as a function of energy in Fig. 5.4. The parametrization eq. 4.4 was fitted to the electron data with the result as follows:

$$\begin{aligned} a &= 14.2\% \pm 0.6\% \\ b &= 1.6\% \pm 0.4\%. \end{aligned} \tag{5.1}$$

For hadrons the parametrization eq. 4.6 was used, yielding

$$\begin{aligned} a &= 29.6\% \pm 1.2\% \\ b &= 3.2\% \pm 0.5\%. \end{aligned} \tag{5.2}$$

Table 5.7: Mean Response and Energy Resolutions of the T60UA Calorimeter for Electrons and Hadrons at 3, 5, 7 and 8.75 GeV

	ELECTRONS		HADRONS	
E [GeV]	$< PH(e)_{1-2} >$ [ADC CH.]	$\frac{\sigma_E(e)_{1-2}}{\sqrt{E[GeV]}}$ [%]	$< PH(h)_{1-4} >$ [ADC CH.]	$\frac{\sigma_E(h)_{1-4}}{\sqrt{E[GeV]}}$ [%]
3	1150.1 ± 1.4	14.5 ± 0.2	1110.8 ± 3.7	34.7 ± 0.5
5	1893.3 ± 4.2	14.3 ± 0.4	1806.0 ± 6.8	37.7 ± 0.7
7	2654.2 ± 2.2	14.8 ± 0.2	2537.0 ± 4.5	38.6 ± 0.4
8.75	3246.2 ± 3.6	15.0 ± 0.2	3136.8 ± 5.1	38.5 ± 0.4

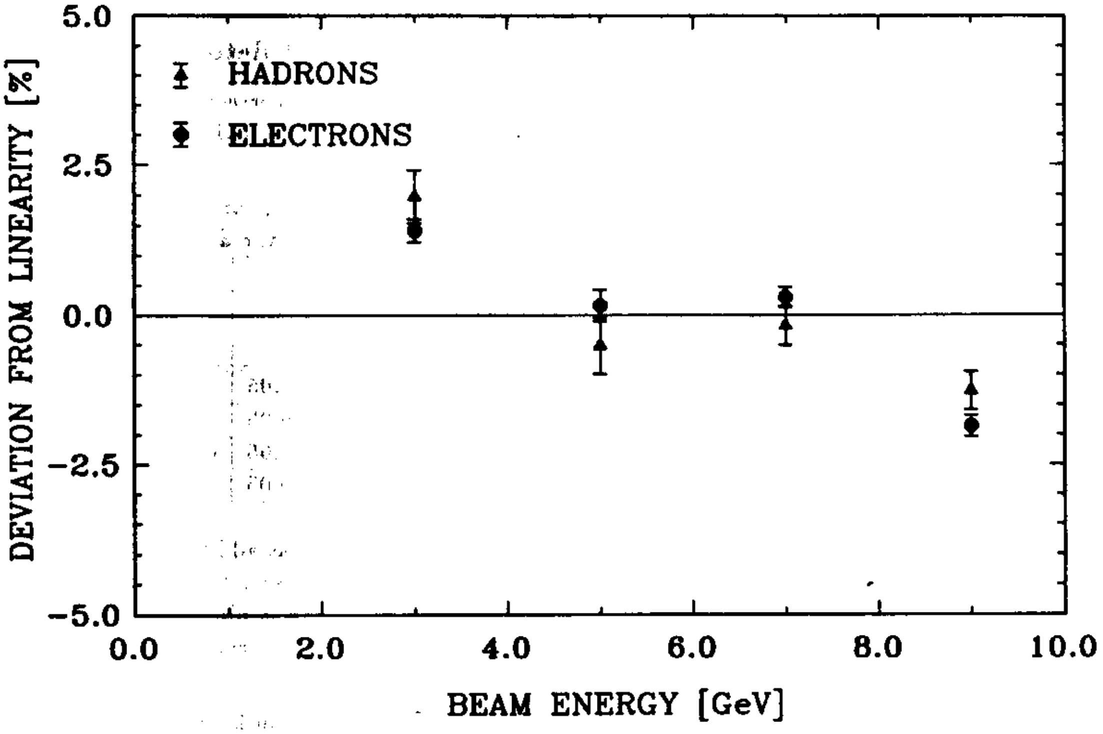

Figure 5.5: Deviation from Linearity in [%] for Electrons and Hadrons in the T60UA Calorimeter

The estimated error given for parameter a of 4% is mainly due to calibration uncertainties, the error on the additive constant is obtained from the fit. For electrons the value for b of 1.6% is caused by the beam momentum spread of $\frac{\Delta p}{p} = 1\%$ and due to imperfect light readout. In the case of hadrons the constant term of 3.2% reflects the fact that the intrinsic e/h-ratio is not equal to 1.

The contribution from photoelectron statistics to the total energy resolution shown in Fig. 5.4 has been determined from the difference signal due to electrons of the left and right photomultipliers (eq. 4.11). The obtained result is:

$$\frac{\sigma_{L-R}}{< PH_{L+R} >}(e) = \frac{(3.42 \pm 0.05)\%}{\sqrt{E[GeV]}} \oplus (0.71 \pm 0.04)\%. \qquad (5.3)$$

According to EGS4 calculations the sampling fluctuations are:

$$\frac{\sigma_s(e)}{E} = \frac{(14.5 \pm 0.2)\%}{\sqrt{E[GeV]}}. \qquad (5.4)$$

Using eq. 4.11 the average number of photoelectrons per GeV of incident energy in the T60UA calorimeter has been determined to $< N_{pe} > = 820 \pm 27$. With the electromagnetic sampling fraction of $\hat{e} = 7.31\%$ calculated with EGS4 this corresponds to 11 photoelectrons per MeV of visible electromagnetic shower energy, which can be compared with the same yield obtained with the T60Pb calorimeter. Summing eq. 5.3 and eq. 5.4 quadratically yields:

$$\frac{\sigma_t(e)}{E} = \frac{(14.92 \pm 0.23)\%}{\sqrt{E[GeV]}} \oplus (0.71 \pm 0.04)\%, \tag{5.5}$$

in good agreement with the measured energy resolution for electrons (eq. 5.1).

The response of the calorimeter is linear within ± 2% for both electrons and hadrons. Fig. 5.5 shows the deviation from the mean linearity.

5.1.5 The e/h- and $\hat{e}/\widetilde{mip}$-Ratio of the T60 Uranium-Scintillator Calorimeter

The calculation of the e/h- and $\hat{e}/\widetilde{mip}$-ratio has been performed with the corrected values of electron and hadron responses. The correction for longitudinal nonuniformity as described in sec. 4.5.4 was applied to both electrons and hadrons. The averaged hadron response was additionally corrected for transverse leakage out of the left and right sides of the calorimeter (see sec. 4.3.1). The results are given in Tab. 5.8. The e/h- and the $\hat{e}/\widetilde{mip}$-ratio as a function of energy is plotted in Fig. 5.6. The errors have been determined in the same way as for the T60Pb calorimeter (sec. 4.6).

Table 5.8: Electron-, Muon- and Hadron-Response of the T60UA Calorimeter, corrected for Longitudinal Nonuniformity (e, h) and for Leakage (h), and the resulting e/h- and $\hat{e}/\widetilde{mip}$-ratio at 3, 5, 7 and 8.75 GeV

E [GeV]	e [ADC CH.]	h [ADC CH.]	μ [ADC CH.]	$\frac{e}{h}$	$\frac{\hat{e}}{\widetilde{mip}}$
3	1274.3 ± 13.8	1162.1 ± 42.9	155.7 ± 6.1	1.10 ± 0.05	0.71 ± 0.03
5	2089.8 ± 24.4	1880.8 ± 64.2	166.2 ± 7.8	1.11 ± 0.05	0.68 ± 0.04
7	2920.9 ± 30.9	2629.2 ± 86.3	170.0 ± 8.6	1.11 ± 0.05	0.68 ± 0.04
8.75	3565.4 ± 37.7	3244.1 ± 105.5	174.3 ± 10.1	1.10 ± 0.05	0.66 ± 0.04

Table 5.9: Electromagnetic Sampling Fraction from the Measurement and from EGS4 Simulations for the T60UA Calorimeter

E	$\hat{e}$ [%]	
[GeV]	measured	EGS4
3	9.57 ± 0.42	7.31 ± 0.02
5	9.19 ± 0.47	7.32 ± 0.03
7	9.18 ± 0.50	7.30 ± 0.01
8.75	8.87 ± 0.55	7.29 ± 0.01

Tab. 5.9 gives the measured and simulated (EGS4) electromagnetic sampling fractions, showing that the agreement is not as good as in the case of the lead calorimeter with the same scintillator thickness. The cut-off energies for electrons and photons were chosen to $E_C = 1000\,keV$ and $P_C = 10\,keV$. The simulation was repeated for 5 GeV with much lower cut-off values, namely $E_C = 10\,keV$ and $P_C = 1\,keV$; furthermore, the fractional energy loss per step was set to 0.5% in high-Z and 0.1% in low-Z materials. Because of the CPU-time consumption for the calculations the statistics is very low (10 events). The result of $\hat{e} = 8.05\%$ is much closer to the measured value, but still with a deviation of about 10%. Because of the dependence of the calculated electromagnetic sampling fraction on the cut-off energies and on the fractional energy loss per step one can not say what causes the discrepancy between the measured and calculated electromagnetic sampling fraction.

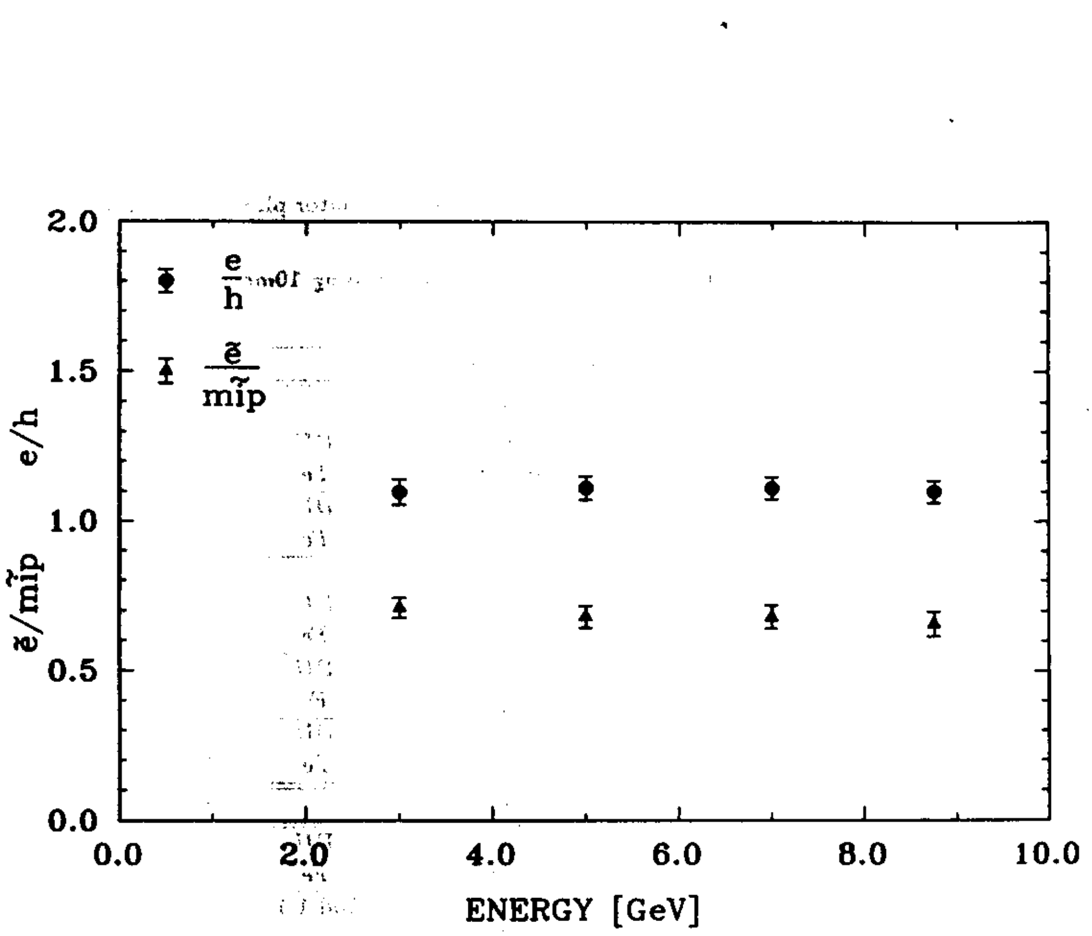

Figure 5.6: e/h- and $\tilde{e}/\widetilde{mip}$-Ratio of the T60UA Calorimeter as a Function of the Energy

The conclusion to be drawn from this measurement is that depleted uranium as passive absorber in a hadron calorimeter together with scintillator plates as active aborbers improve the hadronic energy resolution compared to a lead calorimeter of similar thicknesses of the passive and active absorber plates. However, the influence of those thicknesses on the energy resolution and the e/h-ratio had still to be investigated. Therefore the ratio of the scintillator to the uranium plate thickness was varied in the next steps of the measurements.

5.2 Varying Thicknesses

The measurements with the T60 3.2 *mm* DU-5 *mm* scintillator calorimeter described in the previous section showed that a significant improvement in the energy resolution was obtained compared to the T60 4.75 *mm* Pb-5 *mm* scintillator calorimeter. Simultaneously the e/h-ratio changed from ~ 1.35 to ~ 1.10 indicating that both quantities are related and that the material of the passive absorber is one crucial parameter in optimizing the energy resolution of a hadron calorimeter.

Results from the WA78 collaboration [DEV86] from measurements with a DU-scintillator calorimeter show that the e/h-ratio also depends on the thickness of the absorber plates. In the energy range from 135 to 210 *GeV* an e/h-ratio of 0.8 (20×10 *mm* U, 32×15 *mm* U, 48×25 *mm* Fe) and 0.9 (20×5 *mm* U, 32×15 *mm* U, 48×25 *mm* Fe) was measured which shows that the hadronic response can even be tuned to be greater than the electromagnetic one (overcompensation).

To confirm this dependence of the e/h-ratio in a much wider energy range, i.e. 5 to 210 *GeV*, the measurements with the WA78 calorimeter to be described in the next section were carried out.

5.2.1 Description of the WA78 Calorimeter and the Beam Set-Up

The WA78 calorimeter consisted of two sections, the uranium section with 48 plates of depleted uranium (*DU*) and scintillator plates grouped into 12 modules, and the iron part also with 48 elements in 12 modules (Fig. 5.8). The uranium plates, cladded with 1 *mm* steel, were 10 *mm* thick, the thickness of the iron plates was 25 mm; both sections used 5 mm thick scintillator plates (NE 110).

Table 5.10: Dimensions and Specifications of the WA78 Calorimeter using 10mm thick Depleted Uranium and 5mm thick Scintillator Plates

Calorimeter				
Lateral Dimensions	$600 \times 600\,mm^2$			
	$600 \times 600\,mm^2$†	DU	$96.58X_0$	$3.34\lambda_0$
	$600 \times 600\,mm^2$	Fe	$28.67X_0$	$3.11\lambda_0$
Number of Modules	12	DU		
	13	Fe		
Number of Layers per Module	4			
Total Depth of 1 Layer	17 mm	DU	$3.28X_0$	$0.114\lambda_0$
	30 mm	Fe	$1.43X_0$	$0.156\lambda_0$
Total Depth of 1 Module	68 mm	DU	$13.14X_0$	$0.45\lambda_0$
	120 mm	Fe	$5.73X_0$	$0.62\lambda_0$
Total Depth of Calorimeter	816 mm	DU	$157.6X_0$	$5.4\lambda_0$
	1560 mm	Fe	$74.5X_0$	$8.1\lambda_0$
Passive Layer				
Lateral Dimensions	$500 \times 500\,mm^2$	DU		
	$600 \times 600\,mm^2$	Fe		
Thickness of Plates	1 mm Fe	Mod 1-12		
	10 mm DU			
	1 mm Fe			
Total	12 mm		$3.27X_0$	$0.107\lambda_0$
Thickness of Plates	25 mm Fe	Mod 12-24	$1.42X_0$	$0.149\lambda_0$
Material	DU, Fe			
Active Layer				
Dimension of Scintillator	$600 \times 600\,mm^2$			
Thickness of Plates	5 mm		$0.01X_0$	$0.006\lambda_0$
Material	NE 110 (Polyvinyl Toluene Base)			
Readout				
Optical Fibre	Ø1.5mm, ~ 90cm long			
Material	DUPONT Crofon OE-1060			
Number of Fibres per Module	200			
Photomultiplier	Thorn EMI D254A			
Preamplifier	LeCroy VV100 BTB			

† The DU absorber plates are $500 \times 500\,mm^2$, surrounded by a 50 mm Fe-frame

The light generated in 4 scintillator plates was collected in one low-gain photomultiplier by optical fibres; the analog signal of the photomultiplier was amplified by VV100BTB (LeCroy) preamplifiers. FERA 4300 Analog Digital Converters (LeCroy), current integrating with a dynamic range of 11 bits with a gain of 4 counts/pC ± 3%, recorded and digitized the signals that have been split in order to measure with two gate length, namely 45 ns and 75 ns.

Tab. 5.10 shows the specifications of the WA78 calorimeter; more details can be found in [CAT87a]. The H3-beam line of the SPS (Super Proton Synchrotron; Ø2200 $m, p \leq 450\,GeV/c$) at CERN (West Area) was used for this measurement. The SPS cycle has a duration of 14.4 s with a flat top over $\sim$ 2.8 s at 450 GeV/c.

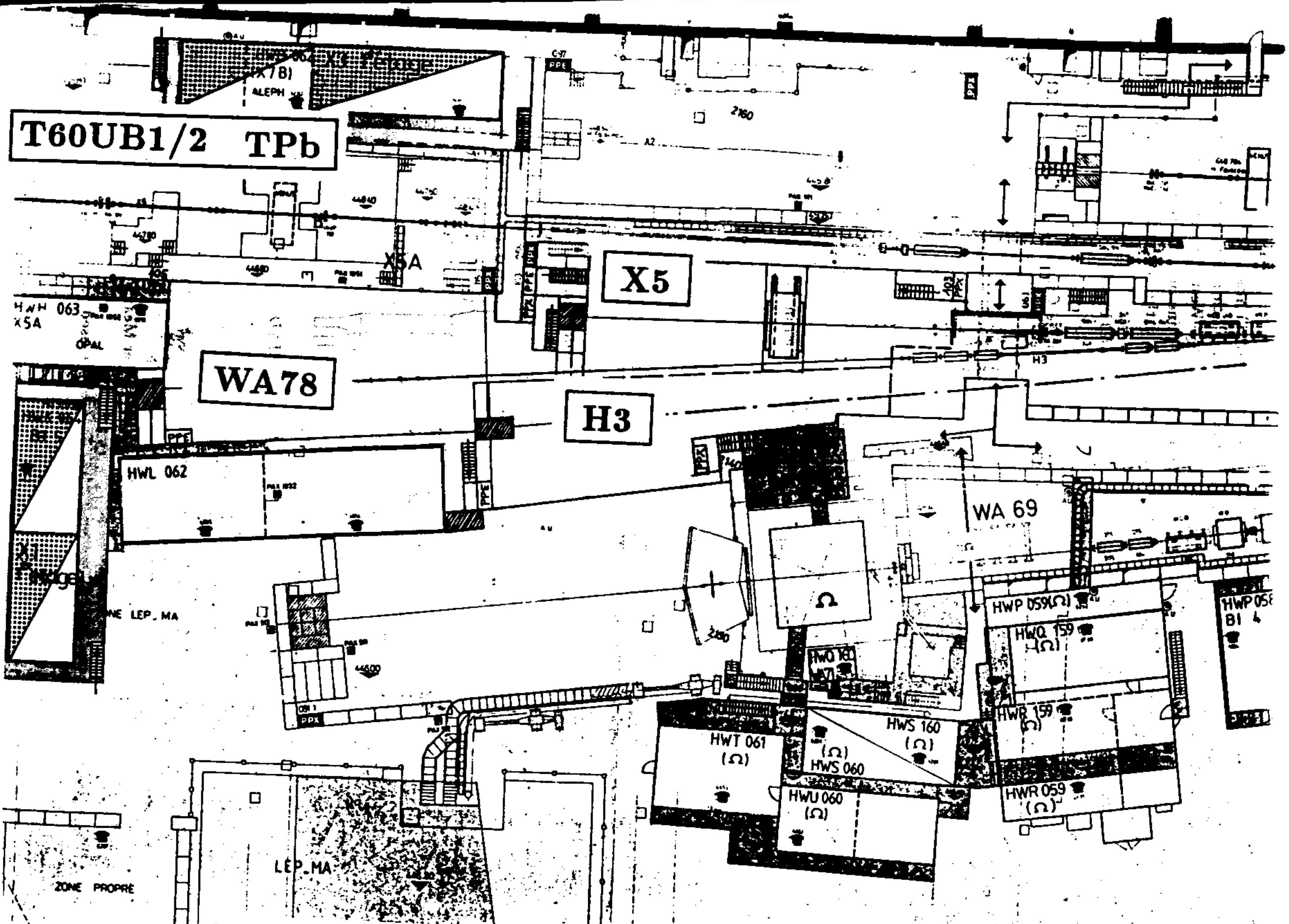

Figure 5.7: Layout of the SPS Beam Lines at the West Area at CERN (WA78, T60UB1/2 and TPb indicate the Place of the Calorimeter Modules in the Beam Line)

On the flat top the slow extracted primary proton beam ($\sim 10^{12}$ protons) hits the target T1 and produces $\sim 10^{11}$ secondary particles per spill of 2.1 s, a small fraction of which is transported along the H3-beam line. Fig. 5.7 gives a schematic layout of the beam lines at the West Area at CERN.

A secondary target was installed for this measurement in the H3-beam line in order to reach low particle momenta. This left only a small range of magnetic bending behind the secondary equipped target resulting in a poor momentum resolution.

The muon, electron and hadron content of the beam is listed in Tab. 5.11 [KRÜ86, CAT87b]. A beam particle trigger had to fulfill the following coincidence condition:

Table 5.11: Contents of H3-Beam at the CERN SPS as determined with the Cherenkov Counter

E [GeV]	μ [%]	e [%]	h [%]
5.1	3.5	52.6	43.9
10.1	3.7	22.4	73.9
20.2	3.9	7.2	88.9
30.3	4.3	4.5	91.2
40.3	3.5	2.7	93.8

$$\mathrm{BEAM} = B_1 \cdot B_2 \cdot \bar{H}_1 \cdot \bar{H}_2 \cdot \bar{A},$$

where B_1, B_2 etc. denote the signals from the scintillator counters sketched in Fig. 5.8.

$\check{C}$	Čerenkov Counter	B_1	Beam Trigger 1
A	Anticounter	B_2	Beam Trigger 2
F	Finger Hodoscope	H_1	Veto Wall 1
AC	Albedo Counter	H_2	Veto Wall 2
EM	Electromagnetic Calorimeter	HAD	Hadronic Calorimeter

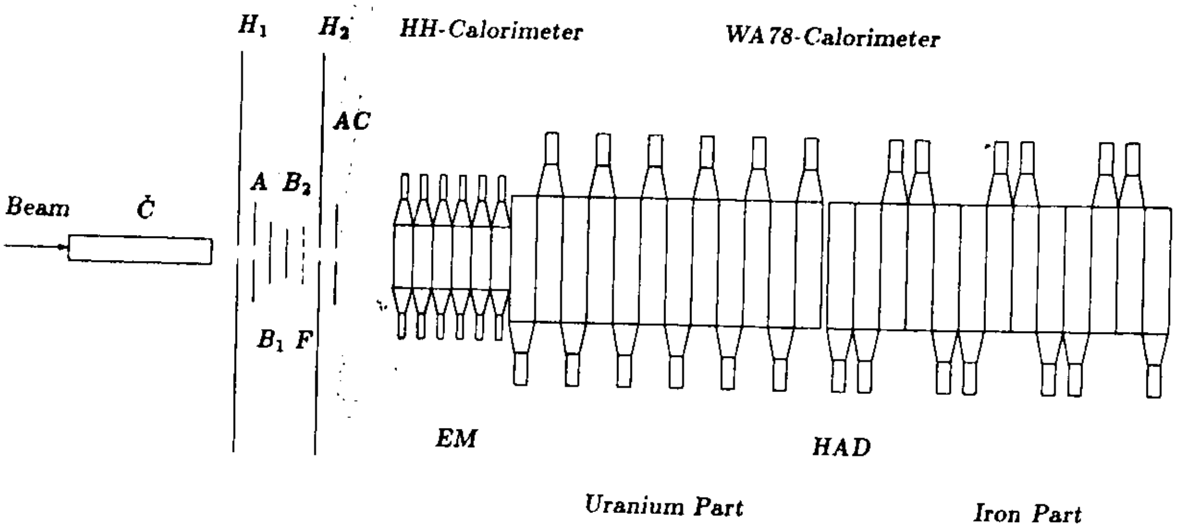

Figure 5.8: Experimental Set-Up of the WA78 Calorimeter Measurement

The 11m long threshold Cerenkov Counter filled with He gas was used for electron and hadron separation.

One module of the WA78 calorimeter is sketched in Fig. 5.9 showing 4 layers of DU-scintillator plates with the fibre connections to 1 photomultiplier; the modules are assembled on two iron rails and can be moved longitudinally.

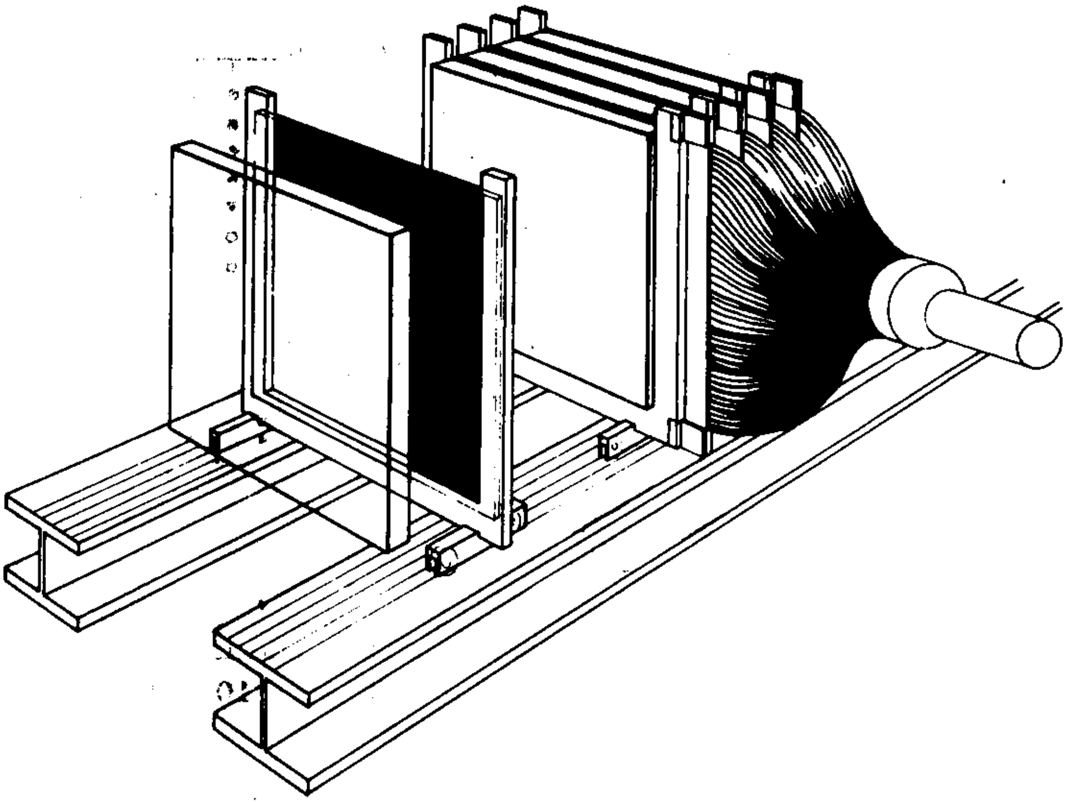

Figure 5.9: Sketch of a WA78 Calorimeter Module

5.2.2 Calibration and Particle Selection

The calibration of the individual photomultipliers has been performed with hadrons according to the method described in [DEV86]. It is based on the assumption that the average longitudinal shower development is independent of the position of the shower vertex. The hadron sample is subdivided into samples of showers with their vertices located in the individual modules. The average shower development in each sample is similar under the given assumption, hence for each sample the mean pulse height of a module can be taken as a reference signal for calibration. The threshold pulse height which defines the position of the shower vertex was determined iteratively by requiring that the number of vertices has to follow an exponential decrease [KRÜ86] (see also sec. 4.3.2).

The mean energy loss of muons was used to check this calibration method, especially for the first module where the signal is influenced by backscattered hadrons. The first module needed a small correction according to the muon signal, for all other modules the agreement was found to be good [KRÜ86].

The two calorimeter sections (DU-SCI, Fe-SCI) were intercalibrated by requiring the same pulse height for a particle completely contained in either the DU-SCI or in the Fe-SCI section.

Electrons and hadrons were identified using the signal of the threshold Cherenkov Counter. Muons were identified from the calorimeter response in a similar manner as described in sec. 4.2 (for details see [KRÜ86]), electrons could be separated from hadrons by a cut in the Cherenkov spectrum.

The combined information from the Cherenkov counter and the calorimeter was used for final particle separation.

5.2.3 Longitudinal Shower Development

The fine longitudinal segmentation of the WA78 calorimeter allowed a precise measurement of the longitudinal development of a hadronic shower. This is not only of general interest for the understanding of hadronic showers but also for the design of hadron calorimeters. The study has been done by [KRÜ86] and is fully described in [KRÜ86, CAT87b]. Here it is restricted to the longitudinal shower distributions which are shown in Fig. 5.10 for events with their shower vertex in the first module. The distribution represents the energy deposition $\frac{dE}{dx}(x)$ of the hadronic showers as a function of the distance x from the shower vertex. It has been parametrized as follows:

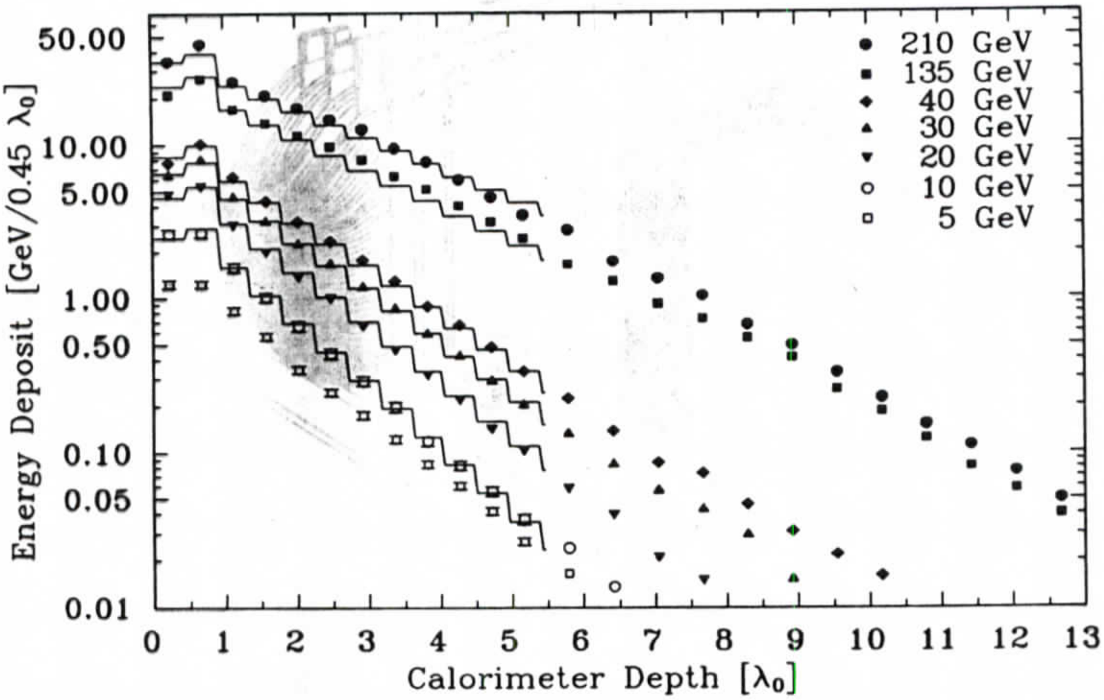

Figure 5.10: Longitudinal Shower Distribution in a Uranium-Scintillator Calorimeter at 5, 10, 20, 30, 40, 135 and 210 GeV for Events with their Shower Vertex in the first Module

$$\frac{dE}{dx}(x) = E\left\{\alpha \frac{b^{a+1}}{\Gamma(a+1)} x^{a} \exp(-bx) + (1-\alpha)\, c \exp(-cx)\right\} \tag{5.6}$$

where:

$E \ldots$ incident energy in $[GeV]$
$\Gamma(a+1) \ldots$ gamma function.

The first term has the form of an electromagnetic shower while the second term describes the exponential behaviour of the shower at large distances from the shower vertex. The parameters a and b were chosen to describe electromagnetic showers in uranium at 20 GeV, where a is a constant and b describes the slope of the electromagnetic shower:

$$\begin{aligned} a &= 3 \\ b[\lambda_0{}^{-1}] &= 19.5. \end{aligned}$$

The description of the data was found to be not very sensitive to those values because of the coarse

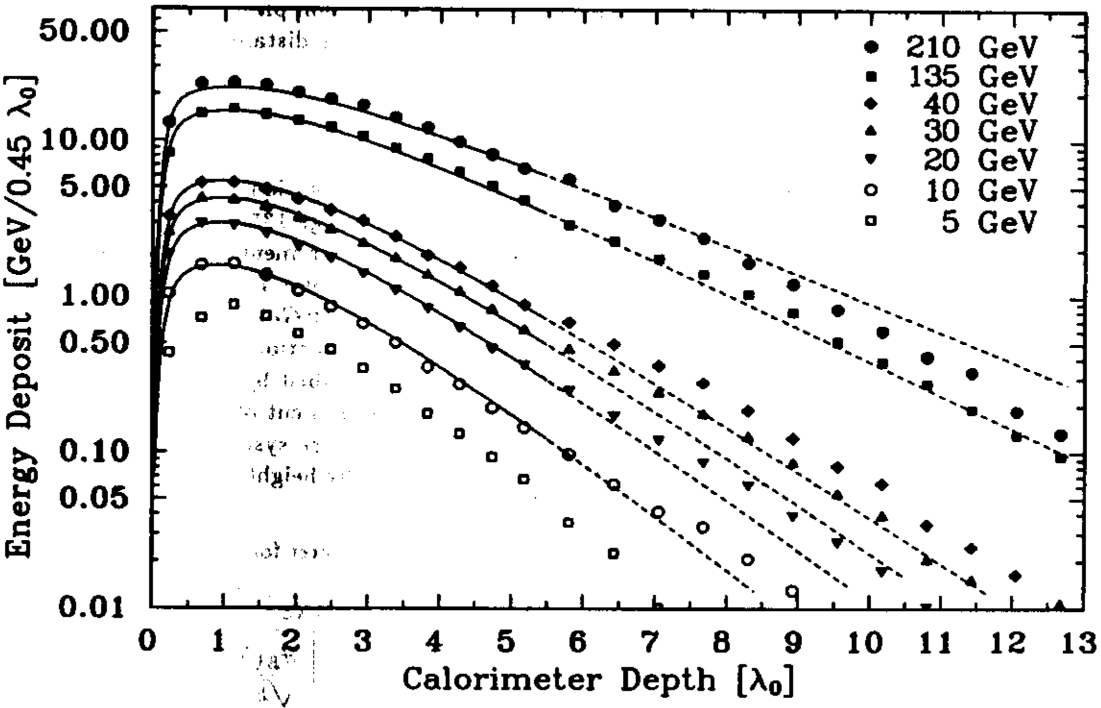

Figure 5.11: Longitudinal Shower Distribution in a Uranium-Scintillator Calorimeter for 5, 10, 20, 30, 40, 135 and 210 GeV for all Events

longitudinal segmentation with respect to the electromagnetic shower development. The remaining parameters α and c have been obtained by fitting eq. 5.6 to the distributions of the events with their shower vertex in the first module. This resulted in the follwing values:

$$\begin{aligned}
\alpha &= 0.13 \pm 0.02 \\
c[\lambda_0{}^{-1}] &= c_1 + c_2 \ln \frac{E\,[GeV]}{50} \\
c_1[\lambda_0{}^{-1}] &= 0.67 \pm 0.03 \\
c_2[\lambda_0{}^{-1}] &= -0.166 \pm 0.003.
\end{aligned}$$

The parameter α is related to the electromagnetic fraction of the hadronic shower while c describes the slope of the hadronic component.

In Fig. 5.11 the shower distributions for all events in the energy range 5 to 210 GeV are shown. Taking the obtained parameter values given above, the phenomenological function eq. 5.7 was deduced to parametrize the data:

$$\frac{dE}{dt} = \frac{1}{\lambda_\pi} \int_0^t \exp\left(-\frac{x}{\lambda_\pi}\right) \frac{dE}{dx}\,(t-x)\,dx \qquad (5.7)$$

with:

$\lambda_\pi[\lambda_0]\ldots$ interaction length of the incoming hadrons in units of the nuclear interaction length λ_0 of protons; $\lambda_\pi = 1.11$.

It describes the shower distributions for all particles (without vertex selection) measured from the front end t of the calorimeter. The exponential decrease of the interaction probability is convoluted with eq. 5.6, i.e. with the energy deposition of hadronic showers along the distance x from the shower vertex.

5.2.4 Energy Resolution of the WA78 Calorimeter

The emphasise on this measurements was to extend the previous investigations of the WA78 collaboration performed with the uranium calorimeter in the high energy range 135 to 350 GeV [DEV86] to lower energies [CAT87b]. In this section the results from the measurements at low energies are discussed; they will be compared with the ones at higher energies in chapter 7.

In Fig. 5.12 the pulse height distributions for electrons, hadrons (5 to 40 GeV) and muons (30 GeV) in the uranium section of the WA78 calorimeter are plotted. A Gauss-function has been fitted to the electron and hadron distribution while the muon data have been described by a convoluted Moyal-Gauss-function. For electrons and hadrons the fits were performed with a cut of $\pm 3\sigma$ resulting in the mean pulse heights and widths listed in Tab. 5.12 [CAT87b]. Quoted are systematic errors of $\pm 5\%$ mainly due to the uncertainty of the calibration [PET86]. The mean pulse height for hadrons have been corrected for longitudinal and transverse leakage. The amount of longitudinal leakage was determined by calculating the fraction of energy on the incident energy deposited beyond a certain calorimeter depth [KRÜ86, CAT87b]. The values given in Tab. 5.13 have been obtained for the fraction of energy deposited beyond the depth of the uranium section (5.4 λ_0). The amount of transverse leakage was estimated to be 3%. This estimation is based on the measurement with the T60UB1/2 calorimeter (Tab. 5.24, 5.22) having comparable lateral dimensions.

Table 5.12: **Mean Response and Energy Resolutions of the WA78 Calorimeter for Electrons and Hadrons at 5, 10, 20, 30, and 40 GeV**

	ELECTRONS		HADRONS	
E [GeV]	$< PH(e)_{1-12} >$ [ADC CH.]	$\frac{\sigma_E(e)_{1-12}}{\sqrt{E[GeV]}}$ [%]	$< PH(h)_{1-12} >$ [ADC CH.]	$\frac{\sigma_E(h)_{1-12}}{\sqrt{E[GeV]}}$ [%]
5.1	176.6 ± 8.8	41.0 ± 2.9	236.8 ± 11.9	53.5 ± 2.7
10.1	337.2 ± 16.9	40.1 ± 2.8	438.9 ± 21.9	55.7 ± 3.9
20.2	638.8 ± 31.9	43.8 ± 3.1	835.5 ± 41.8	61.5 ± 4.3
30.3	955.1 ± 47.8	46.1 ± 3.3	1260.2 ± 62.9	66.6 ± 4.7
40.3	1236.4 ± 63.2	48.8 ± 3.5	1672.4 ± 83.6	70.8 ± 5.0

Table 5.13: **Fraction of Hadronic Energy Deposited beyond the Uranium Section (5.4 λ_0) of the WA78 Calorimeter (Longitudinal Leakage)**

E [GeV]	Longitudinal Leakage [%]
5.1	1.86
10.1	2.89
20.2	4.05
30.3	5.22
40.3	5.91

The small amount of magnet bending after the target in which these measurements have been performed provided a poor momentum resolution as mentioned in sec. 5.2.1. Therefore the measured energy resolutions for electrons and hadrons have to be corrected for the contribution of the momentum spread of the beam. Two independent methods are used:

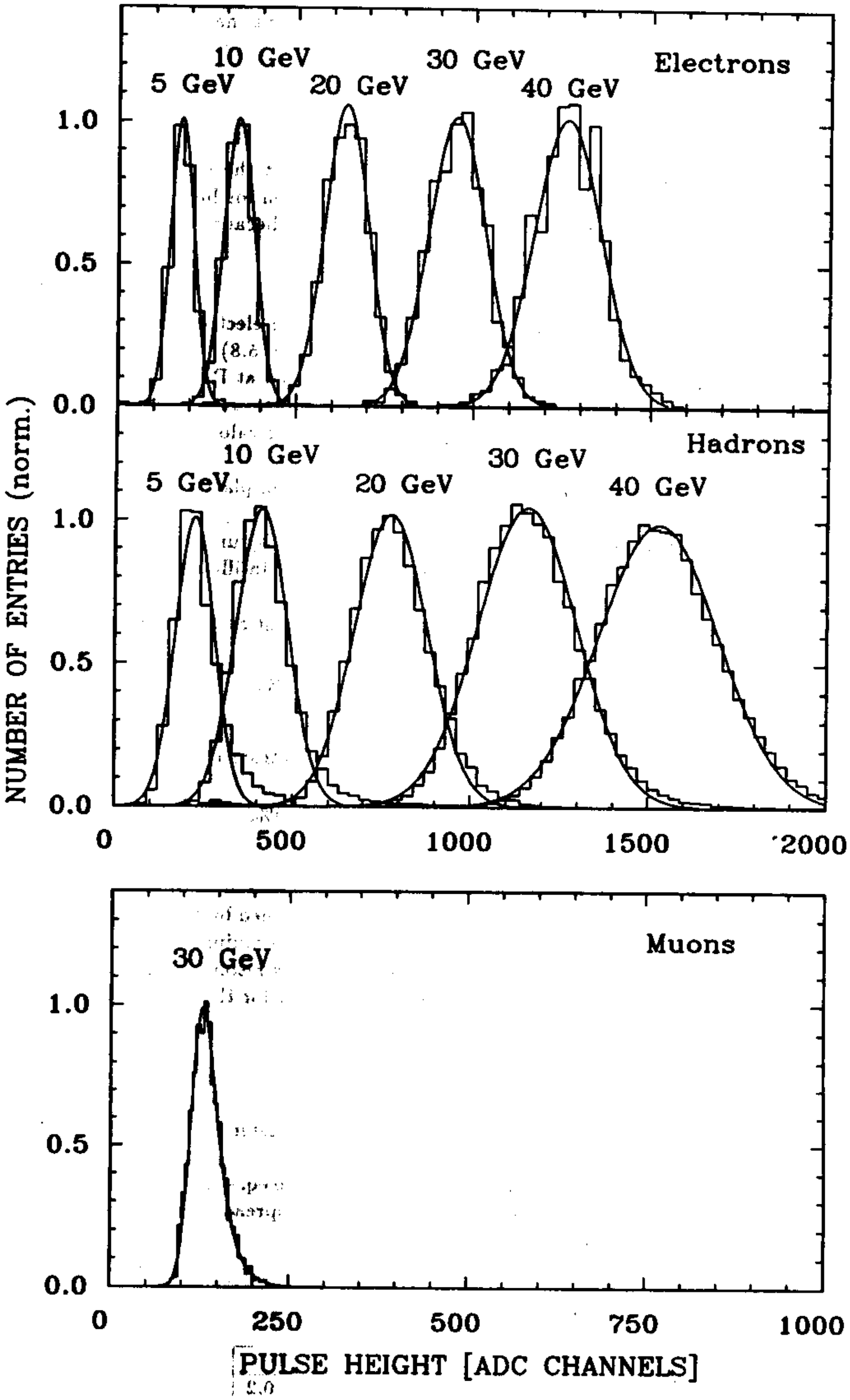

Figure 5.12: Electron-, Hadron- and Muon-Response of the WA78 Calorimeter

1. Method 1:
   From beam optics calculations taking multiple scattering into account the momentum resolution was estimated to be approximately [CAT87b]:
   $$\frac{\sigma(p)}{p} \approx \frac{14\%}{\sqrt{p}} \oplus 7\%. \tag{5.8}$$
   Using this parametrization the values of the momentum spread at the different energies have been subtracted quadratically from the measured energy resolution for hadrons. However, the estimation is not very precise; it can not be applied for electrons because of the constant term in eq. 5.8 which is larger than the measured one.

2. Method 2:
   A part of this measurement has been performed together with an electromagnetic calorimeter installed in front of the WA78 calorimeter (*HH-Calorimeter* in Fig. 5.8) [GEN87]. This electromagnetic calorimeter has been exposed before to an electron beam at DESY so its well known energy resolution for electrons could be used to determine the momentum spread of the H3-beam line at CERN. For the measurement at DESY the electromagnetic calorimeter was used in the following configuration [GEN87]:
   6 modules, each with $8 \times 3\,mm$ Pb and $9 \times 4\,mm$ *SCSN-38* scintillator plates, enclosed in $2 \times 4\,mm$ Al boxes per module; the total length is 26.8 X_0.
   For the measurment at CERN the lead plates have been replaced by uranium plates:
   6 modules, each with $8 \times 1.57\,mm$ ^{238}U + $1\,mm$ Fe plates, with scintillator and Al enclosure as above, yielding the same total length in X_0.
   The obtained energy resolution for electrons from the measurement at DESY was [GEN87]:
   $$\frac{\sigma_E}{E}(e) = \frac{(9.7 \pm 0.1)\%}{\sqrt{E[GeV]}} \oplus (0.9 \pm 0.3)\%. \tag{5.9}$$
   The measurement at CERN yielded an energy resolution for electrons of:
   $$\frac{\sigma_E}{E}(e) = \frac{(26.0 \pm 0.3)\%}{\sqrt{E[GeV]}} \oplus (4.6 \pm 0.1)\%. \tag{5.10}$$
   In a first approximation the energy resolution for electrons is supposed to be independent of the absorber material because the energy resolution is mainly determined by the sampling frequency which is the same in units of X_0 for the lead and the depleted uranium configuration. Under this consideration the quadratic difference of the measured energy resolution eq. 5.10 and eq. 5.9 gives the measured momentum spread of the H3-beam line used for the measurement with the WA78 calorimeter:
   $$\frac{\sigma_E}{E} = \frac{24.1\%}{\sqrt{E[GeV]}} \oplus 4.53\%. \tag{5.11}$$

In Tab. 5.14 the values of the energy resolutions of the WA78 calorimeter for electrons and hadrons are listed, corrected according to both methods mentioned above.

The parametrization of the measured energy resolution according to eq. 4.4 for electrons and eq. 4.6 for hadrons before and after the corrections for the beam momentum spread yield the following values for the parameter a and the additive constant b:
for electrons:

ELECTRONS	a [%]	b [%]
uncorrected	38.6 ± 1.9	4.6 ± 0.2
Correction Method 2	28.7 ± 1.9	1.9 ± 1.2

and for hadrons:

HADRONS	a [%]	b [%]
uncorrected	43.1 ± 5.6	4.3 ± 1.3
Correction Method 2	37.7 ± 4.8	3.4 ± 1.1

Table 5.14: Energy Resolutions of Electrons and Hadrons at 5, 10, 20, 30, and 40 GeV after two Correction Methods for the Momentum Spread (see text)

	ELECTRONS	HADRONS	
	Method 2	Method 1	Method 2
E [GeV]	$\frac{\sigma_E(e)_{1-12}}{\sqrt{E[GeV]}}$ [%]	$\frac{\sigma_E(h)_{1-12}}{\sqrt{E[GeV]}}$ [%]	$\frac{\sigma_E(h)_{1-12}}{\sqrt{E[GeV]}}$ [%]
5.1	31.6 ± 2.3	49.2 ± 3.5	46.7 ± 3.3
10.1	26.9 ± 1.9	49.1 ± 3.5	47.2 ± 3.3
20.2	30.5 ± 2.2	50.9 ± 3.6	52.8 ± 3.7
30.3	30.5 ± 2.2	52.4 ± 3.7	56.8 ± 4.0
40.3	31.4 ± 2.2	53.3 ± 3.8	60.0 ± 4.2

The measured values of the energy resolution of the WA78 calorimeter for electrons and hadrons are shown in Fig. 5.13 as a function of energy. The values corrected according to method 2 are also shown and the parametrizations eq. 4.4 (electrons) and eq. 4.6 (hadrons) with the obtained parameters a and b given above are fitted to the measured and corrected data.

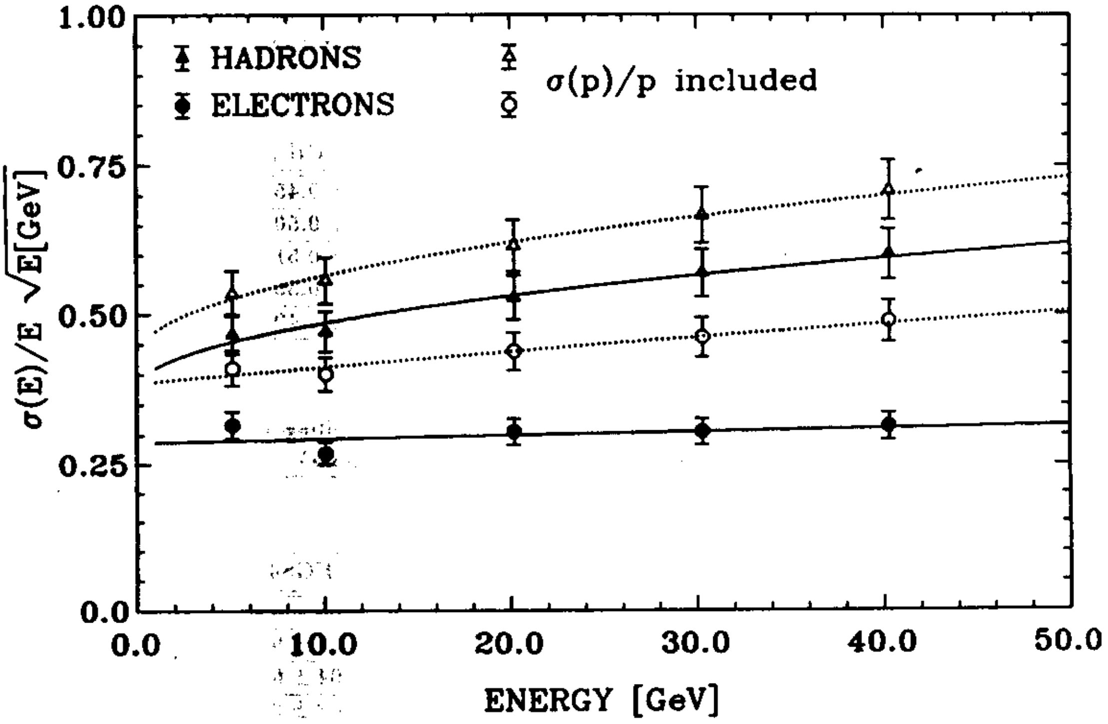

Figure 5.13: Energy Resolution of the WA78 Calorimeter for Electrons and Hadrons as a Function of Energy and the Contribution from Photostatistics; open Circles and dashed Lines: measured Values, full Dots and Lines: Beam Momentum Spread subtracted according to Method 2 (see text)

To measure the contribution from photoelectron statistics to the total energy resolution the light of a LED was distributed to the photomultipliers via optical fibrers. From the width of the measured distribution the number of photoelectrons was determined by using eq. 4.9:

$$\frac{\sigma_{pe}(< N_{pe} >)}{< N_{pe} >} = (10.74 \pm 0.03)\%. \tag{5.12}$$

The average number of photoelectrons per GeV of incoming energy is $< N_{pe} > = 87 \pm 1$, which corresonds to 4.3 photoelectrons per MeV of visible electromagnetic shower energy at an electromagnetic sampling fraction calculated with EGS4 of $\tilde{e} = 2.04\%$.

The contribution from sampling fluctuations to the energy resolution calculated with the EGS4 Monte Carlo is:

$$\frac{\sigma_s(e)}{E} = \frac{(28.9 \pm 1.5)\%}{\sqrt{E[GeV]}}. \tag{5.13}$$

Adding the contribution from photoelectron statistics quadratically to the calculated sampling fluctuations results in a total energy resolution for electrons of 30.8% which is larger than the measured energy resolution for electrons after the correction for the beam momentum spread (method 2). This indicates the uncertainties in the correction for the beam contribution. However, the energy resolution for electrons at 10.1 GeV seems to be too low compared to the values at other energies. This may underestimate the value of the energy resolution obtained from the parametrization.

5.2.5 The e/h- and $\tilde{e}/\widetilde{mip}$-Ratio of the WA78 Calorimeter

For the WA78 calorimeter longitudinal nonuniformities are a minor effect as each scintillator plate is read out by optical fibres and only 4 scintillator plates are read put by one photomultiplier. The transverse nonuniformity due to the absorption length of the scintillator plates is small.

Table 5.15: The e/h- and $\tilde{e}/\widetilde{mip}$-ratio measured with the WA78 Calorimeter at 5, 10, 20, 30 and 40 GeV

E [GeV]	$\frac{e}{h}$	$\frac{\tilde{e}}{\widetilde{mip}}$	μ [ADC CH.]
5.1	0.746 ± 0.053	0.651 ± 0.061	5.91 ± 0.45
10.1	0.768 ± 0.054	0.641 ± 0.064	6.06 ± 0.50
20.2	0.765 ± 0.054	0.627 ± 0.063	6.15 ± 0.51
30.3	0.758 ± 0.054	0.619 ± 0.060	6.37 ± 0.50
40.3	0.755 ± 0.053	0.607 ± 0.056	6.59 ± 0.49

Table 5.16: Values for Ionization Loss of Muons in NE110 and the Resulting Electromagnetic Sampling Fraction of the WA78 Calorimeter (Measured Values and EGS4 Calculations)

E	$\frac{dE}{dx}\Big\|^{ION}(\mu)$ in NE110	$\tilde{e}$ [%]	
[GeV]	$[\frac{MeV\,cm^2}{g}]$	measured	EGS4
5.1	2.3040	2.79 ± 0.26	2.03 ± 0.01
10.1	2.4151	2.75 ± 0.27	2.03 ± 0.01
20.2	2.5274	2.68 ± 0.26	2.04 ± 0.01
30.3	2.5966	2.65 ± 0.25	2.03 ± 0.01
40.3	2.6462	2.60 ± 0.24	2.04 ± 0.01

The measured electron and hadron response can thus be taken directly for the calculation of the e/h-ratios. They are listed in Tab. 5.15. The mean values of the hadron response have been corrected for longitudinal and transverse leakage (sec. 5.2.4). The $\tilde{e}/\widetilde{mip}$-ratios are also given in this table, calculated by using the values for the ionization loss of muons in NE110 scintillator listed in Tab. 5.16. Both ratios are plotted versus energy in Fig. 5.14. The electromagnetic sampling fraction measured

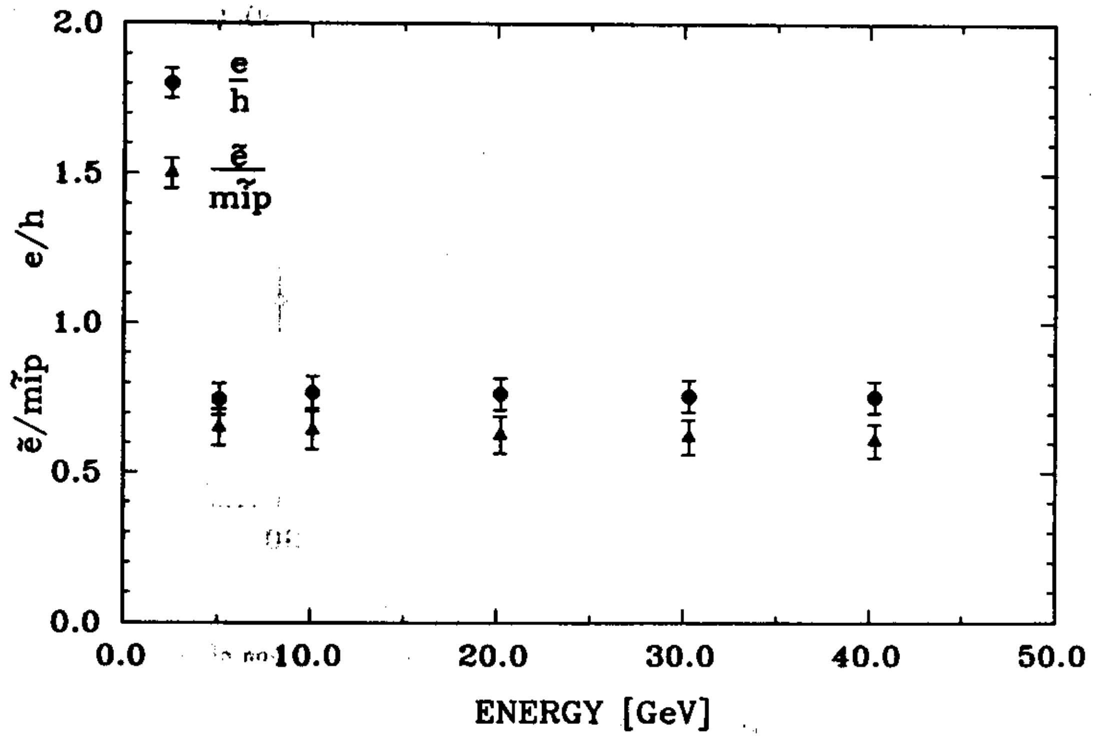

Figure 5.14: e/h- and $\tilde{e}/\widetilde{mip}$-Ratio of the WA78 Calorimeter as a Function of the Energy

with the WA78 calorimeter and calculated with the EGS4 Monte Carlo program for this configuration are compared in Tab. 5.16. The cut-off energies for the simulation had been chosen to 1000 keV for electrons and 10 keV for photons. For 10.1 GeV the simulation has been performed with lower cut-off energies, namely 10 keV for electrons and 1 keV for photons. The fractional energy loss per step has been reduced to 0.1% in the scintillator material and 0.5% in the uranium plates. The obtained value for the electromagnetic sampling fraction is $\tilde{e} = 2.28\%$, which is still lower than the measured value.

The most important result of this measurement is the e/h-ratio: the use of uranium plates 2 times thicker than the scintillator plates enhances the hadron response beyond the electron response. This result has already been found in the high energy region (135 to 350 GeV, [DEV86]) and is now also confirmed at lower energies (5 to 40 GeV).

Dependence of the e/h-ratio on the Gate Time

In sec. 3.3 the different mechanisms contributing to hadronic showers and the time dependence of the energy deposited by neutrons and nuclear γ-rays were discussed. This time dependence was actually measured with the WA78 calorimeter, as can be seen from Fig. 5.15. The e/h-ratio decreases with increasing gate time of the ADC. The effective gate length is smaller by about 15 ns than indicated in the plot because the rising edge of the gate pulse preceeded that of the photomultiplier signal by this time. At integration times $< 100\,ns$ one reduces the signal from the photomultiplier which, after amplification has a typical length of about 100 ns. This effects the electron signal in the same way as the hadron signal so that this effect cancels out in the e/h-ratio. The time dependence of the e/h-ratio is then only due to the increase of the hadronic signal with time.

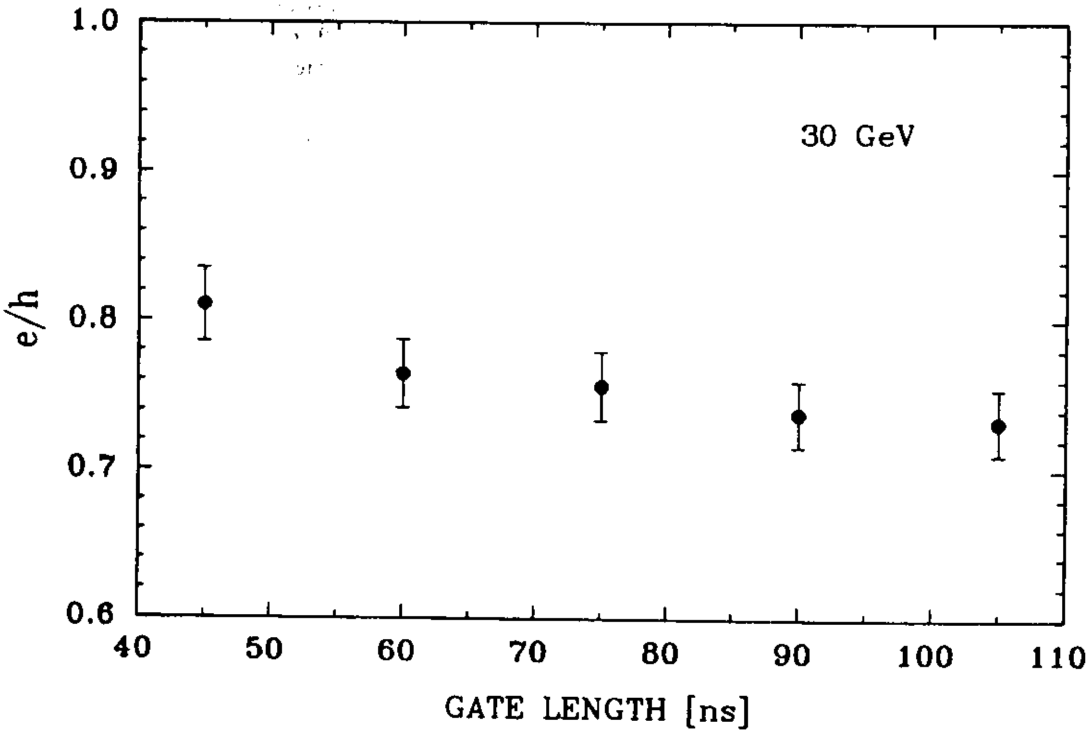

Figure 5.15: The e/h-Ratio of the WA78 Calorimeter at 30 GeV as a Function of the ADC Gate Length

5.3 Achieving Compensation

The measurements described so far together with calculations done by [BRÜ86, WIG86] predicted a thickness ratio of passive to active absorber of $R_d \approx 1.0 - 1.2$ (sec. 3.5) for the optimum energy resolution of a uranium-scintillator calorimeter. In order to confirm this prediction two measurements have been done by the ZEUS collaboration:

1. T35 [AND86]: $R_d = \frac{3.0\,mm\,DU}{2.5\,mm\,SCI} = 1.2$
2. T60B: $R_d = \frac{3.2\,mm\,DU}{3.0\,mm\,SCI} = 1.07$

Results of the first measurements can be found in the reference stated above, in the following the second measurements will be discussed.

5.3.1 The T60B1 Uranium-Scintillator Calorimeter Characteristics

The thin absorber plates proposed to be inserted into the T60 calorimeter modules required some mechanical modifications in order to make air gaps as small as possible and to increase the depth of the calorimeter to reduce longitudinal leakage.

The overall T60UB1 calorimeter consisted of 4 identical modules stacked with 45 layers of 3.2 *mm DU* and 3.0 *mm* scintillator (module 1-3) and 45 layers of 3.0 *mm DU* and 3.0 *mm* scintillator (module 4). One module of the previous measurements, namely 3.2 *mm DU* and 5.0 *mm* scintillator, was followed to measure longitudinal leakage.

Specifications of the calorimeter are given in Tab. 5.17, a top and side view of the fifth module is drawn in Fig. 4.1 which is almost identical to the first 4 modules except that the number of layers and the longitudinal dimensions are different (for specifications see Tab. 5.1).

Additionally, each photomultiplier of module 1-4 was fed by individual high voltages instead of module 5 where a group of 12 photomultipliers was provided with common high voltage.

Table 5.17: Dimensions and Specifications of the T60UB1 Calorimeter inserted with 3.2mm and 3mm thick Depleted Uranium and 3mm thick Scintillator Plates

Calorimeter				
Lateral Dimensions	**600 × 600 mm^2**	**Mod 1-3** **Mod 4**	**$98.51X_0$** **$95.48X_0$**	**$3.32\lambda_0$** **$3.25\lambda_0$**
Number of Modules	**4**			
Number of Layers per Module	**45**			
Total Depth of 1 Layer	**9 mm**	**Mod 1-3** **Mod 4**	**$1.02X_0$** **$0.95X_0$**	**$0.034\lambda_0$** **$0.033\lambda_0$**
Total Depth of 1 Module	**405 mm**	**Mod 1-3** **Mod 4**	**$45.81X_0$** **$42.97X_0$**	**$1.55\lambda_0$** **$1.46\lambda_0$**
Total Depth of Calorimeter	**1620 mm**		**$180.4X_0$**	**$6.1\lambda_0$**
Airgap	**2.8 mm** **3.0 mm**	**Mod 1-3** **Mod 4**		
Passive Layer				
Lateral Dimensions	**600 × 600 mm^2**			
Thickness of Plates	**3.2 mm DU** **3.0 mm DU**	**Mod 1-3** **Mod 4**	**$1.01X_0$** **$0.95X_0$**	**$0.031\lambda_0$** **$0.029\lambda_0$**
Material	**DU:** **0.2% ^{235}U** **99.8% ^{238}U**			
Active Layer				
Dimension of Scintillator Strip	**50 × 600 mm^2**			
Number of Strips	**12**			
Thickness of Plates	**3 mm**		**$0.01X_0$**	**$0.004\lambda_0$**
Material	**SCSN-38 (Polystyrene Base)**			
Readout				
Wavelength Shifter	**50 × 405 mm^2**			
Thickness of WLS	**3 mm**			
Material	**PMMA Base, UV absorbant** **K27 (120 mg/l)**			
Lightguide	**Bent Plexiglass**			
Photomultiplier	**XP 2011**			

The T60UB1 calorimeter was exposed to the X5-beam line of the SPS at CERN (see Fig. 5.7) which is the extended H3-beam after a splitter system (the H3-beam line was already described in sec. 5.2.1). The tertiary low intensity beam ($10^2 - 10^4$ particles) after the secondary target in the X5-beam line consists of electrons, hadrons and muons and covers the momentum region of 10 to 100 GeV/c. Lead, beryllium or copper could be chosen as secondary target material in order to enhance the electron or hadron component in the beam.

Fig. 5.16 shows the experimental set-up. Two 10 m long threshold Cherenkov counters filled with He ($\check{C}_1$) and N_2 ($\check{C}_2$) are used for tagging beam particles. The scintillation counters B_1, B_2, B_4 and B_3 as an anticounter to suppress the beam halo define the beam particles.

Particles have been selected by the following trigger definitions:

$$\begin{aligned} \textbf{Hadrons:} \quad \mathrm{h} &= B_1 \cdot B_2 \cdot \bar{B}_3 \cdot \bar{\check{C}}_1 \cdot \bar{\check{C}}_2 \\ \textbf{Electrons:} \quad \mathrm{e} &= B_1 \cdot B_2 \cdot \bar{B}_3 \cdot \check{C}_1 \cdot \check{C}_2 \\ \textbf{Muons:} \quad \mu &= B_1 \cdot B_2 \cdot \bar{B}_3 \cdot B_4 \end{aligned}$$

At a collimator width of ± 5 mm the event rates per spill at 10 GeV/c were:

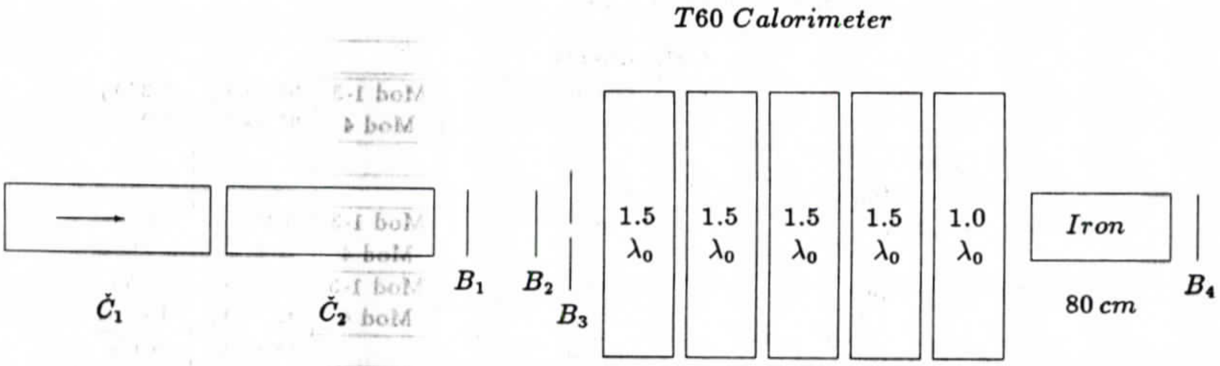

Figure 5.16: **Beam Set-Up for the T60 Measurements at the SPS at CERN**

$B_1 \cdot B_2 = 70$ Cu target
$B_1 \cdot B_2 = 250$ Pb target
$B_1 \cdot B_2 \cdot \bar{B}_3 = 25$ Cu target
$B_1 \cdot B_2 \cdot \bar{B}_3 = 100$ Pb target

The beam content has been determined using the Cherenkov counter efficiencies according to the method described in [KRÜ86]. The values are given in Tab. 5.18.

Table 5.18: **Contents of X5-Beam at the CERN SPS as determined with the Cherenkov Counter**

E [GeV]	μ [%]	e [%]	h [%]	Target
10	29.0	7.3	63.7	Cu
	23.0	29.0	48.3	Be
20	16.2	4.3	79.5	Cu
	9.0	31.4	59.6	Be
30	14.6	3.5	81.8	Cu
50	16.3	2.7	81.0	Cu

5.3.2 Calibration and Particle Selection

Calibration

To calibrate each individual module the procedure used for T60UA (sec. 5.1.2) was applied. A precalibration was already done by adjusting the high voltages of the photomultipliers to give equal average pulse heights for the uranium noise signal in all readout channels. Thus one could follow shifts in the gain by high-voltage readjustments. The mean value of the uranium noise signal was at $\sim$ 300 $ADC\,CH$. with a rms of $\sim$ 25 $ADC\,CH$.. In addition, calibration runs have been taken regularly for a precise offline calibration.

An intercalibration of all 5 modules, individually calibrated with the uranium noise, was tried with hadrons in the same way as the calibration of the WA78 calorimeter has been performed (sec. 5.2.2). For this procedure hadronic events have been selected according to their shower vertices (sec. 4.3.2) leading to 5 subsamples (1 per module) of the total hadronic event sample. With this calibration the hadronic energy resolution was found to be worse than with the uranium noise calibration alone. It seemed that because of the coarse longitudinal segmentation of the T60 calorimeter the information on the longitudinal shower profile was not sufficient.

Because the fourth module of the T60UB1 calorimeter was equipped with thinner uranium plates than module 1-3 the need for an additional calibration was investigated. First of all it was calibrated in the same way as module 1-3 using the uranium noise signal. A calibration with hadrons resulted in a deterioration of the energy resolution, as described above. In its simplest way the thickness ratio of the uranium plates was taken as calibration constant for module 4 because the shower propagates through less denser material with respect to module 1-3. The same effect on the energy resolution for hadrons has been observed, i.e. it became worse than taking the uranium noise calibration only.

The calibration constant of module 4 has then been varied to find a minimum in the relative width of the hadronic response of module 1 to 5. The minimum was found at 1, i.e. for the calibration done with the uranium noise. Therefore, no additional calibration constant was used for module 4.

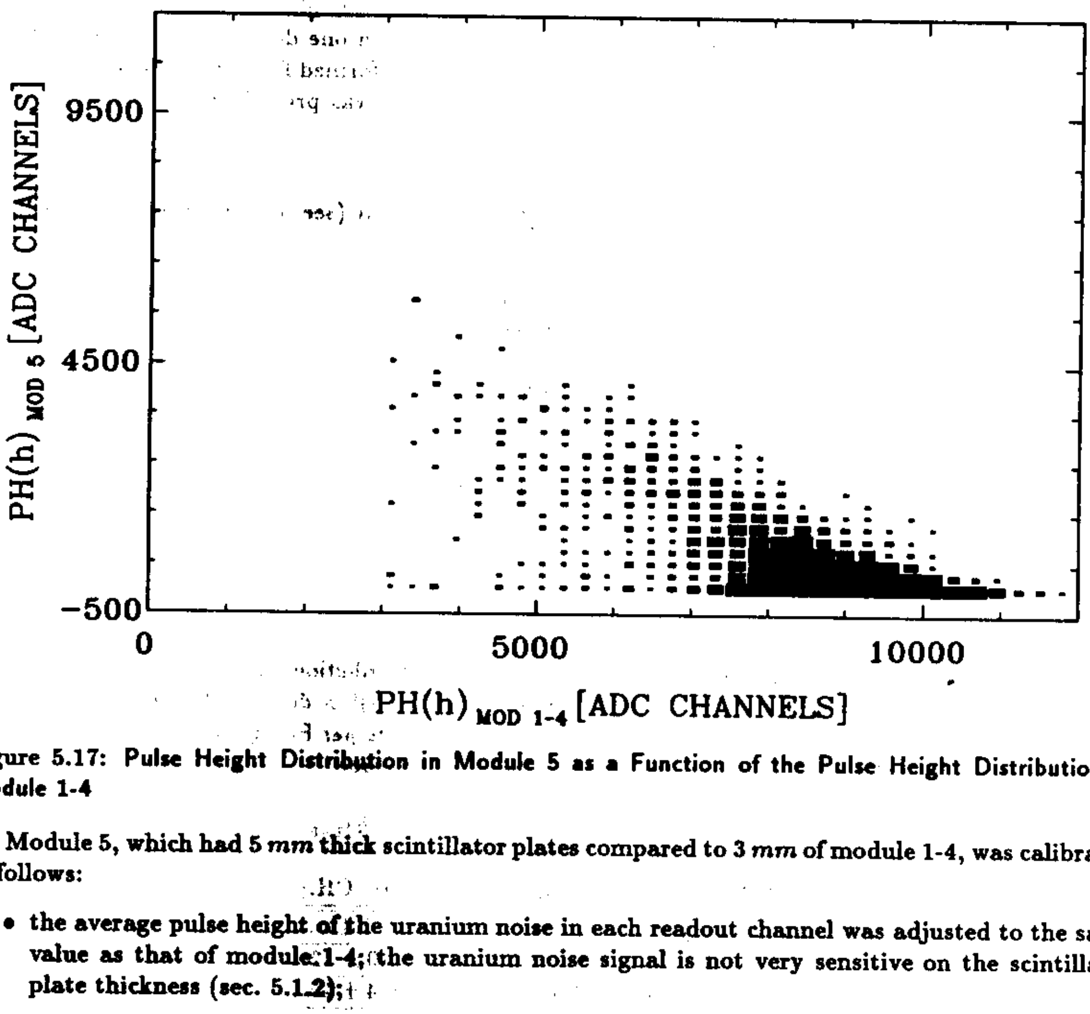

Figure 5.17: Pulse Height Distribution in Module 5 as a Function of the Pulse Height Distribution in Module 1-4

Module 5, which had 5 *mm* thick scintillator plates compared to 3 *mm* of module 1-4, was calibrated as follows:

- the average pulse height of the uranium noise in each readout channel was adjusted to the same value as that of module 1-4; the uranium noise signal is not very sensitive on the scintillator plate thickness (sec. 5.1.2);
- calibrated this way the most probable value of the muon pulse height distributions of module 1-4 was compared to that of module 5; it is expected that the signals of module 1-4 should be 3/5 times the signal of module 5, which was found to be the case:

$$\begin{aligned}\frac{< PH(\mu)_{1-4} >}{< PH(\mu)_5 >} &= \frac{93.4}{152.7} \\ &= 0.61\,;\end{aligned}$$

- the muon calibration is not suited for hadrons because the fraction of energy visible in the detector is different for hadrons and muons. To ensure that module 5 yields the same response for hadrons as module 1 to 4 one has to determine a calibration factor for module 5 using the hadronic signal. Therefore the pulse height distribution of hadrons in module 5 has been plotted versus the sum of the hadronic pulse height distribution of module 1 to 4 (Fig. 5.17). For different intervals in the pulse height distribution of module 5 the corresponding mean pulse height of the distribution in module 1 to 4 has been determined. The values obtained are listed in Tab. 5.20 (second and third column). With decreasing mean pulse height in module 1 to 4 ($< PH(h)_{1-4} >$) the weighted mean pulse height of each interval in the distribution of module 5 ($< PH(h)_5 >$) increases. The sum of both quantities should be constant for all intervals if module 5 is properly calibrated which corresponds to a straight line in the plot $< PH(h)_{1-4} >$ versus $< PH(h)_5 >$ with a slope of 1. In this way one can calibrate module 1-4 relative to module 5. This is shown in Fig. 5.18 where the measured quantity $< PH(h)_{1-4} >$ is plotted versus $< PH(h)_5 >$; the straight line is a fit to the data yielding a slope from which one determines the calibration factor for module 5. The described calibration method was performed for different energies. The obtained values are listed in Tab. 5.19. Note that module 5 was precalibrated with the ratio 0.61 derived from muons.

Table 5.19: Calibration Constants for Module 5 obtained from Hadrons (see Text for Description of the Method)

E [GeV]	$\frac{< PH(h)_{1-4} >}{< PH(h)_5 >}$
10	0.78 ± 0.06
20	0.86 ± 0.01
30	1.02 ± 0.02
50	1.02 ± 0.01
75	1.05 ± 0.02
100	1.26 ± 0.04

Table 5.20: Values for the Mean Pulse Height of the Hadron Distribution at 50 GeV in Module 1-4 ($< PH(h)_{1-4} >$) for Different Energy Intervals of Module 5 ($< PH(h)_5^i >$ denotes the weighted Mean in Interval i). The obtained Energy Resolution and the Number of Events per Energy Interval are also given. The Values for Module 1-5 after the Calibration are given for Comparison.

$\frac{E_5}{E_{1-4}}$ [%]	$< PH(h)_5^i >$ [ADC CH.]	$< PH(h)_{1-4} >$ [ADC CH.]	$\frac{\sigma_E(h)_{1-4}}{\sqrt{E[GeV]}}$ [%]	$< PH(h)_{1-5} >$ [ADC CH.]	$\frac{\sigma_E(h)_{1-5}}{\sqrt{E[GeV]}}$ [%]	Events
< 0.25	-1.1	9152.3 ± 5.8	41.6 ± 0.3	9145.7 ± 5.9	41.5 ± 0.3	4436
0.25 - 1	68.8	9114.1 ± 12.2	40.7 ± 0.7	9182.0 ± 12.1	40.7 ± 0.7	986
1 - 2	142.9	9001.4 ± 15.4	43.9 ± 1.0	9149.4 ± 16.1	43.2 ± 1.0	663
2 - 5	316.8	8854.4 ± 15.8	47.2 ± 1.0	9162.0 ± 15.8	45.3 ± 1.0	736
5 - 10	651.5	8465.9 ± 20.9	51.5 ± 1.4	9123.7 ± 20.1	46.7 ± 1.3	508
10 - 20	1266.2	7879.1 ± 27.0	57.4 ± 2.0	9159.8 ± 23.5	44.4 ± 1.5	362
20 - 30	2191.6	6830.7 ± 72.2	100.1 ± 8.3	9016.8 ± 59.0	68.5 ± 4.5	157
30 - 40	3130.8	5704.0 ± 138.2	-	8960.0 ± 128.6	-	56
> 40	4178.8	4467.0 ± 188.8	-	8845.0 ± 160.1	-	28
				$< 9082.7 >$ ± 116.2		

The calibration method has been checked by determining the mean pulse height of module 1-5 at 50 GeV for the different energy intervals of the calibrated signals of module 5. One finds that $< PH(h)_{1-5} >$ is constant within ±1.3% (Tab. 5.20).

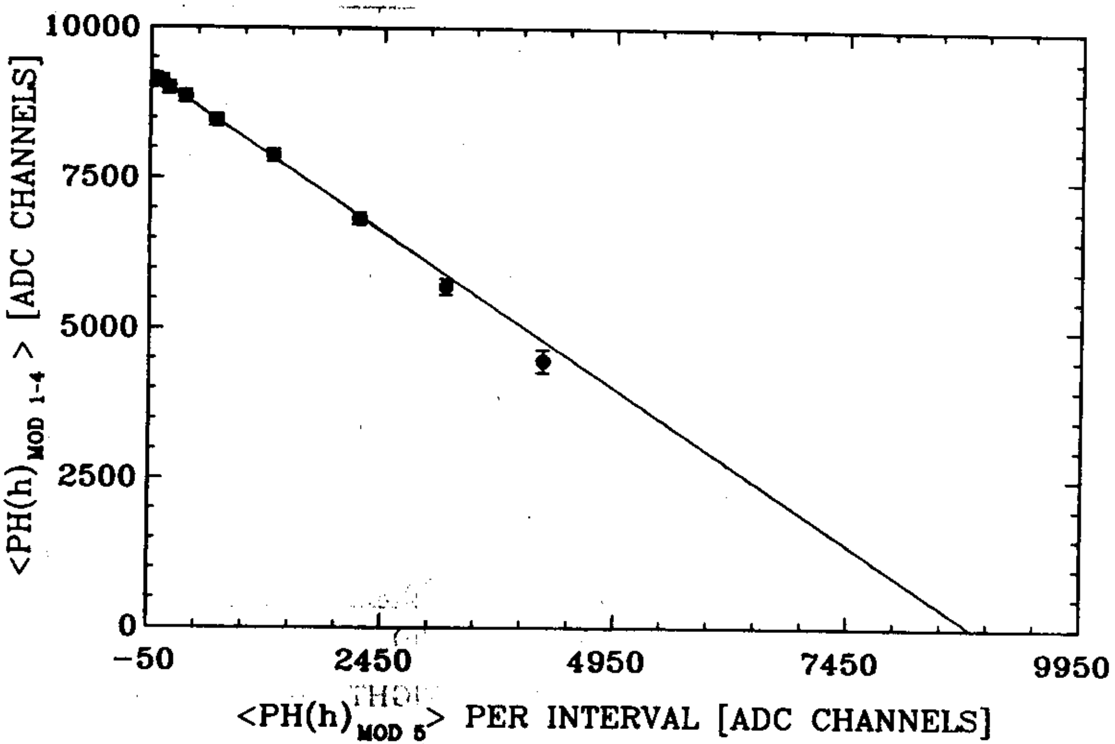

Figure 5.18: Mean Pulse Height of Module 1-4 as a Function of the Weighted Mean Values of the Energy Intervals in Module 5

Particle Selection

The X5-beam that has been used for this measurement contained muons, electrons and hadrons with the relative fractions quoted in Tab. 5.18. The particle selection has been done by means of the calorimeter and the Cherenkov counter. To separate muons from the overall event sample the calorimeter information has been used as described in sec. 4.2. The electron-hadron separation during this period has been done independently from the calorimeter by the use of the signal from the threshold Cherenkov counter. For a given beam momentum the pressure of this counter was adjusted to a value just below the muon threshold. In this way, only electrons produced a Cherenkov signal but not the particles of higher mass. The efficieny to produce a signal when an electron passed the threshold counter was determined according to the method described in [KRÜ86]. A clean electron and hadron sample is selected using the calorimeter information; each of the two integrated pulse height spectra of the Cherenkov counter for both electrons and hadrons is equal to a detection efficiency of 100%. A cut at a certain pulse height separates electrons and hadrons with an efficiency equal to the area of the integrated spectrum that is leftover above the cut.

Fig. 5.19 shows the pulse height spectrum of the Cherenkov counter for hadrons and electrons of $10\,GeV$ as they were separated by the cut indicated at *ADC CHANNEL* 30. This value was selected in order to have $< 1\%$ of electrons in the hadron sample without reducing the hadron statistics significantly. The detection efficiency for electrons at this cut was determined to be 98.5%. The beam content at this energy was already given in Tab. 5.18 where for the particular run a beryllium target has been used.

For hadron runs the copper target was used instead of the beryllium target because of the lower electron fraction (see Tab. 5.18). The measured electron and hadron fractions for the runs at $10 - 50\,GeV$ as well as the detection efficiencies of the Cherenkov counter for electrons at the given cuts are listed in Tab. 5.21. The percentage of electrons still contained in the 'hadron' sample increases with energy because of the reduced detection efficiency of the threshold counter at higher energies. It

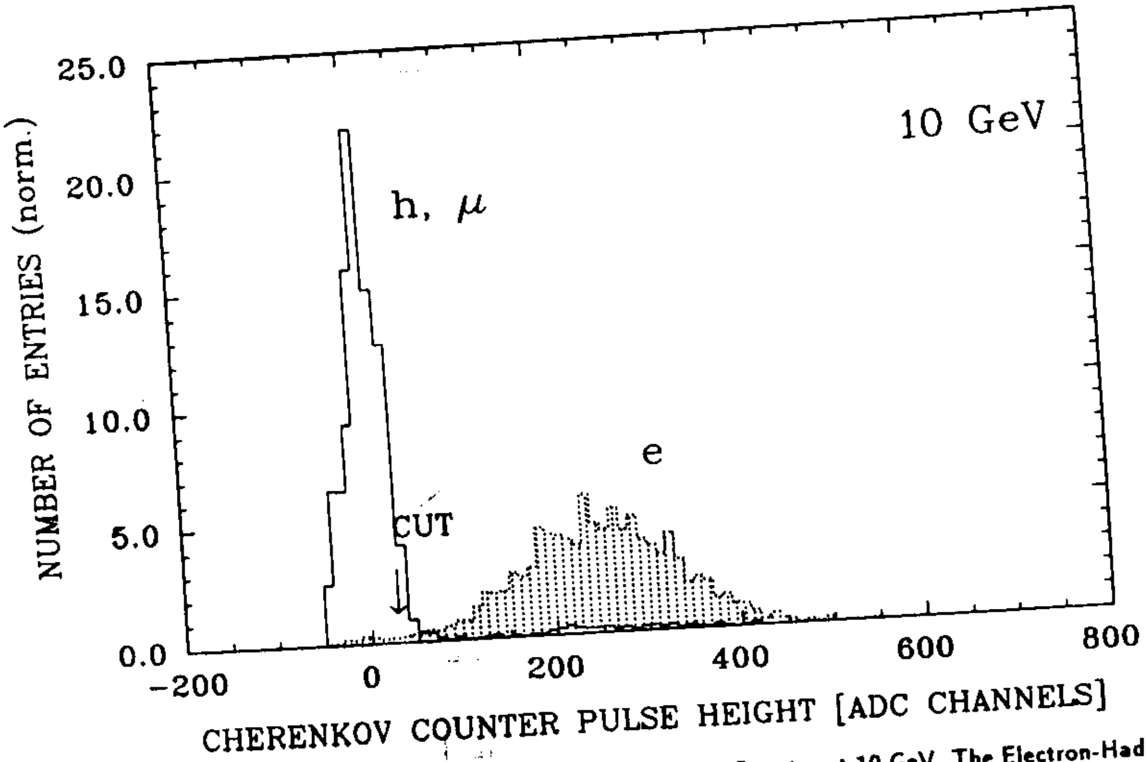

Figure 5.19: Pulse Height Spectrum of the Threshold Cherenkov Counter at 10 GeV. The Electron-Hadron Separation results from the indicated Cut at ADC CHANNEL 30 (dashed histogram: Electrons)

does, however, not exceed ~ 3 %. This clean electron-hadron separation is necessary to determine the e/h-ratio.

Table 5.21: Detection Efficiency for Electrons (third column) of the Threshold Cherenkov Counter used for Electron-Hadron Separation, Electron Contamination of the 'Hadron' Sample (fourth column) and Electron-Hadron Fractions of the Beam (fifth column)

E [GeV]	Cut [ADC CH.]	Electron Efficiency [%]	Electrons in 'Hadrons' [%]	Electrons in Beam [%]	Hadrons in Beam [%]
10	90	89.7	1.2	10.3	89.7
20	100	54.2	2.4	5.1	94.9
30	30	27.3	3.1	4.2	95.8
50	40	29.6	2.3	3.2	96.8

5.3.3 Transverse and Longitudinal Leakage of Hadronic Energy

Transverse Leakage

The transverse leakage of hadronic energy out of the T60UB1 calorimeter was determined according o the method discussed in sec. 4.3.1. In a first step the amount of transverse leakage was determined while in a second step a correction according to the obtained values was applied. The obtained values or the top and bottom sides of the calorimeter are listed in Tab. 5.22. The values of total transverse eakage are twice the values of the leakage out of the top and bottom side of the entire calorimeter.

In the second step the correction for transverse leakage on an event-by-event basis for the top and ottom sides has been applied (sec. 4.3.1). In Tab. 5.23 the obtained mean pulse height values of he calorimeter ($< PH(h)_{1-6} >$) are given together with the width of the pulse height distribution

Table 5.22: Transverse Leakage out of the T60UB1 Calorimeter

E [GeV]	top [%]	bottom [%]	top + bottom [%]	total [%]
10	1.7 ± 0.6	1.8 ± 0.6	3.6 ± 0.8	7.2 ± 1.6
20	1.0 ± 0.3	0.7 ± 0.2	1.7 ± 0.3	3.4 ± 0.6
30	0.9 ± 0.2	0.7 ± 0.1	1.6 ± 0.2	3.2 ± 0.4
50	0.8 ± 0.2	0.6 ± 0.1	1.4 ± 0.2	2.8 ± 0.4
75	0.9 ± 0.1	0.7 ± 0.1	1.5 ± 0.1	3.2 ± 0.2
100	0.8 ± 0.1	0.7 ± 0.1	1.6 ± 0.1	3.0 ± 0.2

Table 5.23: Corrected Hadronic Response on an Event-by-Event Basis for Transverse Leakage out of the Top and Bottom Side of the T60UB1 Calorimeter

	without Trans. Leak. Corr.		with Trans. Leak. Corr.		
E [GeV]	$< PH(h)_{1-5} >$ [ADC CH.]	$\sigma(h)_{1-5}$ [ADC CH.]	$< PH(h)_{1-5} >$ [ADC CH.]	$\sigma(h)_{1-5}$ [ADC CH.]	$\frac{\Delta < PH(h)_{1-5} >}{< PH(h)_{1-5}^{without\ TLC} >}$ [%]
10	1809.9 ± 6.7	219.0 ± 5.2	1859.2 ± 6.7	217.8 ± 5.2	2.7
20	3665.4 ± 8.1	311.2 ± 6.4	3734.9 ± 8.0	309.5 ± 6.1	1.9
30	5530.4 ± 4.6	402.2 ± 3.5	5631.7 ± 4.6	407.3 ± 3.6	1.8
50	9147.2 ± 6.5	562.2 ± 5.2	9305.6 ± 6.6	566.9 ± 5.2	1.7
75	13746.9 ± 12.8	694.0 ± 9.9	14032.8 ± 13.0	702.0 ± 10.1	2.0
100	18556.5 ± 26.2	861.8 ± 20.5	18994.3 ± 26.5	876.9 ± 20.8	2.3

$\sigma(h)_{1-5}$. For comparison, the uncorrected values are quoted, too, and the difference of the mean pulse heights in %.

Longitudinal Leakage

The measurements with the T60UB1 calorimeter (4 modules, 6.1 λ_0 total depth, Tab. 5.17) have been performed with an additional module of the T60UA calorimeter (1.1 λ_0, Tab. 5.1) placed behind in order to receive informations on the longitudinal leakage of the T60UB1 calorimeter. The intercalibration of the T60UB1 calorimeter with the T60UA module was discussed in sec. 5.3.2. The mean pulse height of each module is plotted as a function of the calorimeter depth in units of λ_0 in Fig. 5.20 for different energies. They are taken from the measurements with the T60UB2 calorimeter which was identical to the T60UB1 calorimeter but equipped with graded light filters in order to improve the longitudinal uniformity of the wavelength shifter readout (sec. 5.4).

Table 5.24: Fraction of Total Energy beyond 7.2 λ_0 at Different Energies according to the Shower Profile Parametrization

E [GeV]	Fraction of Energy beyond 7.2 λ_0 [%]
10	0.9
20	1.3
30	1.7
50	2.3
75	3.2
100	3.9

The parametrization of the longitudinal hadronic shower profile was done using eq. 5.6 with the given parameters (see also [CAT87b]) and is plotted in Fig. 5.20. The agreement with the data is quite

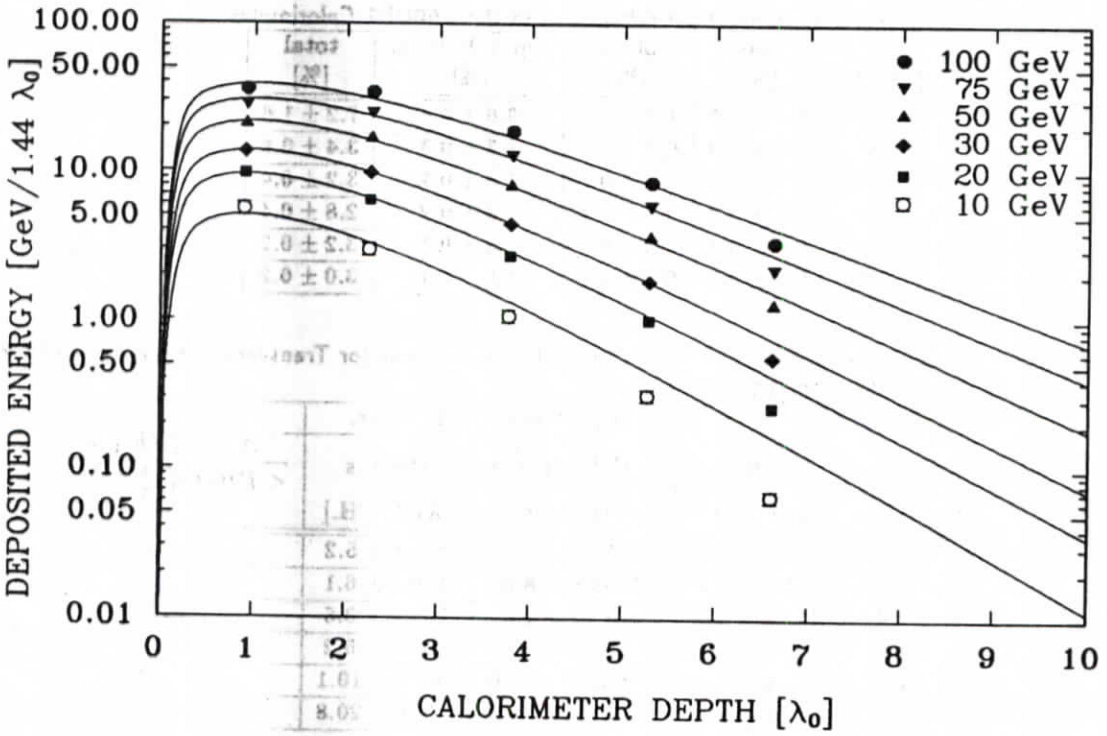

Figure 5.20: Longitudinal Shower Profile measured in the T60UB2 Calorimeter

good except for the last data point which is that of module 5. This can be attributed to the fact that this module is quite different (3 *mm* DU-5 *mm* SCI, 1.1 λ_0 in depth, uncorrected for the longitudinal nonuniformity) compared to the other modules and that the intercalibration with hadrons has still some uncertainties.

From the parametrization of the measured shower profile one can calculate the longitudinal leakage out of the entire calorimeter. The entire calorimeter is 7.2 λ_0 deep if module 5 is included. The fraction of longitudinal energy leakage direction beyond 7.2 λ_0 is given in Tab. 5.24 for different energies.

5.3.4 Energy Resolution of the T60B1 Uranium-Scintillator Calorimeter

The response of the T60UB1 calorimeter to electrons and hadrons at 10, 20, 30, 50, 75 and 100 *GeV* and to muons at 10 *GeV* is plotted in Fig. 5.21. The pulse height distributions of electrons and hadrons are fitted by a Gauss function with a cut of $\pm 3\,\sigma$ while that of the muons is fitted by a convoluted Moyal-Gauss function. The fitted curves are also drawn in Fig. 5.21.

Table 5.25: Relative Deviation in [%] of the Mean Pulse Height and the Energy Resolution if the Sum of Module 1 is considered only as the Electron Response in the T60UB1 Calorimeter

E [GeV]	$\frac{<PH(e)_1> - <PH(e)_{1-4}>}{<PH(e)_{1-4}>}$ [%]	$\frac{\frac{\sigma_E(e)_1}{E} - \frac{\sigma_E(e)_{1-4}}{E}}{\frac{\sigma_E(e)_{1-4}}{E}}$ [%]
10	$+0.32 \pm 0.11$	-5.14 ± 1.43
20	-0.19 ± 0.08	-3.18 ± 1.45
30	$+0.48 \pm 0.07$	-2.85 ± 1.50
50	$+0.40 \pm 0.06$	-1.29 ± 1.55

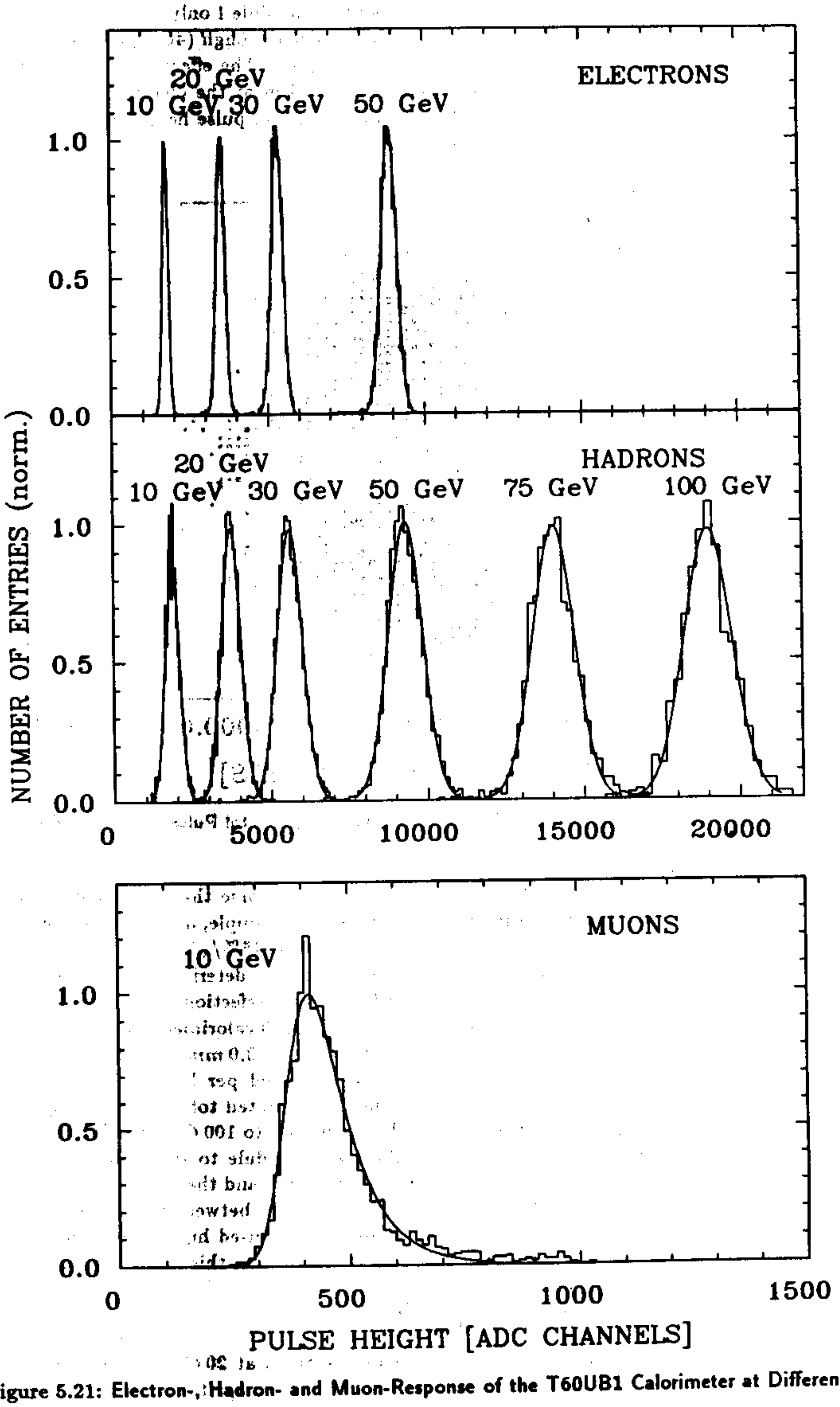

Figure 5.21: Electron-, Hadron- and Muon-Response of the T60UB1 Calorimeter at Different Energies

The distribution of electrons shown in Fig. 5.21 is obtained from module 1 only in order to suppress the uranium noise contribution from module 2-5. One module is deep enough (46 X_0) to contain the entire electromagnetic shower so no leakage will effect the total signal. The effect on the mean pulse height and the energy resolution if the signal from module 1 is taken as the electron response can be seen from Tab. 5.25. In this table the relative deviation of the mean pulse height and the energy resolution in module 1 from that in module 1 to 4 is given.

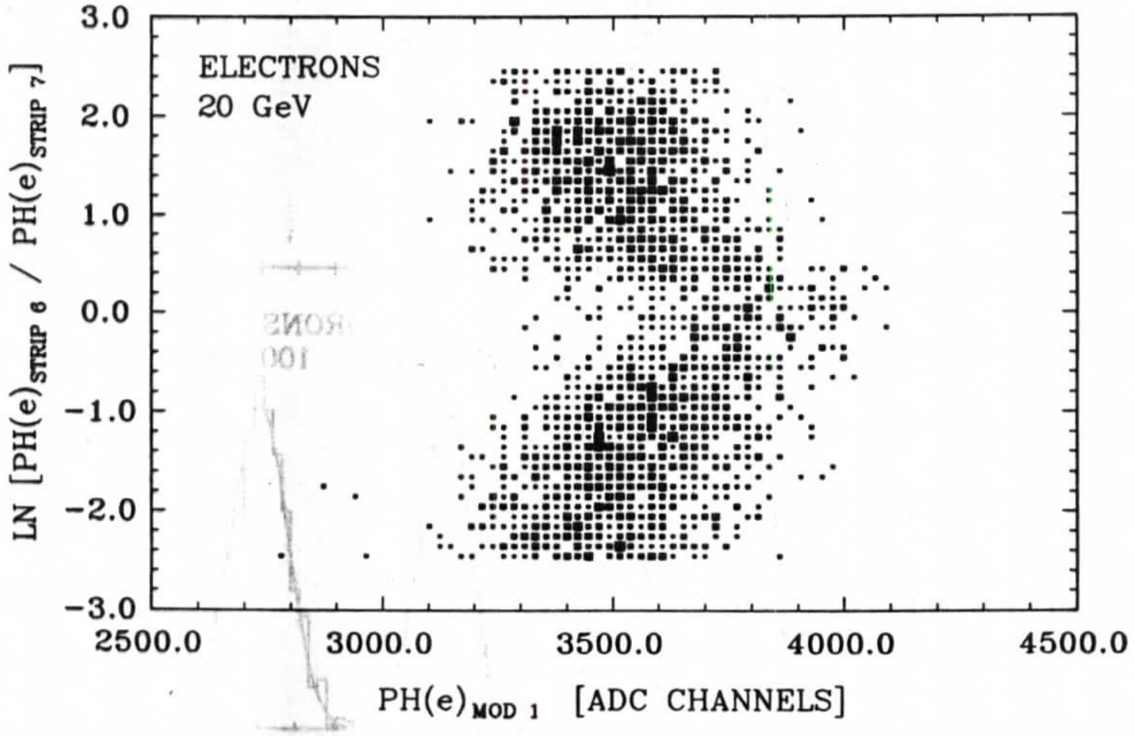

Figure 5.22: The Ratio R=ln($PH(e)_{STRIP6}/PH(e)_{STRIP7}$) versus the Total Pulse Height for Electrons at 20 GeV (see text for explanation)

In a first glance the energy resolution for electrons was slightly worse than expected from the previous measurements with the T60UA calorimeter. At 20 GeV, for example, an energy resolution of $19.6\%/\sqrt{E[GeV]}$ was determined from the T60UB1 measurement while $15\%/\sqrt{E[GeV]}$ was measured with the T60UA calorimeter (see Tab. 5.7). A careful study of this deterioration of the energy resolution for electrons showed that it was caused by a mechanical imperfection of the calorimeter: the dimension of the delivered depleted uranium plates used for the T60 calorimeter were $600 \times 300 \times 3.2\,mm^3$, $600 \times 200 \times 3.2\,mm^3$, $600 \times 100 \times 3.2\,mm^3$ and $600 \times 200 \times 3.0\,mm^3$. In order to obtain the lateral dimension of $600 \times 600\,mm^2$, 2, 3 or 6 plates were needed per layer. Because of the slightly undulated edges of the uranium plates they could not be mounted totally flush to form one layer. During the measurements at the SPS the beam with energies up to 100 GeV has been directed in between the two central strips 6 and 7 of the T60 calorimeter module to share the total signal among both strips. In this way the ADC was prevented from saturation and the muon signal was well separated from the pedestals. However, the beam hit also the small gaps between the uranium plates. The reduced density of the calorimeter module in that small region caused higher pulse heights for particles that penetrate exactly into this region, as Fig. 5.22 illustrates. In this figure the ratio

$$R = \ln \frac{PH(e)_{STRIP6}}{PH(e)_{STRIP7}}$$

is plotted versus the total pulse height of the calorimeter for electrons at 20 GeV. The region of R $>\mid 0.6 \mid$ is due to electrons that deposit their energy in either of both strips totally while the region of R $< | 0.6 |$ is due to electrons striping both scintillator edges. The average total pulse height of region R $< | 0.6 |$ is $\sim$ 6% higher than that of R $> | 0.6 |$. Electrons of the region R $< | 0.6 |$ have been cut out thus improving the energy resolution to $18.0\%/\sqrt{E[GeV]}$ for electrons at $20\,GeV$. This cut has been applied for electrons at all energies and the resulting pulse height distributions are shown in Fig. 5.21. The energy resolution for hadrons was not influenced by this effect.

The hadron distributions shown in Fig. 5.21 were obtained by summing the pulse heights of module 1-5 where module 5 has been calibrated in the way described in sec. 5.3.2. In addition, a cut of $PH(h)_{M=5} \leq 0.02 \cdot < PH(h)_{M=1-4} >$ against longitudinal leakage has been applied in the pulse height distribution of module 5. The effect of this cut on the mean pulse height and the width of the distribution can be read off from Tab. 5.26. For the transverse leakage from the top and bottom side the correction method described in sec. 4.3.1 has been performed.

Table 5.26: Difference Between the Mean Pulse Heights of Module 1 to 4 ($\Delta < PH(h)_{1-4} >$) with and without a Longitudinal Leakage Cut in Module 5 of 2% of the Total Energy, relative to the Signal in Module 1 to 4 without the Cut; the equivalent Difference ($\Delta\sigma(h)_{1-4}$) is also given for the Width of the Distributions, Relative to the Width of the Distribution in Module 1 to 4; the Fraction of Events rejected by this Cut is given in the fourth Column

E [GeV]	$\frac{\Delta < PH(h)_{1-4} >}{< PH(h)_{1-4} >}$ [%]	$\frac{\Delta\sigma(h)_{1-4}}{\sigma(h)_{1-4}}$ [%]	Event Rejection [%]
10	$+0.08 \pm 0.38$	-0.63 ± 2.35	10.2
20	$+0.48 \pm 0.23$	-2.09 ± 1.99	11.2
30	$+0.86 \pm 0.09$	-6.67 ± 0.89	20.5
50	$+1.10 \pm 0.08$	-10.91 ± 0.90	23.4
75	$+1.33 \pm 0.11$	-15.29 ± 1.64	31.2
100	$+1.93 \pm 0.16$	-21.49 ± 2.41	43.0

The values of the energy resolution for electrons and hadrons as obtained from the Gauss fits with $\pm 3\,\sigma$ cut are listed in Tab. 5.27. For hadrons the values without any leakage correction are given for comparison. The obtained values for the energy resolution for electrons and hadrons are plotted in Fig. 5.23. The parametrization eq. 4.4 for electrons and eq. 4.6 for hadrons results in the follwing values for a and b:

Table 5.27: Mean Response and Energy Resolutions of Electrons and Hadrons at 10, 20, 30, 50, 75 and 100 GeV obtained from the T60UB1 Calorimeter

	ELECTRONS		HADRONS	
E [GeV]	$< PH(e)_1 >$ [ADC CH.]	$\frac{\sigma_E(e)_1}{\sqrt{E[GeV]}}$ [%]	$< PH(h)_{1-5} >$ [ADC CH.]	$\frac{\sigma_E(h)_{1-5}}{\sqrt{E[GeV]}}$ [%]
10	1730.1 ± 1.9	17.3 ± 0.3	1852.2 ± 7.1	38.4 ± 1.0
20	3504.8 ± 2.9	17.9 ± 0.3	3731.1 ± 8.4	36.9 ± 0.8
30	5316.6 ± 3.7	18.6 ± 0.3	5609.9 ± 4.9	39.1 ± 0.4
50	8884.9 ± 5.5	19.7 ± 0.3	9308.2 ± 7.2	41.4 ± 0.4
75			14038.8 ± 14.8	41.0 ± 0.7
100			18989.3 ± 30.3	40.0 ± 1.2

for electrons

$$\begin{aligned} a &= 16.7\% \pm 0.5\% \\ b &= 1.5\% \pm 0.1\% \end{aligned} \tag{5.14}$$

and for hadrons

$$\begin{aligned} a &= 35.5\% \pm 1.1\% \\ b &= 0.7\% \pm 0.2\%. \end{aligned} \tag{5.15}$$

The quoted errors are 3% for parameter a while the error for b is obtained from the fit. The contribution from photostatistics to the energy resolution was taken from the difference signal of electrons (eq. 4.11) yielding:

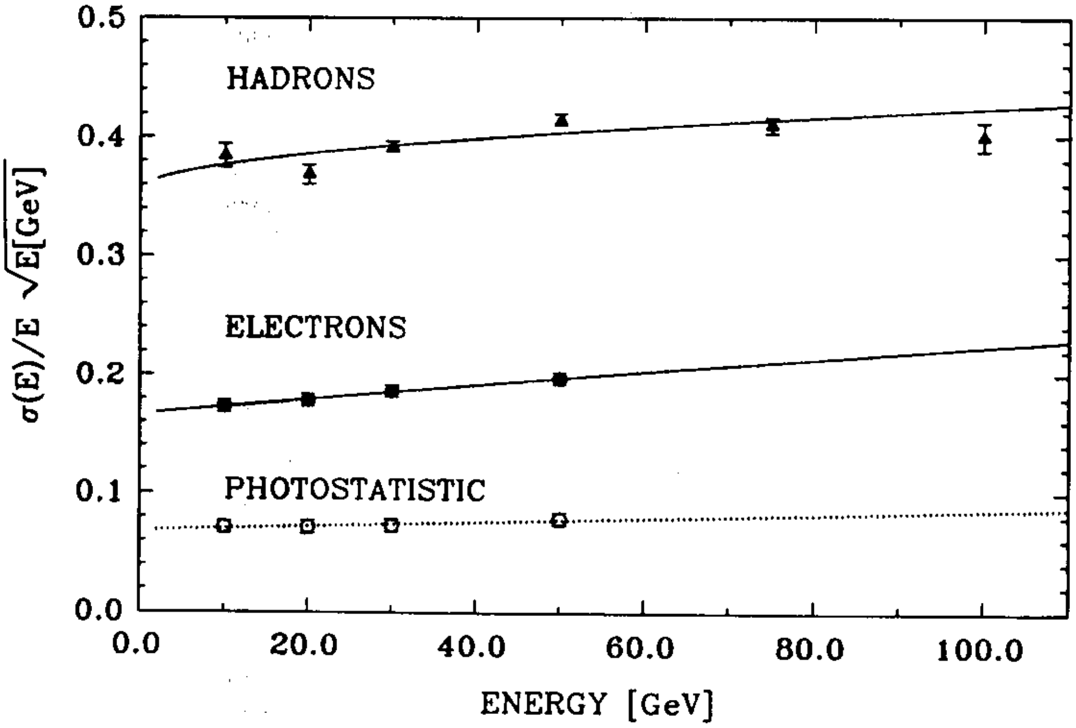

Figure 5.23: Energy Resolution of the T60UB1 Calorimeter for Electrons and Hadrons as a Function of Energy and the Contribution from Photostatistics

$$\frac{\sigma_{L-R}}{< PH_{L+R} >}(e) = \frac{(6.82 \pm 0.09)\%}{\sqrt{E[GeV]}} \oplus (0.51 \pm 0.04)\%. \tag{5.16}$$

The sampling fluctuations according to the EGS4 calculations are:

$$\frac{\sigma_s(e)}{E} = \frac{(16.97 \pm 0.03)\%}{\sqrt{E[GeV]}}. \tag{5.17}$$

From eq. 5.16 one obtains the number of photoelectrons per GeV incident energy according to eq. 4.11: $< N_{pe} > = 214 \pm 6$, corresponding to 4 photoelectrons per MeV of visible electromagnetic shower energy at an electromagnetic sampling fraction of $\bar{e} = 4.74\%$, as calculated with EGS4.

The total energy resolution for electrons obtained from the quadratic sum of the sampling fluctuations and the contributions from photostatistics is:

$$\frac{\sigma_t(e)}{E} = \frac{(18.29 \pm 0.09)\%}{\sqrt{E[GeV]}} \oplus (0.51 \pm 0.04)\%. \tag{5.18}$$

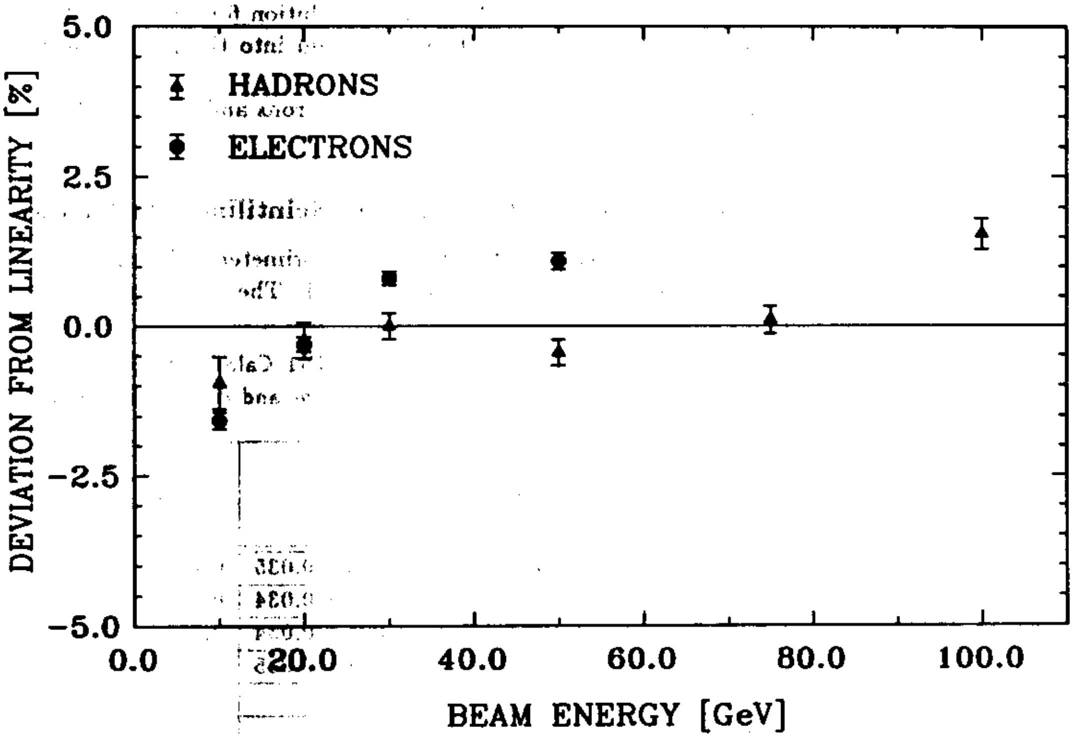

Figure 5.24: Deviation from Linearity in [%] for Electrons and Hadrons in the T60UB1 Calorimeter

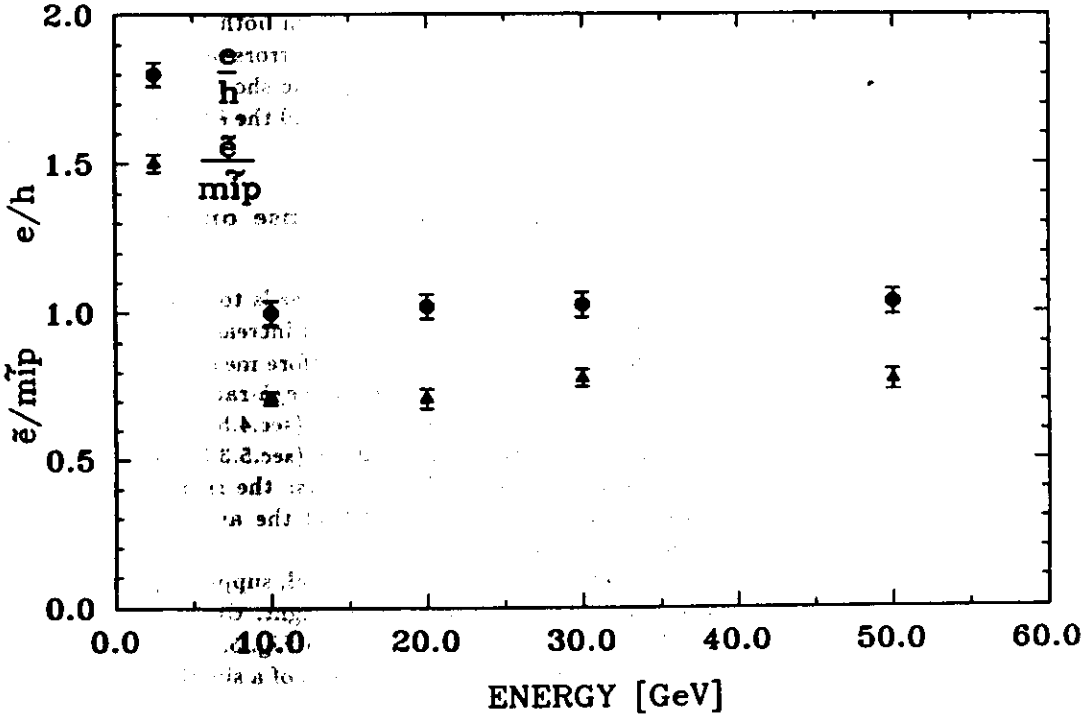

Figure 5.25: The e/h- and $\tilde{e}/\widetilde{mip}$-Ratio of the T60UB1 Calorimeter as a Function of the Energy

The value is larger than the value obtained from the parametrization of the measured resolution (eq. 5.14). This reflects still remaining uncertainties in the energy resolution for electrons after the applied cut since the beam was directed between two central strips and into the gap between the uranium plates.

The response of the calorimeter is linear within ± 1.5% for both electrons and hadrons. Fig. 5.24 shows the deviation from the mean linearity.

5.3.5 The e/h- and $\tilde{e}/\widetilde{mip}$- Ratio of the T60B1 Uranium-Scintillator Calorimeter

The mean electron and hadron response measured with the T60UB1 calorimeter had to be corrected for the nonuniformity of the wavelength shifter as described in sec. 4.5.4. The mean pulse height of hadrons was corrected for transverse leakage out of the right and left edge of the calorimeter with the values obtained from the leakage from the top and bottom edges according to the method described in sec. 4.3.1. The obtained mean pulse heights for electrons, hadrons and muons are given in Tab. 5.28 together with the determined e/h- and $\tilde{e}/\widetilde{mip}$-ratios. The total errors on both ratios result from the propagation of the statistical errors on the measured pulse heights, the errors on the measurement of the light attenuation curve, the statistical errors on the electromagnetic shower simulation and the errors on the parametrization of the hadronic shower profile. The e/h- and the $\tilde{e}/\widetilde{mip}$-ratio are plotted in Fig. 5.25 as a function of energy.

Table 5.28: Mean Electron-, Muon- and Hadron- Response of the T60UB1 Calorimeter, corrected for Longitudinal Nonuniformity (e, h) and for Leakage (h), and the resulting e/h- and $\tilde{e}/\widetilde{mip}$-ratio at 10, 20, 30, 50, 75 and 100 GeV

E [GeV]	e [ADC CH.]	h [ADC CH.]	μ [ADC CH.]	$\frac{e}{h}$	$\frac{\tilde{e}}{\widetilde{mip}}$
10	1922.2 ± 20.3	1925.5 ± 63.6	107.3 ± 1.7	0.998 ± 0.035	0.710 ± 0.022
20	3878.3 ± 40.9	3807.5 ± 121.7	113.5 ± 4.5	1.019 ± 0.034	0.707 ± 0.034
30	5866.8 ± 61.8	5731.3 ± 181.8	106.6 ± 3.3	1.024 ± 0.034	0.779 ± 0.032
50	9778.8 ± 102.6	9458.5 ± 300.8	111.3 ± 4.4	1.034 ± 0.035	0.774 ± 0.037
75		14269.8 ± 453.5			
100		19319.4 ± 614.2			

5.3.6 Dependence of the Electron- and Hadron-Response on the Integration Time

The time dependence of the neutron component in a hadronic shower leads to a rise of the hadronic response of a calorimeter if the integration time of the hadronic signal increases (see sec. 3.4). The electron and the hadron response of the T60UB1 calorimeter was therefore measured as a function of the integration time. The result is plotted in Fig. 5.26 together with the e/h-ratio. The mean electron and hadron response has been corrected for longitudinal nonuniformities (sec.4.5.4), the mean hadronic pulse height was also corrected for longitudinal and transverse leakage (sec.5.3.3). The effective gate length is shorter than the one given in Fig. 5.26 because of two effects: the rising edge of the gate pulse preceeded the photomultiplier signal by $\sim$ 20 ns; the width of the analog signals from the photomultipliers give rise to an additional time offset.

The starting point t_0 of the shower was defined by the electron signal, supposing that the peak of the analog pulse from the electrons at t_0 gives 50% of the total pulse height. Under this consideration the effective gate length is reduced in total by 30 ns, as can bee seen in Fig. 5.26.

This time offset has been subtracted for comparison with predictions of a simulation program that will be discussed in sec. 7.4.2.

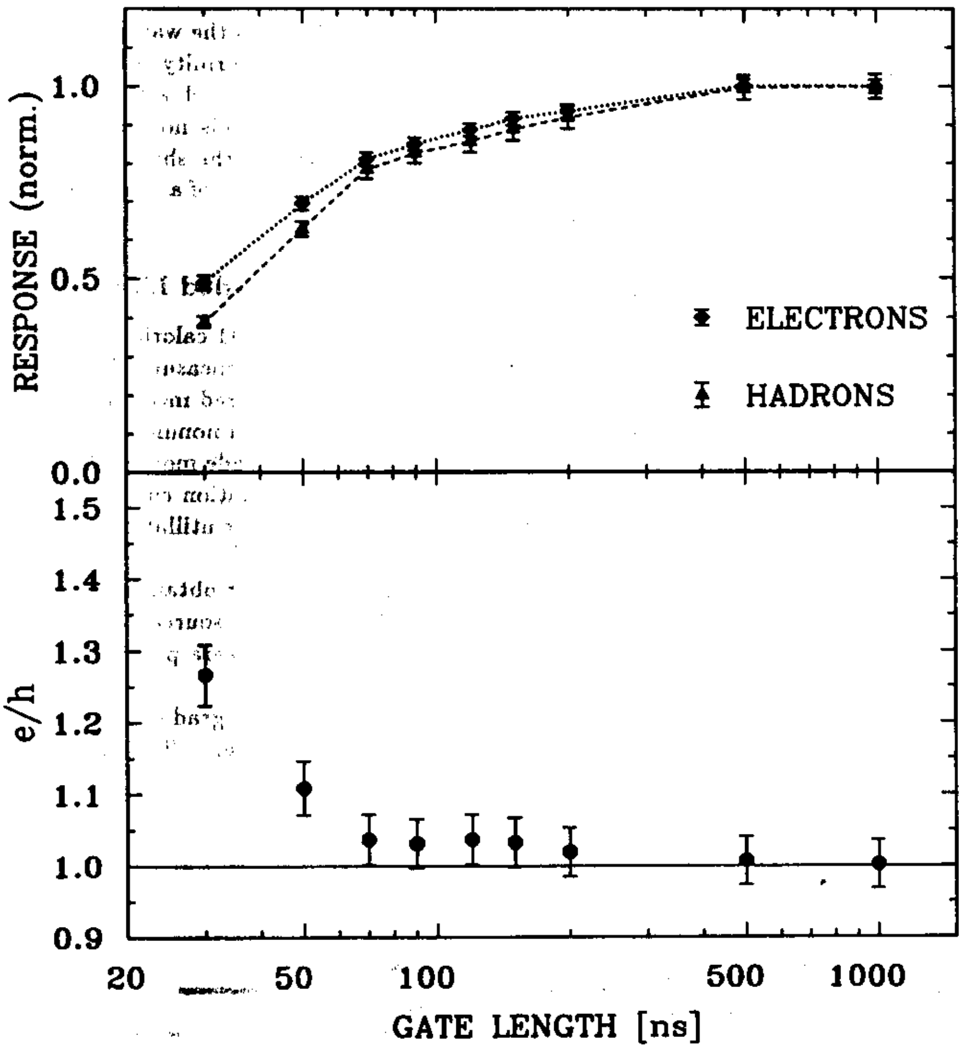

Figure 5.26: Mean Electron and Hadron Response and the e/h-Ratio as a Function of the ADC Gate Length

5.4 Improving the Longitudinal Uniformity

The optical fibre readout of the WA78 calorimeter (sec. 5.10) has the advantage that the light produced in each scintillator plate travels the same distance before reaching the photomultiplier. This readout method provides a good longitudinal uniformity of a calorimeter because of equal light attenuation in each readout channel.

In order to build a compact detector without introducing large dead spaces the wavelength shifter readout of scintillator has been developed. However, a longitudinal nonuniformity is implemented in this readout system because of the different distances the light has to travel within the wavelength shifter bar from different scintillator plates to the photomultiplier. This nonuniformity will be transformed into the signal that is longitudinally distributed according to the shower profile (see sec. 4.5.4). It is therefore necessary to correct for the longitudinal nonuniformity of a calorimeter with a wavelength shifter readout system.

5.4.1 The T60B2 Uranium-Scintillator Calorimeter with Graded Light Filters

In the measurements described previously with the T60Pb, T60UA and T60UB1 calorimeter a correction for the longitudinal nonuniformity has been done offline according to the measured light attenuation curve (sec. 4.5.4, 5.1.5). The method could only be applied to the measured mean pulse heights of electrons and hadrons. In order to reduce the influence of the longitudinal nonuniformity on the energy resolution, especially for hadrons, the longitudinal readout has been made more uniform. This was done by using a light filter with a gradient that is inverse to the attenuation curve. This filter was placed between each wavelength shifter bar and the readout edges of the scintillator plates of the T60UB1 calorimeter.

The attenuation curve that was needed to produce the light filter has been obtained by scanning along a wavelength shifter bar with a scintillator plate radiated by a ^{106}Ru source. According to the attenuation curve graded light filters with a pattern shown in Fig. 5.27 were produced for each wavelength shifter bar.

The light response curve of one wavelength shifter bar after inserting the graded light filter has been measured on one calorimeter module. Fig. 5.28 shows the obtained curve. The measurement was done with a ^{60}Co source that was moved along the top of the T60 module leaving the module unchanged. The light response curve of the wavelength shifter bar without the filter is also given in Fig. 5.28. It was obtained in the same way as with the light filter. This curve was used for the offline correction after it has been corrected for the decrease in the first and last layers (see Fig. 5.28) using informations from the ^{106}Ru-source measurement mentioned above. In both cases the signal-to-uranium noise ratio was low thus making the measurement less precise which leads to some uncertainty in the offline correction method of the longitudinal nonuniformity.

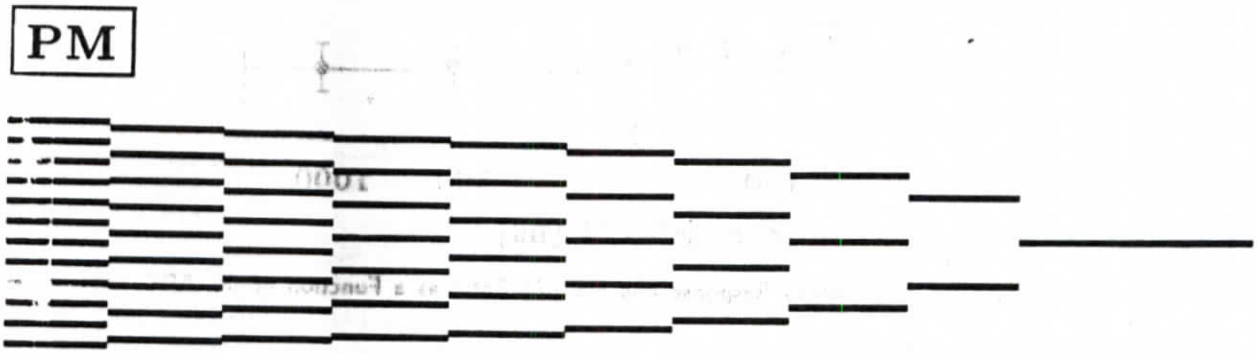

Figure 5.27: Pattern of a Graded Light Filter used to improve the Longitudinal Nonuniformity of the Wavelength Shifter Bars in the T60B2 Calorimeter (PM: Photomultiplier Side)

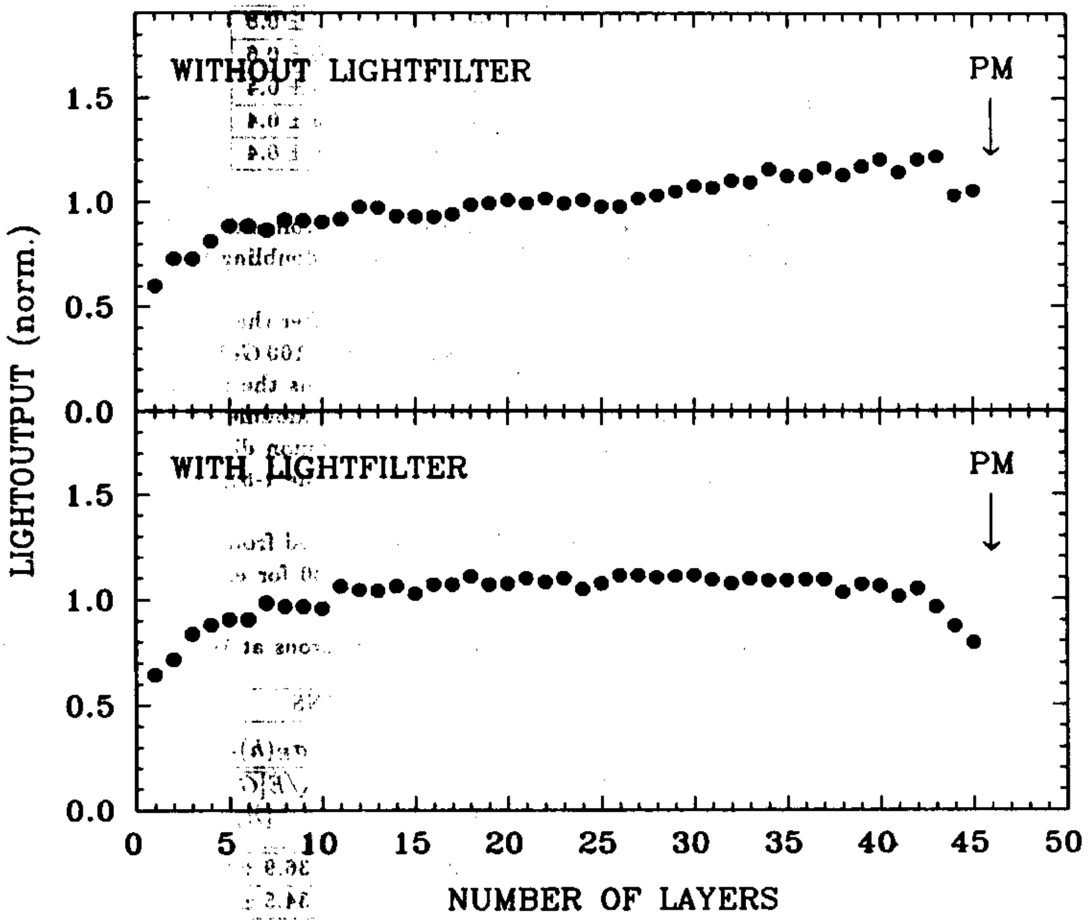

Figure 5.28: Light Response Curve of one Wavelength Shifter Bar of the T60 Module before (top) and after (bottom) inserting a Graded Light Filter (PM: Photomultiplier Side)

5.4.2 Energy Resolution of the T60B2 Uranium-Scintillator Calorimeter

The calibration and particle selction for this measurement was done in a similar way as for the measurement with the T60UA/T60UB1 calorimeter. Due to the insertion of the graded light filter the mean value of the uranium noise distribution decreases to $\sim$ 205 $ADC\,CH.$ with a rms of $\sim$ 18 $ADC\,CH.$. The electron-hadron separation could not be done with the threshold Cherenkov counter because of deffiencies of the counter. The information from the calorimeter was used to separate muons, electrons and hadrons according the method described in sec. 4.2.

The applied leakage corrections are identical to that of the T60UB1 measurement:

- transverse leakage correction for the top and bottom sides of the calorimeter on an event-by-event basis
- calibration of module 5 with muons and hadrons (see sec. 5.3.2)
- cut of $PH(h)_{M=5} \leq 0.02 \cdot < PH(h)_{M=1-4} >$ in module 5 against longitudinal leakage.

Table 5.29: Transverse Leakage in [%] of the T60UB2 Calorimeter, determined for the Top and Bottom Side of the Calorimeter

E [GeV]	top [%]	bottom [%]	top + bottom [%]	total [%]
10	0.8 ± 0.4	0.7 ± 0.3	1.5 ± 0.5	3.0 ± 1.0
20	0.9 ± 0.3	0.7 ± 0.2	1.6 ± 0.4	3.2 ± 0.8
30	0.8 ± 0.2	0.7 ± 0.2	1.5 ± 0.3	3.0 ± 0.6
50	0.7 ± 0.2	0.6 ± 0.1	1.3 ± 0.2	2.6 ± 0.4
75	0.7 ± 0.1	0.6 ± 0.1	1.3 ± 0.2	2.6 ± 0.4
100	0.8 ± 0.1	0.6 ± 0.1	1.4 ± 0.2	2.8 ± 0.4

The amount of transverse energy in [%] leaking out of the top and bottom side of the calorimeter is quoted in Tab. 5.29. The total transverse leakage has been obtained by doubling the top and bottom leakage (sec. 4.3.1).

The entire signal for hadrons is obtained by summing all 5 modules after the corrections have been applied. The distributions are shown in Fig. 5.29 for energies from 10 to 100 GeV. The curves drawn in this figure are fitted Gauss functions with a cut of $\pm 3\sigma$. For electrons the signal from module 1 was taken only in order to suppress the uranium noise contribution from module 2-5. Gauss functions with a $\pm 3\sigma$ cut have been fitted to the distribution (Fig. 5.29). The muon distribution for 10 GeV also shown in this figure is the response of the entire calorimeter (module 1-5); the fitted curve is a convolution of a Gauss with a Moyal function.

The values of the energy resolution for electrons and hadrons obtained from the fits are listed in Tab. 5.30. The values of the energy resolutions are plotted in Fig. 5.30 for electrons and hadrons.

Table 5.30: Mean Response and Energy Resolutions of Electrons and Hadrons at 10, 20, 30, 50, 75 and 100 GeV for the T60UB2 Calorimeter

	ELECTRONS		HADRONS	
E [GeV]	$< PH(e)_1 >$ [ADC CH.]	$\frac{\sigma_E(e)_1}{\sqrt{E[GeV]}}$ [%]	$< PH(h)_{1-5} >$ [ADC CH.]	$\frac{\sigma_E(h)_{1-5}}{\sqrt{E[GeV]}}$ [%]
10	1335.5 ± 2.0	18.1 ± 0.3	1239.4 ± 2.0	36.9 ± 0.4
20	2717.4 ± 2.7	17.6 ± 0.3	2542.1 ± 2.3	34.5 ± 0.3
30	4056.6 ± 3.1	18.0 ± 0.3	3782.5 ± 2.6	34.8 ± 0.3
50	6780.6 ± 4.2	18.9 ± 0.3	6288.9 ± 4.1	36.5 ± 0.3
75			9566.0 ± 5.3	37.8 ± 0.4
100			12707.9 ± 4.9	38.6 ± 0.3

They were parametrized according to eq. 4.4 (electrons) and eq. 4.6 (hadrons) and the following values have been achieved:
for electrons

$$\begin{aligned} a &= 17.4\% \pm 0.5\% \\ b &= 1.0\% \pm 0.2\% \end{aligned} \tag{5.19}$$

and for hadrons

$$\begin{aligned} a &= 32.9\% \pm 1.0\% \\ b &= 0.5\% \pm 0.1\%. \end{aligned} \tag{5.20}$$

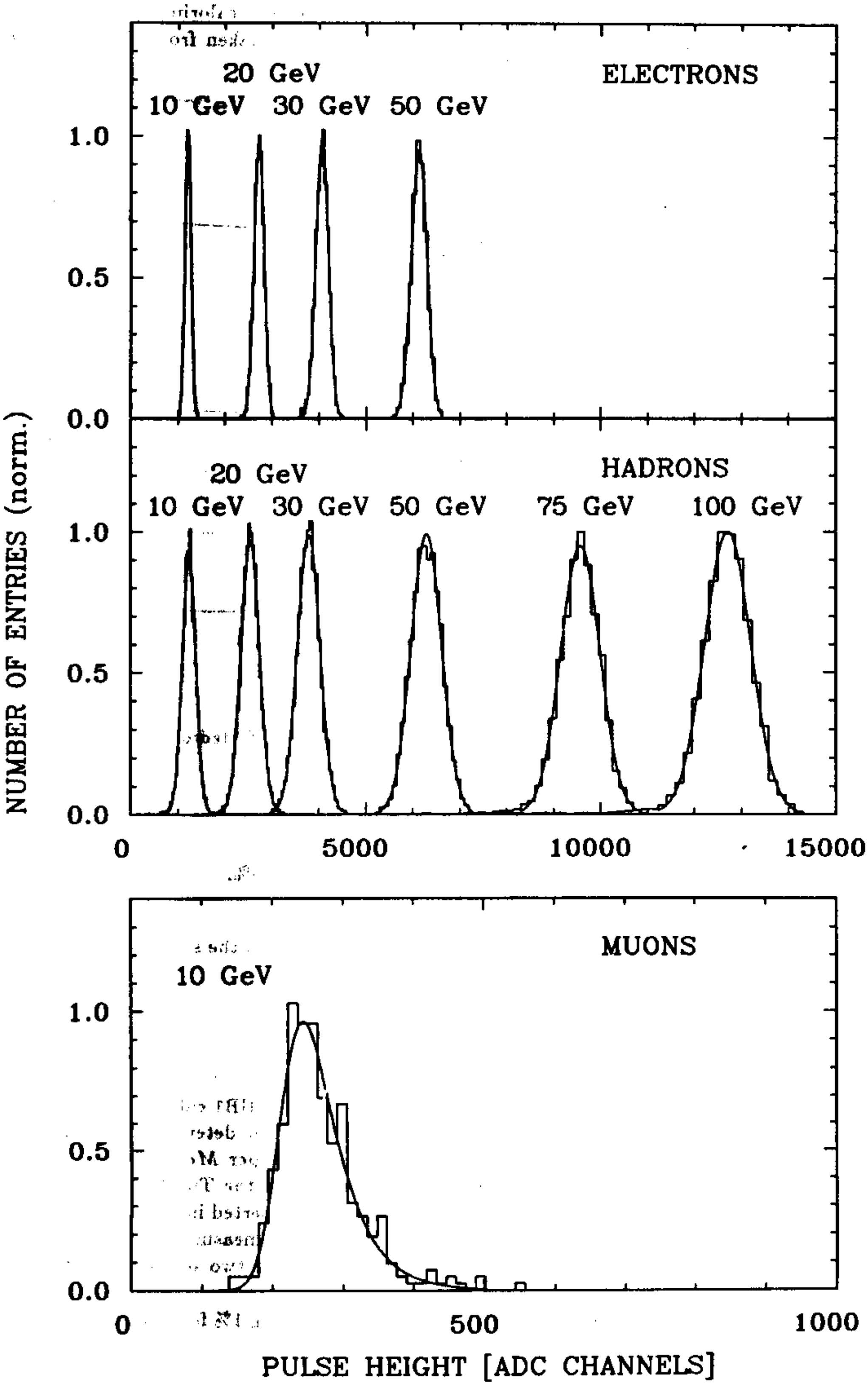

Figure 5.29: Electron-, Hadron- and Muon-Response of the T60UB2 Calorimeter at Different Energies

The estimated errors are found to be of the same order as for the T60B1 calorimeter (sec. 5.3.4). The contribution from photostatistics is also plotted in Fig.5.30. It was taken from the difference

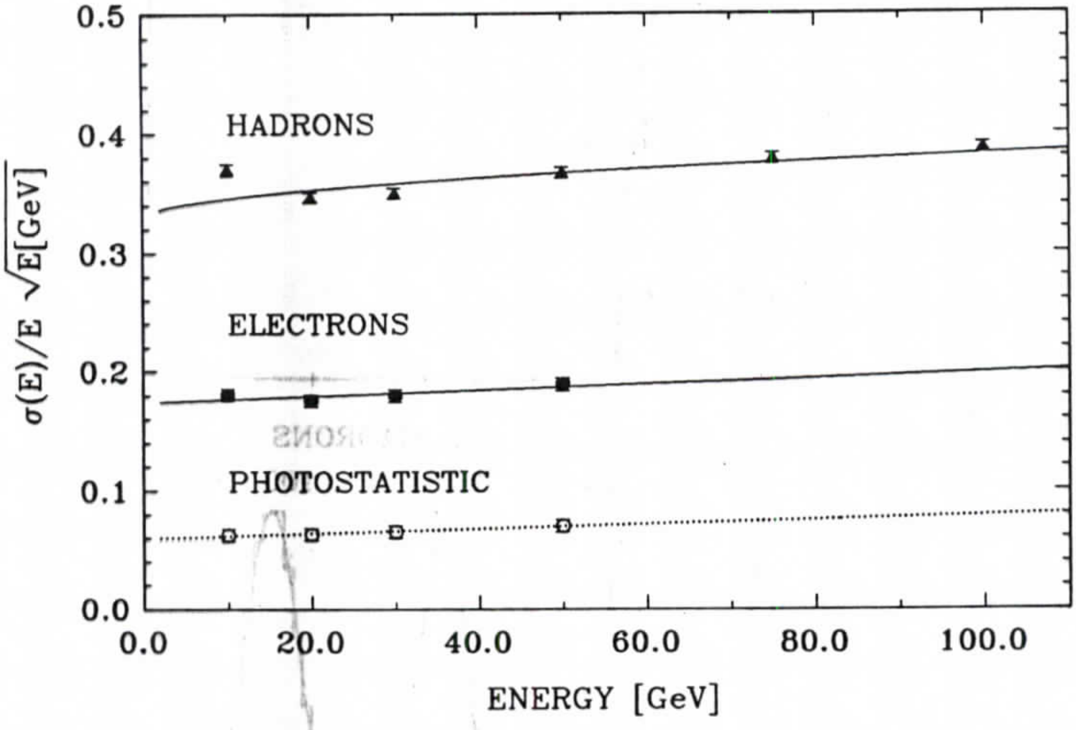

Figure 5.30: Energy Resolution of the T60UB2 Calorimeter for Electrons and Hadrons as a Function of Energy

signal of electrons eq. 4.11 and the parametrization yields:

$$\frac{\sigma_{L-R}}{< PH_{L+R} >}(e) = \frac{(5.94 \pm 0.09)\%}{\sqrt{E[GeV]}} \oplus (0.52 \pm 0.04)\%. \tag{5.21}$$

The total energy resolution for electrons obtained from the quadratic sum of the sampling fluctuations and the contributions from photostatistics is:

$$\frac{\sigma_t(e)}{E} = \frac{(17.98 \pm 0.09)\%}{\sqrt{E[GeV]}} \oplus (0.52 \pm 0.04)\%. \tag{5.22}$$

The sampling fluctuations are identical to the value calculated for the T60UB1 calorimeter (eq. 5.17).

The number of photoelectrons per GeV of incident energy has been determined according to eq. 4.11, yielding $< N_{pe} > = 281 \pm 8$, corresponding to 6 photoelectrons per MeV of visible electromagnetic shower energy. The determined number of photoelectrons for the T60UB2 calorimeter is higher than that of the T60UB1 calorimeter although a light filter was inserted in the T60UB2 calorimeter. This can be explained by the width of the difference distribution measured with the T60UB1 calorimeter to be to large caused by the beam that was directed between two scintillator strips (see sec. 5.3.4).

The response of the calorimeter is linear within ± 2% for hadrons and ± 1% for electrons. Fig. 5.31 shows the deviation from the mean linearity.

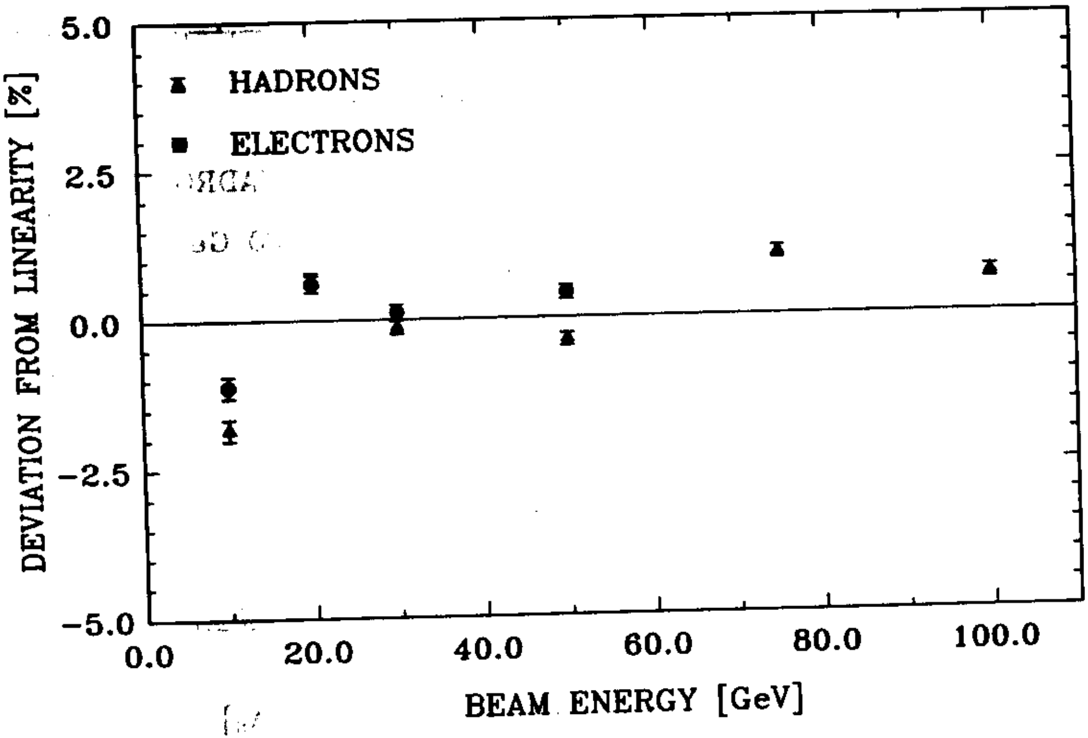

Figure 5.31: Deviation from Linearity in [%] for Electrons and Hadrons in the T60UB2 Calorimeter

5.4.3 Influence of Transverse and Longitudinal Leakage on the Energy Resolution

The energy resolution of hadrons obtained from the previously described measurements with the T60 calorimeter were influenced by longitudinal and transverse leakage. The longitudinal segmentation of the T60B calorimeter into 5 modules as well as the transverse segmentation into 12 strips allowed a systematic study of the influence of leakage on the energy resolution.

The investigation of this influence has been performed in the following way:

- the transverse leakage of hadronic energy has been increased stepwise by reducing the number of strips that contribute to the total pulse height of the calorimeter;
- to increase the longitudinal leakage the number of modules that contribute to the total pulse height of the calorimeter has been reduced stepwise.

Table 5.31: Influence of the Transverse Leakage on the Mean Pulse Height and on the rms of the Pulse Height Distribution for Hadrons at 20 GeV

Lateral Size λ_0	$< PH(h)_{1-5} >$ [ADC CH.]	rms [ADC CH.]
3.24	2492.3 ± 2.5	233.9 ± 28.7
2.70	2458.5 ± 2.5	235.4 ± 28.9
2.16	2391.9 ± 2.5	238.6 ± 29.3
1.62	2270.5 ± 2.8	251.1 ± 30.8
1.08	2062.9 ± 3.0	280.7 ± 34.4
0.54	1620.1 ± 3.7	341.2 ± 41.9

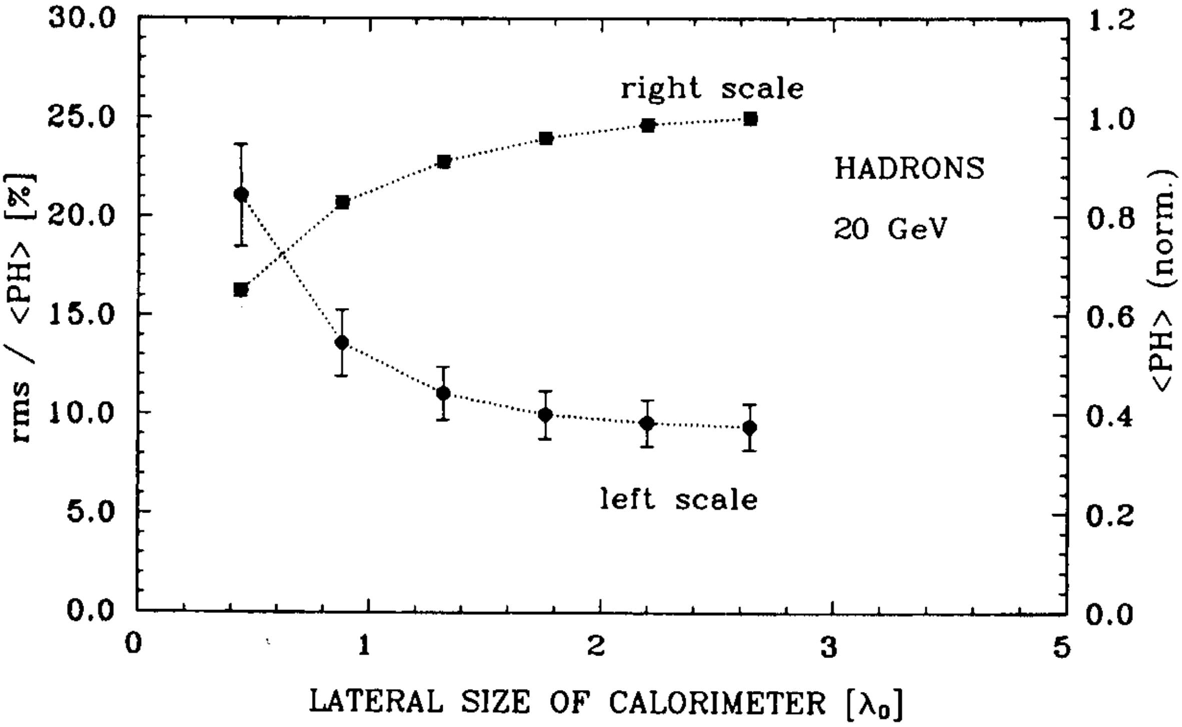

Figure 5.32: Hadronic Energy Resolution at 20 GeV ($rms/ < PH(h)_{TOT} >$, left Scale) and Mean Pulse Height (normalized, right scale) as a Function of the Lateral Size of the Calorimeter

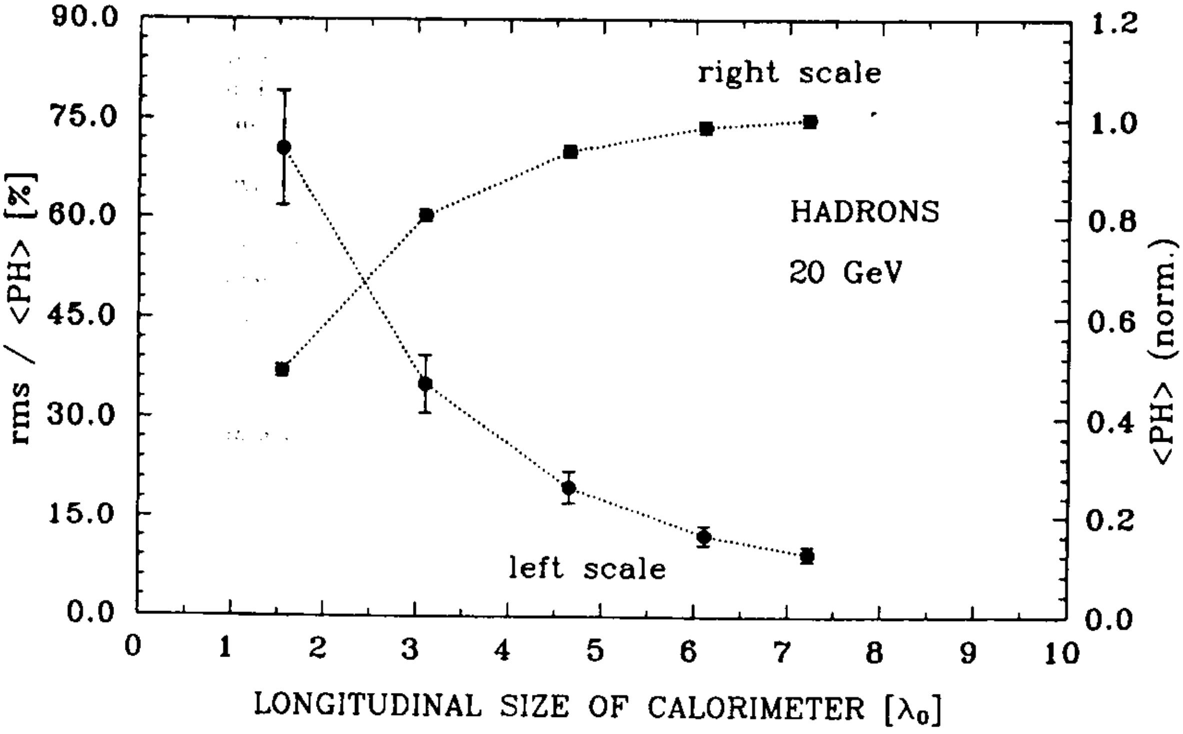

Figure 5.33: Hadronic Energy Resolution at 20 GeV ($rms/ < PH(h)_{TOT} >$, left Scale) and Mean Pulse Height (normalized, right scale) as a Function of the Longitudinal Size of the Calorimeter

The mean pulse height and the rms of the pulse height distribution obtained for hadrons at 20 GeV are given in Tab. 5.31 and Tab. 5.32. Fig. 5.32 shows the relative width $rms/ < PH(h)_{TOT} >$ of the total pulse height distribution in [%] (left scale) as a function of the lateral size of the calorimeter, given in units of λ_0. As the lateral size of the entire calorimeter (3.2 λ_0 effective) shrinks, the resolution deteriorates while the mean pulse height decreases (right scale; values are normalized to the mean pulse height obtained from the entire calorimeter). The same behaviour is observed if the longitudinal size of the calorimeter (7.2 λ_0) shrinks (Fig. 5.33), but with a much stronger variation of the resolution and the mean pulse height. Fig. 5.34 shows the deterioration of the energy resolution for an increasing fraction of leakage and the values are given in Tab. 5.33. The hadronic energy resolution at 0 is the energy resolution obtained with a longitudinal leakage cut in module 5 of 2% of the total energy and with a correction for transverse leakage from the top and bottom side of the calorimeter (sec.5.3.3). Obviously, the longitudinal leakage deteriorates the energy resolution much stronger than transverse leakage of the same amount.

Table 5.32: Influence of the Longitudinal Leakage on the Mean Pulse Height and on the rms of the Pulse Height Distribution for Hadrons at 20 GeV

Longitudinal Size λ_0	$< PH(h)_{1-5} >$ [ADC CH.]	rms [ADC CH.]
7.22	2492.3 ± 2.5	233.9 ± 28.7
6.11	2453.3 ± 3.2	299.4 ± 36.7
4.65	2330.7 ± 4.9	458.0 ± 56.2
3.10	2004.4 ± 7.5	703.8 ± 86.4
1.55	1230.2 ± 9.2	867.6 ± 106.4

Table 5.33: Influence of the Transverse and Longitudinal Leakage on the relative rms of the Pulse Height Distribution for Hadrons at 20 GeV

LATERAL		LONGITUDINAL	
Fraction of Leakage [%]	$\frac{rms}{< PH(h)_{1-5} >}$ [%]	Fraction of Leakage [%]	$\frac{rms}{< PH(h)_{1-5} >}$ [%]
0.0	8.44 ± 1.07	0.0	8.44 ± 1.07
0.34	9.39 ± 1.15	0.34	9.39 ± 1.15
1.69	9.58 ± 1.17	1.90	12.20 ± 1.50
4.35	9.98 ± 1.22	6.80	19.65 ± 2.41
9.21	11.06 ± 1.36		
17.51	13.61 ± 1.67	19.85	35.11 ± 4.31
35.22	21.06 ± 2.59	50.81	70.52 ± 8.67

This behaviour has also been observed with the CHARM calorimeter [CHA80]. It is explained by the fluctuations about the average longitudinal energy loss that are much larger than the ones for the transverse energy loss [FAB85].

5.4.4 The e/h- and $\tilde{e}/\widetilde{mip}$-Ratio of the T60B2 Uranium-Scintillator Calorimeter

After the improvement of the longitudinal uniformity of the T60UB1 calorimeter by inserting graded light filters between the scintillator plates and the wavelength shifter bars a nonuniformity of ±5% could still be observed (see Fig. 5.28). In addition, the light response very near the photomultiplier side drops down rapidly which is assumed to be due to the bent light guide.

To investigate the influence on the average electron response the first module was turned by 180° so that the response of the electromagnetic shower at the far end of the photomultiplier could be

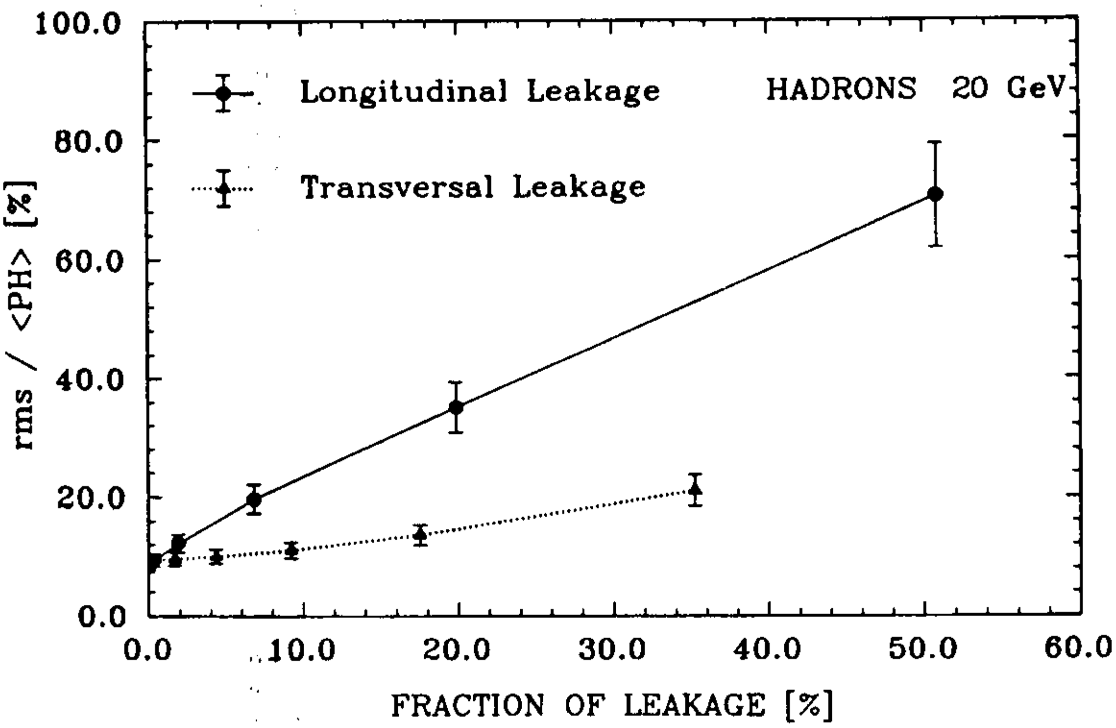

Figure 5.34: Deterioration of the Hadronic Energy Resolution as a Function of the Fraction of the Total Energy Leaking into Longitudinal or Transverse Direction; the Hadronic Energy Resolution at 0 is the Energy Resolution obtained with a Longitudinal Leakage Cut in Module 5 of 2% of the Total Energy and with a Correction for Transverse Leakage from the Top and Bottom Side of the Calorimeter

compared with that of the near end. The obtained values deviated by about 10%. Assuming that the nonuniformity curve decreases almost linear by this amount one can take the average of both mean pulse heights to get the nearly actual electron response.

The mean pulse height for hadrons has been corrected for the transverse leakage from the left and right side of the calorimeter (the top and bottom correction was done event-by-event), as in the case of all other T60 measurements (sec. 4.6, 5.1.5, 5.3.5). The resulted values of the mean pulse heights for electrons, hadrons and also for muons, for which no correction is needed, are listed in Tab. 5.34. Also given in Tab. 5.34 is the e/h- and the $\tilde{e}/\widetilde{mip}$-ratio with quoted statistical errors; the total error is 3%. The e/h- and the $\tilde{e}/\widetilde{mip}$-ratio as a function of energy are plotted in Fig. 5.35.

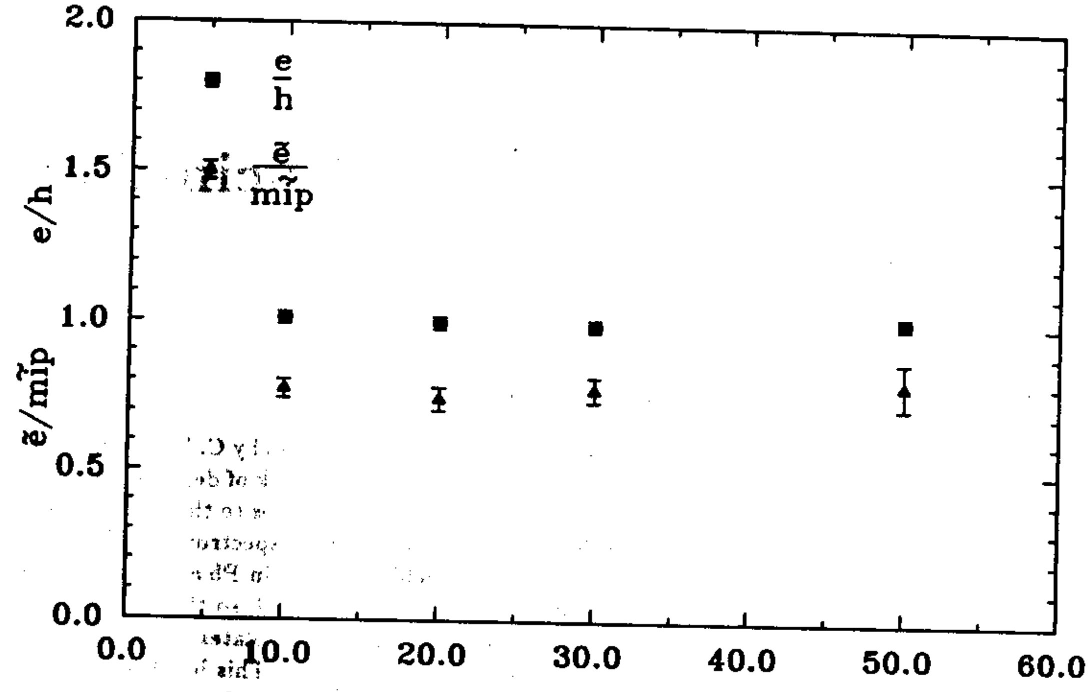

Figure 5.35: *e/h*- and $\tilde{e}/\widetilde{mip}$-Ratio of the T60UB2 Calorimeter as a Function of the Energy

Table 5.34: Electron-, Muon- and Hadron-Response of the T60UB2 Calorimeter, corrected for Longitudinal Nonuniformity (e, h) and for Leakage (h), and the resulting *e/h*- and $\tilde{e}/\widetilde{mip}$-ratio at 10, 20, 30, 50, 75 and 100 GeV; Statistical Errors are quoted, the Total Error is 3%

E [GeV]	e [ADC CH.]	h [ADC CH.]	μ [ADC CH.]	$\frac{e}{h}$	$\frac{\tilde{e}}{\widetilde{mip}}$
10	1273.0 ± 1.2	1257.7 ± 6.0	65.2 ± 2.0	1.012 ± 0.005	0.774 ± 0.031
20	2575.2 ± 1.9	2583.5 ± 9.6	71.8 ± 3.4	0.997 ± 0.004	0.742 ± 0.039
30	3805.9 ± 2.2	3839.6 ± 10.7	69.3 ± 3.3	0.991 ± 0.003	0.777 ± 0.042
50	6452.4 ± 2.5	6371.6 ± 12.2	71.8 ± 6.6	1.013 ± 0.002	0.799 ± 0.077
75		9693.2 ± 16.4			
100		12888.5 ± 20.0			

Chapter 6

Compensation with a Lead-Scintillator Calorimeter

6.1 The Proposed Calorimeter Configuration

The measurement of the induced radioactivity in different calorimeter blocks by C. Leroy and coworkers [LER85] has been briefly discussed in sec. 3.4. In addition to a massive block of depleted uranium they also exposed a massive lead block interleaved with a few thin uranium plates to the beam. In this way the neutron yield of lead was measured and informations on the neutron spectrum had been derived. Compared to the massive ^{238}U block the measured neutron yield is smaller in Pb and the total neutron spectrum is harder (Tab. 3.7). The neutron yield of lead is sufficiently high so that it should also be possible to achieve compensation with a hadron calorimeter built of lead plates as passive absorbers and an active absorber that is able to generate a signal via *np*-collisions. This has been proposed by R. Wigmans [WIG87] and H. Brückmann [AND87a]. For a compensating lead-scintillator calorimeter the ratio of lead to scintillator thickness is unusual high, namely 3 to 5, as predicted by R. Wigmans and H. Brückmann.

A calorimeter with 10 mm Pb and 2.5 mm scintillator (TPb) has been built and exposed to a hadron beam by U. Kötz and coworkers [BER87] in order to find out if compensation can also be achieved with a lead-scintillator calorimeter.

6.2 Description of the Lead-Scintillator Calorimeter

The entire calorimeter consisted of 9 towers arranged in a 3×3 matrix, with 3 towers combined to 1 module (see Fig. 6.1). One tower was subdivided into a 1 λ_0 (29 X_0) deep electromagnetic and a 4 λ_0 deep hadronic section. The electromagnetic section consists of 16 layers and the hadronic section of 65 layers. One layer is made of a 10 mm thick lead plate and a 2.5 mm thick scintillator plate.

The lead plates contained 4% antimony for mechanical stability. They were kept parallel at a distance of 3.5 mm by 2 spacers at the top and bottom of each plate. The whole stack in one module was held together by steel rods fed through the spacers and the lead plates.

The scintillator plates have been polished at all edges and wrapped into white paper leaving the readout edge open. The three scintillator plates in one module are separated by 2 mm thick PVC rods (see Fig. 6.1).

The lead and scintillator plates in the hadronic section are smaller in lateral direction by 7 mm than in the electromagnetic section because each section is read out separately on each side by two wavelength shifter bars of 2 mm thickness; therefore space has to be granted for the wavelength shifter bars of the hadronic part (see Fig. 6.1).

The collected light in the wavelength shifter bars was transmitted via plexiglass light guides to the photomultipliers (XP 2011). In Tab. 6.1 the dimensions and specifications of the TPb calorimeter are compiled.

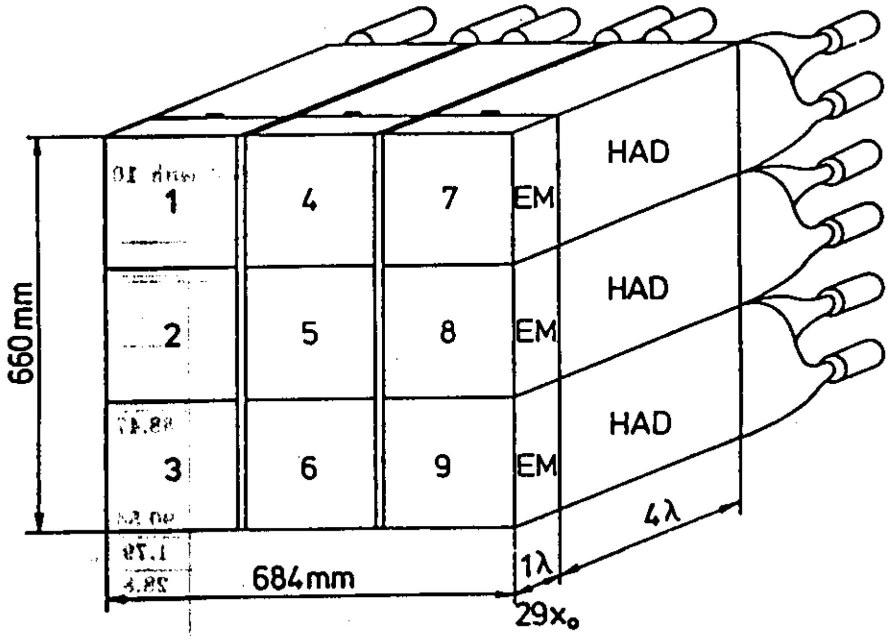

TPb CALORIMETER

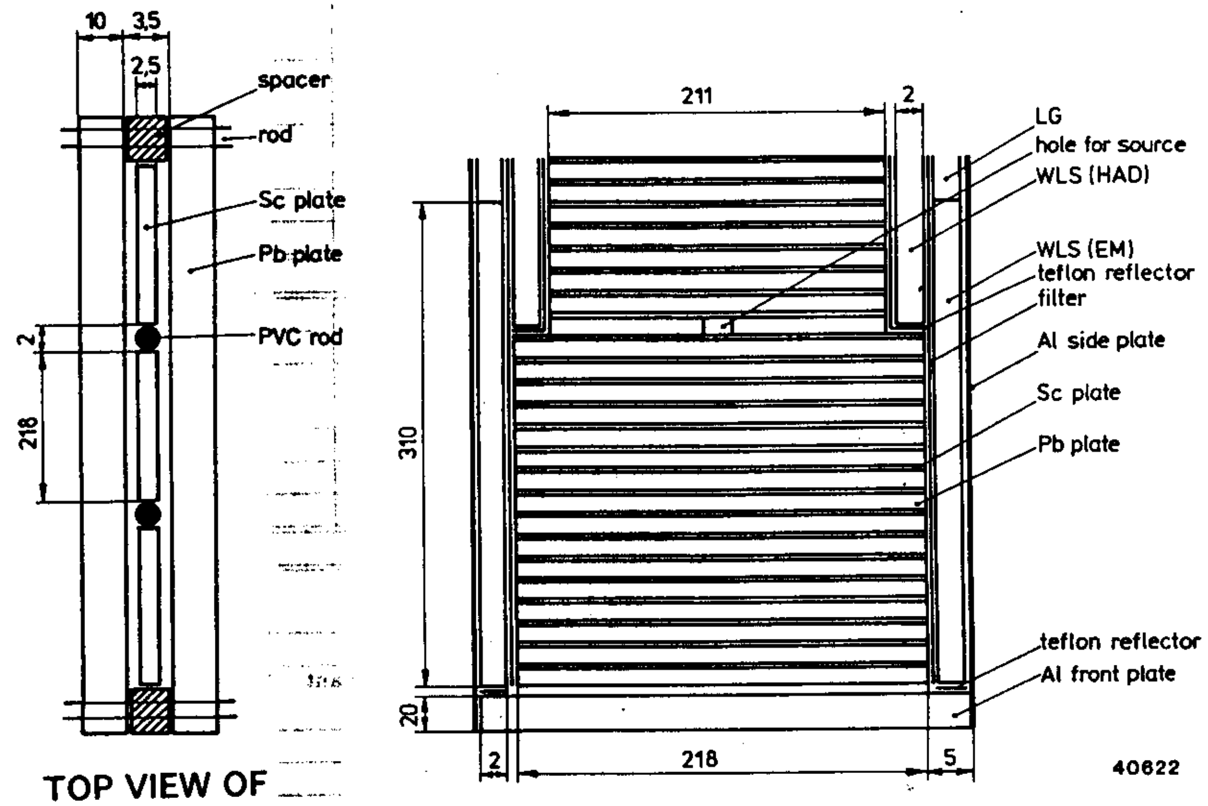

TOP VIEW OF 1 CALORIMETER LAYER

TOP VIEW OF 1 CALORIMETER TOWER

Figure 6.1: Schematic View of the TPb Calorimeter

Table 6.1: Dimensions and Specifications of the TPb Calorimeter inserted with 10mm thick Lead and 2.5mm thick Scintillator Plates

Calorimeter				
Lateral Dimensions of Calorimeter	660 × 684 mm^2			
Lateral Dimensions of Module	660 × 228 mm^2			
Lateral Dimensions of Tower	220 × 218 mm^2	EM Section (Al Front Plate Included)	$88.47X_0$	$3.14\lambda_0$
	220 × 211 mm^2	HAD Section	$90.54X_0$	$3.13\lambda_0$
Total Depth of 1 Layer	13.5 mm		$1.79X_0$	$0.062\lambda_0$
Total Depth of 1 Tower		EM Section (Al Front Plate Included)	$28.8X_0$	$1.04\lambda_0$
		HAD Section	$116.2X_0$	$4.01\lambda_0$
	1093.5 mm	EM + HAD	$145.0X_0$	$5.05\lambda_0$
Passive Layer				
Lateral Dimensions (Effective)	660 × 218 mm^2	EM Section		
Lateral Dimensions (Effective)	660 × 211 mm^2	HAD Section		
Number of Layers	16	EM Section		
	65	HAD Section		
Thickness of Plates	10 mm			
Material	96 % Pb, 4% Sb			
Active Layer				
Lateral Dimensions	218 × 218 mm^2	EM Section		
Lateral Dimensions	218 × 211 mm^2	HAD Section		
Number of Layers	16	EM Section		
	65	HAD Section		
Thickness of Plates	2.5 mm			
Material	SCSN-38 (Polystyrene Base)			
Airgap	1.0 mm			
Readout				
Wavelength Shifter	310 × 220 mm^2			EM Section
	918 × 220 mm^2			HAD Section
Thickness of WLS	2 mm			
Material	PMMA Base, UV absorbant K27 (125 mg/l)			
Lightguide	Plexiglass			
Photomultiplier	XP 2011			

To measure in the low energy range from 3 to 10 GeV the calorimeter was exposed to the T7-beam at the CERN PS. The same set-up was used as for the measurements with the T60Pb and T60UA calorimeter (sec. 4.1) except for the data aquisition system which was a computer based on the Motorola 68020 CPU instead of the PDP 11. In addition, two Cherenkov counters filled with CO_2 gas have been used for electron identification. The set-up is sketched in Fig. 4.3 where instead of the T60 calorimeter the TPb calorimeter has been installed. The TPb calorimeter was put on a moveable support. This allowed a horizontal scan of the central towers of the calorimeter.

For the high-energy range of 10 to 100 GeV the calorimeter was moved to the X5-beam at the SPS at CERN. In this environment the measurnments with the T60UB1/2 calorimeter were performed. The same set-up was used (see Fig. 5.16) with the TPb calorimeter replacing the T60 calorimeter. One module of the T60UB2 calorimeter (1.5 λ_0 in depth) was placed about 80 cm behind the lead calorimeter in order to gain information on the longitudinal leakage. The TPb calorimeter was installed on a moveable stage for a horizontal and vertical scan of all towers.

In order to avoid a saturation of the ADC at the highest energies and to measure the muon signal well separated from the pedestals the analog signals of the photomultipliers have been splitted passively into a 3/4 and a 1/4 fraction.

6.3 Calibration and Particle Selection

6.3.1 Calibration

The TPb calorimeter has been calibrated with three different methods:

- a ^{60}Co source of 3 mCi (111 MBq), inserted into a hole in the middle of the lead plate separating the electromagnetic from the hadronic part, was used for online calibration and to monitor the gain stability. The signal of each tower due to this source was integrated over 10 μs and the high voltage was adjusted according to the mean pulse height;
- the electromagnetic sections of each tower were calibrated by equalizing the mean pulse heights of electrons at 10 GeV. Similarly, the hadronic sections were calibrated by equalizing the mean pulse heights of hadrons at 10 GeV;
- the intercalibration between the electromagnetic and hadronic sections was done by varying a multiplication factor α for all hadronic sections, demanding that the energy resolution for hadrons will become minimal. This calibration has been compared with the muon response at 50 GeV in both sections. The ratio of the muon response of both sections should almost be equal to the ratio of the number of scintillator plates, namely $65/16 = 4.06$ if ionization loss is the only process of energy deposition of the muons. At 50 GeV, however, one has to correct the energy loss of muons for bremsstrahlung and pair production which has been estimated to be about 5% [BER87].

At the T7-beam the 3 central towers of the TPb calorimeter could be calibrated only with beam particles because the entire calorimeter was only moveable in horizontal direction. The outer towers have been calibrated with the ^{60}Co source. The calibration of the central towers with the ^{60}Co source has been compared with the electron, hadron and muon response, showing differences of 5%. These differences are attributed to the fact that the ^{60}Co source irradiated only the closest scintillator plates while the beam particles reached almost all plates.

At the X5-beam all 9 towers were calibrated with beam particles. A first online calibration by adjusting the high voltages was done with the signal from the ^{60}Co source. The difference between the electron and hadron calibration of the electromagnetic section was ±1%, the difference between the muon and electron calibration was ±5%. The hadron and muon calibration in the hadronic section differed by ±2%.

6.3.2 Particle Selection

In addition to the online particle separation according to the trigger conditions given in sec. 4.2 and sec. 5.1.2 a particle selection by means of the Cherenkov counter and the calorimeter itself has been performed in the offline analysis. Two quantities were mainly used for the selection, namely

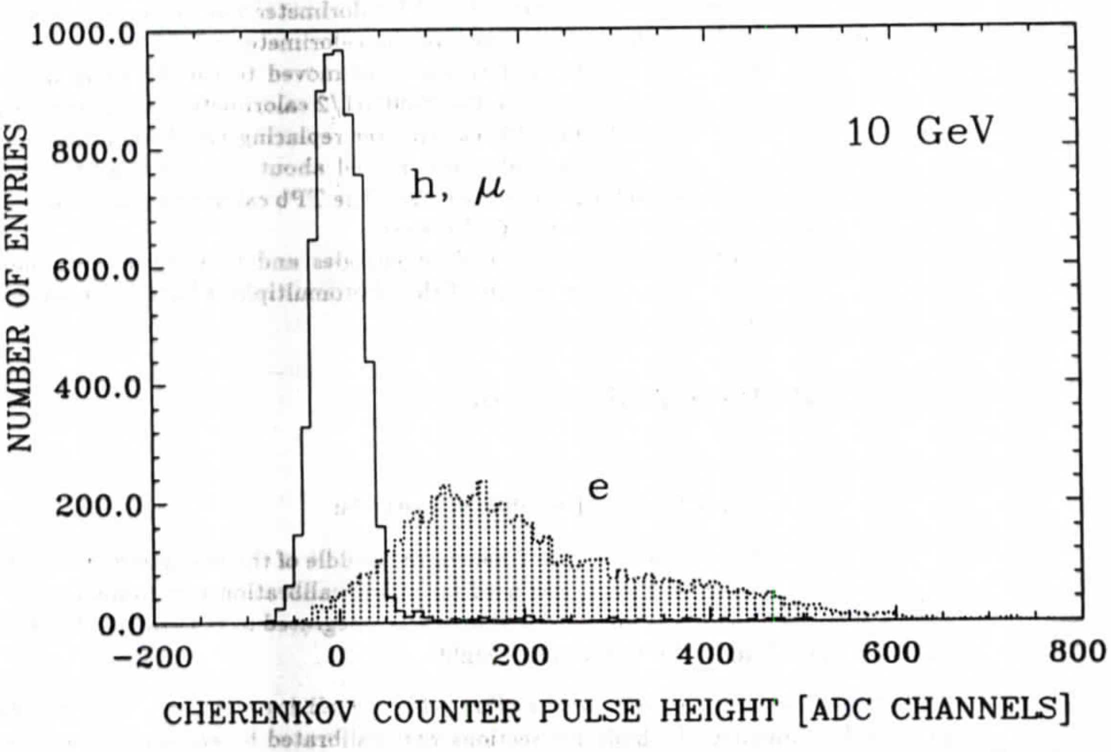

Figure 6.2: Spectrum of both Cherenkov Counters at 10 GeV used for Electron Separation from Hadrons and Muons

$C_{12} = C_1 + C_2$, which is the sum spectrum of both Cherenkov counters (Fig. 6.2), and $E_{OUT} = \sum_{OUT} PH(e, \mu, h)_{OUT}$ (Fig. 6.3), where the sum of the pulse height for electrons, muons and hadrons is performed over all outer towers (OUT), i.e. except the central one. In Fig. 6.2 one observes well separated electrons from hadrons and muons while in Fig. 6.3 muons are well separated from hadrons.

For muons it was required that the deposited energy in the outer towers was smaller than $\sim 100\,MeV$. An equal response in the left and right photomultiplier of the central tower was also demanded from a muon event.

Electrons were separated from hadrons by a cut in C_{12}. Electron events had to fulfill the additional condition that the total energy deposited outside the electromagnetic section in which the electromagnetic shower was contained should be less than $\sim 500\,MeV$. The contamination of the electron sample with hadrons was estimated to be about 0.1 %.

For the selection of hadrons the muons have to be separated by a cut in Fig. 6.3. Electrons have already been separated with C_{12}.

6.4 Uniformity and Light Yield of the Readout System

6.4.1 Transverse Uniformity in the Scintillator

The transverse uniformity of light collection in the scintillator plates has been determined by horizontal and vertical scans of the central tower with the beam.

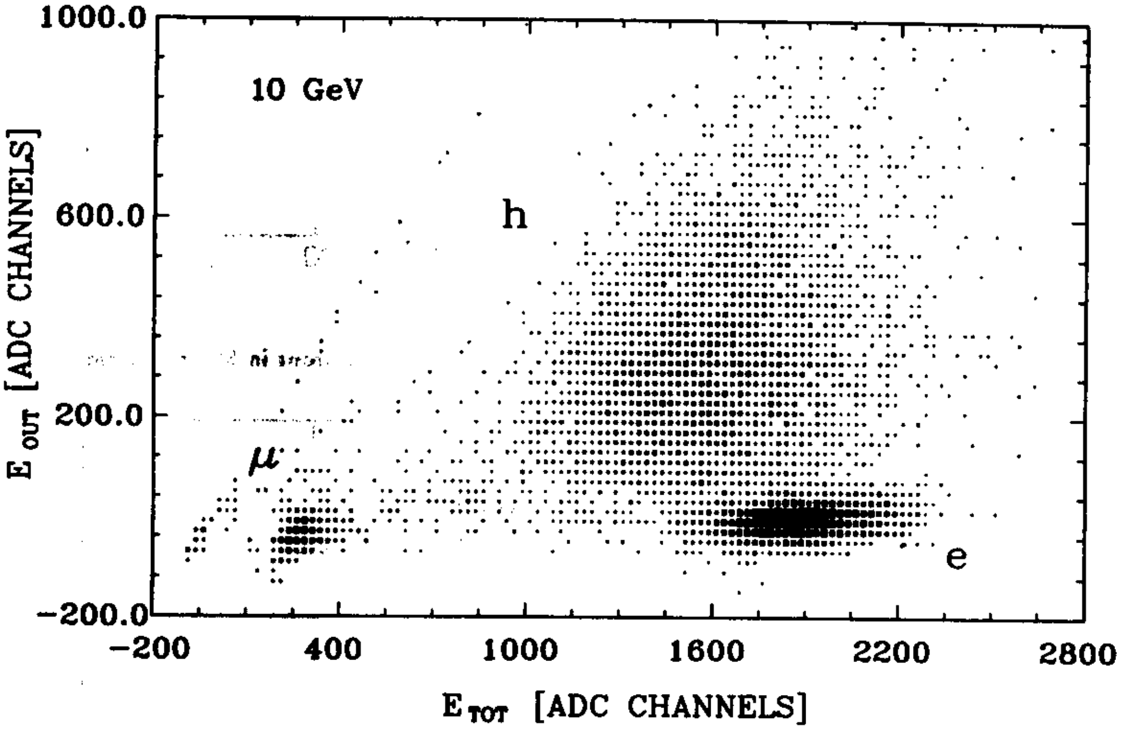

Figure 6.3: The Energy in the outer Towers (E_{OUT}) versus the Energy in the Entire Calorimeter for Electrons, Hadrons and Muons

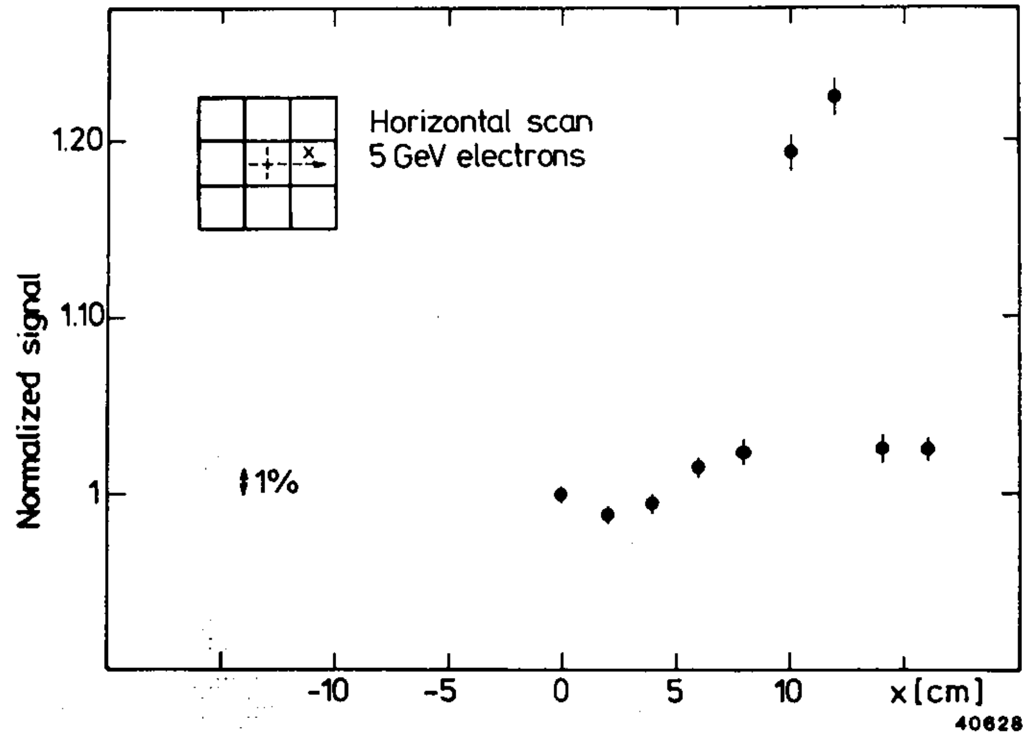

Figure 6.4: Horizontal Scan of the Central Tower with 5 GeV Electrons in Steps of 1 cm

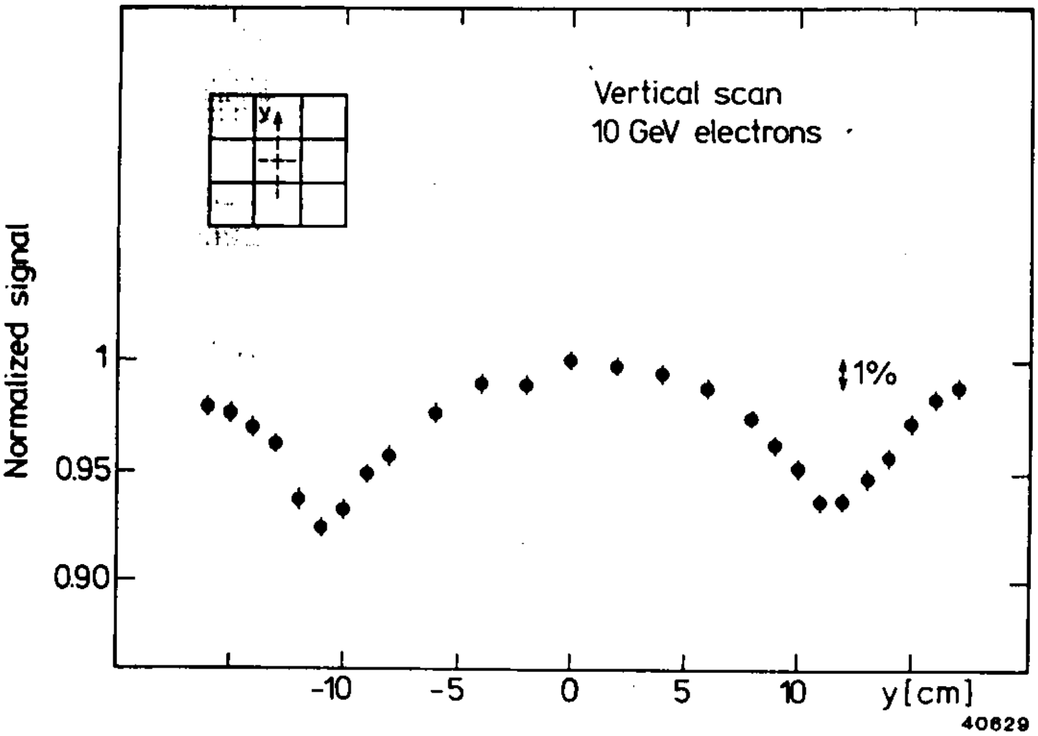

Figure 6.5: Vertical Scan of the Central Tower with 10 GeV Electrons in Steps of 2 cm

The horizontal scan was performed with 5 *GeV* electrons at the T7-beam in steps of 2 *cm*, the vertical scan with 10 *GeV* electrons in steps of 1 *cm* at the X5-beam. The response was found to be uniform within ±1% in a region of ±6 *cm* around the centre of the scintillator plate (Fig. 6.4). At the edges of the plates in vertical direction the light yield increased by about ~ 20% which is attributed to nonexponential effects in addition to the attenuation in the scintillator plates. These effects have also been observed with the T60 modules and explanations are given there (sec. 4.5.3).

At the edges of the scintillator plates in vertical direction the light yield decreased by 8% (Fig. 6.5) due to the dead area introduced by the PVC rods and the influence of the close reflecting edge.

6.4.2 Longitudinal Uniformity of the Wavelength Shifter

The longitudinal uniformity of the wavelength shifter has been optimized in a similar way as for the T60UB2 calorimeter (sec. 5.4.1). The attenuation curve of the wavelength shifter has been measured on a dismanteled wavelength shifter bar and according to this curve a graded light filter has been produced.

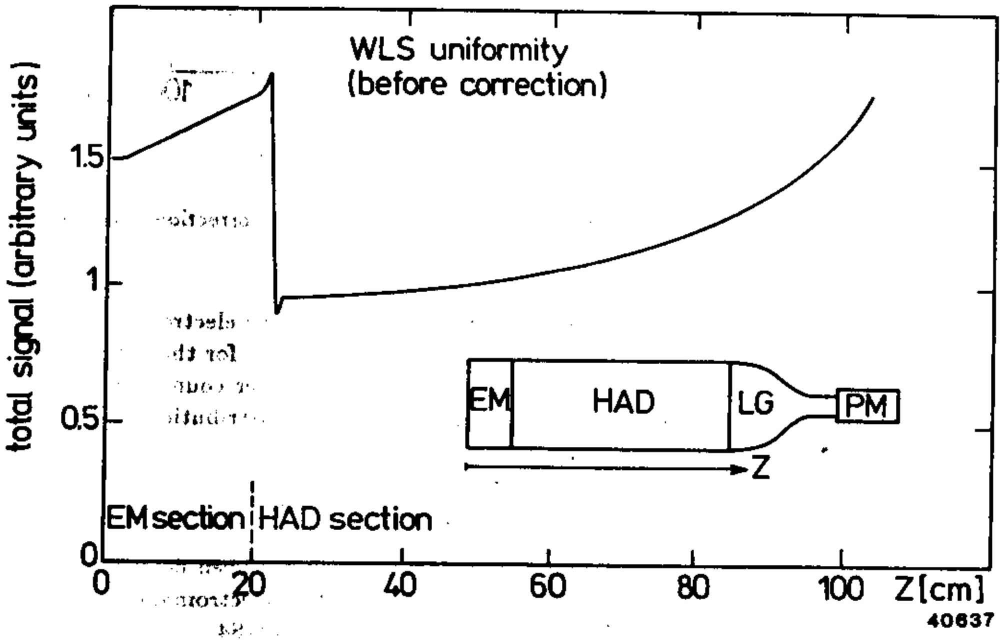

Figure 6.6: Longitudinal Light Response of the Wavelength Shifter without any Correction

The separate readout of the electromagnetic and hadronic section introduced a sharp decrease of the light yield in the direction of the penetrating particle (Fig. 6.6). To reduce this effect the wavelength shifter bar of the hadronic section overlapped that of the electromagnetic section by 10 *cm* (see Fig. 6.1). However, this correction was insufficient, but with the light filter inserted between the readout edges of the scintillator plates and the wavelength shifter bars an overall uniformity of ±5% has been achieved (Fig. 6.7).

6.4.3 Light Yield of one Tower of the Lead-Scintillator Calorimeter

The amount of light that is collected from the left and right side of one tower of the TPb calorimeter is given by the average number of photoelectrons converted by the photomultipliers per incident energy. The average number of photoelectrons has been determined from the relative width

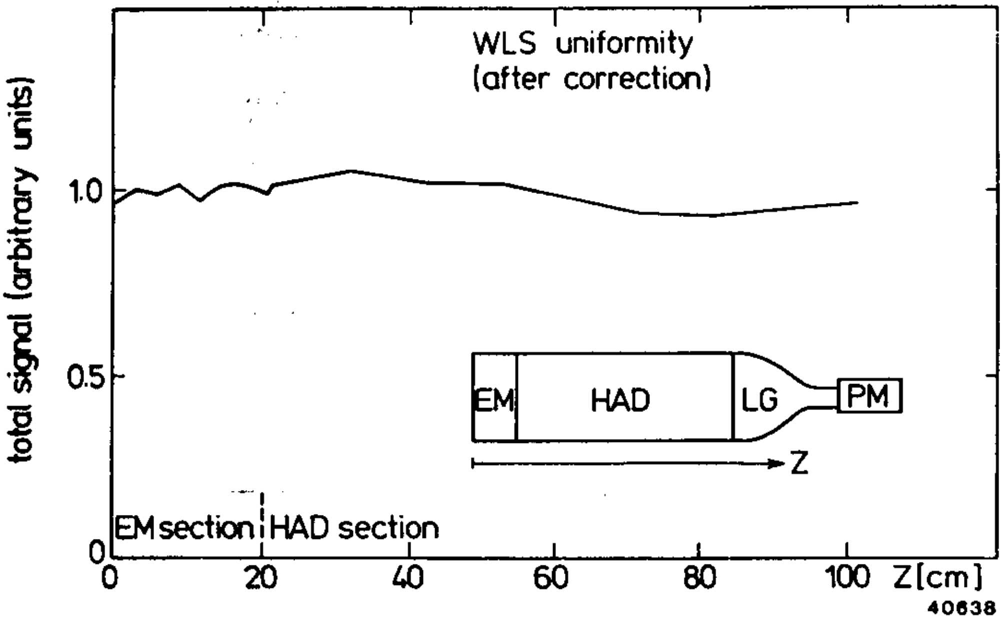

Figure 6.7: Longitudinal Light Response of the Wavelength Shifter after a Correction with a Graded Light Filter

$\sigma_{L-R}(e)/ < PH_{L+R} >(e)$ of the difference distribution of electrons in the electromagnetic section using eq. 4.11. The measurements done at the SPS have not been included for the determination since $\sigma_{L-R}(e)/ < PH_{L+R} >(e)$ is sensitive to the beam spot size and no finger counter has been used for the SPS measurements. The obtained relative width of the difference distribution is:

$$\frac{\sigma_{L-R}}{< PH_{L+R} >}(e) = \frac{(6.6 \pm 0.1)\%}{\sqrt{E[GeV]}}. \tag{6.1}$$

From this the number of photoelectrons per GeV of incident energy has been determined to $< N_{pe} >$ $= 230 \pm 7$. This corresponds to 10 photoelectrons per MeV of visible electromagnetic shower energy at an electromagnetic sampling fraction of $\hat{e} = 2.4\%$ calculated with EGS4.

6.5 Transverse and Longitudinal Leakage of Hadronic Energy in the Lead-Scintillator Calorimeter

6.5.1 Transverse Leakage

The amount of hadronic energy leaking into the tranverse direction has been measured by shooting into the central tower of each module and determine the energy in the outer towers. A fraction of $\sim$ 80% of the total signal is contained in the central tower within the energy range of 3 to 75 GeV. The average transverse leakage was determined from the energy deposition in the individual towers when the beam was directed to the center of the outer towers. An average transverse leakage of 4-5% has been observed which is independent of the incident energy. The obtained values for different energies are given in Tab. 6.2.

Table 6.2: Transverse Leakage measured with the TPb Calorimeter

E [GeV]	Transverse Leakage in Fraction of Total Energy [%]
5	4.8
10	4.4
20	4.7
30	4.2
50	4.6
75	4.5

6.5.2 Longitudinal Leakage

The longitudinal leakage of hadronic energy out of the TPb calorimeter has been measured with the T60UB2 calorimeter module placed behind. The determined fraction of total energy leaking into the longitudinal direction is listed in Tab. 6.3.

Table 6.3: Longitudinal Leakage out of the TPb Calorimeter measured with the T60UB2 Calorimeter Module placed behind

E [GeV]	Longitudinal Leakage in Fraction of Total Energy [%]
10	0.8
20	3.2
30	4.7
50	6.5
75	7.7

Because of the significant influence of the longitudinal leakage on the hadronic energy resolution one tries to select only those hadronic events which are almost fully contained in the TPb calorimeter. Two different methods have been applied as in the case of the T60Pb and the T60UA calorimeter (sec. 4.3.2, 5.1.3):

1. All events that deposit less than 1.5 *GeV* in the T60UB2 calorimeter module have been included in the hadronic event sample. The fraction of hadronic events decreases due to this cut from 4% at 10 *GeV* to 50% at 75 *GeV*, as can be seen from Tab. 6.4. The rejected events are mainly those with a large shower length or those which start to shower only very deep in the calorimeter.

Table 6.4: Event Reduction due to Longitudinal Leakage Cut according to Method 1 (see text)

E [GeV]	Fraction of Hadronic Event Reduction [%]
10	3.5
20	12.7
30	21.1
50	36.6
75	49.3

2. All events that deposit less than 1.5 *GeV* in the electromagnetic section of the calorimeter have been rejected from the hadronic event sample. The rejected events are those hadrons which cross the scintillator plates of the electromagnetic section under minimum ionization loss before their nuclear interactions generate a shower. In this way the hadron sample consists of showers with their start vertex placed within the first nuclear interaction length of the entire calorimeter. About 55% of the total hadron sample passed this cut, rather independent of the beam energy.

6.6 Energy Resolution of the Lead-Scintillator Calorimeter

The pulse height distribution for electrons and hadrons obtained from the measurements at the PS for 3 to 10 GeV are plotted in Fig. 6.8 together with the muon pulse height distribution at 5 GeV. The same distributions obtained from the measurements at the SPS are shown in Fig. 6.9 in the energy range 10 to 75 GeV (electrons and hadrons) and at 10 GeV for muons. The pulse height distribution of hadrons are obtained from the event sample left over after the longitudinal leakage cut according to method 1. The curves fitted to the electron and hadron distributions are Gauss functions, where for hadrons a $\pm 2\sigma$ cut around the mean value has been applied to suppress the small tails mostly due to leakage. The muon distribution in the same figure is the response of the electromagnetic section only. A convoluted Moyal-Gauss function has been fitted to the data.

The mean values and the widths of the pulse height distributions to calculate the energy resolution of the calorimeter have been obtained from the fits. They are quoted in Tab. 6.5.

Table 6.5: **Mean Values and Energy Resolutions of Electrons and Hadrons at 3, 5, 7 and 10 GeV (PS measurements) and 10, 20, 30, 50 and 75 GeV (SPS measurements); ($< PH(e,h)_T >$ denotes the total pulse height in the calorimeter, i.e. in the EM plus the HAD section)**

	ELECTRONS		HADRONS	
E [GeV]	$< PH(e)_T >$ [ADC CH.]	$\frac{\sigma_E(e)}{\sqrt{E[GeV]}}$ [%]	$< PH(h)_T >$ [ADC CH.]	$\frac{\sigma_E(h)}{\sqrt{E[GeV]}}$ [%]
3	750.4 ± 1.4	23.9 ± 0.3	630.8 ± 1.8	43.1 ± 0.5
5	1259.8 ± 1.9	23.7 ± 0.3	1084.6 ± 2.1	45.0 ± 0.5
7	1742.6 ± 2.1	23.1 ± 0.3	1506.2 ± 1.3	46.0 ± 0.5
10	2508.0 ± 2.9	23.8 ± 0.3	2213.3 ± 2.9	45.8 ± 0.5
10	1924.0 ± 3.4	24.2 ± 0.4	1726.0 ± 3.0	45.6 ± 0.7
20	3933.0 ± 5.1	23.9 ± 0.5	3535.0 ± 6.0	42.0 ± 0.7
30	5877.0 ± 6.0	24.3 ± 0.5	5386.0 ± 7.0	43.7 ± 0.7
50	9691.0 ± 16.0	25.1 ± 0.6	8839.0 ± 10.0	42.5 ± 0.7
75	14537.0 ± 31.0	25.9 ± 1.3	13371.0 ± 13.0	44.2 ± 0.8

The values for the energy resolution are plotted in Fig. 6.10 as a function of energy. The contribution to the energy resolution from the photoelectron statistic (eq. 6.1) is also plotted. The parametrizations eq. 4.4 (electrons) and eq. 4.6 (hadrons) have been fitted to the data. The achieved parameters a and b for electrons are

$$\begin{aligned} a &= 23.5\% \pm 0.7\% \\ b &= 1.2\% \pm 0.2\% \end{aligned} \tag{6.2}$$

and for hadrons

$$\begin{aligned} a &= 44.2\% \pm 1.3\% \\ b &= 0.0\% \pm 0.0\%. \end{aligned} \tag{6.3}$$

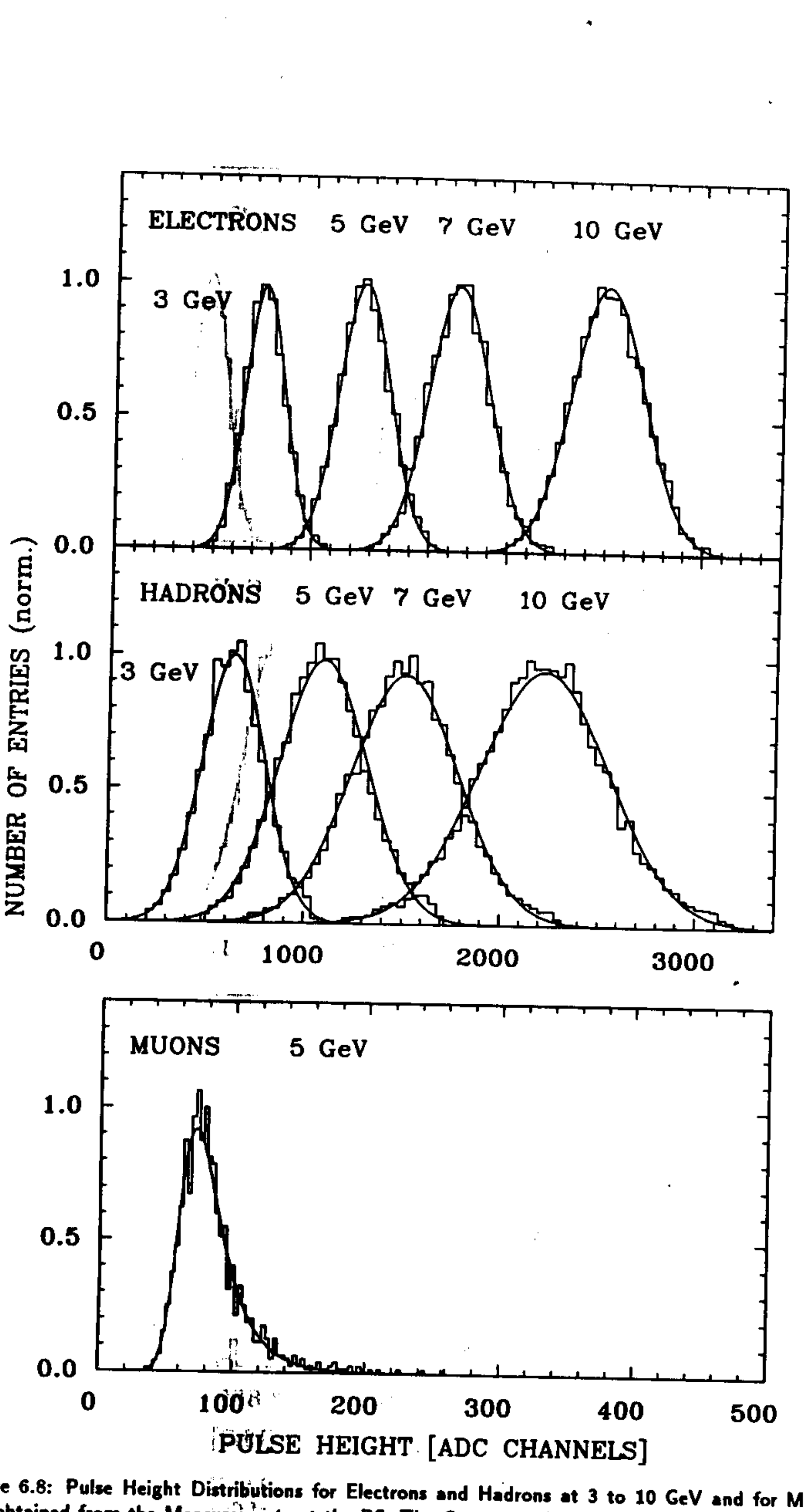

Figure 6.8: Pulse Height Distributions for Electrons and Hadrons at 3 to 10 GeV and for Muons at 5 GeV obtained from the Measurements at the PS. The Curves are Fits of Gauss Functions (Electrons and Hadrons) and of a Convoluted Moyal-Gauss Function (Muons)

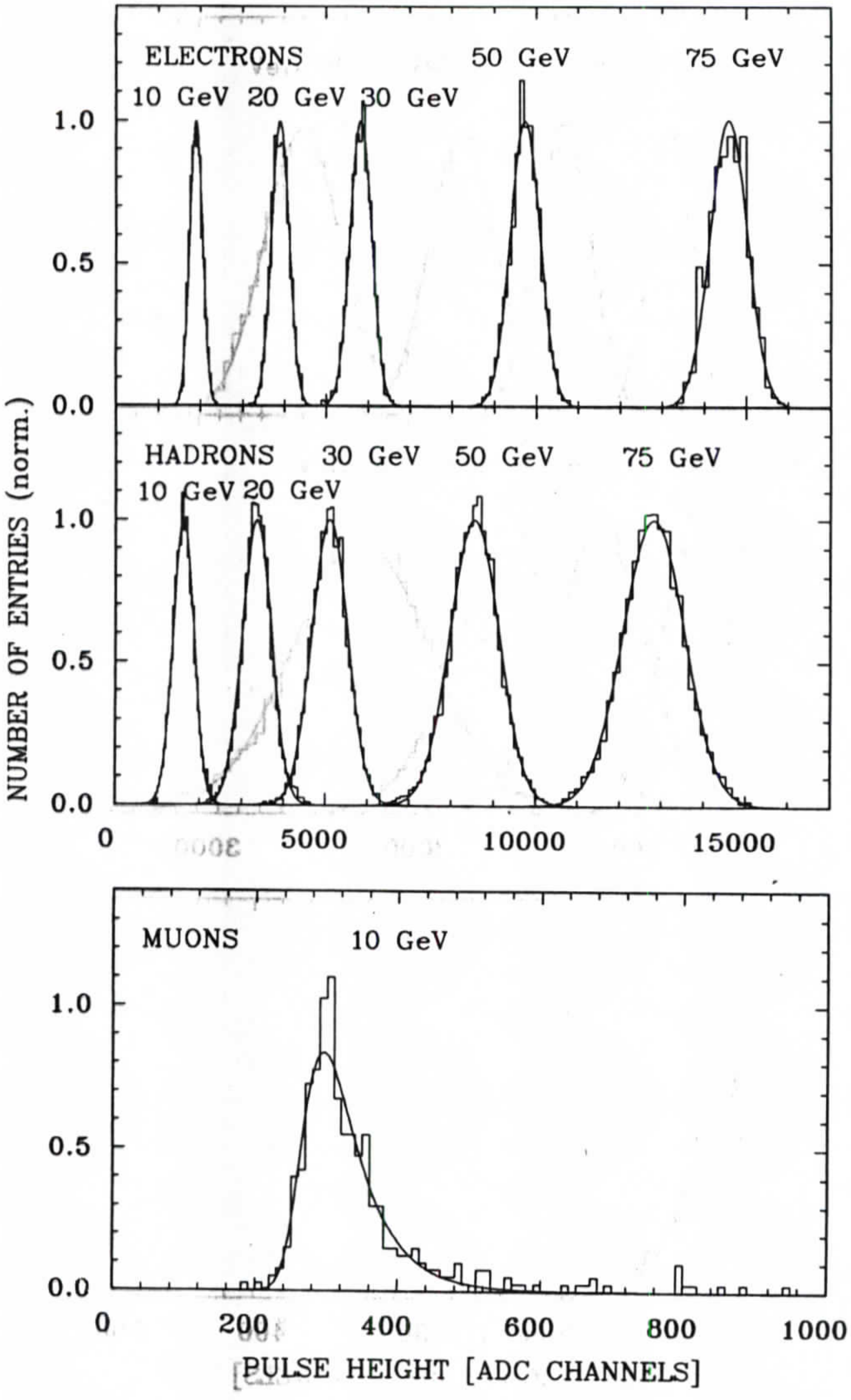

Figure 6.9: Pulse Height Distributions for Electrons and Hadrons at 10 to 75 GeV and for Muons at 10 GeV obtained from the Measurements at the SPS. The Curves are Fits of Gauss Functions (Electrons and Hadrons) and of a Convoluted Moyal-Gauss Function (Muons)

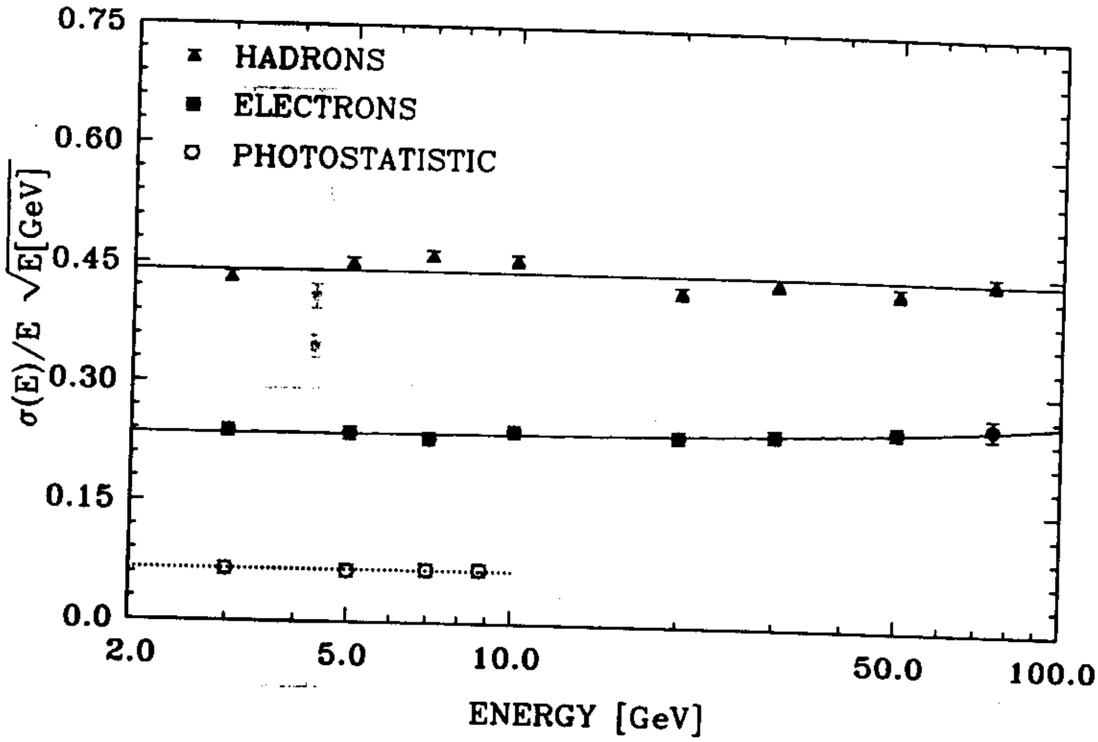

Figure 6.10: Energy Resolution of the TPb Calorimeter for Electrons and Hadrons as a Function of Energy and the Contribution from Photostatistic

According to EGS4 calculations the sampling fluctuations are:

$$\frac{\sigma_s(e)}{E} = \frac{(22.0 \pm 0.5)\%}{\sqrt{E[GeV]}}. \tag{6.4}$$

Summing eq. 6.1 and eq. 6.4 quadratically yields:

$$\frac{\sigma_t(e)}{E} = \frac{(23.0 \pm 0.5)\%}{\sqrt{E[GeV]}}, \tag{6.5}$$

in good agreement with the measured energy resolution for electrons.

The response of the calorimeter is linear within ± 1% for electrons and ± 2.5% for hadrons. Fig. 6.11 shows the deviation from the mean linearity.

6.7 The e/h- and $\tilde{e}/\widetilde{mip}$-Ratio of the Lead-Scintillator Calorimeter

From the measured mean values of the electron and hadron pulse height distributions the e/h-ratio has been calculated in the energy range from 3 to 75 GeV. The major influence on this ratio, the longitudinal nonuniformity and the longitudinal leakage, have both already been corrected: the nonuniformity has been improved by a graded light filter with a remaining nonuniformity of ±5% while for the longitudinal leakage a cut (method 1) on the hadrons sample has been applied. The transverse leakage that was found to be of the order of 5% independent of the incident energy has still to be taken into account for the mean hadron response quoted in Tab. 6.5. The mean values of the hadron response corrected for the transverse leakage are listed in Tab. 6.6. Also listed are the mean values of the muon response and the calculated e/h- and $\tilde{e}/\widetilde{mip}$- ratio. The total error on the e/h-ratio was estimated to be about 4%. The e/h- and $\tilde{e}/\widetilde{mip}$-ratio are plotted in Fig. 6.12 as a function of the energy.

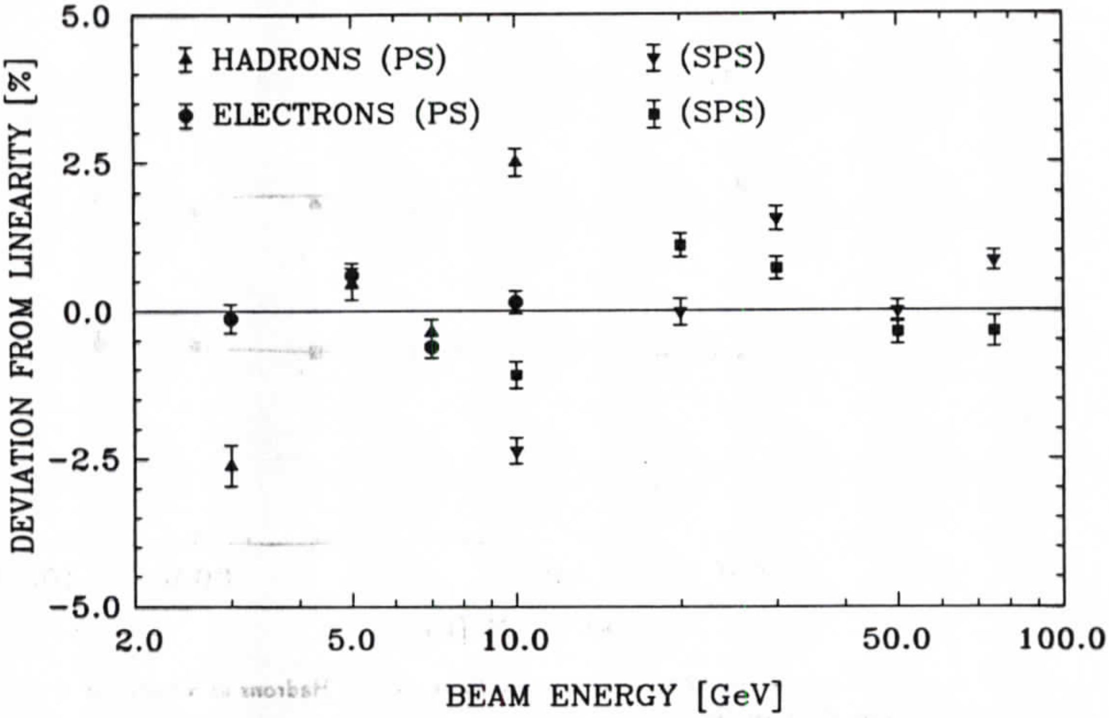

Figure 6.11: Deviation from Linearity in [%] for Electrons and Hadrons in the TPb Calorimeter

Table 6.6: Mean Response of Muons and Hadrons (corrected for Transverse Leakage), e/h- and $\tilde{e}/\widetilde{mip}$-ratio for 3, 5, 7 and 10 GeV (PS measurements) and for 10, 20, 30, 50 and 75 GeV (SPS measurements); ($< PH(\mu)_{EM} >$ denotes the Mean Pulse Height of Muons in the EM Section while $< PH(h)_T >$ denotes the Mean Pulse Height of Hadrons in the Total Calorimeter; Statistical Errors are quoted)

E [GeV]	$< PH(\mu)_{EM} >$ [ADC ch.]	$< PH(h)_T >$ [ADC ch.]	$\frac{e}{h}$	$\frac{\tilde{e}}{\widetilde{mip}}$
3	84.2 ± 1.0	659.2 ± 1.9	1.138 ± 0.004	0.717 ± 0.020
5	84.6 ± 1.0	1133.5 ± 2.2	1.111 ± 0.003	0.749 ± 0.020
7	86.1 ± 1.0	1574.1 ± 1.4	1.107 ± 0.002	0.745 ± 0.020
10	87.9 ± 1.0	2313.0 ± 3.0	1.084 ± 0.002	0.753 ± 0.020
10	68.6 ± 1.2	1803.8 ± 3.1	1.067 ± 0.003	0.740 ± 0.022
20	71.7 ± 1.2	3694.3 ± 6.3	1.065 ± 0.002	0.755 ± 0.022
30	71.5 ± 1.2	5628.6 ± 7.3	1.044 ± 0.002	0.774 ± 0.023
50	74.0 ± 1.2	9237.2 ± 10.5	1.049 ± 0.002	0.768 ± 0.023
75	75.6 ± 1.2	13973.4 ± 13.6	1.040 ± 0.002	0.779 ± 0.023

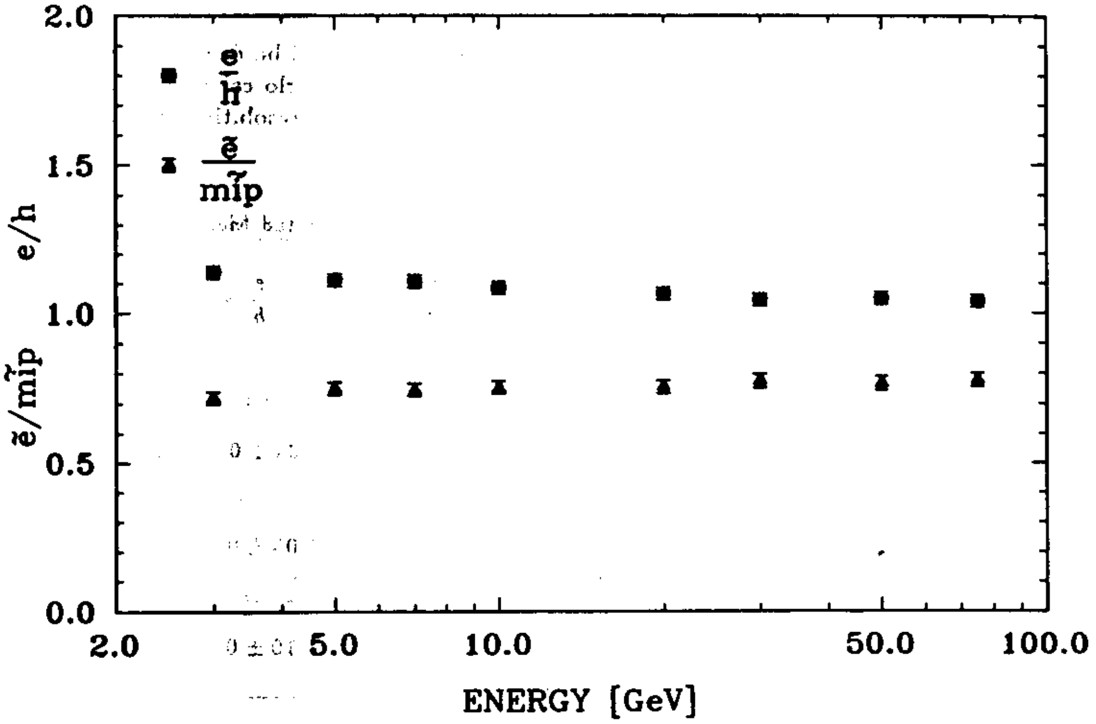

Figure 6.12: The e/h- and $\tilde{e}/\widetilde{mip}$-ratio of the TPb Calorimeter as a Function of the Energy

Chapter 7

Comparison of the Results

7.1 Compilation of the Results

In this chapter the presented results of the described measurements will be discussed and compared with results from other measurements and predictions from Monte Carlo calculations. The values obtained from the previously described measurements for the energy resolution, the e/h- and the $\tilde{e}/\widetilde{mip}$-ratio averaged over all energies are compiled in Tab. 7.1.

Table 7.1: Compilation of the Results obtained from the presented Measurements

CALORIMETER CONFIGURATION		R_d	$\frac{\sigma_E(e)}{\sqrt{E[GeV]}}$ [%]	$\frac{\sigma_E(h)}{\sqrt{E[GeV]}}$ [%]	$< \frac{e}{h} >$	$< \frac{\tilde{e}}{\widetilde{mip}} >$
T60Pb	4.75 *mm Pb* 0.5 *mm Al* 5.0 *mm SCSN-38*	0.95	11.7 ± 0.8 $\oplus$ 2.5 ± 0.4	41.0 ± 4.8 $+$ 6.1 ± 2.1	1.34 ± 0.05	0.65 ± 0.10
TPb	10.0 *mm Pb* 2.5 *mm SCSN-38*	4.00	23.5 ± 0.7 $\oplus$ 1.2 ± 0.2	44.2 ± 1.3	1.05 ± 0.04	0.75 ± 0.03
T60UA	3.2 *mm DU* 5.0 *mm SCSN-38*	0.64	14.2 ± 0.6 $\oplus$ 1.6 ± 0.4	29.6 ± 1.2 $+$ 3.2 ± 0.5	1.10 ± 0.04	0.68 ± 0.04
T60UB1	3.2 *mm DU* 3.0 *mmSCSN-38* without lightfilter	1.07	16.7 ± 0.5 $\oplus$ 1.5 ± 0.1	35.5 ± 1.1 $+$ 0.7 ± 0.2	1.02 ± 0.03	0.74 ± 0.03
T60UB2	3.2 *mm DU* 3.0 *mm SCSN-38* with lightfilter	1.07	17.4 ± 0.5 $\oplus$ 1.0 ± 0.2	32.9 ± 1.0 $+$ 0.5 ± 0.1	1.00 ± 0.03	0.77 ± 0.05
WA78	10.0 *mm DU* 2.0 *mm Fe* cladding 5.0 *mm NE110*	2.00	38.6 ± 1.9 $\oplus$ 4.6 ± 0.2	43.1 ± 5.6 $+$ 4.3 ± 1.3	0.76 ± 0.05	0.63 ± 0.06
	$\ominus \frac{\sigma(p)}{p}$		28.7 ± 1.9 $\oplus$ 1.9 ± 1.2	37.7 ± 4.8 $+$ 3.4 ± 1.1		

7.2 Discussion of the Presented Results

A first comparison of the presented data is done for the e/h-ratio as a function of the ratio of the passive to active plate thickness $R_d = d(passive)/d(active)$ (Fig. 7.1). The e/h-ratios of the two calorimeters using lead as passive absorber are clearly distinguishable from the ones of the calorimeters assembled with depleted uranium plates. Because the active absorber is the same in both cases, the passive absorber material is one of the essential parameter that influences the e/h-ratio. For a given absorber material the results in Fig. 7.1 show that the ratio R_d is the crucial parameter to tune the e/h-ratio: increasing R_d of a depleted uranium-scintillator calorimeter from 0.64 to 1.0 and 2.0 varies the e/h-ratio from 1.10 (no compensation) to 1.00 (compensation) and 0.76 (overcompensation). The same behaviour is observed for the lead-scintillator calorimeter, but with different values of R_d: for $R_d = 0.94$, $e/h = 1.34$ (no compensation), where for $R_d = 4.00$ compensation has almost been achieved (e/h = 1.05).

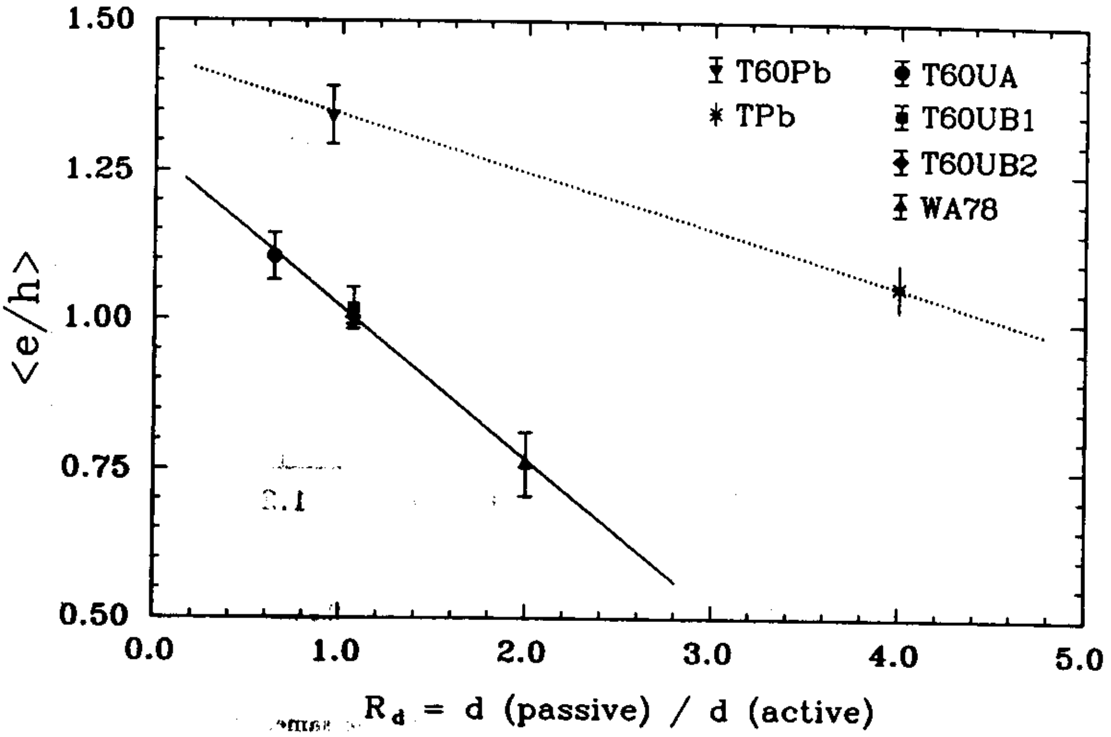

Figure 7.1: The mean e/h-Ratio as a Function of R_d, the Thickness Ratio of the Passive to Active Absorber Plate (Curves are only drawn to guide the Eye)

Comparing the lead-scintillator with the depleted uranium-scintillator calorimeter at almost equal ratio of R_d (T60Pb: $R_d = 0.95$; T60UB1: $R_d = 1.07$) one observes that the hadronic response has been amplified by exchanging the lead with depleted uranium plates. A similar amplification of the hadron response was obtained with a lead-scintillator calorimeter of R_d that is 4 to 5 times greater than that of a uranium-scintillator calorimeter. The variation of the e/h-ratio with the thickness ratio R_d is stronger for the uranium-scintillator calorimeter than for the lead-scintillator calorimeter.

The dependence of the hadronic energy resolution on e/h is plotted in Fig. 7.2. The values are calculated for 10 GeV using the parametrization given in Tab. 7.1. For the WA78 measurement the parametrization subtracted by the contribution from the beam momentum spread has been taken. The influence of the longitudinal nonuniformity of the T60UB1 calorimeter is clearly visible. The correction for the nonuniformity in the T60UB1 calorimeter could only be applied for the mean electron and hadron response. The hadronic energy resolution is therefore still influenced by the nonuniform readout. The measured e/h-ratio of both the T60UB1 calorimeter and the T60UB2 calorimeter are

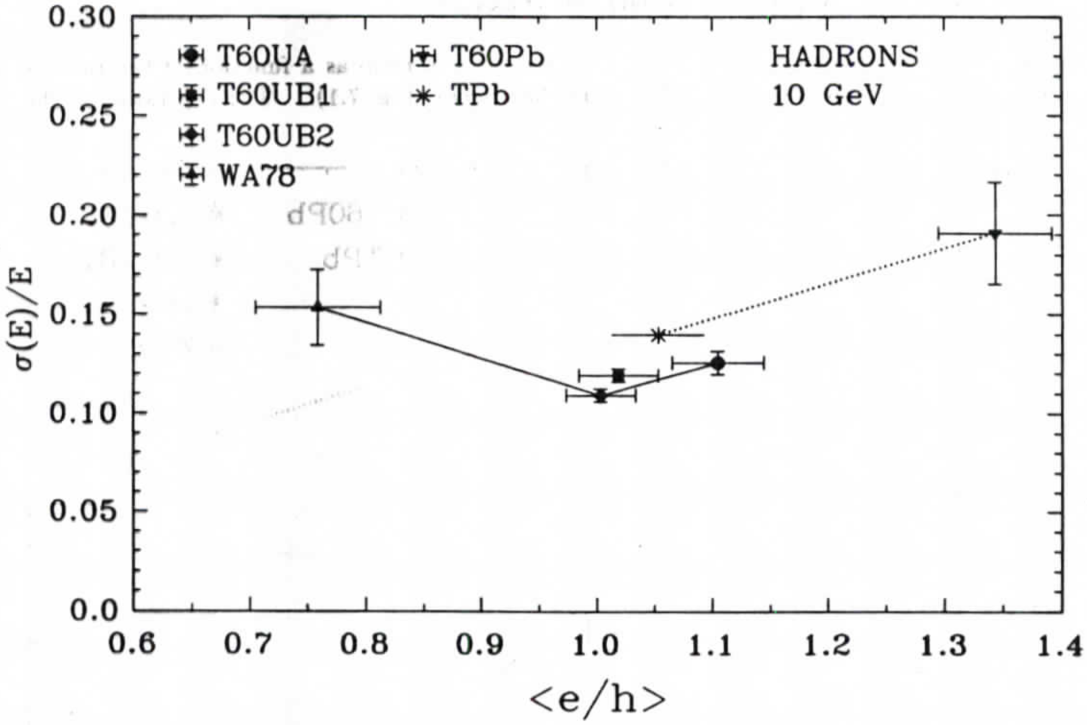

Figure 7.2: The Hadronic Energy Resolution at 10 GeV as a Function of the mean e/h-Ratio (Curves are only drawn to guide the Eye)

still slightly different, although the intrinsic e/h-ratio should be the same. The difference reflects the uncertainty in the different corrections for the longitudinal nonuniformity. The optimum in the hadronic energy resolution of the uranium-scintillator calorimeters is achieved at an e/h-ratio of 1. Although there are only two measurements with lead-scintillator calorimeters of different ratios R_d one observes that the hadronic energy resolution of lead-scintillator calorimeters improves if one approaches $e/h = 1$.

The measured energy resolution for electrons are plotted in Fig. 7.3 as a function of R_d. It is mainly determined by the contribution from the sampling fluctuations that is proportional to the thickness of a sampling layer. One observes that the energy resolution for electrons increases with increasing thickness ratio R_d, independent of the passive absorber material.

7.3 Comparison of the Presented Results with Predictions

In chapter 3.5 the predictions of H. Brückmann and R. Wigmans for the e/h-ratio [BRÜ87, WIG87, ZEU87] and the hadronic energy resolution [WIG87] for different calorimeter configurations are given. The presented measurements can now be compared to those numbers. The predicted values by [WIG87] are approximately only because they have been taken from the figures. The simulated T60Pb configuration simulated by [BRÜ87] is different from the one used for the measurement, namely 6 mm Pb and 5 mm scintillator (SCSN-38). The R_d ratio is 1.2 for which the predicted e/h-ratio is 1.13 [AND87b, ZEU87]. The quoted value in Tab. 7.2 is an extrapolation to $R_d = 1$. The quoted $\tilde{e}/\widetilde{mip}$-ratio is the one for $R_d = 1.2$.

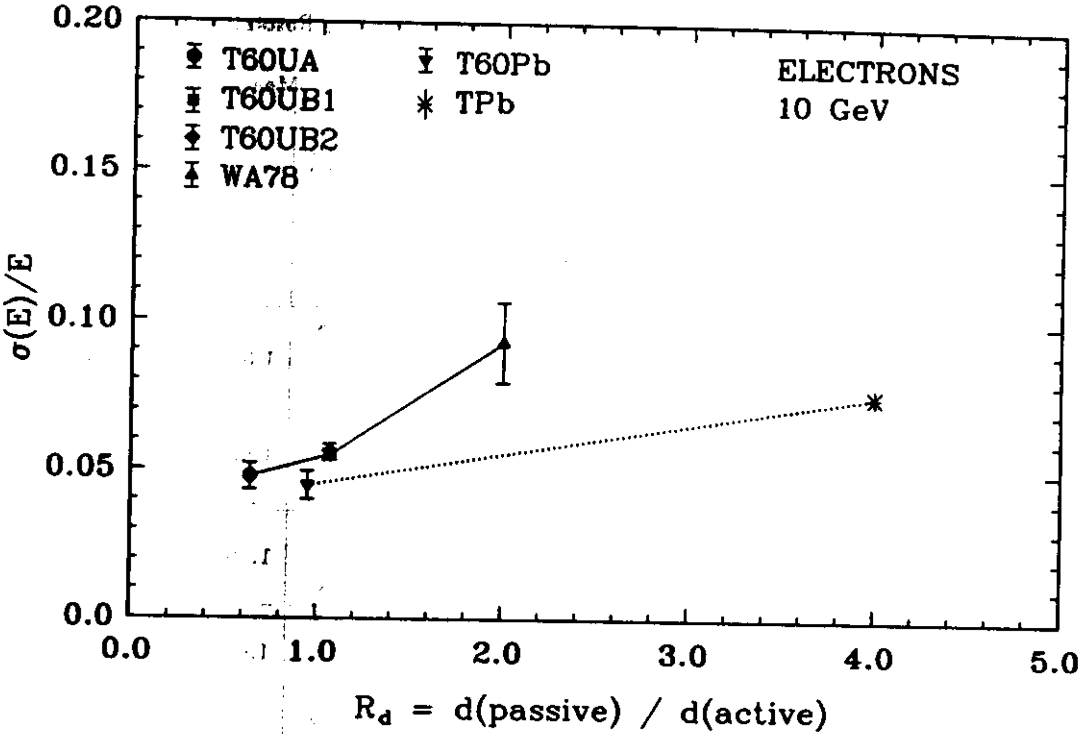

Figure 7.3: The Electromagnetic Energy Resolution at 10 GeV as a Function of the R_d, the Thickness Ratio of the Passive to Active Absorber Plates (Curves are only drawn to guide the eye)

7.4 Comparison with other Measurements

7.4.1 Results obtained with Lead-Scintillator Calorimeters

The results obtained with the lead-scintillator calorimeters can be compared with the result of a measurement done by O. Botner and coworkers. A 3.1 λ_0 deep lead-scintillator calorimeter module surrounded by copper-scintillator calorimeter modules has been exposed to a electron and hadron beam of 5.6, 7.7 and 9.9 GeV [BOT81b]. Each of the calorimeter modules consisted of 100 layers with 5 *mm* thick lead and 2.5 *mm* thick scintillator plates (R_d = 2.0) per layer. The achieved hadronic energy resolution was parametrized as:

$$\frac{\sigma_E}{E}(h) = \frac{0.522}{\sqrt{E[GeV]}} + 0.004\sqrt{E[GeV]}$$

The additive term is caused by the non-containment of hadronic energy. The measured e/h-ratio is 1.37 ± 0.03 at 5.6 GeV and 1.38 ± 0.02 at 7.7 GeV where, according to [BOT81b], the hadron response is slightly overestimated because of the surrounding copper modules.

7.4.2 Results obtained with Uranium-Scintillator Calorimeters

There are more data available from measurements with uranium-scintillator calorimeters. In the following the calorimeter configurations are described briefly before the obtained results for the energy resolution and the e/h-ratios will be compared with the presented measurements.

1. O. Botner et al. performed measurements with three different uranium-scintillator calorimeter configurations [BOT81b], namely:

Table 7.2: Comparison of the e/h-Ratio, the $\tilde{e}/\widetilde{mip}$-Ratio and the Energy Resolution for Hadrons of the presented Measurements with Predictions

	Prediction				Measurement		
	$\frac{\sigma_E}{E}(h) \times\sqrt{E[GeV]}$ [%]	$<\frac{e}{h}>$		$<\frac{\tilde{e}}{\widetilde{mip}}>$	$\frac{\sigma_E}{E}(h) \times\sqrt{E[GeV]}$ [%]	$<\frac{e}{h}>$	$<\frac{\tilde{e}}{\widetilde{mip}}>$
	[WIG87]	[BRÜ87] [ZEU87]	[WIG87]	[BRÜ87]			
T60Pb	~ 48	~ 1.21	~ 1.17	~ 0.60	41.0 ± 4.8 $+$ 6.1 ± 2.1	1.34 ± 0.05	0.65 ± 0.10
TPb	$40 - 41$	1.13	~ 0.95	0.62	44.2 ± 1.3	1.05 ± 0.04	0.75 ± 0.03
T60UA	~ 38	1.08	~ 1.02	0.57	29.6 ± 1.2 $+$ 3.2 ± 0.5	1.10 ± 0.04	0.68 ± 0.04
T60UB1	~ 34	1.03	~ 0.96	0.59	35.5 ± 1.1 $+$ 0.7 ± 0.2	1.02 ± 0.03	0.74 ± 0.03
T60UB2	~ 34	1.03	~ 0.96	0.59	32.9 ± 1.0 $+$ 0.5 ± 0.1	1.00 ± 0.03	0.77 ± 0.05
WA78	$\sim 51 - 63$	0.82	~ 0.81	0.50	37.7 ± 4.8 $+$ 3.4 ± 1.1	0.76 ± 0.05	0.63 ± 0.06

- Configuration I: $187 \times (1.7\,mm\ U,\ 3\,mm\ PMMA)$ $R_d = 0.57$
- Configuration A: $160 \times (2.0\,mm\ U,\ 2.5\,mm\ PMMA)$ $R_d = 0.80$
- Configuration B: $10 \times (2.0\,mm\ U,\ 2.5\,mm\ PMMA)$
  $125 \times (3.0\,mm\ U,\ 2.5\,mm\ PMMA)$ $< R_d > = 1.17$.

2. The HELIOS collaboration used 3.0 mm uranium and 2.5 mm scintillator plates for their calorimeter of $\sim 9\ \lambda_0$ in depth; $R_d = 1.2$ [AKE87].

3. B. Anders et al. [AND86] also performed measurements with a uranium-scintillator calorimeter of $133 \times (3.0\,mm\ U,\ 2.5\,mm\ SCSN\text{-}38)$; $R_d = 1.2$.

4. The WA78 group exposed two different calorimeter configurations to a hadron beam of 135 and 210 GeV [DEV86]:
   - U5: $20 \times (5\,mm\ U,\ 2\,mm\ Fe,\ 5\,mm\ NE110)$;
     $32 \times (15\,mm\ U,\ 2\,mm\ Fe,\ 5\,mm\ NE110)$;
     $48 \times (25\,mm\ Fe,\ 5\,mm\ NE110)$;
     $< R_d$ (uranium part)$> = 2.23$
     (the steel cladding of 2 mm Fe has been neglected in R_d)
   - U10: $20 \times (10\,mm\ U,\ 2\,mm\ Fe,\ 5\,mm\ NE110)$;
     $32 \times (15\,mm\ U,\ 2\,mm\ Fe,\ 5\,mm\ NE110)$;
     $48 \times (25\,mm\ Fe,\ 5\,mm\ NE110)$;
     $< R_d$ (uranium part)$> = 2.62$.
     (the steel cladding of 2 mm Fe has been neglected in R_d).

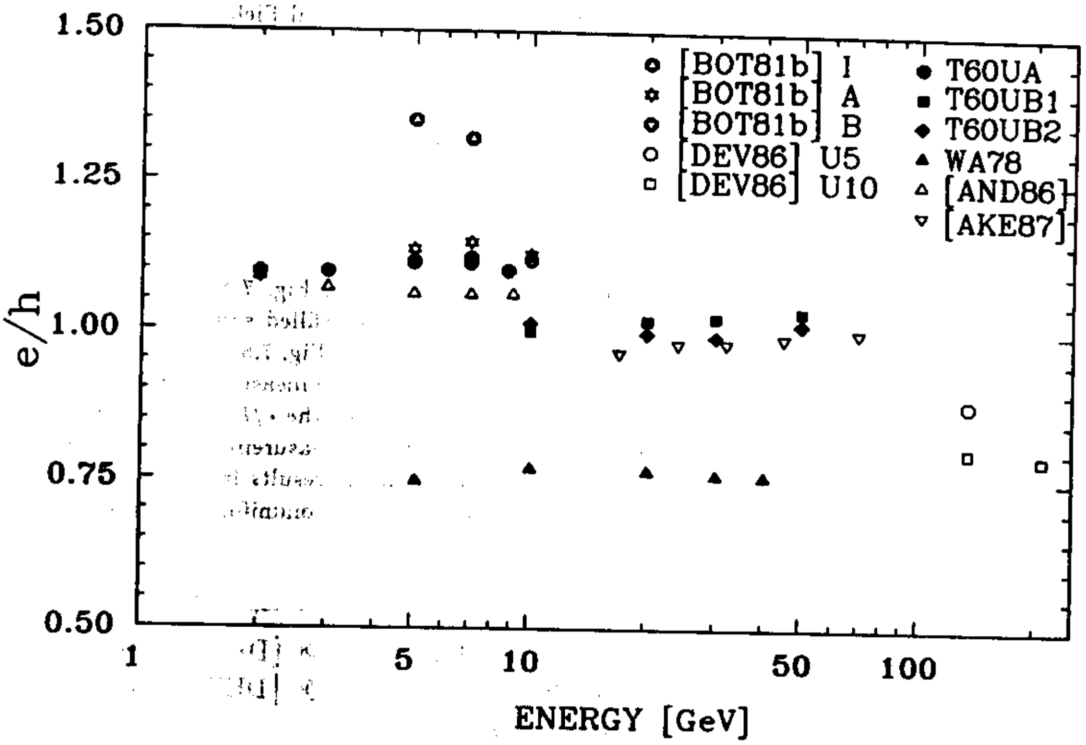

Figure 7.4: The e/h-ratio as a Function of the Energy of these Measurements (filled Symbols) compared to Values of other Measurements according to the given References (open Symbols)

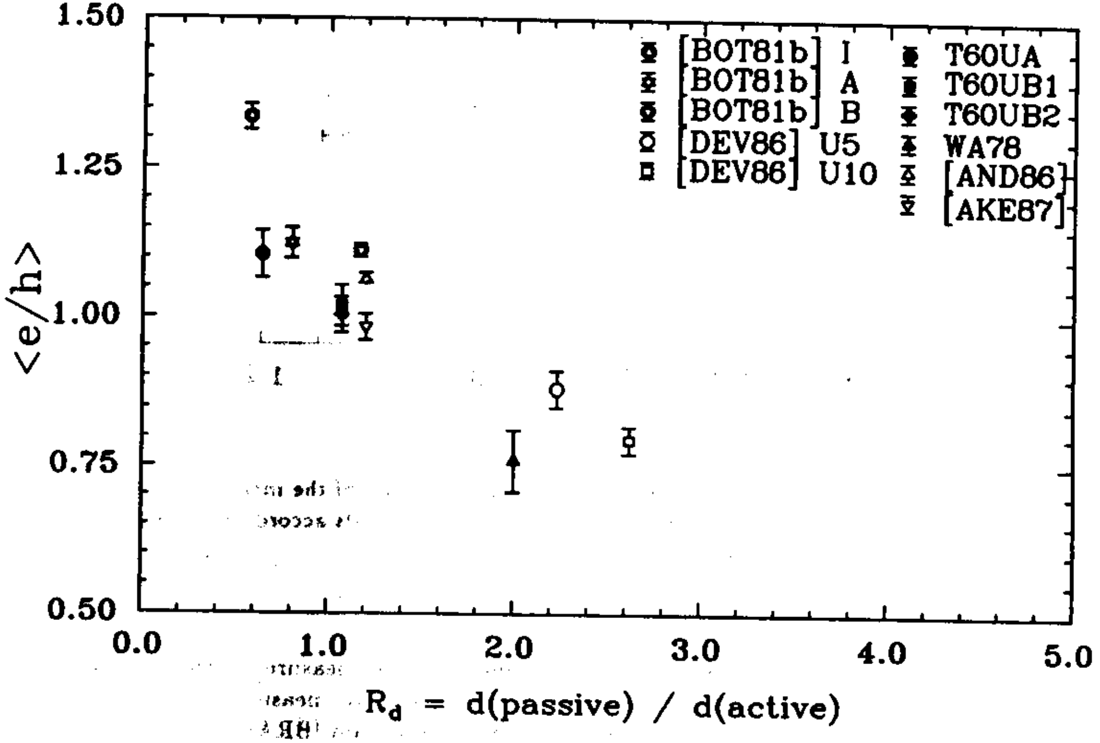

Figure 7.5: The mean e/h-ratio as a Function of R_d of this Measurements (filled Symbols) compared to Values of other Measurements according to the given References (open Symbols)

5. A uranium-copper mixture was used in the calorimeter of the Axial Field Spectrometer (AFS) [AKE85] with the following characteristics:
   $10 \times (2\,mm\ U,\ 2.5\,mm\ PMMA)$;
   $76 \times (3\,mm\ U,\ 2.5\,mm\ PMMA)$ and
   $38 \times (5\,mm\ Cu,\ 2.5\,mm\ PMMA)$, alternatively stacked;
   $< R_d > = 1.47$.

Energy Resolution and e/h-Ratio

The e/h-ratios of the measurements mentioned above are plotted in Fig. 7.4 as a function of energy (open symbols) together with the ones presented in this work (filled symbols). Part of them ([BOT81b, AND86]) are not corrected for longitudinal nonuniformity. Fig. 7.5 shows the e/h-ratios of the presented measurements as a function of R_d in comparison with the measurement listed above. In Fig. 7.6 the energy resolution for hadrons at $10\,GeV$ is plotted versus the e/h-ratio as obtained from the presented measurements in comparison with the results of the measurements mentioned above. The agreement of the measurements presented in this work with the results from the measurements listed above is quite good if one takes the uncertainties of longitudinal nonuniformity, different leakage corrections etc. into account.

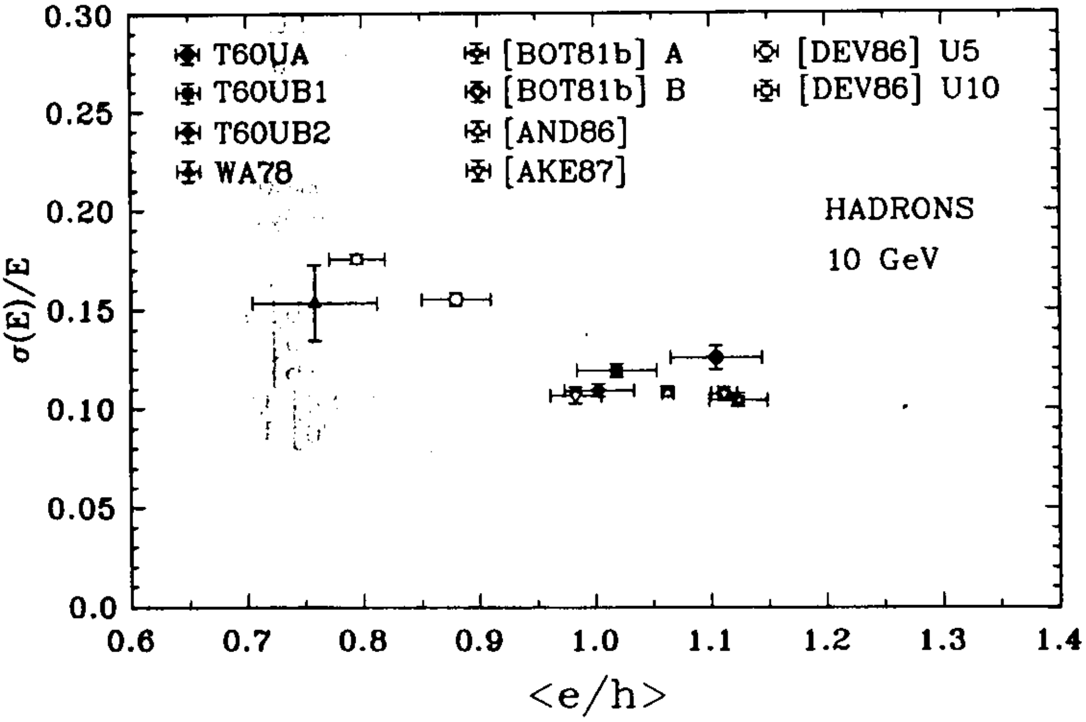

Figure 7.6: The Hadronic Energy Resolution at 10 GeV as a Function of the mean e/h-Ratio, as obtained from these Measurements, compared to the Values of other Measurements according to the given References

Time Dependence of the e/h-Ratio

The variation of the e/h-ratio with the integration time has been measured with the WA78 and the T60UB1 calorimeter. Fig. 7.7 shows the results in comparison to measurements by [AKE85] and [AND86]. Results from calculations done with the DYMO program [BRA86] are also given in this figure [AND87a] for the configuration mentioned in sec. 3.4, Fig. 3.10. The gate length of the T60UB1 measurement has been reduced by $30\,ns$ for the reasons explained in sec. 5.3.6. For the same reasons,

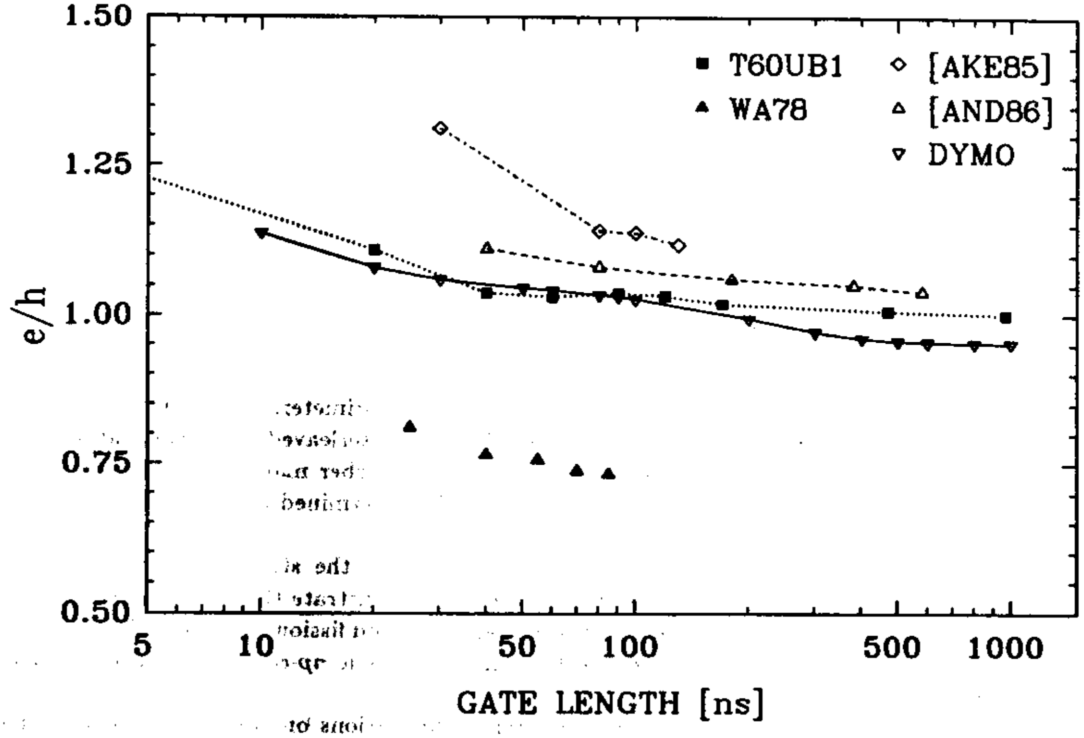

Figure 7.7: The e/h-ratio as a Function of the Gate Length of these Measurements (filled Symbols) compared to Values of other Measurements according to the given References and to Predictions of the DYMO Calculation [AND87a] (open symbols; Curves are only drawn to guide the Eye)

the gate lengths of the other measurements (WA78, [AKE85, AND86]) had to be reduced, but because there is no informations on the effective gate time an estimated offset of 20 ns has been assumed and is subtracted in Fig. 7.7.

Chapter 8

Conclusion

This work presents results of measurements on hadron sampling calorimeters. The calorimeters consisted of lead- or depleted uranium plates of different thicknesses, interleaved with scintillator plates of different thicknesses. From these measurements the kind of absorber material and the optimum thickness of both the active and passive absorber plates could be determined in order to optimize the energy resolution of hadron sampling calorimeters.

The energy resolution of a hadron calorimeter is influenced by the strong fluctuations in the fraction of nondetectable energy. The presented results clearly demonstrate that one can compensate for this fluctuating energy fraction by making use of the spallation- and fission-neutrons released in the hadronic shower. The neutrons generate a measurable signal by elastic *np*-collisions in the hydrogen containing scintillator material.

Comparing the measurements of different calorimeter configurations one observes a relation between the hadronic energy resolution and the e/h-ratio. This is because of the fluctuating electromagnetic fraction in hadronic showers. A calorimeter with an e/h-ratio of 1, i.e. equal response to electrons and hadrons, compensates for these fluctuations leading to the optimum energy resolution of a hadron calorimeter.

The measurements presented here have been performed to investigate how compensation can be achieved. The results for the hadronic energy resolution and the e/h-ratio are summarized as follows:

- 4.75 *mm Pb*, 5 *mm* Scintillator

$$\frac{\sigma_E}{E}(h) = \frac{(41.0 \pm 4.8)\%}{\sqrt{E[GeV]}} + (6.1 \pm 2.1)\% \qquad < \frac{e}{h} >= 1.34 \pm 0.05$$

- 10 *mm Pb*, 2.5 *mm* Scintillator

$$\frac{\sigma_E}{E}(h) = \frac{(44.2 \pm 1.3)\%}{\sqrt{E[GeV]}} \qquad < \frac{e}{h} >= 1.05 \pm 0.04$$

- 3.2 *mm DU*, 5 *mm* Scintillator

$$\frac{\sigma_E}{E}(h) = \frac{(29.6 \pm 1.2)\%}{\sqrt{E[GeV]}} + (3.2 \pm 0.5\%) \qquad < \frac{e}{h} >= 1.10 \pm 0.04$$

- 3.2 *mm DU*, 3 *mm* Scintillator, without graded light filter

$$\frac{\sigma_E}{E}(h) = \frac{(35.5 \pm 1.1)\%}{\sqrt{E[GeV]}} + (0.7 \pm 0.2)\% \qquad < \frac{e}{h} >= 1.02 \pm 0.03$$

- 3.2 *mm DU*, 3 *mm* Scintillator, with graded light filter

$$\frac{\sigma_E}{E}(h) = \frac{(32.9 \pm 1.0)\%}{\sqrt{E[GeV]}} + (0.5 \pm 0.1)\% \qquad < \frac{e}{h} >= 1.00 \pm 0.03$$

- $10\,mm\ DU$, $5\,mm$ Scintillator

$$\frac{\sigma_E}{E}(h) = \frac{(37.7 \pm 4.8)\%}{\sqrt{E[GeV]}} + (3.4 \pm 1.1)\% \qquad < \frac{e}{h} >= 0.76 \pm 0.05.$$

One concludes that

- the optimum energy resolution of a hadron calorimeter has been achieved with a uranium-scintillator calorimeter of $3.2\,mm\ DU$ and $3\,mm$ scintillator where the longitudinal uniformity has been improved by inserting a graded light filter between the scintillator and the wavelength shifter;
- the e/h-ratio depends on the ratio R_d, i.e. on the thickness ratio of the passive to the active absorber plate of a sampling calorimeter; the ratio R_d can be used to tune e/h;
- the hadronic energy resolution of a sampling calorimeter depends on the e/h-ratio; for $e/h = 1$ the hadronic energy resolution reaches its optimum;
- compensation has almost been achieved with a lead-scintillator calorimeter of $R_d = 4.0$; the dependence of the e/h-ratio on R_d and of the energy resolution on e/h are similar to that of a uranium-scintillator calorimeter;
- an equal energy response for electrons and hadrons has been achieved by varying the thickness ratio R_d of the passive to the active absorber plate. In this way the mean electron response has been decreased while the hadronic response increased via the signal from neutrons;
- the amplification of the hadron response in a calorimeter is due to slow neutrons that deposit their energy in the scintillator by elastic np-collisions; the moderation of the released neutrons to low energies is time dependent leading to a rising hadronic signal with increasing integration time. This behaviour is observed in two measurements (WA78 and T60UB1 calorimeter) and is compatible with other measurements and with predictions from calculations.

The results of the presented measurements are in good agreement with previous measurements. They are also compatible with predictions of simplified [WIG87] and more elaborated [BRÜ86, BRÜ87, ZEU87] calculations.

Appendix A

Energy Loss of Muons in Matter

The *mean* energy loss of heavy charged particles like protons or muons in matter results from inelastic scattering of the charged penetrating particle with the atomic electrons of the medium. A first quantum mechanical treatment of this problem by ignoring the dielectric properties of the medium has been done by C. Møller (1932), H.A. Bethe (1930, 1933) and F. Bloch (1933) ([CRI70], and references therein). The influence of the dielectric properties of the medium on the ionization loss was evaluated with classical methods, at first quantitatively by E. Fermi (1940) and has lateron been calculated numerically by R.M. Sternheimer (1961) with several improvements ([STE84], and references therein). The resulting stopping power formula, known as the Bethe-Bloch formula, for a single incident particle of charge $z = 1$ can be written as follows [STE84], ignoring the shell correction term:

$$-\frac{1}{\rho}\frac{dE}{dt} = \frac{b}{\beta^2}\frac{Z}{A}\left\{2\ln\frac{2\,m_e\,c^2\,\beta^2\,\gamma^2}{I(Z)^2} - 2\beta^2 - \delta\right\}\frac{MeV\,cm^2}{g} \qquad \text{(A.1)}$$

where:

$-\frac{1}{\rho}\frac{dE}{dt}\ldots$	mean energy loss per unit path length in $\left[\frac{MeV\,cm^2}{g}\right]$
$t\ldots$	thickness of material in $\left[\frac{g}{cm^2}\right]$.
$\rho\ldots$	density of the medium in $\left[\frac{g}{cm^3}\right]$
$b = 0.153536\ \ldots$	constant in $[MeV\ cm^2]$, calculated from different natural constants
$\beta = \frac{v}{c}\ldots$	velocity of the incident particle in units of the velocity of light
$\gamma = \frac{1}{\sqrt{1-\beta^2}}\ldots$	relativistic quantity
$Z\ldots$	charge number of the atom of the traversed medium
$A\ldots$	mass number of the atom of the traversed medium in $[g]$
$m_e\ldots$	electron mass in $\left[\frac{MeV}{c^2}\right]$
$I(Z)\ldots$	mean ionization potential of the medium in $[eV]$
$\delta\ldots$	density correction.

In eq. A.1 it has been assumed that the maximum energy transfer E_m between a heavy particle, i.e. $M \gg m_e$, and the atomic electrons is approximately given by:

$$E_m \approx 2\,m_e\,c^2\,\beta^2\,\gamma^2\,MeV. \qquad \text{(A.2)}$$

The density correction as a function of the parameter $X \equiv \log\left(\frac{p}{m_e\,c}\right)$ is given by:

$$\delta(X) = 4.605\,X + a(X_1 - X)^m + C \qquad \text{for} \quad (X_0 < X < X_1) \qquad \text{(A.3)}$$

$$\delta(X) = 4.605\,X + C \qquad \text{for} \quad (X > X_1) \qquad \text{(A.4)}$$

$$\delta(X) = \delta(X_0) \times 10^{2(X - X_0)} \qquad \text{for} \qquad (X \leq X_0) \tag{A.5}$$

(for metallic conductors)

(A.6)

where:

a, m, C, X_0, X_1 ... material specific constants (see [STE84]).

Values of $\frac{1}{\rho}\frac{dE}{dx}$ for some materials have been given in the text; a more quantitative description will be considered here.

As a function of the energy E of the incident particle the ionization loss decreases with $1/E$ in the medium energy range $I(Z) \ll E \ll M c^2$, where M is the rest mass of the penetrating particle. At $E \approx 3 M c^2$ a minimum in the ionization loss occurs while at higher energies the $\ln 1/(1 - \beta^2)$ term dominates, leading to a relativistic rise in the ionization loss. This rise is due to an increase in the maximum transferable energy in a single collision and an increased transverse component of the electric field of the incident particle. The polarization of the medium by the electric field of the incoming particle becomes effective for distant collisions, an effect that is known as density effect. The density effect is much stronger in easily polarizable materials like organic scintillators than in gaseous media which leads to a less pronounced relativistic rise in organic scintillators. In the stopping region at very low energies the ionization loss becomes high before the particle reaches the end of its range and the ionization loss drops rapidly to zero.

So far the *mean* energy loss of heavy charged particles passing through matter has been discussed. However, the process is a statistical phenomenon with a distribution that in general may have large fluctuations leading to a tail at higher energies. This high-energy tail is due to collisions in which a large amount of energy is transferred to the atomic electron of the target material. The thinner the absorber material, the larger the fluctuations in the total energy loss and hence the more pronounced the tail in the resulting distribution.

An estimation on the number of large energy-loss collisions during the passage of the particle through matter can be derived from the quantity K, which is defined by [CRI70]:

$$K = \frac{\xi}{E_m} \tag{A.7}$$

with:

$$\xi = \frac{b\,Z\,z^2}{A\,\beta^2} \cdot t \quad MeV. \tag{A.8}$$

For a single charged incident particle of charge number $z = 1$, K is the ratio of the total energy loss to the maximum possible energy loss, approximately given by:

$$K \approx \frac{b\,Z}{A\,\beta^2\,E_m} \cdot t. \tag{A.9}$$

The quantity K is useful to distinguish between the different probability distributions that are valid for different estimated numbers of high energy transfers in single collisions of the incident particle. The probability distribution of the energy loss has been developped by L. Landau [LAN44], and a generalization of this distribution was given by P.V. Vavilov ([SCH74, CRI70], and references therein). The Vavilov distribution takes the maximum allowed energy transfer into account. Three cases can be distinguished:

1. $K \leq 0.01$:
   Here the number of collisions with high-energy transfer in each energy-loss interval is small, resulting in a relatively large statistical variation in this number that leads to large fluctuations in the energy loss per interval. The resulting distribution is asymmetric with a long high-energy tail and a broad peak, known as the Landau distribution.

2. $0.01 \leq K \leq 1.0$:
   The energy loss distribution of this intermediate region is well described by the Vavilov distribution. In addition, the distributions are practically Landau ($K \leq 0.01$) and Gaussian in shape ($K \geq 1.0$) [CRI70].

3. $K \geq 1.0$:
   The number of collisions with high-energy transfer in each energy-loss interval is large and the effect of fluctuations is negligible. The distribution is Gaussian.

The *most probable* energy loss corresponding to the peak of the asymmetric Landau distribution is given by:

$$\frac{\epsilon_{mp}}{t} = \frac{b}{\beta^2}\frac{Z}{A}\left\{\ln\frac{2\, m_e c^2 \beta^2 \gamma^2 \,(b\frac{Z}{A}t)}{I(Z)^2} - \beta^2 + 0.198 - \delta\right\}\frac{MeV\ cm^2}{g} \qquad (A.10)$$

where:

$\frac{\epsilon_{mp}}{t}$ ... *most probable* energy loss in $\left[\frac{MeV\ cm^2}{g}\right]$ per absorber plate of thickness t

t ... thickness of absorber in $\left[\frac{g}{cm^2}\right]$.

Values for K are given in Tab. A.1 for two energies and for the materials of interest here. However, the smallest layer unit of all the calorimeter configurations described previously read out more than a single scintillator plate. The resulting muon distribution is a convolution of individual Landau distributions. In addition, the measured signal of muons in a calorimeter layer is influenced by different other effects: i) the statistical distribution of photoelectrons; ii) variations in the amount of light collected from different regions of the scintillator; iii) variations in the path length etc.. If all these fluctuations are assumed to be distributed gaussian one can try to describe the measured muon distribution with a convolution of a Landau with a Gauss distribution.

Table A.1: Values of K as calculated according to eq. A.9 for Uranium, Lead, Iron and Polystyrene

Material	Energy of incident Muon [GeV]	K
U	1.0	0.013567
Pb	1.0	0.008320
Fe	1.0	0.000679
Polystyrene	1.0	0.000264
U	10.0	0.000235
Pb	10.0	0.000144
Fe	10.0	0.000012
Polystyrene	10.0	0.000005

The Landau density distribution function can approximately be calculated with a program package developped by B. Schorr [SCH74]. For easier handling an analytic expression of the energy-loss distribution given by J.E. Moyal [MOY55] has been used for a convolution with a Gauss function to fit the measured data. The Moyal function is given by:

$$\chi(\lambda) = \frac{1}{\sqrt{2\pi}}\exp\left\{-\frac{1}{2}\left[\lambda + \exp(-\lambda)\right]\right\} \qquad (A.11)$$

The Moyal function is an approximation of the Landau distribution. Deviations from the Landau distribution have been discussed in [MOY55].

Appendix B

Cross Sections for ${}^{238}_{92}U$, ${}^{207}_{82}Pb$ and ${}^{1}_{1}H$

The following nuclear interactions occur in a hadronic shower that arises in a calorimeter with ${}^{207}_{82}Pb$ or ${}^{238}_{92}U$ as passive absorber and scintillator as active absorber containing ${}^{1}_{1}H$:

- high-energy proton induced fission: ${}^{207}_{82}Pb\ (p,\ f)$ and ${}^{238}_{92}U\ (p,\ f)$
- fast neutron ($E_n > 1.2\,MeV$) induced fission: ${}^{238}_{92}U\ (n,\ f)$
- neutron capture: ${}^{238}_{92}U\ (n,\ \gamma)$
- elastic *np*-collisions: ${}^{1}_{1}H\ (n,\ n)$

The cross-sections $\sigma_f\,(p, f)$ for nuclear binary fission of heavy nuclei induced by protons in the energy range from 0.59 GeV to 23 GeV have been measured by R. Brandt and coworkers [BRA71]. Details of the measurement can be found in [BRA71], here only the results obtained for ${}^{238}_{92}U$, ${}^{235}_{92}U$ and ${}^{207}_{82}Pb$ † are given (Tab. B.1).

Table B.1: Fission Cross Sections for (p,f) Reactions in ${}^{238}_{92}U$, ${}^{235}_{92}U$ and ${}^{207}_{82}Pb$

Target Nucleus	Incident Proton Energy $[GeV]$				
	0.59	2.9	11	18	23
	$\sigma_f\,(p, f)\,[mb]$				
${}^{238}_{92}U$	1060 ± 140	1070 ± 160	1090 ± 140	910 ± 90	752 ± 70
${}^{235}_{92}U$	1600 ± 320	–	–	1050 ± 200	850 ± 130
${}^{207}_{82}Pb$	144 ± 18	149 ± 23	–	132 ± 20	105 ± 13

The fraction of the fission-cross section $\sigma_f\,(p, f)$ on the total inelastic cross-section σ_{in} called fissility is plotted in Fig. B.1 as a function of the proton energy in GeV for ${}^{238}_{92}U$ and ${}^{207}_{82}Pb$.

The cross-sections $\sigma_{tot}\,(n, X)$, $\sigma_\gamma\,(n, \gamma)$, and $\sigma_f\,(n, f)$ for ${}^{238}_{92}U$ is plotted in Fig. B.2, B.3 and B.4 [GAR76] as a function of the neutron energy in MeV.

The total and elastic cross-section $\sigma_{tot}\,(n, X)$ and $\sigma_{el}\,(n, n)$ for ${}^{1}_{1}H$ is plotted in Fig B.5.

---

† ${}^{207}_{82}Pb$ means the natural occurence of Pb with $A = 207.21$; the most abundant isotopes are ${}^{206}_{82}Pb$ (26%), ${}^{207}_{82}Pb$ (21%) and ${}^{208}_{82}Pb$ (52%)

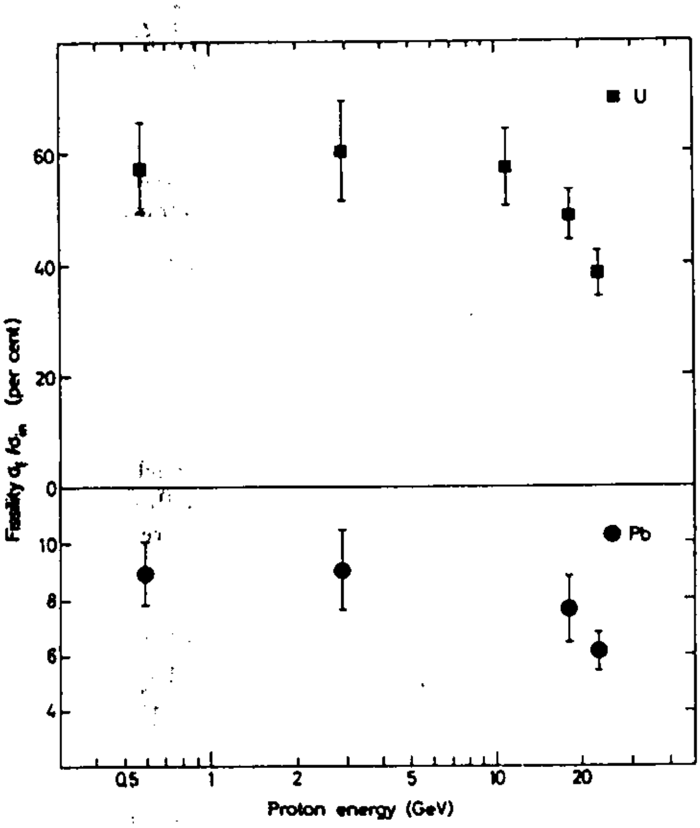

Figure B.1: Fissility $(\sigma_f(p,f)/\sigma_{in})$ in $^{238}_{92}U$ and $^{207}_{82}Pb$ as a Function of the Proton Energy in GeV [BRA71]

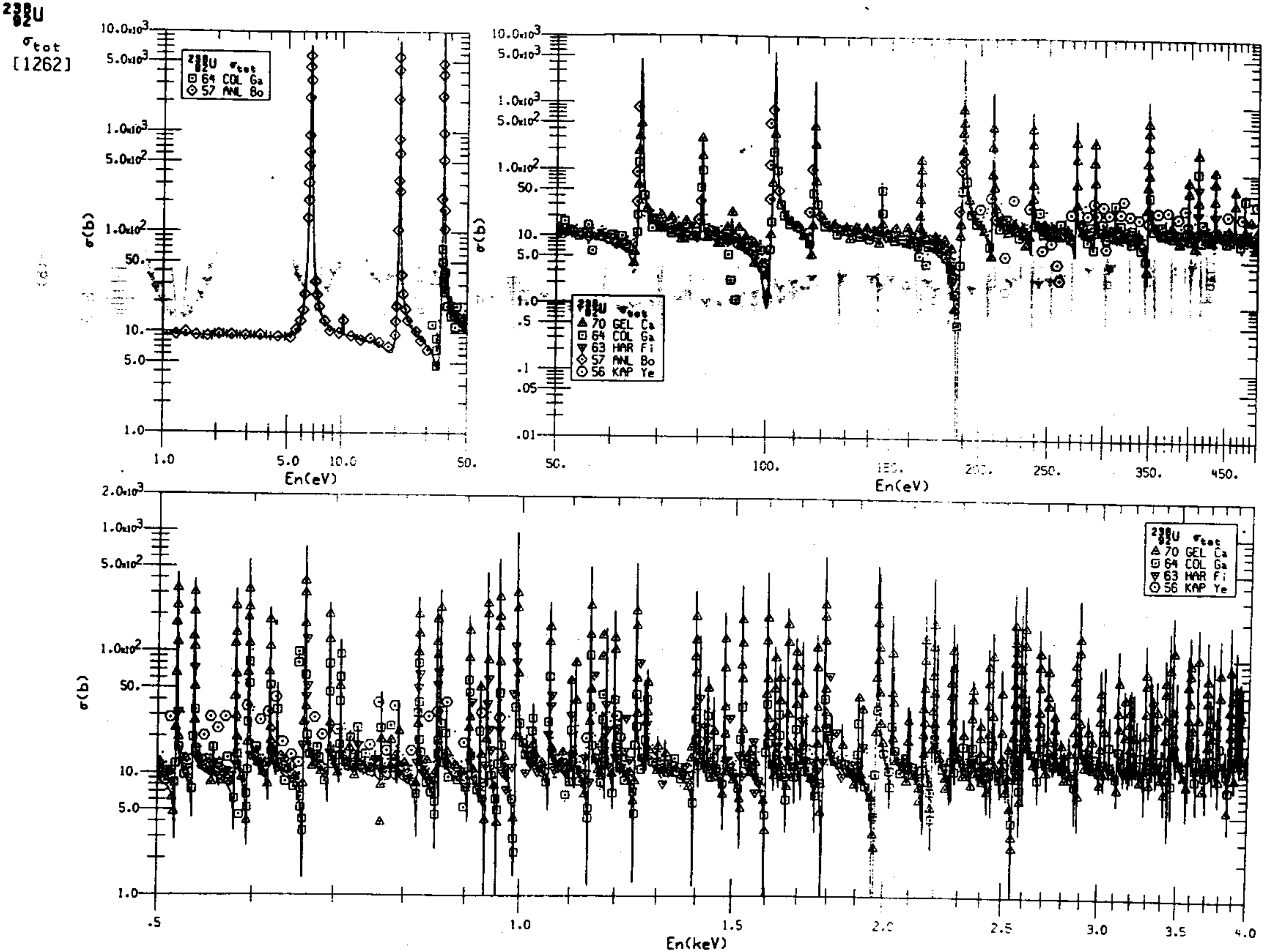

Figure B.2: Cross-Section σ_{tot} (n, X) for ${}^{238}_{92}U$ as a Function of the Neutron Energy in MeV [GAR76]

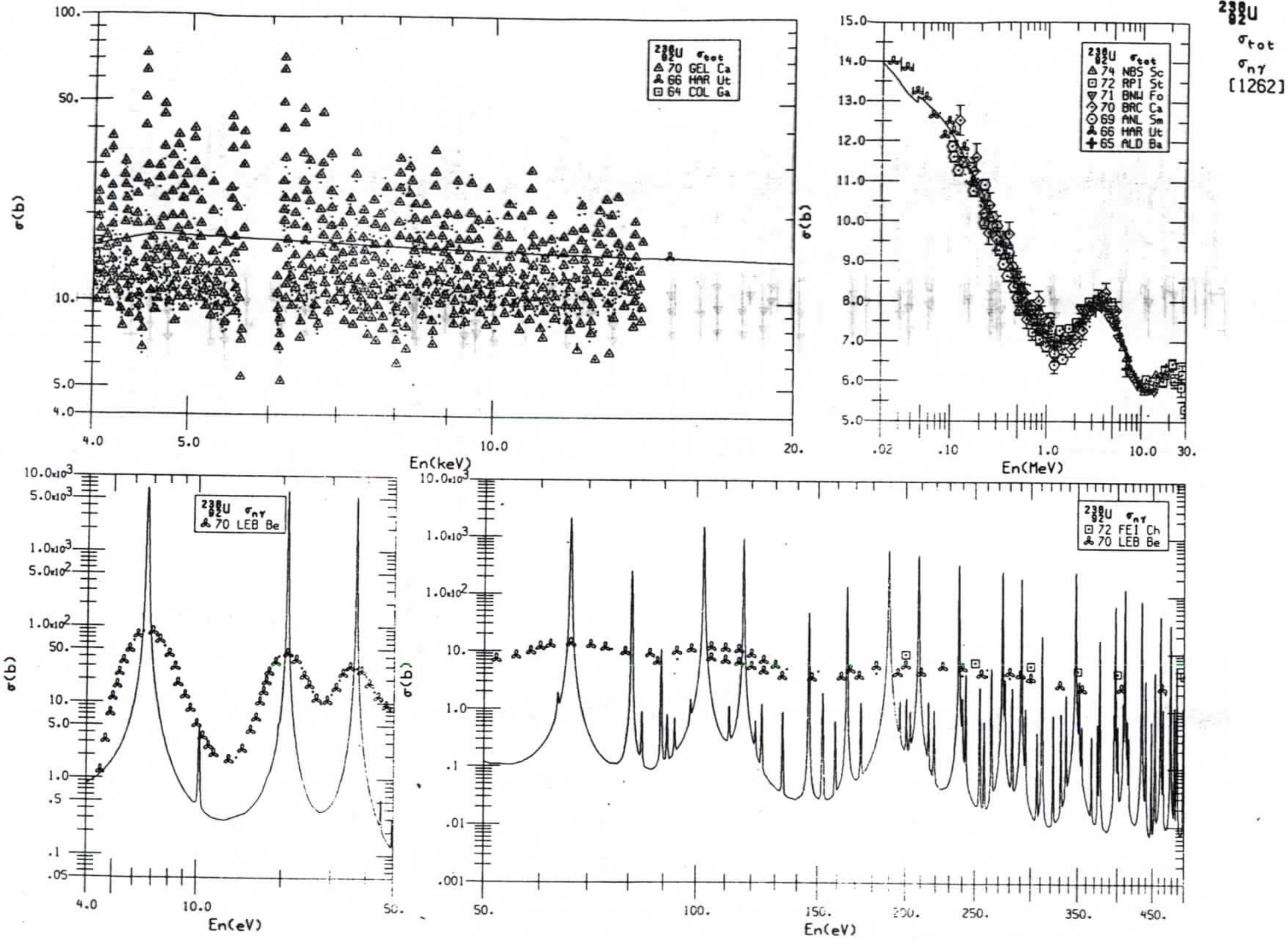

Figure B.3: Cross-Section $\sigma_{tot}(n,X)$ and $\sigma_{\gamma}(n,\gamma)$ for $^{238}_{92}U$ as a Function of the Neutron Energy in MeV [GAR76]

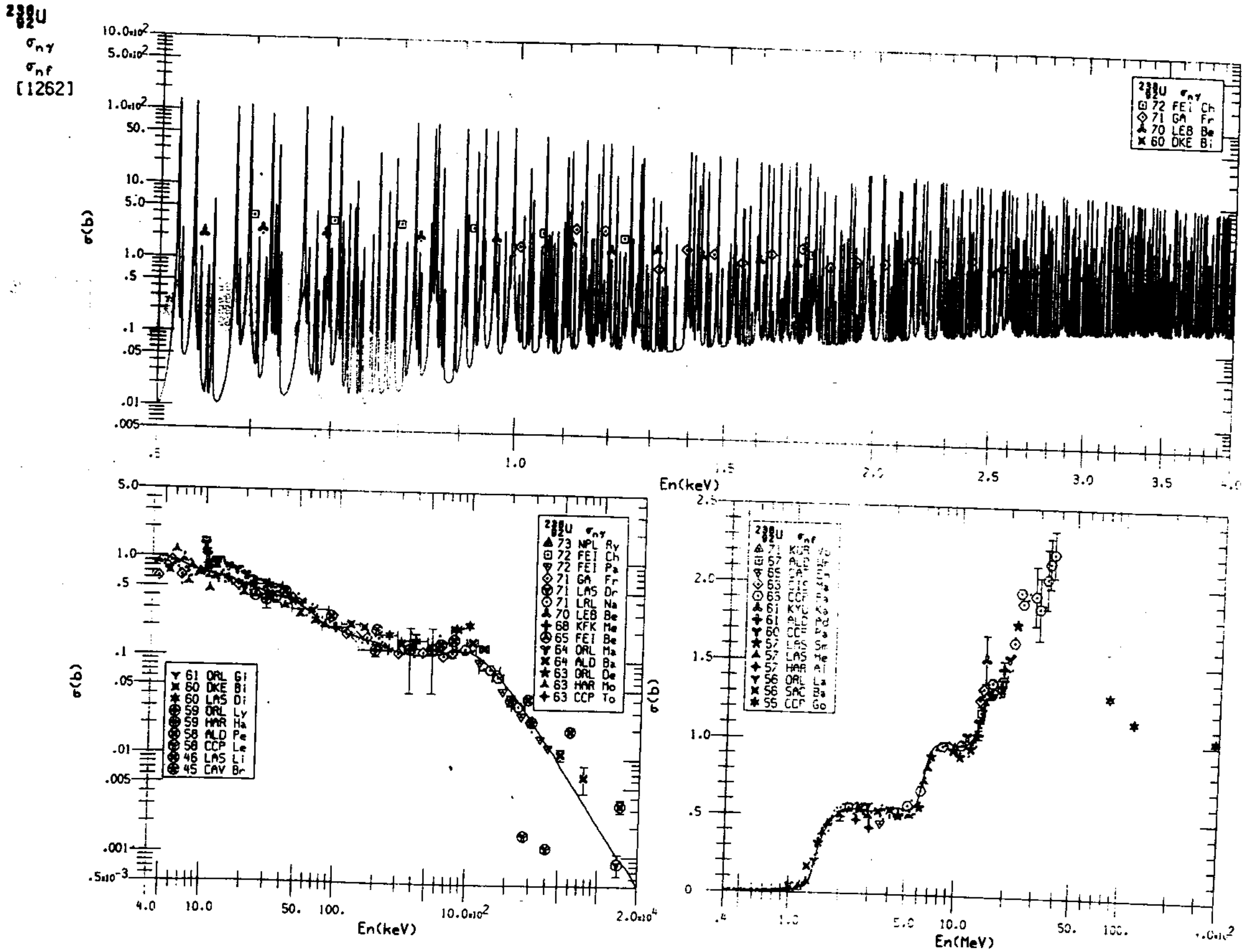

Figure B.4: Cross-Section $\sigma_{\gamma}(n,\gamma)$ and $\sigma_f(n,f)$ for $^{238}_{92}U$ as a Function of the Neutron Energy in MeV [GAR76]

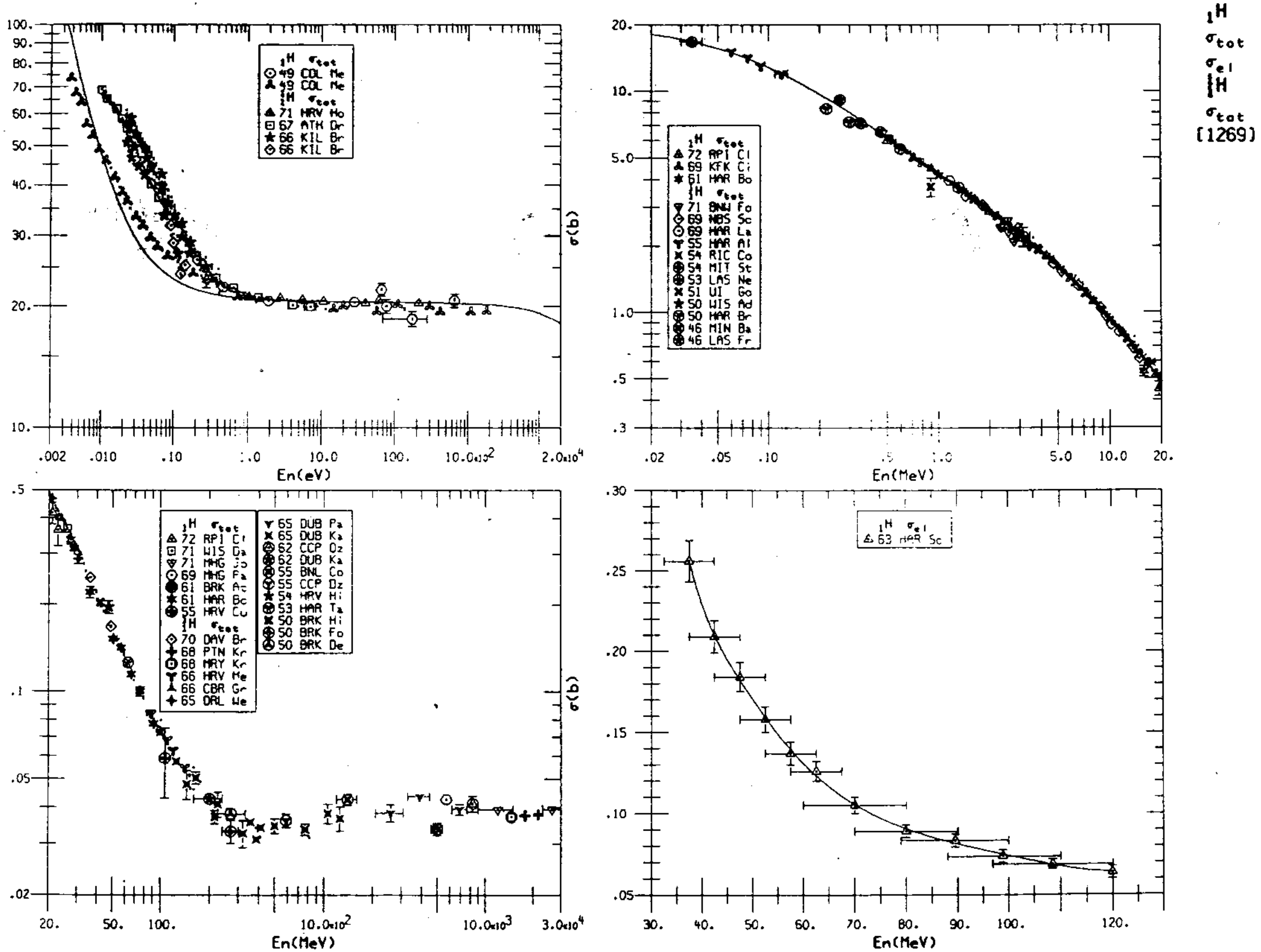

Figure B.5: Cross-Section $\sigma_{tot}(n,X)$ and $\sigma_{el}(n,n)$ for ^1_1H as a Function of the Neutron Energy in MeV [GAR76]

Appendix C

Properties and Decay Schemes of $^{238}_{92}U$

Some of the properties of depleted uranium metal are compiled in Tab. C.1 [BNF74, HOL58].

Table C.1: Properties of Depleted Uranium Metal

Composition	~ 99.7 – 99.8% ^{238}U ~ 0.2 – 0.3% ^{235}U
Melting Point	1132°
Boiling Point	3700 – 4200°
Metal Properties	thermal conductive electrical conductor opaque malleable
Colour	Slow oxidation in air converts the colour through golden-yellow and brown to black
Reactivity	Very reactive with all non-metals Turnings and powder are capable of self-sustaining combustion in air, oxygen, nitrogen and carbon dioxide Slow reaction with water and most acids
Radioactivity	Low specific radioactivity (see below) $\alpha-$, $\beta-$, and γ-radiation: - radiation dose mainly from β-radiation - γ-radiation accounts for less than 5% of the β dose at the surface - α-radiation is of particular significance if material is ingested or inhaled
Toxicity	When inhaled on a mass concentration basis in air comparable with lead
Combustibility	In its massive form not easily burnable, but in form of swarf or finely divided metal

The decay scheme of $^{238}_{92}U$ is sketched in Fig. C.1 [PEG85]. It decays via fourteen steps into the stable $^{206}_{82}Pb$. The specific activity has been given by [PEG85]:

$$T_{1/2}(^{238}U) = 4.5 \times 10^{9}\, y \tag{C.1}$$

$$a_{*} = 2.3 \times 10^{5}\, \frac{decays}{cm^{3}\, s} \tag{C.2}$$

$$N = 3.5 \times 10^{4}\, \frac{decays}{cm^{2}\, s} \tag{C.3}$$

In eq. C.3 a density of $\rho = 19.04\,g/cm^3$ for ^{238}U has been inserted. N gives the measurable number of events on one side of the uranium plate under the assumption of a 2π- geometry.

The radiation of $3\,mm$ thick ^{238}U plates has been measured by C. Pegel and H. Prause [PEG85] using a *Si*(*Li*)-detector for α- and β-particles and a *Ge*-detector for γ-rays. Fig. C.2 shows the measured α- and β-spectrum of ^{238}U, Fig. C.3 the γ- (X-ray)-spectrum of ^{238}U in the energy range of $10-100\,keV$ and Fig. C.4 the γ-spectrum of ^{238}U in the energy range above $100\,keV$.

The event rate calculated from eq. C.4 of all γ-transitions in ^{238}U with energies greater than $0.7\,MeV$ (1.4%) is:

$$N\,(E_\gamma > 0.7\,MeV) = 3.84\,\frac{decays}{cm^2\,s} \tag{C.5}$$

The transition with the maximum energy of $2.29\,MeV$ in the β-spectrum is the one from $^{234}_{91}Pa$ to the ground state of $^{234}_{92}U$ (96.8%). It corresponds to a range of nearly $1\,mm$ in uranium. The approximate countrate of this β-decay with a mean energy of $0.92\,MeV$ and a mean range of about $0.4\,mm$ is:

$$N\,(\beta) \approx 2600\,\frac{decays}{cm^2\,s}. \tag{C.6}$$

The number does not include the low energy β-decays (< 0.2) which have been found with very low intensity ($< 1\%$). The countrate is expected to be slightly enhanced in the energy region below $60\,keV$.

The α-particles do not contribute to the total countrate because of their low range of $7\,\mu m$ in uranium.

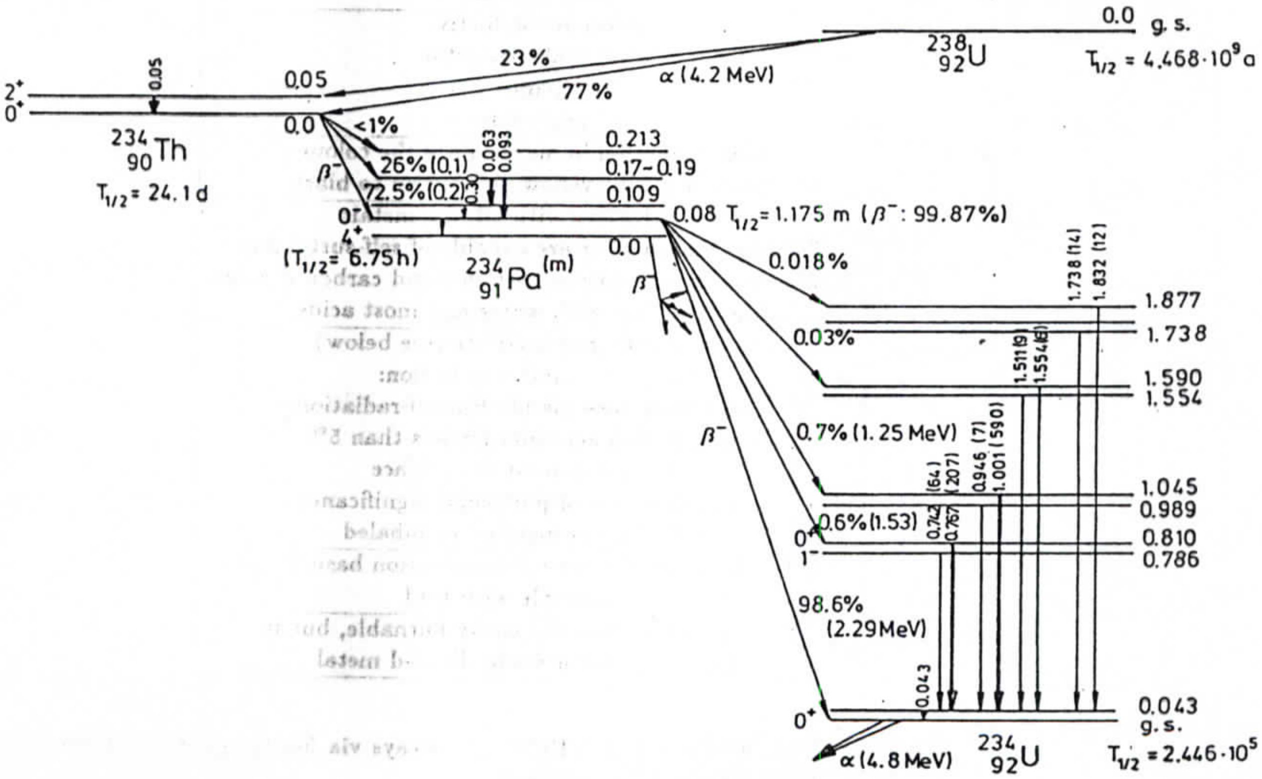

Figure C.1: The Decay Scheme of $^{238}_{92}U$ [PEG85]

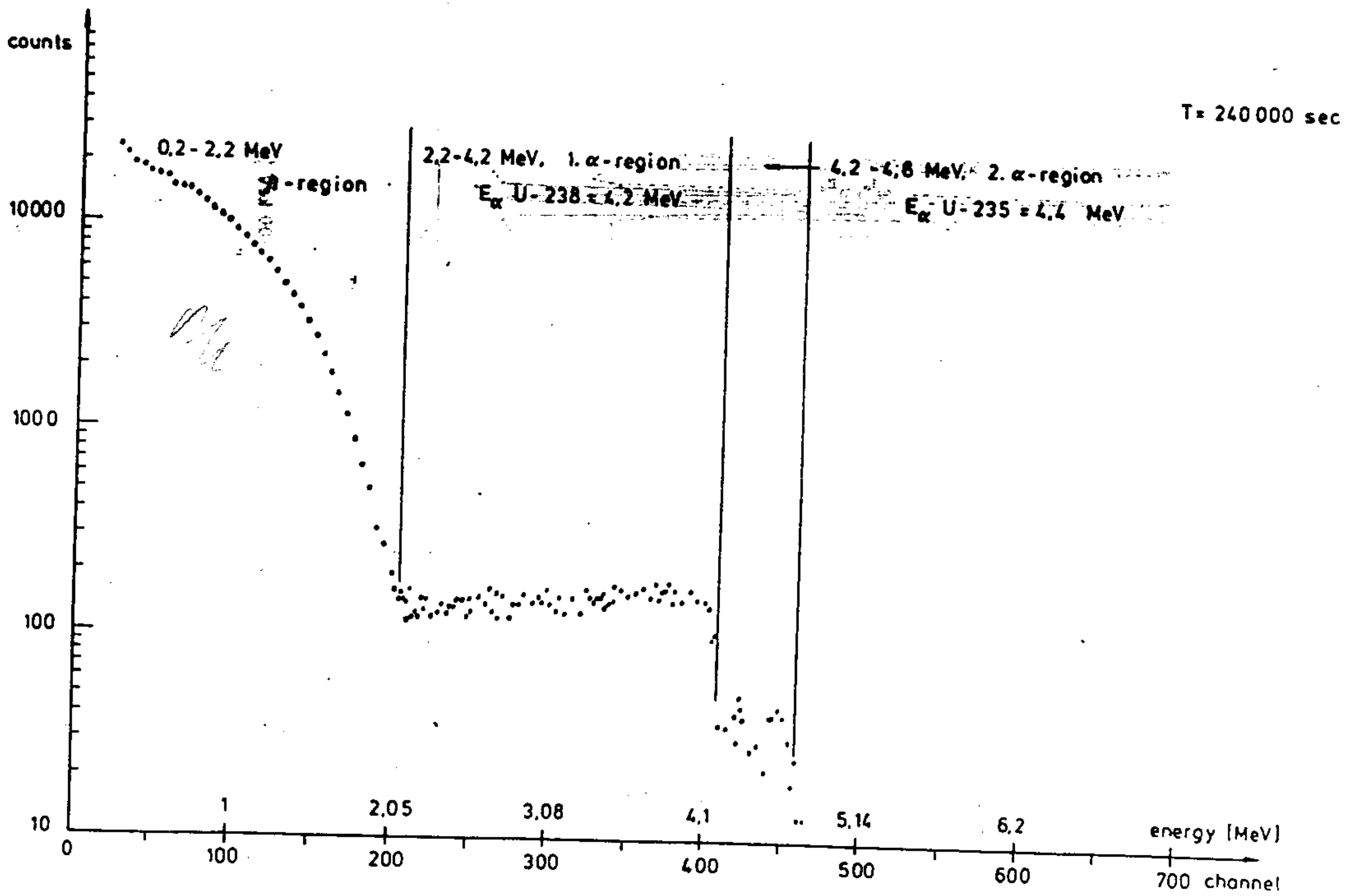

Figure C.2: The α- and β-Spectrum of $^{238}_{92}U$ [PEG85]

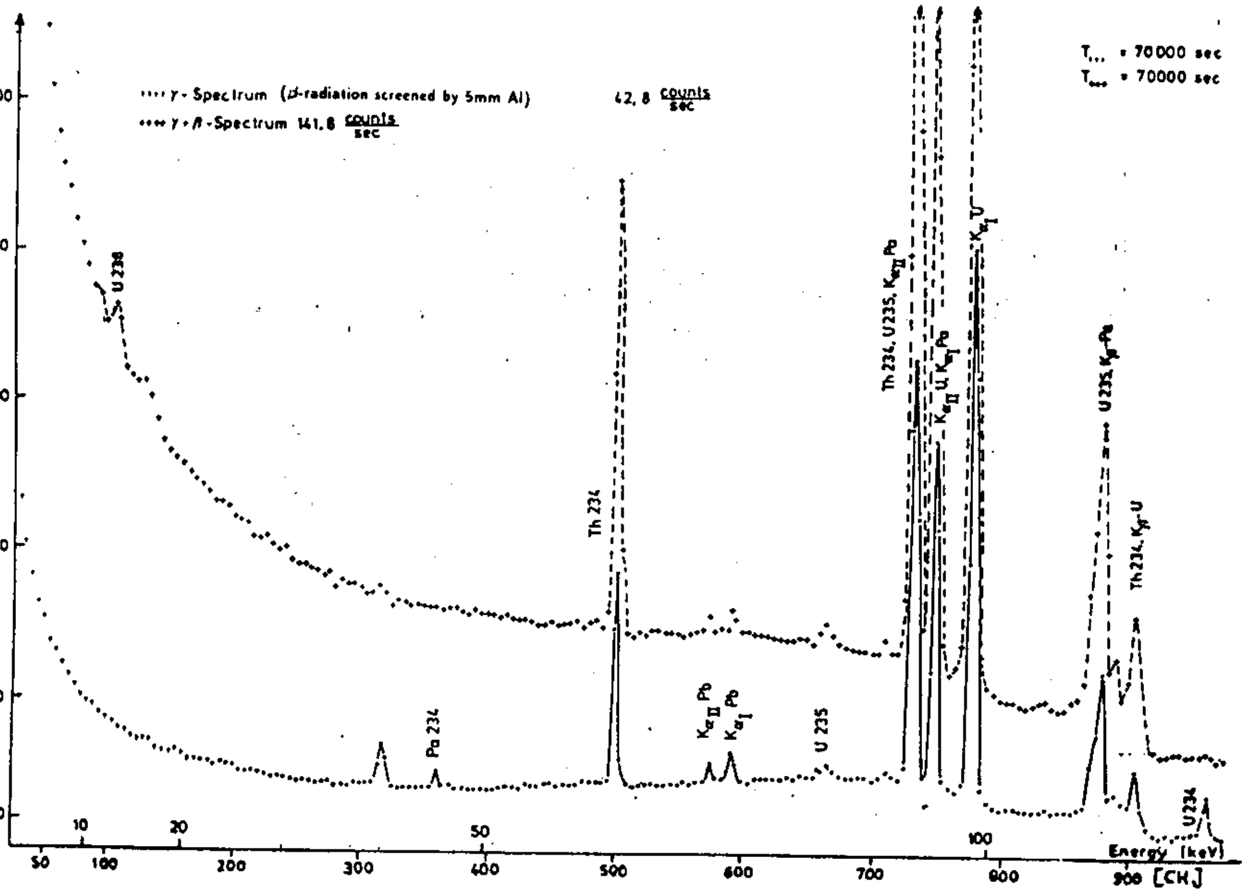

Figure C.3: The γ-Spectrum of ${}^{238}_{92}U$ in the Energy Range of 10 - 100 keV [PEG85]

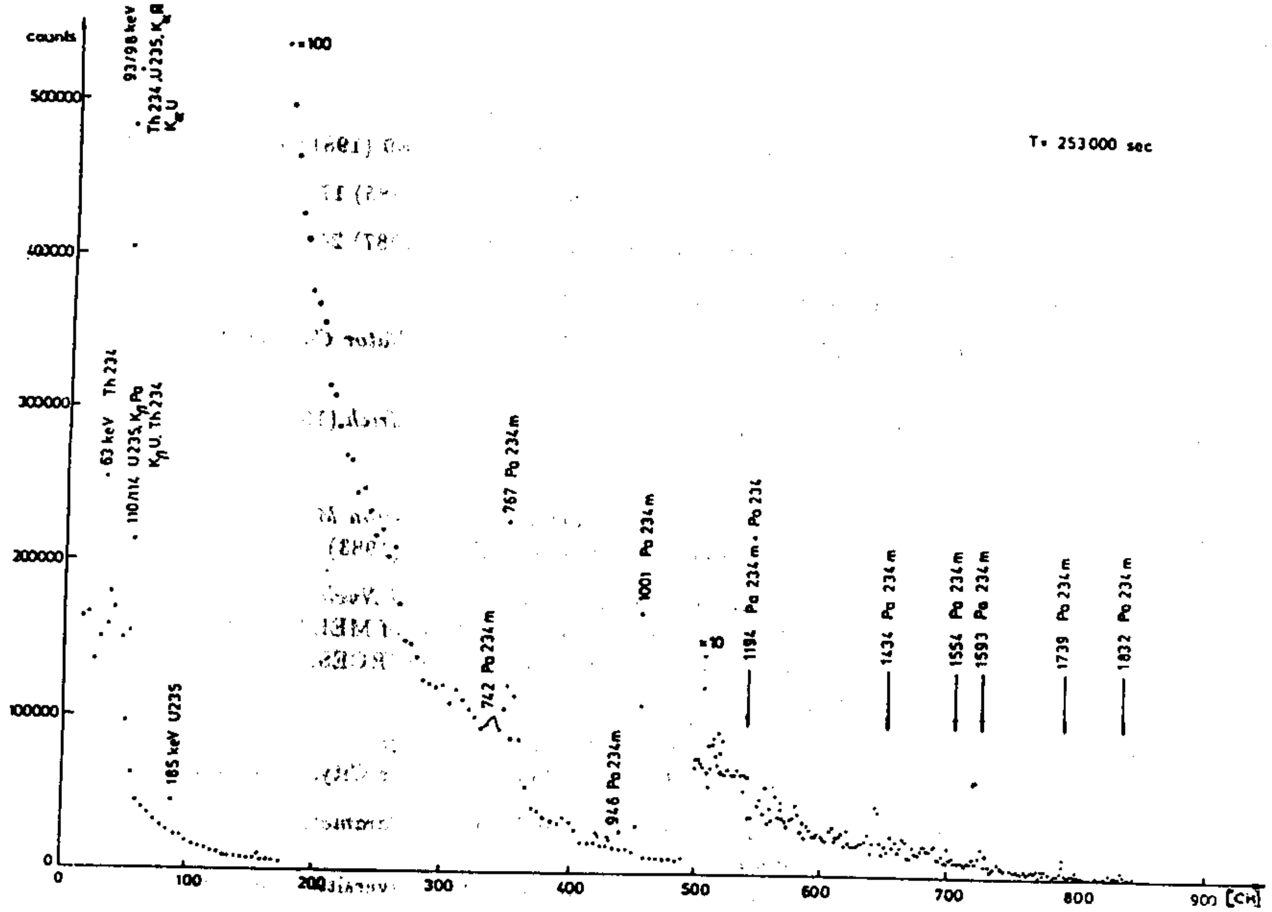

Figure C.4: The γ-Spectrum of ${}^{238}_{92}U$ in the Energy Range above 100 keV [PEG85]

References

[ABR81] **ABRAMOWICZ, H. et al.**; Nucl. Instr. and Meth. **180** (1981) 429

[AKE85] **AKESSON, T. et al.**; Nucl. Instr. and Meth. **A241** (1985) 17

[AKE87] **AKESSON, T. et al.**; Nucl. Instr. and Meth. **A262** (1987) 243

[AMA81] **AMALDI, U**; Phys. Scripta **23** (1981) 409

[AND86] **ANDERS, B. et al.**; *Performance of a Uranium Scintillator Calorimeter;* DESY 86-105 (1986)

[AND87a] **ANDERS, B.**; *DPG Frühjahrstagung Teilchenphysik, Zürich* (1987)

[AND87b] **ANDERS, B.**; private communication

[ARM83] **ARMSTRONG, T. W. et al.**; *An Investigation of Fission Models for High-Energy Radiation Transport Calculations;* Jül-1859 (1983)

[ATC79] **ATCHISON, F.**; *Spallation and Fission in Heavy Metal Nuclei under Medium Energy Proton Bombardement;* in: Proc. of MEETING ON TARGETS FOR NEUTRON BEAM SPALLATION SOURCES, Jülich, Jül-Conf-34 (1980) 17

[BAR87] **BARTEL, W.**; *Status of HERA and HERA-Experiments* Invited Talk given at the 1987 APS/DPF Conf., Salt Lake City, Utah (1987)

[BEC85] **BECKMANN, R. et al.**; *Measurement of Birks' kB-Parameter for Different Plastic Scintillators;* Jahresbericht, I. Institut für Experimentalphysik der Universität Hamburg (1984/85) 71

[BEN75] **BENVENUTI, A. et al.**; Nucl. Instr. and Meth. **125** (1975) 447

[BER86] **BERNARDI, E. et al.**; *Uniformity Test on an Electromagnetic Calorimeter with Wavelength Shifter Readout;* ZEUS Note 86-020 (1986)

[BER87] **BERNARDI, E. et al.**; Nucl. Instr. and Meth. **A262** (1987) 229

[BIR64] **BIRKS, J. B.**; *The Theory and Practice of Scintillation Counting;* Pergamon Press, Oxford (1964)

[BNF74] **BNFL**; *Information Sheet - Health and Safety; Uranium Metal;* British Nuclear Fuels Limited (1974)

[BOT81a] **BOTNER, O. et al.**; Nucl. Instr. and Meth. **179** (1981) 45

[BOT81b] **BOTNER, O. et al.**; Phys. Scripta **23** (1981) 556

[BRA71] **BRANDT, R. et al.**; *The Study of Nuclear Fission Induced by High-Energy Protons;* CERN 17-2 (1971)

[BRA85] **BRAU J. & GABRIEL, T. A.**; Nucl. Instr. and Meth. **A238** (1985) 489 (see also: IEEE Trans. Nucl. Sci. **NS-32** (1985) 697)

[BRA86] **BRANDENBURG, U.**; *Neutronendynamik in Hadronen-Sampling-Kalorimetern;* Diploma Thesis, I. Institut für Experimentalphysik der Universität Hamburg; External Report HH 86-04 (1986)

[BRÜ85] **BRÜCKMANN, H.**; *Hadron Calorimetry - A Puzzle of Physics;* in: Proc. of WORKSHOP ON COMPENSATED CALORIMETRY, Pasadena; CALT-68-1305 (1985)

[BRÜ86] **BRÜCKMANN, H., ANDERS, B. & BEHRENS, U.**; *Hadron Sampling Calorimetry - A Puzzle of Physics - ;* DESY 86-155 (1986)

[BRÜ87] **BRÜCKMANN, H. et al.**; *On the Theoretical Understanding of Sampling Calorimeters;* DESY 87-064 (1987)

[CAS87] **CASHMORE, R. J.**; *The Physics at ep Colliders;* Ox. Nucl. Preprint OUNPL 75/86, to be published in: Proc. of BERKELEY CONFERENCE ON HEP (1986)

[CAT87a] **CATANESI, M. G. et al.**; Nucl. Instr. and Meth. **A253** (1987) 222

[CAT87b] **CATANESI, M. G. et al.**; Nucl. Instr. and Meth. **A260** (1987) 43

[CHA72] **CHANDLER, K. C. & ARMSTRONG, T. W.**; *Operating Instructions for the High-Energy Nucleon-Meson Transport Code HETC;* Oak Ridge National Laboratory Report ORNL-4744 (1972)

[CHA80] **CHARM** Collaboration: **DIDDENS, A. N. et al.**; Nucl. Instr. and Meth. **178** (1980) 27

[CHA87] **CHARM** Collaboration: **DORENBOSCH, J. et al.**; Nucl. Instr. and Meth. **A253** (1987) 203

[CRI70] **CRISPIN, A. & FOWLER, G. N.**; Rev. Mod. Phys. **42** (1970) 290

[DEV86] **DE VINCENZI, M. et al.**; Nucl. Instr. and Meth. **A243** (1986) 348

[DIS85] **DISCUSSION MEETING ON HERA EXPERIMENTS** Genoa, Italy; DESY HERA 85-001 (1985)

[DIS79] **DISHAW, J. P.**; *The Production of Neutrinos and Neutrino-like Particles in Proton-Nucleus Interactions;* Ph.D. Thesis, SLAC-Report 216 (1979)

[DRE83] **DRESCHER, A. et al.**; Nucl. Instr. and Meth. **205** (1983) 125

[ECF80] **STUDY ON THE PROTON-ELECTRON STORAGE RING PROJECT HERA**; ECFA-Report; DESY HERA 80-001 (1980)

[EIC83] **EICHTEN, E. J., LANE, K. D. & PESKIN, M. E.**; Phys. Rev. Lett. **50** (1981) 811

[EXP83] **EXPERIMENTATION AT HERA**; Proc. of the WORKSHOP AT NIKHEF, Amsterdam; DESY HERA 83-020 (1983)

[FAB75] **FABJAN, C. W. et al.**; Phys. Lett. **60B** (1975) 105

[FAB85] **FABJAN, C. W.**; *Calorimetry in High-Energy Physics;* CERN-EP/85-54 (1985)

[FLA85] **FLAUGER, W.**; Nucl. Instr. and Meth. **A241** (1985) 72

[GAB73] **GABRIEL, T. A. & CHANDLER, K. C.**; Part. Accelerators **5** (1973) 161

[GAB78] **GABRIEL, T. A.**; Nucl. Instr. and Meth. **150** (1978) 145

[GAB85] **GABRIEL, T. A.**; *Codes, Models, Cross Sections for Use in Analysing Compensating Calorimeters;* in: Proc. of WORKSHOP ON COMPENSATED CALORIMETRY, Pasadena; CALT-68-1305 (1985)

[GAL86] **GALAKTIONOV, YU. et al.**; Nucl. Instr. and Meth. **A251** (1986) 258

[GAR76] **GARBER, D. I.**; *Neutron Cross Sections Vol. II, Curves;* BNL 325 (1976)

[GEN87] **GENNIS, M.**; *Entwurf und Test eines elektromagnetischen Kalorimeters;* Diploma Thesis; DESY Interner Bericht F14-87-02 (1987)

[HER81] **HERA**; *A Proposal for a Large Electron-Proton Colliding Beam Facility at DESY;* DESY HERA Report 81-010 (1981)

[HIN81] **HINO, Y. et al.**; *Measurement of the High Energy Component of the Neutron Spectrum from a Moderated Source;* in: Proc. of the 5th MEETING OF THE INTERNATIONAL COLLABORATION ON ADVANCED NEUTRON SOURCES, Jülich, Jül-Conf-45 (1981) 489 (see also: p 215, 313, 333 in same Proc.)

[HOF82] **HOFMANN, W. et al.**; Nucl. Instr. and Meth. **195** (1982) 475

[HOL58] **HOLDEN, A. N.**; *Physical Metallurgy of Uranium;* II. Intern. Conf. on the Peaceful Uses of Atomic Energy, Geneva, 1958; Addision-Wesley Publishing Company Inc., Massachusetts, USA

[HUG72] **HUGHES, E. B. et al.**; IEEE Trans. Nucl. Sci. **NS-19** (1972) 126

[HÜB81] **HÜBEL, H.**; *Reaktorphysik;* Nachschrift einer Vorlesung an der Universität Bonn (1981) (and references therein)

[HYD64] **HYDE, E. K.**; *The Nuclear Properties of the Heavy Elements III, Fission Phenomena;* Prentice Hall Inc., Englewood Cliffs, N.J. (1964) 289

[IWA79] **IWATA, S.**; *Calorimeters (Total Absorption Detectors) for High-Energy Experiments at Accelerators; (A Review for TRISTAN Workshop);* DPNU-3-79 (1979)

[KAM83] **KAMON, T. et al.**; Nucl. Instr. and Meth. **213** (1983) 211

[KLA86] **KLANNER, R., LEVMAN, G. & LÖHR, B.**; *An Electromagnetic Calorimeter with Wavelength Shifter Readout;* ZEUS Note 86-003 (1986)

[KRÜ86] **KRÜGER, J.**; *Shower Development in a Uranium/Scintillator Calorimeter (WA78) and the Requirements for the Hadron Calorimeter of the ZEUS Detector;* ZEUS Note 86-019 (1986)

[LAN44] **LANDAU, L.**; J. Phys. U.S.S.R. **8** (1944) 201 (English Translation)

[LER86] **LEROY, C., SIROIS, Y. & WIGMANS, R.**;
Nucl. Instr. and Meth. **A252** (1986) 4

[LOH85] **LOHMANN, W., KOPP, R. & VOSS, R.**;
Energy Loss of Muons in the Energy Range 1-10000 GeV;
CERN 85-54 (1985)

[LOH83] **LOHRMANN, E. & MESS, K.-H.**;
Remarks on the Kinematics of e-p Collisions in HERA;
DESY HERA 83-008 (1983)

[LOH87] **LOHRMANN, E.**; *The HERA Machine - Status and Opportunities*
DESY Internal Report F35D-87-01 (1987)

[LON75] **LONGO, E. & SESTILI, I.**;
Nucl. Instr. and Meth. **128** (1975) 283

[LOR87] **LORENZ, E. et al.**; Nucl. Instr. and Meth. **A527** (1987) 512

[MAY79] **MAYER-KUCKUCK, T.**; *Kernphysik;* Teubner-Studienbuch
Stuttgart (1979)

[MOY55] **MOYAL, J. E.**; Phil. Mag. **46** (1955) 263

[MUR67] **MURZIN, V. S.**; *Principles and Application of the Ionization Calorimeter;*
in: Progress in Elementary Particle and Cosmic Ray Physics; ed. J. G. Wilson,
S.A. Wouthuysen; North Holland Publishing Company, Amsterdam,
(1967) Vol. IX, 245

[NEL85] **NELSON, W. R., HIRAYAMA, H. & ROGERS, D.W.O.**;
The EGS4 Code System; SLAC-Report-265 (1985)

[PAP66] **PAPPAS, A. C.**; Zeitr. für Naturforschg. **21a** (1966) 995

[PDG86] **PARTICLE DATA GROUP**; Phys. Lett. **170B** (1986) 38, 48

[PEG85] **PEGEL, C. & PRAUSE, H.**; *Radiation from Thick Plates of Depleted* ^{238}U*;*
Internal Report, Zyklotron - S2/85 (1984)

[PER81] **PERKINS, D. H.**; *Deep Inelastic Lepton-Nucleon Scattering;*
in: Proc. of a NATO Advanced Study Institute on Techniques and Concepts
of High-Energy Physics, St. Croix; ed. Th. Ferbel; Plenum Press, New York
(1981) 279

[PET86] **PETERS, J. H.**; *Untersuchungen an einem Uran-Szintillator-Kalorimeter mit Elektronen und Hadronen;* Diploma Thesis;
DESY Interner Bericht F14-86-03 (1986)

[PRE84] **PRESCOTT, CH. Y.**; *Electromagnetic Shower Development and Applications to Sampling Calorimeters;* SLAC-PUB-3384 (1984)

[ROS52] **ROSSI, B.**; *High-Energy Particles,* Prentice Hall, New York (1952)

[RÜC84] **RÜCKL, R.**; Nucl. Phys. **B234** (1984) 91

[RÜC86] **RÜCKL, R.**; *Physics at HERA - Present Prospects from a Theorist's Point of View;* DESY 86-022 (1986)

[RÜC87] **RÜCKL, R.**; *Physics at HERA*
DESY 87-021 (1987)

[SCH74] **SCHORR, B.**; Comput. Phys. Commun.**7** (1974) 215
(see also: Comput. Phys. Commun. **31** (1984) 97)

[SEG77] **SEGRÉ, E.**; *Nuclei and Particles;* W. A. Benjamin, Inc.;
New York (1977)

[SNQ81] **SNQ-Realisierungstudie zur Spallations-Neutronenquelle,**
Teil I; Hrsg.: Bauer, G. S. et al.; Jül-Spez-113/KfK 3175 (1981)

[SSC86] **SSC Central Design Group**; Report of the Task Force on Detector Research and Development for the Superconducting Super Collider; SSC-SR-1021 (1986)

[STE84] **STERNHEIMER, R. M., BERGER, M. J. & SELTZER, S. M.**;
Atomic Data and Nuclear Data Tables **30** (1984) 261

[TIE87] **TIECKE, H.**; private communication

[WIG87] **WIGMANS, R.**; Nucl. Instr. and Meth. **A259** (1987) 389

[WOL86] **WOLF, G.**; *HERA: Physics, Machine and Experiments;*
DESY 86-089 (1986)

[ZEU85] **ZEUS Collaboration**; *ZEUS - A Detector for HERA, Letter of Intent*
(1985)

[ZEU86] **ZEUS Collaboration**; *The ZEUS Detector, Technical Proposal*
(1986)

[ZEU87] **ZEUS Collaboration**; *The ZEUS Detector, Status Report 1987*
(1987)

Acknowledgement

I am greatly indebted to the following people for their help and support during the past years, making it possible that this thesis could come about:

Prof. Dr. E. Lohrmann for enabling me to start with the thesis, and for his permanent support and guidance all the time when I was working on it;

Dr. R. Klanner for his enthusiasm and dedication in teaching me experimental physics while doing the measurements or looking at the results;

Dr. B. Anders, Dr. U. Kötz, Dr. J. Krüger and Dr. H. Tiecke for enlightening discussions and innumberable conversations about all aspects of physics and beyond;

all the people which have been grouped together for the short time of the measurements, coming from the WA78 collaboration, from the H1 collaboration and most of them from the ZEUS collaboration;

Prof. Dr. E. Hilger, now again at the University of Bonn, who helped me coming to DESY and getting started, and Prof. Dr. R. Wedemeyer, University Bonn, for his kindness in making it possible to get my first impression of the DESY laboratory;

all the students of the TASSO F35 group, with whom I got experienced with an old, but running experiment;

Dr. Ch. Youngman for converting my basic English into an understandable language;

and finally the DESY directorate, in particular Prof. Dr. P. Söding, for granting me financial support during my stay at DESY.